The Carbon Cycle of Galactic Atmospheres: Connecting Star-Formation and Cosmic Gas Flows with the Physical Conditions of the Circumgalactic Medium

Samantha Lucía Garza

A dissertation
submitted in partial fulfillment of the
requirements for the degree of

Doctor of Philosophy

University of Washington

2025

Reading Committee:

Jessica Werk, Chair

Yakov Faerman

Sarah Tuttle

Arianna Long

Program Authorized to Offer Degree:
Astronomy

University of Washington

Abstract

The Carbon Cycle of Galactic Atmospheres: Connecting Star-Formation and Cosmic Gas Flows with the Physical Conditions of the Circumgalactic Medium

Samantha Lucía Garza

Chair of the Supervisory Committee:
Jessica Werk
Astronomy

The diffuse gaseous atmosphere surrounding the star-filled inner region of a galaxy is known as its circumgalactic medium (CGM). Galaxies draw gas from the CGM to fuel star formation; internal processes within the galaxies, in turn produce feedback that ejects gas and material back out into the CGM. This constant cycling of gas allows the CGM to maintain a record of how a galaxy builds its star population and holds key information on how galaxies begin to quench. By investigating this record, we can tell a richer story of a galaxy's past and make strides in predicting its future. In this dissertation I describe the work I have done using observations and analytical models focused on the metal ion C IV to answer two main questions. First, is there a correlation between the pc-scale physics of black hole growth and the global, kpc-scale gas flows of the CGM in observations, and how does this compare to simulations? Garza et al. (2024) suggest that C IV column density does not vary with SMBH mass; however, sSFR is highly correlated with the ionization content of the CGM. This raises the question: what do C IV observations reveal about the ionization state, temperature, and processes responsible for this ionization mechanism in the CGM? Garza et al. (2025) investigates whether a dichotomy exists for C IV between star-forming and passive galaxies ($9.5 \leq \log_{10} M_\star/M_\odot \leq 11.2$). Results are statistically consistent ($\geq$ 99%) with dichotomy findings for C IV in sub-L$\star$ galaxies (Bordoloi et al., 2014) and O VI in L* galaxies (Tumlinson et al., 2011). This suggests that C IV is more O VI-like than "low-ion-like," indicating it traces gas maintained by star formation and/or feedback, unlike other low-ionization state gas (e.g., H I, Si II, C III). In a follow-up paper, we find that C IV and O VI are kinematically coincident but the relationship between these intermediate to high ions and lower ions is not straightforward. To explore the origins of C IV and O VI, we employed a simple cooling flow model under collisional ionization (PI) and find that O VI is very consistent with the predictions for an expected temperature range, while C IV is not consistent and has column densities on average 2.5 times higher than the predictions. Since C IV has a lower ionization energy than O VI, it is possible that C VI has contributions from both the warm/hot phase and from the cool photoionized (PI) phase. Any successful model of the CGM which incorporates multiphase conditions, must result in ionized gas containing C IV and O VI that is kinematically coexist, but "avoids" existing at the same temperature and density. Ultimately, these analyses help us understand the complex relationships governing galaxy star formation rates, feedback from their supermassive black holes, and the contents of their diffuse gaseous halos.

DEDICATION

Those who seek and those who find

– The Starless Sea

To my Mom, Dad, Gabe - the best brother a person could ask for (My Significant Annoyance), Grammy (Mrs. Calabash), Popo, and Halle. This one is for you...

ACKNOWLEDGMENTS

We are showered every day with gifts, but they are not meant for us to keep. Their life is in their movement, the inhale and the exhale of our shared breath. Our work and our joy is to pass along the gift and to trust that what we put out into the universe will always come back.

– Robin Wall Kimmerer, Braiding Sweetgrass

The research in this dissertation was conducted at the University of Washington in Seattle, which sits on the unceded ancestral land of the Duwamish (Dkhw Duw'Absh) and Coast Salish Peoples past and present. I am grateful to have lived and studied here and I honor the Duwamish Tribe and the land itself. Portions of this work were also completed on the lands of the Carrizo/Comecrudo (Esto'k Gna), Coahuiltecan (Tāp Pīlam), Lipan Apache (Ndé Kónitsąąíí) and Borrados (Rayados) peoples of what is now known as the Coastal Plains and Rio Grande Valley of the state of Texas. It was a privilege to grow up on these lands, the lands of *mis antepasadas*, and I am grateful for their lessons and guidance.

A heart is not judged by how much you love; but by how much you are loved by others.

– L. Frank Baum, The Wonderful Wizard of Oz

Though a heart may be judged by the amount we are loved by others, these acknowledgments are my attempt to express the immense gratitude and love I have to the individuals, communities, and institutions who invested in my success. Their immeasurable gifts of mentorship, love, and friendship forever shaped who I am today. My journey to becoming a *doctora* is in large part due to support and for that I am deeply thankful. These words are my gift to back to you.

I've had a wonderful career here, and if I never have the opportunity to say this again: thank you.

– Scottie Pippen, Last Dance, Episode II

To start in roughly chronological order, I would have to begin with the teachers and mentors that shaped my early education. From pre-K to high school, I was fortunate enough to be taught by several incredible individuals including Mrs. Pierce, Mrs. Roechling, Mrs. Merkt, Coach Rangel, Dr. Black, and Mrs. Eheman. I still talk about my classroom experiences and often think about their stories and life lessons. I'm extremely grateful to have been their student and amazed that several of them made time in their day to watch my defense. Within these years I also spent the majority of my time on the volleyball court

and thus were greatly influenced by my many coaches and teammates. In particular I would like to give a special thanks to my favorite coaches including: Coach Sherryl Thomas who was my first volleyball coach and now good friend; Coach Sokol and Coach App who trained me for countless hours and taught me about dedication, grit, humility, and leadership; and last but not least, Coach Scott who taught me how to love repetition and whose humor and juggling skills always made me laugh through the tough days. I carry the lessons and love that all of these wonderful people shared with me and I'm incredibly thankful that they are a part of my story.

There are so many people to thank at the University of Dallas where I did my undergraduate physics degree and my astronomy career started to take off. Firstly, I'd like to thank Dr. Sally Hicks who did my physics major interview and was one of the main reasons I decided to come to UD. I took her intro to physics class my first semester and under her guidance became heavily involved in SPS and Claire Booth Luce lectures; she even helped me apply to my first astronomy research internships. I'd also like to thank Dr. Jacob Moldenhauer who was my academic advisor, teacher, and a champion of my research and goals. I learned so much from his classes and from working as his teaching assistant. I'm grateful for all his helpful advice and his support in both my education and public outreach career aspirations. I would also like to give a special thanks to Dr. Olenick who is just a wonderful human and was always very patient with me in office hours. I am grateful for the exoplanet research opportunities he provided, his excellent teaching style, and his enthusiasm for school events. To round out the physics department, I would like to thank Dr. Flanagan. I'm forever grateful for the trip to CERN that he facilitated for the physics majors studying in Rome; that tour and the road trip through the Alps is one of my most treasured memories from my studies abroad. Finally, I would like to thank some of the other faculty that made my experience at UD special. I would like to shout out Father Thomas, Dr. Hatlie, Dr. Petersen, and Dr. Crider. Each of these professors taught classes that deeply resonated with me and are included in my top 10 favorite professors.

Throughout my undergraduate experience, I was lucky enough to be accepted into three different REUs where I met the most selfless individuals, made lifelong friends, and grew as a young scientist. My first internship, which I learned about through a flyer for the VLA on a road trip to the grand canyon, was through the National Astronomy Consortium. This program opened the door to astronomy graduate school and held my hand throughout the rest of my academic career. A special thank you goes to Lyndele McCain von Schill, Danielle Rowland, and Jessica Harris (Auntie Jess). Without their support and love I would not be where I am today and for that I am so so grateful. Through NAC, I was placed at the University of Wisconsin-Madison and it was there that I worked with Dr. Bob Benjamin and found my love for studying galaxies. I am so thankful for his lessons about introductory astronomy terms, teaching me how to give presentations, and for being part of my support system to this day. I would also like to thank Dhanesh Krishnarao (DK) for teaching me Python and for being a great role model. I'd like to give a special thanks to Audra Hernandez for leading the REU program and for providing programs that introduced me to all things research and graduate school. Lastly, I'd like to thank all the friends that I made during that research experience; that summer was one of the best summers of my life and its is all thanks to Taylor (Mama Tay), CW, Allison (Cat Burglar), and Andy (The Meme Man).

The following summer, I was accepted to work at the National Radio Astronomy Obser-

vatory in Charlottesville, Virginia. There I worked with the wonderful Dr. Amanda Kepley. I am thankful to her for taking the time to teach me the ins and outs of radio astronomy, how to lead international collaborations, and ways to improve my public speaking. I am also grateful that she agreed to continue working with me over the fall such that my work with her became the bulk of my undergraduate thesis. My final REU was with Dr. Matt Ashby at the Center for Astrophysics (Harvard | Smithsonian) during the early days of COVID. I am so thankful to Matt and Dr. Jonathan McDowell for transitioning the program to a virtual format and making a considerable effort to maintain a sense of community during such a trying time. I'm grateful for everything that Matt taught me and especially thankful for his continued mentoring throughout my time as a graduate student. I would also like to give a special thank you to his partner Julianne, whom I am excited to meet in person one day.

Each of these undergraduate research experiences and incredible mentors led me to the University of Washington where this thesis was completed. I couldn't have asked for a better four years that were filled with late night homework sessions, w(h)ine times, writing research papers, wild planetarium karaoke parties, journal clubs, DIGG meetings, pizza lunches, hikes, ski trips, and friendships. If I had to pick the best part of my experience at UW it would have to be the community that I found with the grad students. Y'alls support, friendship and understanding are a big reason I was able to finish this degree. To my official and un-official office mates: Bonni (Bo) Choi, Anika Slizewski, and Lauyrn Williams thanks for letting me yap at all hours and creating such a welcoming place to work. To the Dynamic Duo: Gabby Engelmann-Suissa and David Wang, y'all made my first year one of the best years. To the DnD Crew: Sam Charney, Jake Kurlander, Dr. Steven Stetzler, Tobin Wainer, Kevin Shafmann, and Charlie Willard, thanks for creating such a creative space and accepting all the silliness that was Morella. To the Fab Five: Bo Choi, Andy Tzanidakis, Dr. Tom Wagg, and Megan Gialluca, thanks for all the memories, laughs, and support. I am so grateful we did this together and I know that we will all be friends for life. And lastly thanks to Dr. Dino Bektesecić, Jess Birky, Dr. John Franklin Crenshaw, Rudy Garcia, Chester Li, Dr. Debby Tran, Dr. Lupita Tovar Mendoza, Barbara Benda, Dr. Brianna McKay, Dr. Tyler Gordon, Dr. Akaxia Cruz, Dr. Hannah Bish, and Dr. Trevor Dorn-Wallenstein for being such wonderful friends.

A huge thank you to my mentors at UW. I'd like to thank Dr. Nicole Sanchez for not only being an incredible friend in graduate school but for then being a wonderful collaborator and even better mentor. Thank you for all your simulation wisdom and checking in on me throughout this process. You are someone that I look up to and greatly admire and I hope that your future students know how lucky they are to have you as a mentor. I am so so grateful to Dr. Kirill Tchernyshyov for taking the time to answer my *many* statistics questions and for never making me feel dumb for asking them in the first place. I will never stop appreciating the guidance and support I received from Dr. Yakov Faerman. Not only have you been my collaborator and mentor, you became my friend and I am so thankful to have been at UW at the same time you were. There are not enough words to describe how thankful and grateful I am to have been advised by Dr. Jess Werk. Thank you so much for believing in me and being such a wonderful person to work with. And of course a special thank you to the rest of my thesis committee, Dr. Arianna Long, Dr. Brooke Nunn, and Dr. Sarah Tuttle, thanks for being so supportive of my graduation timeline and for all of your

comments on my dissertation.

Before we wrap up there are a few special people left to thank whom I met during my time in Seattle. Firstly to the Vollies Crew that grew from the small group that met during some *brutal* 8am Friday Vollies to our eventual Sunday Vollies Gang that now is tournament ready. Thanks for playing with me and bringing me back to the court. I'd also like to thank my ice skating buddies for welcoming me into the sport and making lessons so much fun. A special thank you to Kim Brink for being a huge part of my support system. I'm so happy that every year we became better and better friends and am so grateful to have you in my life. And finally to my partner Ben, thanks for making my time in Seattle even better! These past couple years have been filled with so many memories, road trips, laughs, and adventures. I can't wait to see what the future holds for us!

I love you to Saturn and back...

– Sarah and Gabriel Garza

How do I even start to say thank you? I could barely even get the words out at my defense. I felt so loved with how many of you showed up for me on Zoom, in person, and in prayer that day. Thank you so much for being supportive of my goals and dreams. Everyone of you have a place in my heart but I have a few that have earned an extra shout out. To Dorothy Lillig, thanks for being there for me even when you were half a world away. To Honorable Judge Rosie Speedlin Gonzalez, thanks for accepting me as I am. You are one of the coolest people I know and I still want to grow up to be as awesome as you are. To Grammy and Popo, thanks for being the best grandparents a girl could ask for. To my parents I can't even really put into words everything I feel for y'all or what I want to say but know that I love you to Saturn and back too. To my mom, Sarah Garza, thanks for showing me what true strength is and for always answering my calls no matter the time. And thanks for those two whole organic potatoes. To my dad, Gabriel Garza, thanks for all those late nights doing math at the kitchen table and for ferrying me around to all things volleyball. And finally to my best friend, My Significant Annoyance, Little Person, Gabriel Tomás Garza, thanks for being the best little brother ever. I wouldn't want to do this thing called life with anyone else and I want to thank you for just being you.

Whoever is not with us, all you fuckers, go to hell

– Michael Jordan, Last Dance, Episode III

Lastly I'd like to thank everyone that bet against me and did their best to hold me back. Thanks for the challenges and the lessons. Today we move on to bigger and better things and you'll be exactly where I left you.

CONTENTS

CHAPTER 1

INTRODUCTION

Jordan: Starts off with hard work, ends in champagne. Let's start. Teammate: I'd like to ask y'all one question. What time is it? Team: GAME TIME!

– The Last Dance, Episode VII

As a graduate student I spent a lot of my spare time experimenting in the kitchen. My cooking has improved gradually, but I have learned that baking is one of my passions. I love getting a new recipe, reading between the lines of the original bakers thoughts, and adding my own modifications to make something truly special. Baking has taught me that even the slightest changes can make the biggest impacts in how good your end product is. Over-whipping the batter can result in a flat cake, focaccia dough has to have a certain sticky consistency or it won't make the perfect bubbles, if the water temperature is too hot it will kill the yeast and my rolls will become Play-Doh.

As a baker, and aspiring chef, I am lucky to learn from already crafted recipes, but as an extragalactic astronomer, things aren't always as easy as following a recipe. Often, I am like a gardener looking through a cosmic garden for what "ingredients" are available the day I choose to observe. Once I have "harvested" some ingredients, I transition from gardener to cook and begin searching for recipes I can test using what I have gathered. Sometimes what the garden had to offer doesn't match any current recipes and I can't test out a certain recipe yet. Other times what I "harvested" compliments an already published recipe so with slight modifications it turns out better than expected, a delicious discovery! And even when everything is working well, there are other factors to consider: am I using the correct temperature, does the dough have the correct density, do a certain combinations of ingredients reveal factors unaccounted in the recipe?

Over the past four years at UW, it has been my pleasure to observe (harvest) the halos of nearby galaxies (farms or gardens) and test current theories (recipes) using the information collected from metal ions (cosmic ingredients). But before diving into the details of my dissertation work, we must first touch upon the basics of galactic halos. So dear reader, pull up a chair and grab some tea, for I am about to tell you about our current understanding of galactic halos and my proposed modifications to the ever evolving halo recipe.

1 Farm to Table: How To Use Nature's Tracers To Study The CGM

1.1 Where in the Universe is the CGM?

As I mentioned before, I study the halos or atmospheres of nearby galaxies. These halos, also known as the circumgalactic medium (CGM), are the "farms" or "gardens" I have been referring to. The CGM is roughly defined to start at the end of a galaxy's disk or interstellar medium (ISM) and extend to the virial radius of the galaxy (R_{vir}). This gaseous halo has been found to be a rich "farmland" full of cosmic ingredients (e.g. metal lines such as Lyα, H I, O VI, C IV, Mg II, etc) and is subject to several internal processes that can dictate its density, temperature, and ionization (Tumlinson et al., 2017).

My own interpretation of the CGM is shown in Figure 1.1 and is labeled with the different flows that enrich or deplete this farm of its nutrients to support its crop of metals and future stellar nurseries. Building upon this more simplistic artistic representation, I also refer the reader to Figure 1.2, which previews some of the main points which we will discuss throughout this introduction. Without stealing the thunder of the upcoming sections, I want to highlight some of the main themes that these two figures present. Firstly, the CGM

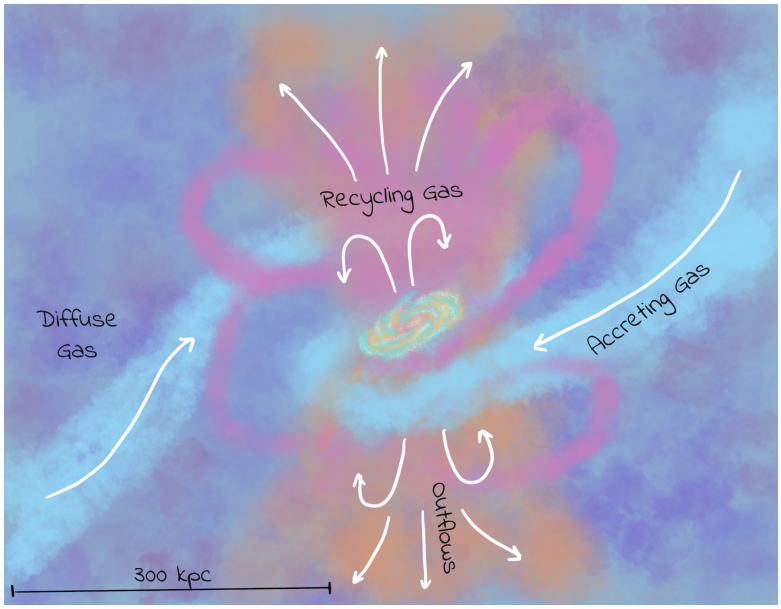

Figure 1.1: My representation of the circumgalactic medium (CGM) depicting the ways material moves in and out of the halo.. The central galaxy (shown with a bulge in red and gaseous disk in blue) is fed by inflowing filamentary accretion from the intergalactic medium (IGM). Outflows, depicted in orange, can also be mixed and recycled back into the galaxy which is shown in pink. The varying tones of purple represent the diffuse gas within the halo that interacts with all these sources.

is roughly a sphere with many responsibilities: it can act like a self sustaining reservoir full of fuel that the galaxy can use later, it maintains a record of the material dumped into it, and it recycles a bulk of its material back onto the galaxy. Secondly, this medium can only be understood by studying both the large scale evolutionary processes (e.g. connecting properties of gas flows in the halo to the intergalactic medium or IGM) and the small scale processes (e.g. describing the multiphase nature gas on the cloud to cloud complex size).

1.2 What Are We Harvesting?

When I say I "harvest cosmic ingredients", I really mean that I observe heavy metals (any element heavier than helium) present in the CGM. Both hydrogen and helium were created a little after the Big Bang, but it look several million years until the conditions were right for heavier elements (like the ones that I observe) to form (Johnson, 2019). This process of producing heavy elements, or nucleosynthesis, is almost entirely due to the life and deaths of stars. The break down of the nucleosynthesis contributions for each element can be seen in Figure 1.3[1]. Due to the dramatic deaths of these stars, stellar winds are generated which carry the metals from the ISM and into the galactic atmospheres where we eventually observe them.

As I think about these elements leaving their stellar origins, about to embark on a long and winding journey to the circumgalactic medium, I sometimes pretend that they feel the same

[1]For more information on how these metals are formed, check out the aside on the stellar life cycle!

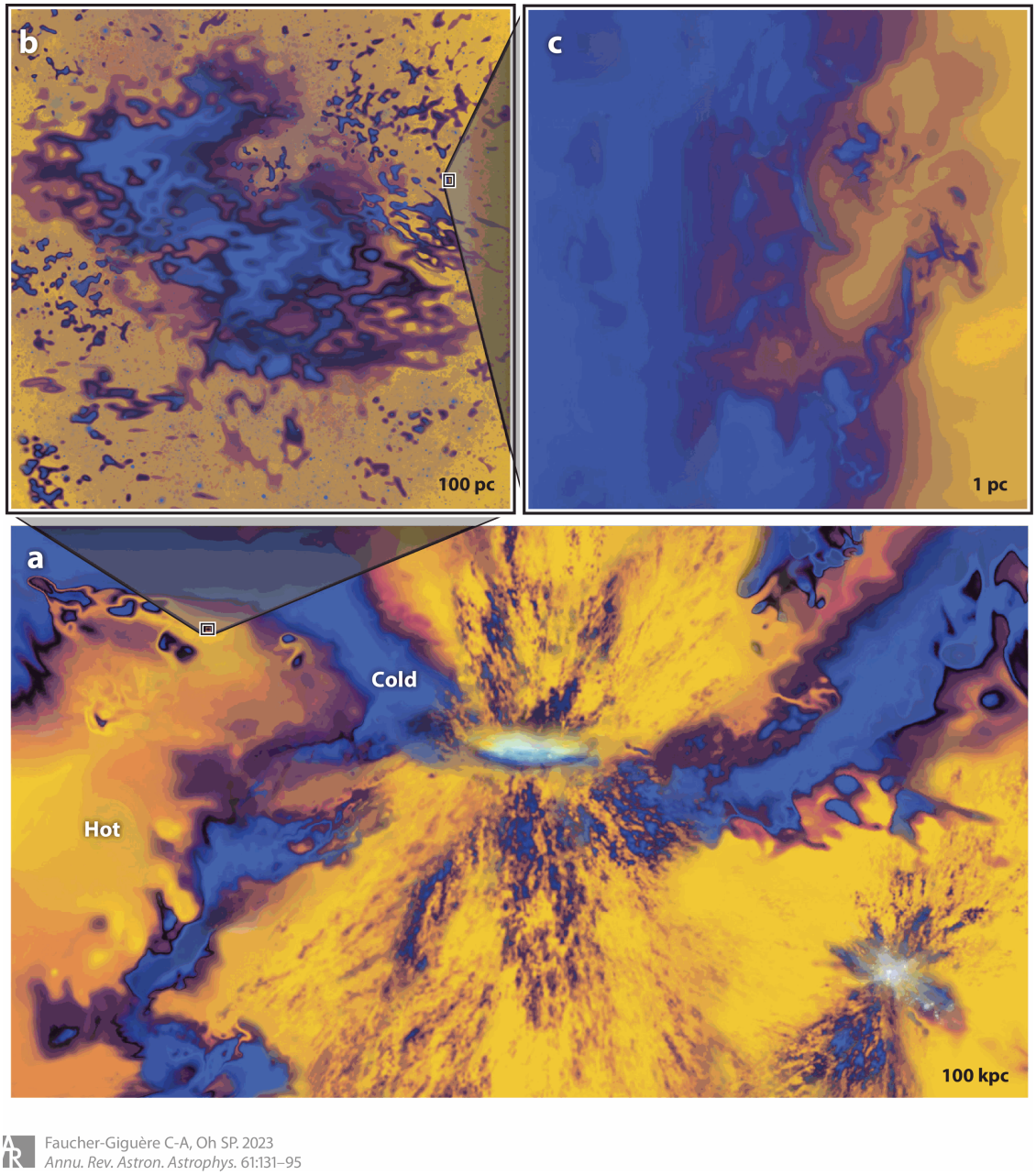

Figure 1.2: Schematic illustration of important properties of the CGM. The CGM is more complex than the simple illustration of Figure 1.1. It involves physics on a wide dynamic range from several hundreds of parsecs to structures well under the parsec scale. The main elements of these halos revolve around the relationship between gas that cools and heats, gas pulled by gravity and the how different temperatures of gas exchange mass, energy, and momentum. The different panels show (a) a central galaxy whose star formation is fueled by a combination of cold (*blue*) and hot (*yellow*) accreting gas. This star formation in turn powers a multiphase galactic wind. The other panels show zoomed in areas of panel (a) where (b) is a highly structured cloud complex and (c) is a turbulent mixing layer. This representation of the CGM is from Faucher-Giguère & Oh (2023).

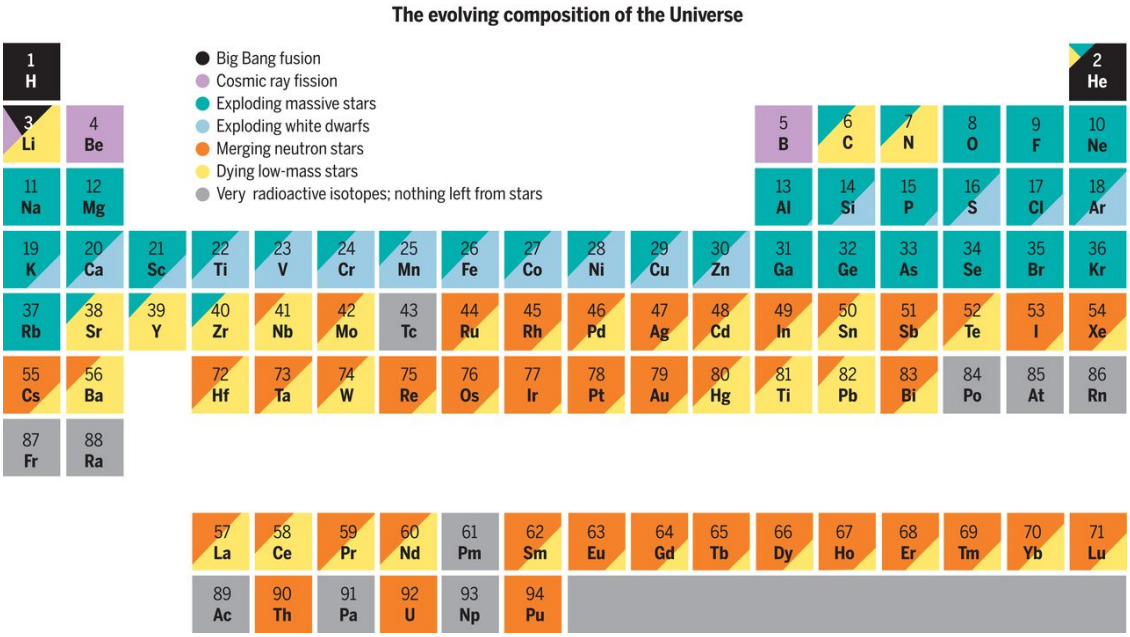

Figure 1.3: Periodic Table of Elements colored by Nucleosynthesis Contributions. Naturally occurring elements found in the Solar System color-coded by the relative contribution of nucleosynthesis sources, scaled to the time of Solar System formation. Artificially made elements or elements produced only through radioactive decay of long-lived nuclei are colored in gray. This figure is from Johnson (2019).

as Bilbo Baggins did when he asked Gandalf *"Can you promise that I will come back?"* and physics that replies *"No. And if you do... you will not be the same"*. This conversation in the Hobbit is a famous moment about the unknown and the transformative nature of journeys and I think it compliments what happens to these elements as the reach the CGM. Each element experiences their own unique transformation dictated by their physical makeup. Their atomic chemistry corresponds to where they will reside within these diffuse halos and how they change along their journey reveals information about the temperature and density of the gas they traveled to. These changes also place limitations on how they are observed or "harvested".

If you are looking for a more detailed dive on the change in elements and the specifics on atom and ion energy level structure, I recommend the well written graduate textbook *Physics of the Interstellar and Intergalactic Medium* by Bruce T. Draine (Draine, 2011). For the purposes of this introduction, I am only including the most relevant details from their text. In that textbook and several others, they describe how the electrons in atoms occupy specific energy levels or electron shells which are fixed distances from the nucleus, with higher energy levels further away. These shells can hold a certain number of electrons each; for example: the first shell (n=1) can hold two electrons and the second shell (n=2) can hold up to eight electrons. By nature, electrons are added to the lowest energy levels first and then fill up the shells moving from inside out.

As these elements travel through mediums of gas on their journey to the CGM or even when they are just living comfortably in the CGM, they often loose or gain electrons by

either absorbing or emitting energy. This changes the structure of their electron shells, their energy level, and also results in a change of their charge. For example, lets say that a Mg atom absorbs an incoming photon on while it is traveling to the CGM in a stellar wind. This photon would need to provide 7.6 eV of energy to remove the electron; this minimum energy required to remove an electron from an atom is called the ionization potential energy (IPE). Once the electron has been removed this Mg atom is now a excited Mg ion with a positive charge (Mg^{+}). Since each element has a different number of electrons they have a unique set of energy levels and therefore a unique ionization energy required to move between levels; for information about other elements, see Appendix D of Draine (2011) for a complete list of commonly observed elements and the various ionization energies needed to move between ionization states. It is customary to identify the different ionization stages of the elements by roman numerals, with I corresponding to the neutral atom, II to singly ionized, III to doubly ionized, and so on. For example, atomic hydrogen is referred to as H I, ionized hydrogen (H^{+}) as H II, and five-times ionized oxygen (O^{+5}) as O VI (Draine, 2011).

Since each element, and its subsequent ions, requires a unique energy, physics dictates that each ionized state has an easily identifiable spectroscopic tracer. It is these natural tracers that we use to confirm that metal ion or cosmic ingredient is in the atmosphere of the galaxy we are observing. So now that we know how to tell what cosmic ingredients are available, let's talk about how we "harvest" them!

1.3 How to Harvest Cosmic Ingredients

On a traditional farm or in a garden, you must abide by the rules of plants you are planning to harvest; the fruits and vegetables have their own timeline for when they are in season and in peak condition to be picked. Then once it is the right season, you need certain tools and machines to have a successful harvest of your desired ingredient. Harvesting the CGM for cosmic ingredients looks a little different, but the same principles apply: you need to pick the right wavelength to get the best observations of the metals in the galactic atmosphere and you need to use certain instruments on telescopes to do so!

A common method of studying the diffuse gas that makes up the CGM utilizes the Cosmic Origins Spectrograph (*COS*; Froning & Green, 2009; Green et al., 2012) on the Hubble Space Telescope (*HST*). This instrument, which was installed in 2009, was designed to be 30 times more sensitive than its predecessors to get far ultra-violet (FUV) observations of faint objects such as quasars (QSOs). With this extra sensitivity, the CGM could be observed using something called an absorption-line spectroscopy experiment. Essentially a QSO, acts like a flashlight that lights up the CGM for the detector to observe. It was with this instrument and this method that we studied the CGM of the Milky Way galaxy and several other nearby galaxies which helped frame our understanding that galactic atmospheres are the constantly recycling tremendous amounts of gas full of hydrogen and other important metal ingredients.

Absorption-line spectroscopy experiments is still one of the most efficient ways of investigating the CGM (e.g. Bahcall & Spitzer, 1969; Bergeron, 1986; Werk et al., 2013) since it provides a direct measurement of the ionized metal species that we wish to "harvest". This is due to its advantages over the other methods: (i) these types of experiments are very sensitive to low column densities, down to $N \simeq 10^{12}$ cm^{-2}, (ii) they can access a wide range of densities and (iii) have an invariance of detection limits according to redshift and the

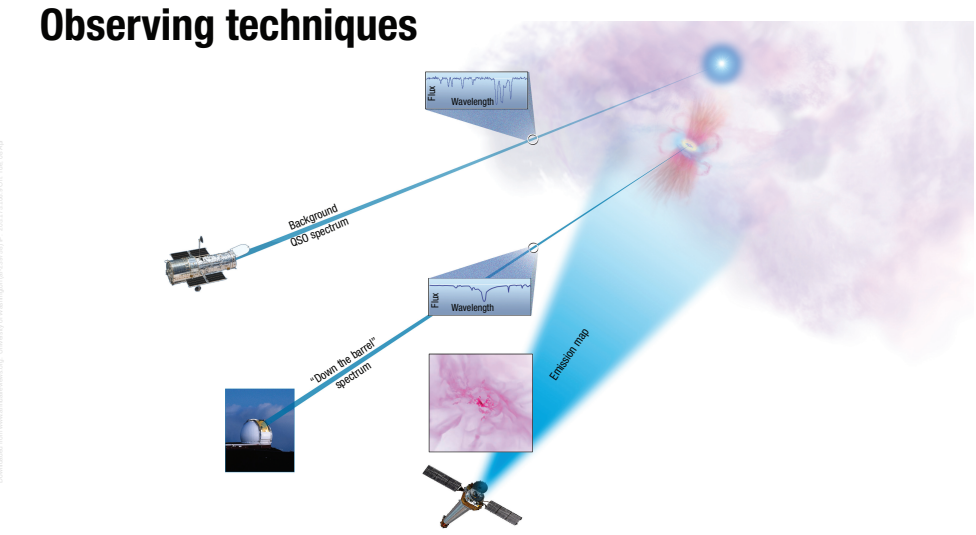

Figure 1.4: Different observing techniques used to study the CGM. For the thesis work described in the following chapters, background quasar absorption line spectroscopy was used to observe the CGM of nearby galaxies. This diagram is a supplemental figure from Tumlinson et al. (2017).

luminosity of the host galaxy (Tumlinson et al., 2017). However, with any methods there are always some drawbacks. Due to the fundamental set up of absorption-line spectroscopy experiments, the absorption observed by the spectrograph is only from a pencil beam line of sight (see Figure 1.4 for schematic of experiment). This means that an observer only gets information (e.g. surface gas density) about the galaxy CGM from that single probe as there is usually only one sightline per galaxy due to the rarity of background quasars that serendipitously lie near a foreground galaxy. As with life there are always exceptions to the rule and for the local Universe (within a few megaparsecs) it is possible to use multiple sightlines to probe the halo of a galaxy (e.g., Lehner et al., 2015, 2020; Bowen et al., 2016). But in general, CGM maps with a good statistical sampling are made from absorption-line measurements from many galaxies.

Due to the massive amounts of absorption spectra from these surveys there is another way to examine the CGM of galaxies. Through "stacking" spectra, sometimes suing hundreds or even thousands of spectra, you can extract faint signals hidden in the absorption. This method reduces the statistical noise you get when looking at the spectra individually so you can get measurements of weak absorption; however the cost is that you lose the information of the individuals at the expense for the bigger picture. Even so, you can still get scientific results when you perform stacking on samples of data that include information about the foreground galaxies (i.e. mass, radius, star-formation rate (SFR), environment, orientation, etc); with this information in hand you can study the variation of the profiles with the galaxy properties (York et al., 2006; Bordoloi et al., 2011; Zhu & Ménard, 2013). The pros

of stacking is that you can detect weak signals in the average properties of gas absorbers but the cons are that you average out any kinematic or ionization structure information which contain important physical implications.

Another method of absorption detection (i.e. cosmic ingredients - ionized metal species) is to use the "down-the-barrel" technique. This type of experiment uses that galaxy's own starlight as the background source to light up the surrounding CGM gas. This method is especially useful when studying star-forming galaxy's inflows and outflows (see §2.1.1 and §2.1.2 for more info) and has been used to do just that for galaxies out to redshifts of $z \sim$ 2-3 (Martin, 2005; Steidel et al., 2010; Bordoloi et al., 2011; Kornei et al., 2012; Rubin et al., 2012, 2014; Heckman et al., 2015; Henry et al., 2015). Using this method you can directly trace current outflows at the galactocentric radii and provide key kinematic information; however, they are limited by the fact that the galactocentric radius of any detected absorption is very unconstrained. Unlike absorption-line spectroscopy that has a defined line of sight, down-the-barrel absorption could be anywhere along the line of sight, which complicates any mass measurement or covering fraction estimate inferred using the spectra.

The final way of "harvesting" ingredients in CGM farms is to use emission-line observations. This method searches for photons emitted directly from the CGM gas. Sounds easy enough but is actually rather difficult in practice. Since the emission measure scales as n^2 and the CGM on average has $n_{\rm H} \sim 10^{-2}$ or less, it is very challenging to find photons. Despite these constraints, this observing technique has been applied to galaxies, but only within ∼10-20 kpc from the targets (Putman et al., 2012). Using the soft X-ray band constraints from using this technique has aided in our understanding of the total mass and baryon fraction of the hot CGM (Humphrey et al., 2011; Anderson et al., 2013, 2016). You can also make emission-line maps using the UV and optical wavelengths (Cantalupo et al., 2014; Prescott et al., 2015; Martin et al., 2015; Hayes et al., 2016), but the challenges from the soft X-ray regime still apply. Emission-line maps in general can constrain the density profile, morphology, and physical extent of the gas more directly than absorption-line measurements can with their pencil beam line of sight (Corlies & Schiminovich, 2016a). But on the flip-side, this technique is extremely difficult and the surface brightness is very small compared to sky and detector backgrounds.

Aside 1.1: Where do Metals Come From?: Stellar Life Cycle

Hi, hello! You want to learn more about stars and the metals that they create? Well you came to the right place. Now, this is just the briefest of asides since I am not a stellar astronomer. If you have more burning questions than I outline for you here then I highly recommended that you do one of three things: (i) google to your heart's desire, (ii) read the wonderful textbook "*Understanding Stellar Evolution*" by Lamers & Levesque (2017), or (iii) find Dr. Tom Wagg or Andy Tzanidakis and pester them with your questions.

A star's life if determined by its mass but life typically begins in a cloud of gas and dust called a nebulae. Gravity causes these clouds to collapse and fragment which form dense regions called protostars. As the protostar collapses, it heats up and begins to spin faster and faster until it reaches the point where nuclear fusion ignites within its core. For a long time the star remains stable and on the main sequence where it gives off a lovely shine and spends its days fusing hydrogen into helium. But when there is no more hydrogen fuel to keep fusing, the star loses a battle to gravity such that the outer layers of the star expands and cools, while the core contracts and heats up. This process leads to the production of heavier elements (i.e. 3-α fusion, C-fusion, Ne photodisintegration, O-fusion, Si nuclear equilibrium, etc)! The star, now in its red giant phase, continues to burn through its remaining fuel until all layers have been expelled. The final stages of a stars life again depend on its mass. For low mass stars, the core is compressed to such a high density that it becomes something called a white dwarf, which is about the size of Earth; this little star remnant slowly cools and fades away. In high mass stars, they end their lives dramatically in supernovae explosions that release the heavily elements that they created out into the surrounding ISM. The core of this stellar remnant can either collapse into a neutron star (very dense object) or a black hole! The heavy elements that were ejected by these supernovae explosions eventually enrich the interstellar medium. Once here they sometimes travel to the CGM and back again, but most elements will be recycled for future stellar nurseries, and thus the life cycle begins again!

1.4 Using the Harvest to Study the Farm

When I was growing up and went grocery shopping with my parents, I wasn't too concerned with where our fruits and vegetables came from. I was more interested in the fruits and vegetables themselves: I got caught up in looking at the variety of bell pepper colors, the feel of a ripe avocado between my sticky fingers, or the soft whispering sound that pinto beans made when I scooped handfuls of them out of open barrels into my mom's waiting shopping bag. But as I got older and more informed about the policies and complex aspects of grown food, I became more interested in the more complicated side of agriculture. I now care more about how the food I buy is grown, what the harvesting practices are of the farmers, and want to know more about the health and longevity of the farm it self. I have become so invested in these types of questions that I now look at the fruits and vegetables in the store with a different point of view than the childhood version of myself did. In essence,

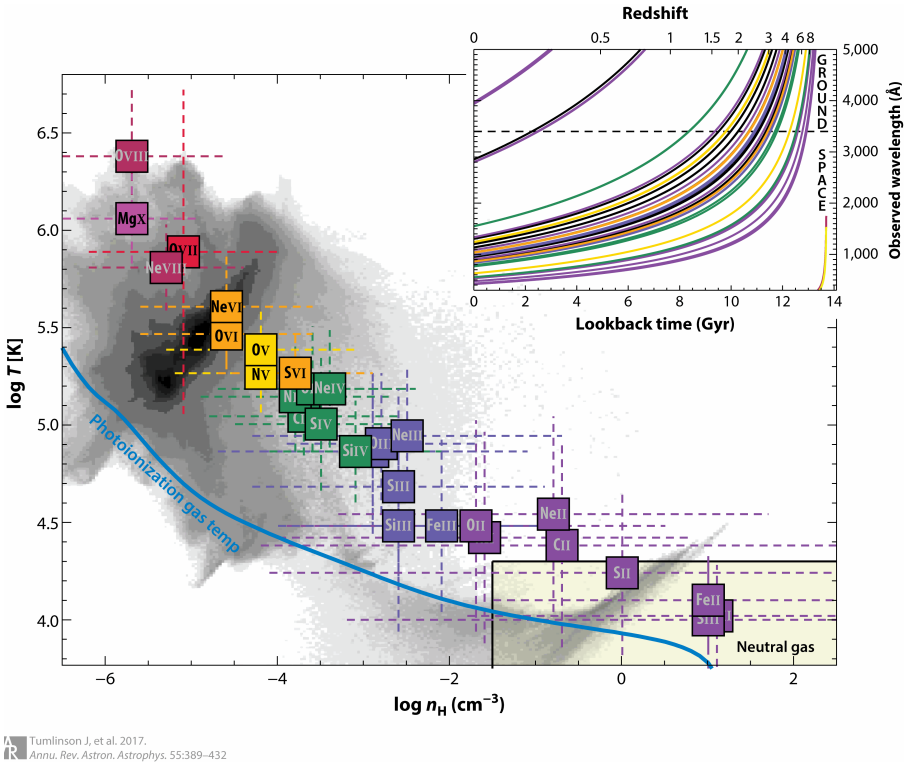

Figure 1.5: Ionized metal species of the CGM as a function of temperature and density. This temperature density diagram includes ions from neutral gas to O VIII (19 $< \lambda_{\rm rest} <$ 6000 Å) within the virial radius. The grayscale background is results from a z = 0 Milky Way mass EAGLE zoom simulation (Oppenheimer et al., 2016). The points are colored according to ionization state, ranging from neutral (I, shaded yellow) to singly ionized (II, purple) to highly ionized (X, magenta). The position of each point is set on the axis where the ion's ionization fraction peaks in collisional ionization equilibrium (CIE) on the temperature axis and a standard photoionization equilibrium (PIE) on density axis Gnat & Sternberg (2007); Oppenheimer & Schaye (2013a). The range bars (dotted lines) represent the temperature and density ranges for each species ionization fraction over half its maximum value (FWHM). This figure is from Tumlinson et al. (2017).

when I am at the store I actively think about what the abundance or lack of certain items can suggest about the nature of their home farm and what that means for the future of agriculture.

In many ways, this type of thinking is what I do in my day job as an astronomer. I use the presence of metal ions and what I know about their nature, as governed by physics, to infer about the physical conditions of the CGM. By the using tools and models, it is possible to characterize the ionization states of the elements. It is through this characterization that we can begin to successfully describe the relationship between the gas and stars in the central part of a galaxy's disk and the diffuse gas of the CGM.

1.4.1 Observables to Physical Properties: Ionization Modeling

To start understanding and describing this relationship, I have to move from the basic observations that we get after we "harvest" metals and transform the information collected to physical properties of the gas. This is a tricky task to complete since the rules of atomic physics, which we touched upon in S1.2, limit ionization states of elements to certain wavelengths. For example, O I and O VI can be seen with strong detectable lines in the far-ultraviolet (FUV: 900 $\lesssim \lambda$ 2000 Å) wavelength range, whereas O III to O V in the extreme ultra-violet (EUV: 400 $\lesssim \lambda$ 900 Å) (Tumlinson et al., 2017). Therefore, to get a full idea of the elemental abundance of oxygen across all ionization states you would need a telescope with the capability to observe across a wide range of wavelengths and be awarded a considerable amount of time on said telescope. As of right now this is kind of telescope is impossible to build! This added observational complexity is why there is still so much to learn about the physical nature of diffuse halos.

Additionally, the ionization states of a single element have different chemical compositions, densities, and temperatures at which they reside making the CGM an even more intricate. Figure 1.5 summarizes common tracers of CGM gas as a function of temperature and density for ionization states from neutral gas to O VIII and is a useful guide that I referenced several times throughout my time completing this dissertation work. The inset diagram on this figure shows the most common strong lines from the species plotted as observed wavelength vs redshift and look back time. In practice we can use the observing techniques we learned about in §1.3 to study subsets of galaxies at different redshifts; for example, FUV lines are available at $z < 1$ with *HST* and $z > 2$ from the ground while EUV lines can be reached at $z \gtrsim$ 0.5-1 with *HST*. Because of these limitations, most studies of the CGM rely on a mixed harvest that includes a variety of ions; in large sample CGM surveys you will see a several low ions (e.g. C, N, Si, Mg; IPE $<$ 40 eV $\lesssim$ 100; T = $10^{4-4.5}$ K), a few intermediate ions (i.e. C and Si; 40 $\gtrsim$ IPE (eV) $\lesssim$ 100; T = $10^{4-5.5}$ K), and a handful of high ions (e.g. Ne and O; IPE $\gtrsim$ 100 eV; T $> 10^{5.5}$ K). Without the full picture of all ionization states, moving from observables to physical properties or, more succinctly, using observations to infer gas density and temperature, we CGM astronomers have to fill the gap through modeling. To make any progress on this front, you have to make several assumptions about the gas that you are modeling. This means that from here on out, any discussions on gas density and temperature can only be understood within the context and limitations of the model used to characterize the ionization state.

There are several types of models available, but the two most foundational classes of models are photoionization equilibrium (PIE), which generally describe low and intermediate ions, and collisional ionization equilibrium (CIE) models, which can well describe high ions. It should be noted however, that these models are not wholly distinct and a combination of the two might be needed to describe what is physically occurring in the gas. For example, collisionally ionized gas may also be affected by incident radiation or much to the dismay of simple modeling have other factors that cause the gas to need more complex modeling than PIE or CIE can handle. However, PIE and CIE models are still very useful and have been implemented by several studies, including my own thesis work (e.g., Bergeron & Stasińska, 1986; Prochaska et al., 2004; Lehnert et al., 2013; Werk et al., 2014; Turner et al., 2015). These studies make use of radiative transfer models like Cloudy (Ferland et al., 2013) which

can build the PIE model. In addition to making assumptions about the ionization and thermal equilibrium, these types of models also assume that the metal ions included in the model arise from a single phase of gas with the same origin. These types of assumptions of a single cloud, single density approximation, have been found to lead to uncertain cloud sizes (Stern et al., 2016; Werk et al., 2014), and don't reproduce all levels of ionization states, which is not ideal when you want to be getting the best constraints possible on the state of CGM gas.

Because of the limitations of PIE and CIE modeling researchers have developed non-equilibrium ionization models which can reproduce intermediate to high-ions that are generally failed to be produced by PIE and some CIE models (e.g. C IV, N V, O VI). These models include, but are not limited to: (a) radiative cooling flows which introduce gas dynamics and self-photoionzation to CIE models (Edgar & Chevalier, 1986; Benjamin, 1994; Gnat & Sternberg, 2007; Wakker et al., 2012); (b) turbulent mixing layers where cool clouds develop thin layers of warm gas under Kevin-Helmholtz instabilities (Begelman & Fabian, 1990; Slavin et al., 1993; Kwak & Shelton, 2010; Kwak et al., 2011; Tan & Oh, 2021; Tan et al., 2021a); (c) conductive interfaces where cool clouds evaporate and hot gas condenses in the surface layer where electron collisions transport heat to the boundary (Borkowski et al., 1990; Gnat et al., 2010; Armillotta et al., 2017); and (d) ionized gas behind a radiative shock most likely produced by strong galactic winds (Dopita & Sutherland, 1996; Heckman et al., 2002; Allen et al., 2008; Gnat & Sternberg, 2009; Grimes et al., 2009). These models are very promising, but as I tend to agree with Tumlinson et al. (2017) which noted that the most accurate description of the CGM will probably come from a combination of PIE, CIE, and complex models.

For your convenience, dear reader, I have included some clarifying definitions. In later chapters we will be using these terms and models to compare to observations, so it is wise to become familiar with them now.

Photoionization: the process where an atom or molecule in space absorbs a photon (light particle) from a nearby energetic source causing it to lose an electron and become an ion. Essentially the light energy is strong enough to kick an electron out of an atom creating a charged particle an contributing to the overall ionization level of the gas.

Collisional ionization: the process where an electron with enough energy from a collision, kicks another electron out of an atom or ion, creating a new ion, essentially ionizing the atom by colliding with it.

Cooling Flow: model for hot gas accretion in halos driven by radiative cooling and neglecting feedback; associated with "hot mode" accretion.

Kevin-Helmholtz instability: a instability that occurs when there is a velocity difference between layers of gas or plasma. For example, motions of cool (T $\sim 10^4$ K) gas clouds within a hot halo can create a Kevin-Helmholtz instability.

Turbulent Mixing Layer (TML): When a Kevin-Helmholtz instability forms at the interface between cold clouds and a hot halo gas it can create so called turbulent mixing layers at the boundaries of different gas phases. These TMLs can produce intermediate (T $\sim 10^5$ K) temperature gas as a result.

1.4.2 Line Profiles & Gas Kinematics

Even with the ambiguity that comes with modeling, we still have some tools in our gardening/farm kit that allow us infer physical properties just using characteristics about the spectra. One of these tools is the line width, or Doppler parameter b, which can be used to infer temperature structure and gas dynamics (Tumlinson et al., 2017). Because of the following equation: $b^2 = (2kT/m_i) + b_{nt}^2$, where k is the Boltzmann constant, T is the temperature, m_i is the atomic mass of the species in question, we see that the Doppler parameter (both thermal and non-thermal (nt) contributions) are a function of temperature; thus, if you use fitting functions such as Voigt profile fitting, and measure the Doppler parameter, you can make constraints on the temperature for different metal ion species. This use of Doppler parameters from UV absorption surveys and modeling (i.e. Figure 1.5 and S1.4.1) to estimate temperatures have indicated that the CGM contains a mixture of photoionized and/or collisonally ionized gas in a low density medium at $10^{4-5.5}$ (e.g., Adelberger et al., 2003; Richter et al., 2004; Fox et al., 2005; Narayanan et al., 2010; Matejek & Simcoe, 2012; Stocke et al., 2013; Werk et al., 2013; Lehner et al., 2014; Savage et al., 2014; Turner et al., 2015).

Another tool we can use is the velocity dispersion and number of components seen in the spectra via profile fitting. Studying these velocities can reveal the kinematics substructure of the CGM of the galaxy you observed. This type of analysis has found that gas near low-z galaxies across a wide range of stellar mass have line-of-sight velocity values that are less than the inferred escape velocity of the halo, even when taking into account projection

effects (Tumlinson et al., 2017); this phenomenon is seen for observed species from H I to O VI (Bergeron & Boissé, 1991; Tumlinson et al., 2013, 2011; Mathes et al., 2014; Johnson et al., 2015a; Nielsen et al., 2015). Thus, the kinematics of the detected absorption are consistent with being bound to the host galaxy and have physical implications for outflows and recycling processes which is something we will touch on in later sections. But even this tool has its challenges and any relationships made using kinematics must take into account scatter introduced by blending of unresolved components in the spectra (and thus reflected in any profile fitting). These complications can arise from *COS* resolution and/or other physical scenarios such as turbulent mixing (e.g., Tripp et al., 2008; Lehner et al., 2014).

Looking at what both of these tools have revealed we can start to understand that the CGM is made up of many metal ions that spans orders of magnitude in ionization potential energy and each of them contribute to the gas being composed of many temperatures and densities. This translates in to astronomers defining the CGM as a multiphase medium and as I have slowly revealed, it can play host to complex mechanisms. Now that we have a good general background of the CGM, what resides in the gas that makes up the CGM, how to observe the metals in the gas, and how to start making constraints on the physical state of this gas we can move on to exploring these complex mechanisms in detail. Over the next couple sections of this introduction, we will learn more about the processes that take place in the CGM; think of us transitioning from talking about the farm and its produce as a whole, and moving on to discussing the internal and external factors that make up the farm's ecosystem. These factors rely heavily on physics and we will be walking through some equations and/or relations. So pull on your galoshes and put on your gloves, there's a lot of hard work ahead... and oh, there's a chance of rain!

2 Cooking with Gas: The CGM Ecosystem

Understanding how galaxies acquire, eject, and recycle their gas through the lens of the CGM, gives us the opportunity to not only characterize the gas's physical properties, but also reveal information about the galaxy's ecosystem. Over the past *several* years, it has become clear that gas inflows or accretion are a necessary component to sustained galaxy star formation and out flowing gas from galactic winds play a crucial role in regulating the rate at which stars form in galaxies (SFR) (Tinsley, 1980; Ford et al., 2014; Muratov et al., 2015; Shattow et al., 2015; Christensen et al., 2016; Corlies & Schiminovich, 2016a). Essentially, the CGM acts like a mediator for interactions between galaxies and the gas well beyond galaxies, the intergalactic medium (IGM). Therefore, by studying the CGM and making constraints on its physical properties (i.e., chemical abundances, mass distribution, kinematics, thermodynamics) you can begin to explain how galaxy formation is regulated and how galaxies evolve (see Figure 1.6).

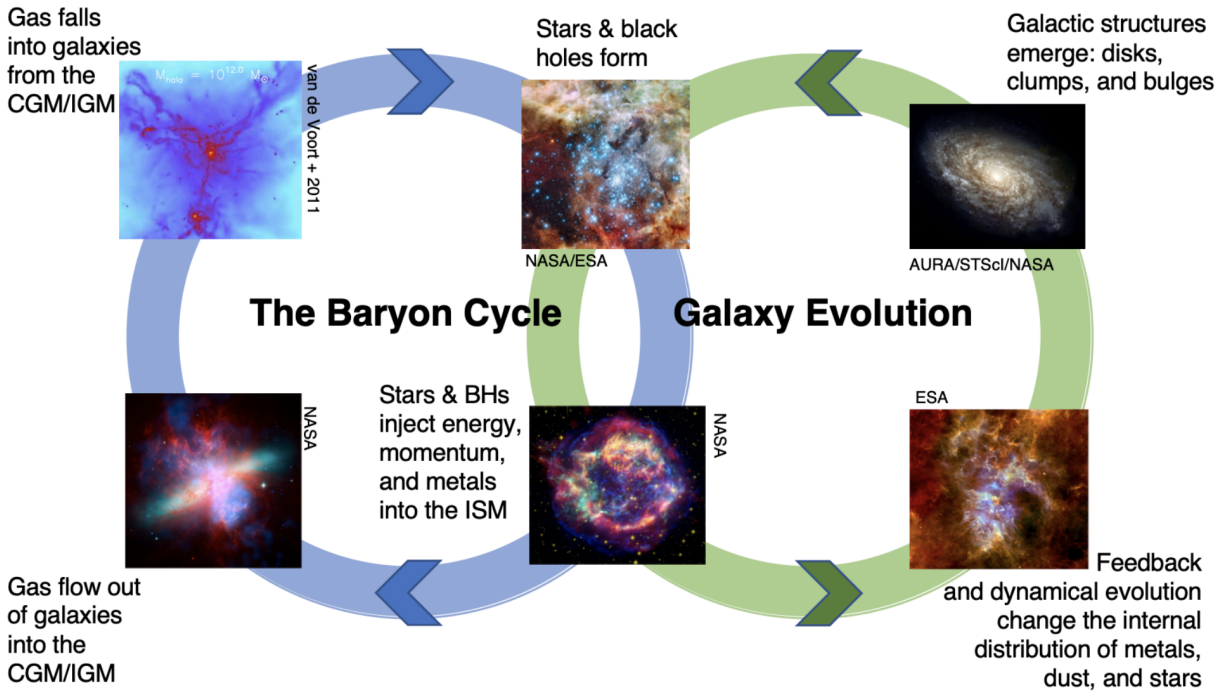

Figure: Newman/Carnegie Institute of Science, 2020

Figure 1.6: The intersection of gas flows and galaxy evolution. Baryons, or normal matter, are thought to move in a cyclical pattern as gas moves from the disks of galaxies to the CGM/IGM and back into galaxies. This cycle determines heavily impacts the chemical enrichment of galaxies and is a driving force in determining the distribution of gas and stars in throughout the universe. Without the baryon cycle there would be no sustained galaxy formation or evolution. This diagram is from a presentation by Carlos Carrillo-Gallegos titled "*Characterizing Gas Flow Using Multiply-lensed Quasars*".

These upcoming sections contain their own set of terms to describe the physics of the CGM ecosystem. To help bridge the gap between you dear reader and the jargon, I have included some helpful definitions here for your reference.

Cold Flows/ Cold Steams: cold halo gas, typically at a temperature T $\sim 10^4$ K and filamentary in morphology; associated with "cold mode" accretion

Virial Temperature: $T_{\rm vir} = (\mu m_{\rm p}/2k)(GM_h/R_{\rm vir})$, where μ is the mean molecular weight ($\approx$0.6 for an ionized plasma), $m_{\rm p}$ is the proton mass, k is the Boltzmann constant, G is the gravitational constant, $M_{\rm h}$ is the halo mass, and $R_{\rm vir}$ is the virial radius

Virialized Gas: gas with thermal velocities set by the gravitational potential; in massive halos, this corresponds to the hot phase ($T_{vir} \gtrsim 10^6$ K)

Important Timescales:

- *Hubble Time:* $t_{\rm H} = 1/H$, where H is the redshift-dependent Hubble parameter
- *Free-fall Time:* $t_{\rm ff}$, free-fall time in a gravitational potential
- *Cooling Time:* $t_{\rm cool}$, cooling time of gas
- *Depletion Time:* $t_{\rm dep} = M_{\rm gas}/SFR_{avg}$, where $M_{\rm gas}$ is the total estimated CGM mass and SFR_{avg} is the mean star formation rate

Subsonic: relating to a speed or speeds less than that of sound.

Supersonic: relating to a speed or speeds more than that of sound.

2.1 Gaseous Galaxy Evolution... it's a Whopper!

This is a *whopper* of a section (to speak in the vernacular of the peasantry), where we will dig into the details of the CGM ecosystem and walk through the various processes that build upon the picture of the CGM we described in S1. We will move from evolutionary processes that discuss the properties and physics of gas flows on the halo scale (inflows: §2.1.1; outflows: §2.1.2), recycling §2.1.3, and galaxy quenching §2.1.4. Again these sections are more physics and math forward than §1; for more general readers unfamiliar with these terms, I have included helpful asides with definitions of terms which can be found at the start of a new section.

2.1.1 Inflows

To begin our discussion on the CGM ecosystem we must first touch upon inflowing gas, or gas accretion, which is arguably one of the most fundamental processes in galaxy formation (Fox & Davé, 2017). As we start this journey, we need to become familiar with the cooling physics of gas in dark matter halos using an idealized approximation of spherical symmetry, neglecting feedback processes (e.g. the common example used in my undergraduate physics

classes was for is to assume a round cow).[2] As a dark matter halo forms from gravitational clustering, gas is pulled towards the center. For low mass halos, the gas inflows remain subsonic due to heating by photoionization by the cosmic ionizing background; for these small halos galaxy formation is actually suppressed (e.g., Efstathiou, 1992; Noh & McQuinn, 2014). In the case of more massive halos, inflows reach supersonic velocities and are shock-heated to a temperature on order of the virial temperature; for example, if the halo mass $M_{\rm h}$ = 10^{12} $M_{\odot}$ at $z = 0$ (conditions similar to the Milky Way), then the virial radius is $\approx$ 260 kpc and the virial temperature $T_{\rm vir} \approx 6 \times 10^5$ K (Barkana & Loeb, 2001). In this realm of relatively massive halos, the methods of how gas accretes onto the central galaxy, and thus the CGM, depends on whether the cooling of the shocked gas is fast or slow relative to the free-fall time, $t_{\rm ff}$. Below I discuss the characteristics of this cooling in terms of cold and hot accretion in the following paragraph.

Cold Accretion: If the cooling time, $t_{\rm cool} < t_{\rm ff}$ then the shocked gas *rapidly* cools and loses its thermal pressure support. The resulting gas is cold at $T \sim 10^4$ K which has a tenancy to fragment, clump, and/or form into narrow filaments known as cold flows or cold streams. If this cold gas is not disrupted by feedback or angular momentum, then it can accrete onto the central galaxy in a free-fall time. **Hot Accretion:** On the flip side, if $t_{\rm cool} > t_{\rm ff}$, then gas cooling becomes a rate-limited step. This shock-heated gas can be supported for an extended period of time $\sim t_{\rm cool}$ in the halo potential by thermal pressure. For the inner regions of the halo, which is within the cooling radius where $t_{\rm cool} < t_{\rm H}$, there is an adequate amount of time for the hot gas to cool and accrete easily onto the galaxy. Again neglecting feedback, these cooling regions tend to a steady state cooling flow in which compressional heating in the inflowing gas balances the radiative losses (e.g., Fabian et al., 1984).

By analyzing the physics of cooling flows in galaxy-scale halos, Stern et al. (2019, 2020), investigated the maximum rate of hot gas accretion. Using our spherically symmetric dark matter halo set up, where there is initially pressure supported, steady flow of gas near the virial temperature, that the maximum hot gas density and accretion rate depend on radius. Thus, for gas in cooling flows, the ratio of the cooling time to the free-fall time *increases* from the inside out (Stern et al., 2020); this means that the outer parts of the CGM can be hot and contain virialized gas ($t_{\rm cool}/t_{\rm ff} > 1$) whereas the inner parts cool rapidly and tend toward free fall ($t_{\rm cool}/t_{\rm ff} < 1$). This crucial information that the inner CGM virializes last is important because it defines the time at which the boundary conditions change for the central galaxy. However, it wouldn't be full diligence, if I didn't mention that other models for the structure of hot gas in the halos the $t_{\rm cool}/t_{\rm ff}$ ratio can be constant or decrease with radius (e.g., Sharma et al., 2012a; Voit et al., 2017; Faerman et al., 2020); but it should be noted that these models assume that heating from the galactic feedback balances cooling in the CGM.

One of the main things that I took away from my physics classes in undergrad is that limits and boundary conditions are *very* important and can are key to defining regions where you can start doing the math and building theories. This lesson is as relevant here as it was in my E&M and Statistical Physics classes; it is these different limits which correspond to different regimes of $t_{\rm cool}/t_{\rm ff}$ that make up the core ingredients of foundational galaxy formation theory

[2]We note that we are heavily summarizing material from the review paper by Faucher-Giguère & Oh (2023) For a more in depth dive on the math, we refer the reader to their publication.

models (e.g., Binney, 1977; Rees & Ostriker, 1977; Silk, 1977; White & Rees, 1978). Building off the implications of these limits for galaxy formation and the CGM many researchers have attacked this question from many angles including analytic and semi-analytic techniques (e.g., White & Frenk, 1991; Somerville & Primack, 1999; Dekel & Birnboim, 2006), idealized numerical solutions (e.g., Birnboim & Dekel, 2003; Fielding et al., 2017b; Stern et al., 2020), and detailed cosmological simulations (e.g., Kereš et al., 2005, 2009; Faucher-Giguère et al., 2011a; van de Voort et al., 2011; Nelson et al., 2015), but even $\sim$ 50 years later, this is still a very active area of research and there is not yet agreement on the effects of cold versus hot accretion for galaxy formation and evolution. We will touch more upon some of these models and simulations in S3.

To sum up[3], it is typically thought that gas flowing into galaxies at $\lesssim 10^{12}$ $M_\odot$ should be dynamically cold and thermally cold, whereas the more massive halos receive their baryons as hotter ($T > 10^5$ K) gas (Dekel & Woo, 2003; Kereš et al., 2005; Dekel & Birnboim, 2006; Kereš & Hernquist, 2009; Stewart et al., 2011). Because of this, cold, dense, metal-poor CGM gas is often interpreted as evidence of direct accretion. These cold streams are predicted to manifest as H I absorbers with column densities that range from $N_{\rm HI} \sim 10^{16-20}$ cm^{-2}, corresponding to Lyman limit systems (LLS) (Faucher-Giguère et al., 2011b; Fumagalli et al., 2011a,b; Ribaudo et al., 2011; van de Voort et al., 2012; Lehner et al., 2013; Fumagalli et al., 2014; Faucher-Giguère et al., 2015; Cooper et al., 2015; Glidden et al., 2016; Hafen et al., 2017). Additionally, the cool bound H I seen in the CGM of $z \sim 0.25$ galaxies could also potentially reveal inflowing gas (Tumlinson et al., 2013). Lastly, findings from the COS-GASS survey (Borthakur et al., 2015) showed that there is a correlation between interstellar and circumgalactic H I. This result together with the LLS and cool H I gas imply that gas within the CGM can potentially become star-forming fuel. Broadly, this indicates that galaxies can use their large gaseous reservoirs (i.e. the CGM) for accretion. However, as noted in Tumlinson et al. (2017), evidence for fuel does not automatically mean evidence for fueling, but we know there is an abundance of cold gas available and we have theory for what this gas most likely does at certain thresholds. Direct observational signatures are the best path forward but they are difficult to disentangle from outflowing gas (§2.1.2).

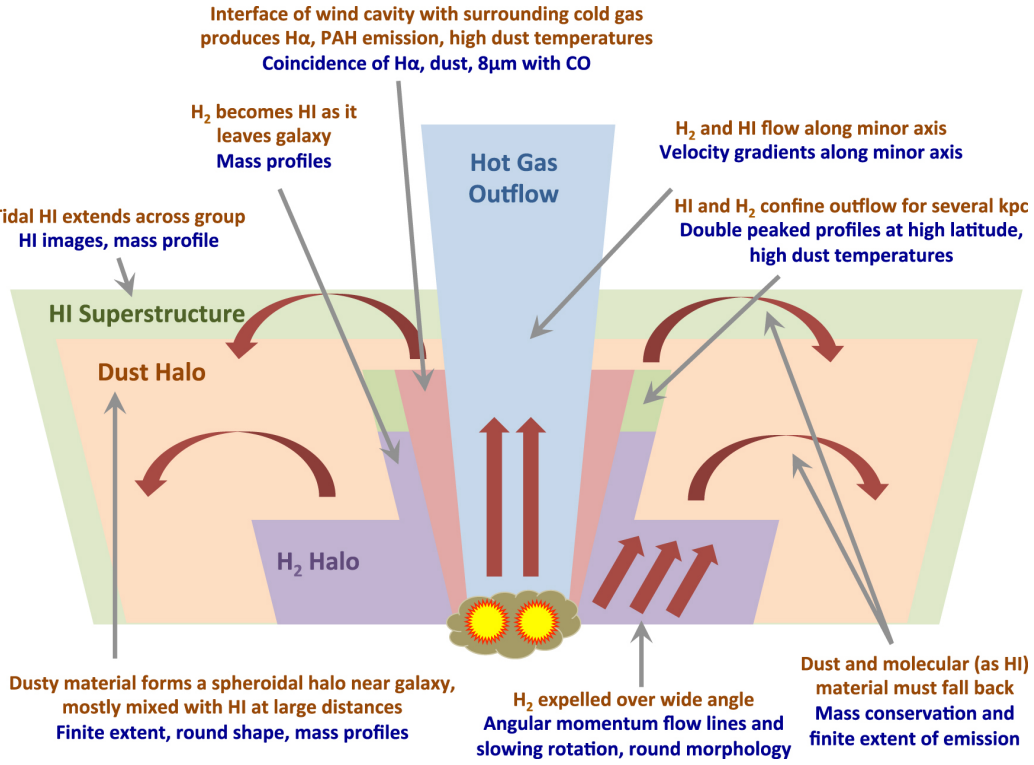

Figure 1.7: A schematic of the view of cool gas and dust around M82. Blue notes cite evidence for the red statements. This schematic is Figure 19 of Leroy et al. (2015).

2.1.2 Star-Formation Driven Outflows

As we begin a brief deep dive on the feedback processes that make up star-formation driven galactic winds/outflows, I have included some more helpful definitions.

Entrainment: the transport of fluid across an interface between two bodies of fluid by a shear-induced turbulent flux; as the two fluids, oscillating systems, mix they assume the same period.

Sublimation: refers to the phase transition of a substance directly from the solid state to the gaseous state, without passing through the liquid state.

Condensation: conversion of hot to cold gas when initially hot gas mixes with cold gas, and the mixed gas cools, the hot gas condenses onto cold gas seeds.

The other side of the large scale processes coin is outflowing gas. These galactic winds and outflows are more foils to inflows than foes as they are another essential ingredient to galaxy formation theories (Schaye et al., 2015; Davé et al., 2017). There are many ways that you could talk about outflows, but specifically for this introduction I have chosen to only touch upon outflows powered by star formation since, (i) I did this as the topic for my general exam

[3]I would like it noted that when this is read it should be read in the voice of Inigo Montoya from the Princess Bride

and I think some of my substantial reading/work on the subject should be showcased again and (ii) I think it is more prevalent to my subsequent chapters[4]. These biconical (Martin et al., 2012; Rubin et al., 2014) star-formation driven outflows are thought to suppress star formation in galaxies up to $\sim L^{\star}$ through their ejective feedback nature for they evacuate gas from the ISM to the CGM or intergalactic medium (IGM) before it can begin forming stars (Heckman et al., 2000; Springel & Hernquist, 2003a,b; Bertone et al., 2007; Schaye et al., 2010; Muratov et al., 2015). As they expand into the CGM, these winds are decelerated by gravity and through entrainment (Faucher-Giguère & Oh, 2023). This entrainment of gas modifies mass outflow rate and chemical composition which produces preventative feedback by either pushing, stirring, and/or shocking the surrounding atmospheric matter through energy and momentum. It is these processes that can delay and/or prevent the accretion of CGM gas onto galaxies (Dekel & Silk, 1986; Benson et al., 2003; Mo et al., 2004; Puchwein & Springel, 2013). Thus galactic winds offer a key insight into why galaxies go dark (i.e. stop forming stars and start to quench), but more on that topic in S2.1.4.

These galactic winds or outflows are not just parameters in a simulation that are necessary to produce the types of metal rich gaseous atmospheres we have come to know, but are directly observed. In fact, outflows have been observed at a wide range of redshifts (Veilleux et al., 2005; Heckman & Thompson, 2017; Naab & Ostriker, 2017). Additionally, multi-wavelength observations from radio to gamma rays have shown that galactic winds in starbursts and star-forming galaxies have a multiphase structure that is generally divided into five phases (e.g., Heckman & Thompson, 2017; Zhang, 2018): very hot ($\sim 10^8$ K), hot ($\sim 10^{6-7}$ K), warm (ionized, $\sim 10^4$ K), cool (neutral atomic, $\sim 10^3$ K), cold (molecular & dust, < 100 K). To start off, the high values of SFR per unit area in starburst galaxies allow the efficient conversion of kinetic energy supplied by core-collapse supernovae (SNe) and winds from massive stars into thermal energy of a very hot fluid (this is because most SN will explode in hot gas prior to dramatically exploding). X-ray satellites using *Chandra* and XMM-Newton observatories have been used to observe the highly ionized X-ray emission of these very hot and hot phases of galactic winds as driven by SN explosions (e.g., Strickland & Stevens, 2000; McDowell et al., 2003; Strickland & Heckman, 2007, 2009; Bravo-Guerrero & Stevens, 2017). Moving to the other phases, X-rays and/or UV has found that the warm phase of winds are accelerated by ram pressure from the hot phase[5] (e.g., van Dokkum et al., 2015; Tunnard et al., 2015; Heckman et al., 2015; Chisholm et al., 2017). Emission lines such as Hα, N II, O II, O III, and absorptions such as Na I D, K I, Mg II (including observations from radio, millimeter, and sub-millimeter) have been used to trace morphologies and velocities of warm, cool and cold outflows in galactic winds, including warm ionized (e.g., Rubin et al., 2014; Cecil et al., 2002; Du et al., 2016; Weiner et al., 2009; Martin et al., 2013; Tang et al., 2014), neutral atomic (e.g., Heckman et al., 2000; Martin, 2005; Chen et al., 2010; Rupke et al., 2005a,b, 2002, 2005c; Kornei et al., 2012; Rupke & Veilleux, 2015), molecular

[4]In galaxies with luminous active galactic nuclei (AGNs), galactic winds/outflows can also be powered by accretion onto massive black holes (e.g., Faucher-Giguère & Quataert, 2012). The galaxies that in my samples, do not have reported AGNs and therefore a discussion on outflows driven by star-formation is more timely.

[5]I would like to note that some new simulations show that a simple ram pressure acceleration scenario may be problematic and a more complicated approach is necessary (e.g., Shopbell & Bland-Hawthorn, 1998; Lockhart et al., 2015; Su et al., 2010)

(e.g., Bolatto et al., 2013; Sakamoto et al., 1999; Veilleux et al., 2009; Westmoquette, 2013; Salak et al., 2013, 2018; Meier et al., 2015; Leroy et al., 2015; Walter et al., 2017; Sakamoto et al., 2009; Tunnard et al., 2015; Zschaechner et al., 2016), and dust (e.g., Hutton et al., 2014; McCormick et al., 2018; Roussel et al., 2010; Meléndez et al., 2015; Hodges-Kluck et al., 2016; Jones et al., 2018) outflows. All of these different phases of galactic winds and their observational evidence are summarized for M82 in Figure 1.7.

Despite *several* studies characterizing the nature of galactic winds, the driving mechanisms of multiphase winds driven by stellar feedback are from from clear and a comparison between theory and observations is still incomplete (see reviews and studies, Heckman et al., 1990, 1993; Veilleux et al., 2005; Rupke, 2018; Zhang, 2018; Veilleux et al., 2020). For the rest of the section, I will briefly discuss some of the feedback processes and the current theory on the make up star-formation driven galactic winds.

Fundamentally, outflows may be "energy-driven" or "momentum-driven" depending on whether radiative losses are negligible or not, respectively and are powered by a combination of feedback processes. These processes include core collapse SNe, radiation, and cosmic rays[6]. First up is core collapse SN explosions since they are the highest contributor to galactic outflows and the best developed models of galactic winds invoke the heating of the ISM by overlapping core-collapse SN explosions.

The simplest of these models is the spherical expansion of a SN remnant in a uniform medium as described by Ostriker & McKee (1988). So when a star with masses between 8-25 $M_\odot$ ends their lives as a core collapse SN, they eject ∼1-10 $M_\odot$ of metal-enriched material with kinetic energy and momentum. What happens to the kinetic energy next depends on the local pre-SN environment. In very low density environments, the ejecta simply remains in a state of free expansion keeping the same kinetic energy and momentum. But in more typical environments, some fraction of the kinetic energy (often called supernova thermalization or feedback efficiency) is quickly transformed into thermal energy through shocks heating the SN ejecta and ambient medium. Once the mass of swept up material is comparable to the mass of the ejecta, the SN remnant enters an adiabatic Sedov–Taylor phase of expansion (Sedov, 1959; Taylor, 1950) where the outer shock radius begins to expand. In this phase the information from the SN ejecta is erased and the properties of the SN remnant depend on the ambient density and the initial SN energy.

Once the temperature drops below $\sim 10^6$ K ($\sim t > t_{\rm cool}$), radiative losses become important, and the SN remnant enters a pressure-driven snowplow phase where the pressure of the interior hot gas is still larger than that of the outside pressure. This means that the thermal energy of the SN remnant interior cannot be neglected. Gradually, the interior pressure decreases to eventually match the outside pressure due to the thermal energy of the SN remnant radiating away, and the remnant continues to expand and sweep up ISM gas as a momentum-conserving snowplow. The SN remnant will expand until its forward shock speed approaches the effective sound speed in the ambient medium. The analytic estimate of SN remnant evolution in a uniform medium has been tested and confirmed by one- and multidimensional hydrodynamic simulations of spherical SN remnants with radiative cooling

[6]Protostellar outflows, stellar winds from young massive stars and Type Ia SN are other feedback processes that contribute to galactic winds, but are not the primary drivers and therefore I chose to leave them out of the discussion. For more information about these other feedback processes see Veilleux et al. (2020).

(Kim & Ostriker, 2015; Chevalier & Gardner, 1974; Cioffi et al., 1988; Thornton et al., 1998; Blondin et al., 1998; Martizzi et al., 2015; Walch & Naab, 2015)[7].

So now that we understand a simple model of a spherical expansion of a SN remnant in a uniform medium, we have need to tackle the question of: what happens if the thermal energy of the remnant cannot be fully radiated away? According to McKee & Ostriker (1977) galactic-scale "super-bubble" forms if the SN remnant net energy cannot be efficiently radiated away by the multiphase ISM, otherwise a "galactic fountain" is produced to interact with the galactic halo. Although the physical processes of galactic wind launching and propagating by SN explosions are complex, a simple, clear analytic estimate can be applied to galactic winds. The classical SN-driven galactic wind model was first developed by Chevalier & Clegg (1985). Now we could walk through the equations and have to understand lots of variables that could make your head hurt, but I am going make the executive decision and just say no. If you want to see the math for yourself, please go read the individual paper, but I already gave a presentation that included this model once and passed, so I'm just gonna move on. The main points from Chevalier & Clegg (1985) are that (i) it is a very good approximation for adiabatic winds and is still consistent with more recent models/simulations (e.g., Strickland & Heckman, 2009; Fielding et al., 2017a; Schneider et al., 2018) (ii) it defines a outlines equations for total energy injection, total mass injection, density, temperature, and velocity. These equations include the control factors α - the thermalization efficiency and/or β - the mass-loading rate, which can be determined using observables.

The more important of the two control factors is β since it quantifies the capability of the wind to act as negative feedback on star formation. Nominally, if $\beta > 1$, then more gas is leaving the region than forming stars (i.e., the outflow is going to deplete gas more quickly and probably result in fewer stars overall). Observations have shown that constraining the mass-loading factor is difficult and can range from 0.02-4 depending on the phase of gas being observed and the type of galaxy. For star-forming and starburst galaxies the mass loading factor was determined to be $\beta_{\rm warm} \gtrsim$ 0.02-0.6 by Rubin et al. (2014) and $\sim$ 1-4 by Heckman et al. (2015). Strickland & Heckman (2009) used X-ray observations for M82 and found $\beta_{\rm hot} \sim$ 0.2-0.6, while Zhang et al. (2014) found $\beta_{\rm hot} \sim 1$ for a range of galaxies which included dwarf starbursts, LIRGs and ULIRGs.

Okay, let's move on to the second feedback process we wanted to discuss: radiation. radiation from individual or multiple stars may also be important in regulating and launching galactic winds. Young massive stars emit mostly in the UV band and create H II regions by heating and ionizing the neutral gas up to a temperature of 10^4 K (Whitworth, 1979; McKee et al., 1984; McKee, 1989; Matzner, 2002; Dale et al., 2012; Emerick et al., 2018). For massive stars, radiation pressure from massive stars acting on dust grains which absorb the direct UV photons and re-emit in the infrared (IR) band may play a more significant role than photoionization to affect the surround ISM[8] (Krumholz & Matzner, 2009; Kuiper et al., 2011, 2012; Klassen et al., 2016; Kuiper et al., 2016; Rosen et al., 2016; Crocker et al.,

[7]However, since the realistic ISM is highly inhomogeneous (Elmegreen & Scalo, 2004), it is important to investigate the expansion of SN remnants in an inhomogeneous medium (for examples of studies that investigate SN remnants in an inhomogeneous medium see, Zhang & Chevalier, 2019; Martizzi et al., 2015; Walch & Naab, 2015; Iffrig & Hennebelle, 2015).

[8]It should be noted that this conclusion is still under debate (Sales et al., 2014; Ishiki & Okamoto, 2017; Ishiki et al., 2018; Haid et al., 2018).

2018). In general, the momentum injection by the SN-driven hot wind is comparable to that by the radiation field. So we expect radiation pressure on dust grains to be an important factor in driving galactic winds.

However, in order for radiation pressure to perform its job of being a key factor in driving galactic winds, some necessary conditions need to be met. First, dust grains need to survive against sublimation. If the radiation temperature is above the condensation temperature, then dust grains will start to sublimate rather than grow. Different dust grains with different sizes have various sublimation temperatures, with a typical value between $\sim$ 500-3,000 K (Veilleux et al., 2020). Secondly, the dust needs to be coupled with the gas. The dust grains obtain momentum from the absorption or scattering of photons, and they collide with the gas (Gilman, 1972), then the drag force between the dust grains and the gas causes the coupling of the dust to the gas. The requirement of the momentum coupling sets up the lower limit of the mass loss rate and velocity of a dust-driven wind (Berruyer & Frisch, 1983; Mastrodemos et al., 1996). The third necessary condition for radiation to be important to galactic winds is that the radiation flux of a galaxy must near or approach the Eddington limit for dust. This last condition is still up for debate since some studies show that you can have radiation impacts in sub-Eddington regimes (Andrews & Thompson, 2011; Coker et al., 2013; Wilson et al., 2014; Barcos-Muñoz et al., 2017, 2018; Zhang et al., 2018; Zhang & Davis, 2017; Thompson & Krumholz, 2016).

And to finish off this section, I want to end by talking a little about how cosmic rays contribute to star-formation driven outflows. It wasn't until I had to prepare for my General Exam that I learned that stellar feedback also includes cosmic rays and that the shocks of SN remnants are efficient accelerators of cosmic rays by diffuse show acceleration to the first order fermi acceleration (Fermi, 1949; Axford et al., 1977; Krymskii, 1977; Bell, 1978a,b; Blandford & Ostriker, 1978; Schlickeiser, 1989a,b). In fact, about $\sim$10% of the SN energy ($\sim 10^{50}$ ergs) can be converted into non-thermal CR energy (Helder et al., 2012; Morlino & Caprioli, 2012; Ackermann et al., 2013), most of which is deposited in protons with their energies following a power-law distribution peaked at $\sim$GeV (Strong et al., 2007; Grenier et al., 2015; Zweibel, 2013, 2017; Webber, 1998). The local energy density of cosmic rays is $\sim$1.8 eV cm^{-3} (Webber, 1998), and the total energy of cosmic rays in our Galaxy is $\sim 10^{56}$ ergs; this information coupled with other factors (e.g., see Veilleux et al., 2020), has driven the proposal that cosmic rays coupled to the gas may also drive large-scale galactic winds in the Galaxy.

One of the first studies of cosmic rays in this context was performed by Ipavich (1975). They found that if cosmic rays travel through a magnetized plasma medium faster than the Alfvén speed, they can be coupled to the plasma by the emission of MHD waves. The mass-loading rate of cosmic ray driven winds can reach $\sim$1-10 M$_\odot$/yr. Socrates et al. (2008) argued that cosmic ray feedback may be important in driving galactic winds in star-forming and starbursts galaxies[9]. More recently, it was found that the momentum injection from an individual SN remnant to the ISM can significantly increase once the effect of cosmic rays produced by the SN remnant is also included (Diesing & Caprioli, 2018). Additionally,

[9]This work built off work studying cosmic rays and thermal effects (Breitschwerdt et al., 1991, 1993, 2002), investigations into the coupling between CRs and plasma (Zirakashvili et al., 1996), CR streaming instability and the transport of relativistic nucleons in cosmic ray driven winds (Ptuskin et al., 1997), and studies on cosmic rays and thermal gas pressure (Everett et al., 2008).

numerical simulations exploring stellar feedback with the combination of SN remnants and cosmic rays are underway, leaving the impact of cosmic rays in star-forming galaxies and starbursts an open question. Interestingly the ones currently available show positive results that cosmic ray feedback does drive galactic winds in various galaxies (e.g., Uhlig et al., 2012; Jacob et al., 2018; Booth et al., 2013; Salem & Bryan, 2014; Fujita & Mac Low, 2018; Jiang & Oh, 2018).

To summarize, multiwavelength observations have found evidence for star-formation driven galactic winds/outflows and determined that these winds have a multiphase structure. The driving mechanisms, which we touched upon briefly, are far from clear from both the theoretical and observational view. From what we do know, SN explosions do the heavy lifting in driving galactic winds while radiation (dust grains/radiation pressure) and cosmic rays play important but more minor roles.

2.1.3 CGM Recycling

By now, we should have a good understanding of how inflows and outflows are fundamental aspects of a galaxy's CGM and that they are necessary processes for galaxy evolution. Another potential key component for this evolution is gas recycling. A reuse of gas previously blown out of the galaxy is intuitive since this is a process we have already sort of discussed; gas is accreted onto the central galaxies when the cooling time is short. This idea of metal enriched accretion is well supported by cosmological simulations. These simulations show that significant fractions of the gas accreting onto galaxies was previously ISM gas, which underwent may cyclical journeys into and out of the galaxy (Ford et al., 2014; Christensen et al., 2016; Muratov et al., 2017); in fact, a majority of the star formation towards the tail end of their runs were fueled by recycled gas (Oppenheimer et al., 2010). The implications of recycling is that a substantial fraction of all the heavy elements on Earth, even the ones potentially in me and you dear reader, were once recycled through the Milky Way's halo at one point and time (Tumlinson et al., 2017)!

Though the idea for recycling is well motivated, the details of how this exactly happens is a little more convoluted and many questions are still relatively unanswered. Is the recycling a simple process in which gas launched at a velocity that is less the escape velocity ($v < v_{\rm escape}$) so that it encounters hydrodynamic resistance and due to gravity it falls back into the galaxy as part of a large-scale halo fountain? Or does recycling fall more in line with the processes that we just discussed so that metal-rich gas precipitates out of the halo and rains onto the galaxy (Fraternali et al., 2015; Voit et al., 2015; Thompson et al., 2016)?

Some insight can come from our understanding of accretion (§2.1.1). Studies of IGM accretion have led to the assumption that this gas has very low metallicity (Lehnert et al., 2013; Cooper et al., 2015; Glidden et al., 2016); however, these metallicity values are rarely below the IGM (or Lyα forest) at the same redshift (Fumagalli et al., 2011b). So either cosmic accretion either entrains metal-enriched circumgalactic gas on its way into the galaxy (similar to entrainment in outflows; e.g. Fraternali et al., 2015), or it is at least partially comprised by material that has previously been in the ISM (Tumlinson et al., 2017). Thus, recycled mode accretion is an essential component of galaxy evolution. This line of thinking only brings on more questions such as: *Does recycled accretion behave in a similarly to outflows, but in the opposite direction, so that inflows sweep up metal-polluted CGM material on its*

way from the IGM to the ISM? and *Do galactic winds preferentially reaccrete, sweeping up cosmic accretion?*

Taking in everything we have discussed in S2.1, we can begin to see the forest through the trees and thus our picture of the CGM ecosystem is now more defined. This ecosystem is driven by inflows that arise in massive reservoirs of cold, metal-enriched gas that is bound to a galaxy's potential well and enter the disk through fast moving clouds and smooth flows of ionized gas. Like we mentioned before, there is most likely some component of gas that comes directly from the IGM that doesn't spend too much time in the CGM acquiring metals, but for the most part these inflows are full of ionizing metals. Also apart of the mix is the ejection of metal-enriched galactic winds; some of them ions in these outflows escape the CGM, but most lack the energy to escape the halo and thus become recycled accretion. This recycled material interacts with the CGM, looses energy to radiation from shocks and eventually cools and re-enters the galaxy. In away, recycling is both inflows and outflows and may be the more accurate way of thinking about how galaxies acquire their gas (Tumlinson et al., 2017).

More helpful definitions!

Precipitation: formation of cold gas via linear thermal instability in gravitationally stratified hot medium; the over dense cold gas eventually falls, like rain.

Isobaric: refers to a process where the pressure of a system remains constant throughout, meaning the pressure doesn't change during the process

Isochoric: thermodynamic process taking place at constant volume. It is also called an isometric process or constant-volume process.

Adiabatic: a process in which no heat transfer takes place. This does not mean that the temperature is constant, but rather that no heat is transferred into or out from the system.

Isotropic: having a physical property which has the same value when measured in different directions; not varying in magnitude according to the direction of measurement

Anisotropic: a material exhibits different properties depending on the direction

2.1.4 Galaxy Quenching

For the better part of this introduction I have been describing the CGM as a farm full of nutrient rich ingredients and is but a single part in a galactic ecosystem that plays host to complex processes. I would now like for you to think of the CGM like a giant bowl of soup. I think any soup will do but, I am imagining a good old fashioned chicken noodle soup from my childhood. This soup was always very brothy and full of healthy ingredients like carrots, celery, onions, and my favorite, double noodles. One of the best parts of this soup is that even by using all the same ingredients, it could taste slightly different each time they would make it. Some times we had an excess of carrots in the fridge that day so they overpowered the celery, much to my joy, while other times it would be packed with chicken so that it was

less soup and more of chicken with some runny sides. But, no matter what the ration, I was always chicken noodle soup.

Now lets go back to our CGM with this idea of soup in mind. We know that all galaxies have these dark matter halos around them and we walked through the different processes that make them metal enriched, but we find that somewhere along the way, some galaxies start to change from actively forming stars to producing less and less. Something is making the soups of galaxies lose their nutrient rich ingredients (chicken, carrots, celery) and leaving only mostly broth. Outside of our metaphor, this translates to not all galaxies possess cold gas within their ISM. Somehow, galaxies transition from actively star-forming (i.e. possess an abundance of cold gas in their ISM and CGM) to a more passive state (i.e. possess little if any cold gas in their ISM and potentially the CGM too). These passive galaxies have entered a quenched state. How and why these massive galaxies that once were effectively producing stars, start to diminish is still an unresolved question in the astronomical community. This is a rather large subject and a very detailed dive into the wide range of possible mechanisms for consuming, removing, and/or heating cold gas is beyond the scope of my thesis introduction; however quenched galaxies are a key part of the work in the upcoming chapters so a brief discussion of the CGM as a factor in galaxy quenching is very relevant.

Continuing to frame our discussion in the context of cold gas, Kereš et al. (2005) was one of the first to argue that star-forming galaxies are fed by cold accretion: this gas enters the galaxy's disk via cold streams while remaining below $T \sim 10^5$ K. For galaxies with stellar masses, $\log M_\star/\mathrm{M}_\odot$, around 10.3-10.5 or corresponding halo masses of 10^{12} $\mathrm{M}_\odot$, the dark matter halo has sufficient mass and pressure from the CGM, to support virial shocks and suppress the cold mode (Tumlinson et al., 2017). It is at this threshold that we start to see a divide in star-forming and passive galaxies and started to draw attention from CGM simulation enthusiasts who predicted that the halos of passive galaxies might possess very little cold gas (e.g., Dekel & Birnboim, 2006; Stewart et al., 2011).

On the observational side, things are not always so clean cut. Results from Tumlinson et al. (2011) and COS-Halos (Werk et al., 2013, 2014) did find a dramatic dichotomy in highly ionized O VI around star-forming and passive $\mathrm{L}^\star$ galaxies, but passive galaxies also have a significant amount of H I in their CGM (i.e. cold gas). Additionally Thom et al. (2012) finds that the equivalent widths and covering fractions of H I do not drop with increasing stellar mass ($\log M_\star \simeq$ 10-11). These observational results are in direct opposition of the predictions from simulations (e.g., Stewart et al., 2011) which expect the covering fractions of H I to drop almost to zero as galaxies transition to the hot mode of accretion[10]. Massive galaxies have also been proven to have reservoirs of cold gas via Mg II observations: Mg II has been found to have covering fractions of 10-20% out to 100-200 kpcs around luminous red galaxies (Gauthier et al., 2010; Bowen & Chelouche, 2011), Bordoloi et al. (2011) found evidence for cold gas in red galaxies and Zhu et al. (2014) expanded upon these results to argue and even stronger detectable level of Mg II in similar galaxies, and Johnson et al. (2015a) found that Mg II absorbers are fairly consistent with being bound to their dark matter halos (i.e., the cold gas is contained with the dynamical influence of the galaxy).

[10]It should be noted that the inner CGM <50 kpc is not always well covered in surveys and it is possible that high-pressure hot gas close to the galaxy prevents cold material from accreting like some models predict Schawinski et al. (2014); Tumlinson et al. (2017)

On the theory side, things are also pretty unresolved. In order to produce quenching, star formation has to be reduced and any accretion and subsequent cooling later in the simulation run has to be suppressed pretty conservatively to align with the idea that galaxies can remain passive for >6 Gyrs (Gallazzi et al., 2008). There are varying ways of accomplishing this from (i) truncating star formation based on halo mass (Somerville & Davé, 2015) to (ii) suppressing star-forming fuel by heating the CGM itself (e.g., Gabor et al., 2010; Gabor & Davé, 2012). However, the biggest draw back from these types of models is that since they manipulate the CGM in differing ways, their results cannot be accurately compared with CGM observations. Fortunately, models that include self-consistent subgrid treatments of feedback can be compared with CGM observations (Schaye et al., 2015; Vogelsberger et al., 2014; Choi et al., 2015). Some of the best advancements in implementation of independent subgrid treatments of feedback are in the Illustris and EAGLE simulations. Results from these simulations, which utilize thermal AGN feedback, are able to reproduce the effects of the O VI dichotomy seen in Tumlinson et al. (2011) (Oppenheimer et al., 2016; Suresh et al., 2017); both simulations are able to have reduced cold CGM in passive galaxies, but not completely destroyed. But, even with tremendous progress on both the observation and theory side, the paradox of quenching remains: what is going on to passive galaxies that cause them to quench their star formation, remain quenched, but still have cold gas present? More work still remains to be done on this subject or we may never know where the soup goes, or maybe more accurately why the soup stops being nourishing to the galaxy.

Now, before continuing on to our discussion of small scale-processes, I did want to note that there are other large-scale evolutionary processes that I have not mentioned. Both angular momentum and satellite galaxies can have a non-negligible effect on the dark matter halo of galaxies and are important parts of the CGM ecosystem. However, some of the aspects of these two processes such as pressure torques, ram pressure stripping, tidal stripping, and winds are subjects that we have already touched upon or will be discussed in upcoming sections or chapters. Thus, if you have more interests on these topics I refer you dear reader to review papers such as Faucher-Giguère & Oh (2023) and references therein.

2.2 Cloudy with a Chance of Rain: Small-Scale Processes

This section is meant to be a helpful tool for understanding where we currently are on the small-scale physical processes that are still relatively unsolved in CGM gas. For simplicity, I have followed Faucher-Giguère & Oh (2023)'s lead and framed this discussion in the context of cold gas[11]. As direct observations of the virialized hot gas component is challenging and observing cold gas is much easier, progress on characterizing the colder atomic ($T \sim 10^4$ K) and sometimes molecular ($T \sim$ 10-100 K). I briefly outline four aspects of these small-scale processes in cold gas throughout the rest of this section: its formation, survival and growth, morphology, and cold gas interactions as seen with from the turbulent mixing layers point of view.

[11]I would like to again note that Faucher-Giguère & Oh (2023) was may main point of reference for this section and that I am essentially giving the cliff notes version of the published material. For a more in depth dive on the physics and math, I refer the reader to their publication.

2.2.1 Cold Gas Formation

To quote Julie Andrews in the *Sound of Music*, *"Let's Start at the Very Beginning, a Very Good Place to Start"*. For us that means with understanding how multiphase mediums develop. The classical mechanism for forming this gas is thermal instability (Field, 1965) where slightly over dense gas cools down faster than the gas surrounding it, loses its pressure, and undergoes compression and runaway cooling until a new equilibrium point has been reached. This process of cold gas forming via thermal instability is the CGM version of precipitation; you can think of condensation as the process where hot gas surrounding the recently formed cold gas mixes to form gas that is not at an intermediate temperature. These processes are linked, sort of like how they are in the traditional water cycle; both of these processes transform hot gas to cold gas through radiative cooling and they can take place simultaneously. For example, as cold gas forms under thermal instability conditions (precipitation) it will "fall" and start to shear against the surrounding hot gas which triggers condensation. There are a whole host of more complex physics on the nature of forming gas clouds and precipitation, however that would require a way more detailed discussion than I can provide in this introduction. As it so happens, this subject was recently reviewed by Donahue & Voit (2022), so if you are looking for a more comprehensive dive on precipitation, I refer you to their work.

Now, to get the multiphase medium we need to take into account a couple of things. First, local thermal instability typically assumes thermal equilibrium for the background medium which requires some form of heating. Without this source of heating, the entropy contrast between cool and hot gas won't develop quickly enough and you get single-phase cooling flows instead of multiphase ones. Additionally, there also is some dampening processes that counteract the fragmentation into multiphase medium. Bringing back the cooling time $t_{\rm cool}$ from S2.1, we can look at the dimensionless ratio $t_{\rm cool}/t_{\rm damp}$, where $t_{\rm damp}$ is the damping time. This ratio determines whether the medium is single phase (high $t_{\rm cool}/t_{\rm damp}$) or multiphase (low $t_{\rm cool}/t_{\rm damp}$). This ratio offers another way of looking at this medium in terms of limits, however you can also look at thermal instability classically as done here: Assuming a uniform medium in thermal equilibrium ($\mathcal{L} = 0$) such that the criterion for thermal instability is $(\delta\mathcal{L}/\delta S)_A > 0$, where $\mathcal{L}$ is the net loss function (cooling minus heating per unit mass), S is entropy, and A is the variable held constant (Field, 1965). Thinking about this in limits, when the sound crossing time is short compared to the cooling time, we see an isobaric thermal instability where the pressure is held constant. When the sound crossing time is long compared to the cooling time, then we see an isochoric thermal instability where density is held constant.

For a gravitationally stratified medium, our original over dense cooling gas is more of a blob that oscillates due to buoyant restoring forces as it falls (precipitates) under gravity. This oscillating background rapidly changes causing the cooling blob to experience a modified thermal instability. Both McCourt et al. (2012) and Sharma et al. (2012b) showed that local thermal instability occurs when $t_{\rm cool}/t_{\rm ff} < 1$ (planar simulations), $t_{\rm cool}/t_{\rm ff} < 10$ (spherical simulations); without these limitations the medium remains in single phase. These cooling blobs are essentially driven damped oscillators where the ratio of $t_{\rm cool}$ and damping time (here $t_{\rm damp} \sim t_{\rm ff} \sim t_{\rm bouy}$, where $t_{\rm bouy}$ is the buoyancy time), determine the existence and saturation amplitude of thermal instability. We have already talked about the outcomes

of the $t_{\rm cool}/t_{\rm ff}$ (§2.1.1) in the context of determining halo virialization. For forming cold clouds, the it is more about the absence or presence of heating (Faucher-Giguère & Oh, 2023). When heating is absent, the tug of war between cooling and and shock virialization of cosmological accretion is what determines the thermal instability (i.e., whether cooling flows or stable virial shocks develop). In the presence of heating and background hydrostatic thermal equilibrium, is is the relationship between cooling and buoyancy that determines local thermal instability (i.e., the fragmentation into a multiphase medium).

There are other physical processes that can influence the development and saturation of thermal instability. Magnetic fields are known to damp buoyant oscillations (via magnetic tension) and cause destabilization. Essentially this allows thermal instability to occur anywhere in the halo, independent of $t_{\rm cool}/t_{\rm ff}$ (Jiang & Oh, 2018). Other influencing factors include: magnetohydrodynamics (have been shown to enhance the amplitude of thermal instability), angular momentum (can suppress buoyant damping of thermal instability by providing rotational support against gravity and deflecting the decent of a condensing blob via Coriolis forces Sobacchi & Sormani, 2019), and turbulence (can both enhance and suppress thermal instability).

No matter what is helping or hindering cold clouds from forming in thermal stability or instability, once dense cold gas is introduced into the halo, the main point is that it cannot stay in equilibrium. This cold gas either precipitates under gravity or it is blown out by a wind (§2.1.2); thus this gas must evolve as it shears against hot gas by either (i) growing via condensation or (ii) diminishing through instabilities. With our new information in hand, we must continue out journey to learn how these cold gas clouds survive and grow.

2.2.2 Cold Gas Survival & Growth

As we learned we learned in the previous section, condensation is the process of turning hot gas into cold gas. This now cold gas shears against the surrounding hot gas and mingles together to produce a well mixed intermediate temperature gas that also begins to cool. This cooled gas actually retains its momentum and over time this new cold phase gas stars to grow and co-move with the hotter phase gas. This mixing-induced thermal instability enforces kinematic coupling between phases, and this high rate of conversion between phases has important implications for the baryon cycle and my own thesis work (see Figure 1.6 and Chapter 4). The rest of this section will discuss how condensation in an essential component of cloud growth and survival through a model and simulation lens and how it impacts certain parameters included in different studies runs.

Cloud Entrainment & Growth: It is well known that condensation is tied to the cloud entrainment problem. Both atomic and molecular gas is observed either outflowing (in galactic winds §2.1.2) or inflowing (as intermediate velocity clouds - IVCs or high velocity clouds - HVCs), at velocities comparable with virial velocities. The main question that arises from these observations is: how can the gas withstand hydrodynamic instabilities? Thus the problem is this: if cold gas is over dense, the timescale for acceleration by hydrodynamic ram pressure, $t_{\rm acc}$, is longer than the timescale for the cloud to mix into its surroundings, the cloud-crushing time $t_{\rm cc}$, by a factor of $t_{\rm acc}/t_{\rm cc} \sim$ 10-30, not taking into account cloud sizes or properties (Klein et al., 1994; Faucher-Giguère & Quataert, 2012; Zhang et al., 2017). In fact, many simulations have highlighted this very problem where clouds in a wind tunnel get

destroyed before they can become entrained (Klein et al., 1994; Mellema et al., 2002; Pittard et al., 2005; Cooper et al., 2009; Scannapieco & Brüggen, 2015; Schneider & Robertson, 2017). To begin to find a solution to this problem, an paradigm has emerged that suggests that hot gas condenses onto cold gas, through mixing and cooling, thereby transferring mass and momentum to the cold phase.

The first time cloud growth rather than cloud destruction was seen was in radiatively cooling wind tunnel simulations showing HVC survival (Marinacci et al., 2010; Armillotta et al., 2016). Just a few years later Gronke & Oh (2018) found that cloud growth by entrainment in a wind and its survival matched simulation results well; for cases of survival, the cloud forms a cometary tail, similar to the observed head-tail morphology of HVCs (Putman et al., 2011), which grows in mass. Thus, it seems like cloud growth and entrainment really are intertwined such that as the hot gas condenses, it imparts momentum and accelerates the cloud. With this relationship more defined, one can start to quantify growth and entrainment times, like was done in Gronke & Oh (2020a). It so happens that cloud growth does not stop once the cloud is entrained despite there being very little shear between different temperature gas to drive mixing. Instead, growth is maximized for co-moving clouds (Faucher-Giguère & Oh, 2023)! In entrained clouds, mixing is driven by cooling-driven cloud pulsations, which arise for clouds that lose sonic contact as gas condensing onto the cloud cools, $t_{\rm cool} \ll t_{\rm sc}$ (where $t_{\rm sc} \sim R/c_{\rm s,c}$ is the sound crossing time). The small loss of pressure balance causes the cloud to contract, overshoot, and subsequently expand, which in turn drives more mixing and cooling and pulsations. This cooling in a pressure-confined cloud drives over-stable buoyant acoustic oscillations governed by $t_{\rm cool}/t_{\rm sc}$, just like cooling in a stratified medium drives over-stable buoyant oscillations governed by $t_{\rm cool}/t_{\rm ff}$.

Other Impacts on Survival & Growth: There are several other factors that play a role in cold gas survival and growth that are by no means settled. We summarize the key points for some of the factors here and refer the reader to sections 3.2.2-6 of Faucher-Giguère & Oh (2023) for more in depth details:

- *Condensation via Magnetic Fields*: Amplified magnetic fields have two important dynamical effects in the context of cloud survival and growth. The first being that magnetic drag can couple the cold and hot gas and reducing their overall acceleration times as compared to hydrodynamic cases (Dursi & Pfrommer, 2008; McCourt et al., 2015). Secondly, magnetic fields can suppress the Kevin-Helmholtz instability via magnetic tension which clearly suppresses mixing in both adiabatic (Jones et al., 1997) and radiative (Ji et al., 2019) Kevin-Helmholtz simulations.

- *Condensation via Thermal Conduction*: Conduction can create a thick boundary layer of warm gas around the cloud which affects mixing and cooling (Faucher-Giguère & Oh, 2023). Simulations with isotropic conduction show some modified cloud-wind interactions (e.g., cloud compressions and slower entrainment), but not dramatic changes (Armillotta et al., 2016; Brüggen & Scannapieco, 2016). But real conduction is actually anisotropic since electrons gyrate around magnetic field lines so that cross-field conduction in strongly suppressed. For this reason, simulations with field-aligned conduction find effects of conduction to weak. Once magnetic fields drape over the cloud, conduction is suppressed and has very little effect on cloud mass evolution relative to magnetohydrodynamic simulations (Li et al., 2020; Jennings et al., 2023).

- *Condensation via Gravity:* We have established that cloud gas clouds can be blown out of a galaxy via an outflow. They can also fall onto a galaxy under gravity and originate from thermal instability in the halo or cosmological accretion. Understanding whether or not clouds from these origins can survive and grow is a critical component of HVC research and filling in our knowledge of how more fuel for star formation makes its way to galaxy disks (Putman et al., 2012). Clouds with outflowing gas origins gradually entrain, so destruction processes become weaker until the cloud co-moves with the hot gas, and hydrodynamic instabilities are quenched (Faucher-Giguère & Oh, 2023). Infalling gas, however, never becomes co-moving since they accelerate under the action of gravity and have to survive incredible amounts of shear at terminal velocity.

2.2.3 Cold Gas Morphology

Now I know this may seem like I am going too niche or in depth with this section but cloud size is actually very important and especially for an observer like me. In fact, in recent years, there has been a growth of observational evidence for small-scale structure in cold CGM gas (e.g., cloudlets, fog, mist) and studies that show how these structures can impact observational interpretations (Hennawi et al., 2015; Lau et al., 2016; McCourt et al., 2018). Cloud sizes can affect the interpretation of a host of observables, ranging from column densities, kinematics, cold gas mass fractions, and radiative transfer (Faucher-Giguère & Oh, 2023); this is mostly because cloud size sets the ratio of volume to surface area. For example, something that deeply matters to the results shown in Chapter 4, the interpretation of kinematic line profiles can change depending on if the absorption comes from discrete clouds or fog of droplets entrained in a hot gas: non-thermal broadening would trace either small-scale cold gas turbulence or large-scale hot gas kinematics, respectively.

But how can clouds fragment to such small scales? Faucher-Giguère & Oh (2023) lays out two scenarios: (i) if $t_{\rm cool}$ falls far below the sound-crossing time $t_{\rm sc}$ in a cool cloud, such that the cloud is strongly under-pressured relative to the surrounding hot gas, $P_{\rm cloud} \ll P_{\rm hot}$, then the cloud-crushing shock can shatter the cloud (McCourt et al., 2018). For large cooling clouds ($R \gg c_{\rm s} t_{\rm cool}$) shattering is easily triggered by large nonlinear perturbations (e.g., via turbulence). Shocks are effective at shattering cold gas through either compression of preexisting cold gas (Mellema et al., 2002) or fragmentation in the radiative shock (Mandelker et al., 2019). Shattering can also arise during initially isobaric linear thermal instability, once the cloud loses sonic contact with its surroundings as it cools (Gronke & Oh, 2020b; Das et al., 2021). (ii) cloudlets can be produced via Kevin-Helmholtz instabilities; for example, the tails of clouds in winds show a sizable sample of dense small clumps (Cooper et al., 2009; McCourt et al., 2018; Sparre et al., 2019), which have a column density distribution that peaks at $\rm N_{cloudlet} \sim 10^{17}\ cm^{-2}$ (Liang & Remming, 2020).

How about in multiphase gas, is there structure on all scales? Just because there is a strong evidence that small-scale structures exist, it doesn't mean that individual clouds have to be long lived; they could be continuously created and destroyed if there is a long lasting cold gas supply (Faucher-Giguère & Oh, 2023). In fact, this seems to be the case for turbulent flows according to a study by Gronke et al. (2022) which showed that growing clouds continually shed small clouds into the hot medium. In essence, cold gas condenses at large scales and then cascades to small scales through different fragmentation processes. So

it seems like there is structure on all scales and whether the large or small scale structure matters, depends on the properties that observers probe (column density, mas, emission measure, covering fraction, etc). This is still an active area of study and there is a long way to go in developing an agreeing theory on cloud mass and size in the CGM community.

2.2.4 Cold Gas Interactions via Turbulent Mixing Layers

Throughout this introduction I have mentioned turbulence. For almost all of these cases I have been discussing what happens at the boundaries between phases; these "in between" places are where velocity shears or differential acceleration is driven by Kevin-Helmholtz or Rayleigh-Taylor instabilities and is known as turbulence. Over the past several years, significant progress has been made in understanding these layers of turbulent mixing (TMLs), with special attention to the relationship between turbulence and radiative cooling (Kwak & Shelton, 2010; Kwak et al., 2011, 2015; Henley et al., 2012; Ji et al., 2018; Fielding et al., 2020; Tan et al., 2021b; Chen et al., 2023; Yang & Ji, 2023).

A TML is essentially something we have already been discussing. In these layers, hot and cold gas mix to form intermediate temperature gas which then cools. A key quantity for TML is the inflow velocity $v_{\rm mix}$ of hot gas into the mixing layer since this determines the mass flux $\dot{m} \sim \rho_{\rm h} v_{\rm mix}$ and the enthalpy flux $\dot{e} \sim (5/2) P v_{\rm mix}[1 + M^2]$, where M^2 is a factor that represents the kinetic energy of the hot gas that is eventually thermalized (Faucher-Giguère & Oh, 2023). Due to inflowing hot gas mixing and cooling, for the steady state $\dot{m}$ gives the cold gas mass growth rate and $\dot{e}$ gives the TML surface brightness. By using $v_{\rm mix}$the following properties of TML has been found:

- TMLs are approximately isobaric. As you increase resolution, the pressure fluctuations are relatively small and tend to decline.

- The inflow velocity is on the order of the cold gas speed so that $v_{\rm mix} \sim c_{s,c}$. For example of the temperature of the cold gas is $T_c \sim 10^4$ K, then $v_{\rm mix}$ is approximately 10 km s^{-1} give or take an order of magnitude. This is rather low compared to average shear velocities ($\sim$ 100-1,000 km s^{-1}) but this is because the inertia of the cold gas limits the rate at which the hot/cold interface deforms and the two phases mix.

- The inflow velocity has different scalings in the fast ($v_{\rm mix} \propto t_{\rm cool}^{-1/4}$; multiphase) or slow ($v_{\rm mix} \propto t_{\rm cool}^{-1/2}$; single phase) cooling regimes. Because they scale with $v_{\rm mix}$, the mass growth rates and surface brightness follow the same scalings. I have introduced both scalings but the fast cooling regime is the most important/interesting since we know that for the most part these TMLs are multiphase and the criterion for cloud survival is $t_{cc}/t_{\rm cool}$.

Highly ionized metals, like O VI, are potential observational diagnostics of TMLS. These high ions, which peak around $T \sim 10^5$ K in collisionally ionized gas, should have short cooling times ($\sim$10 Myrs in CGM conditions), but is a plethora of observations in quasar absorption studies (Prochaska et al., 2011; Tumlinson et al., 2011) and HVCs (Savage et al., 2014)[12]. In fact, a surprising alignment of velocity centroids in low and high ions (Tripp

[12]It is important to note that the cooling time of O VI-bearing gas depends on density. This means that

et al., 2008; Rudie et al., 2019; Haislmaier et al., 2021) has been found to naturally arise in TMLs due to the different portions of a mixing layer participating in the same large-scale turbulence. Even with this observational evidence, there are some challenges on the model side; predicted column densities of individual TMLs are about two orders of magnitude lower than observations (Slavin et al., 1993; Kwak & Shelton, 2010; Ji et al., 2019). So if TMLs are really driving the observations, the sightlines used by the surveys would have to be piercing hundreds of mixing layers; this isn't full implausible considering the CGM could exist as a fog of tiny cloudlets, but probably unlikely. The ratios of different ionized species is another useful diagnostic to differentiate between theoretical models. Ratios like N_{SiIV}/N_{CIV} or N_{CIV}/N_{OVI} depend explicitly on temperatures which makes them slightly complicated since other macroscopic quantities like mass, momentum, and energy transfer between phases are independent of thermal conduction and ratios are not. Chapter 4 touches more upon this subject and uses both O VI and C IV to constrain aspects of CGM gas in nearby $L^{\star}$ galaxies.

3 Building a CGM Cookbook: Simulations

So far throughout this introduction, I have referenced results from work that use analytical models or simulations, but I have mostly focused on what observations have revealed about the CGM. But the time has come to talk about simulations. Simulations come in all forms and sizes from a few parsecs of resolution to cosmological, hydrodynamical simulations that are on the orders of several mega-parsecs in size. And each of these simulations have developed their own cookbook for how they describe and make a galaxy ecosystem. To continue with our cooking metaphors, imagine you are trying to make the perfect chocolate chip cookie. If you're like me, then your first stop might be searching for a recipe on Pinterest. Upon typing chocolate chip cookie recipe into the search bar, you will be bombarded with several recipes all claiming that theirs is the BEST way to make a chocolate chip cookie. After looking though a couple, you will notice common ingredients but they all have slightly different prescriptions for how much to include: one might call for 3 cups of flour instead of 2 and a half, or chunks of chocolate instead of chips. In essence, this is very similar to the spread of simulations in the modern era. They all are accomplishing the same thing (replicating galaxies and their environment) but have slightly different methods of accomplishing this. For the rest of this section, I am just giving the briefest overview of where cosmological, hydrodynamical simulations are currently, but if you are looking to get into the simulation world, I recommend starting with Crain & van de Voort (2023). They give a great overview of the success and challenges that face hydrodynamical simulations. I would also like to point out that my thesis work utilized simulations to compare to our observations and I include a more in depth description of their individual recipes in Chapter 2.

Now, cosmological, hydrodynamical simulations have made a big splash in the scientific community and helped further our understanding of the physics that governs the formation and evolution of galaxies. Modern simulations are able to model realistic feedback associated

in the central regions of halos this gas will have short cooling times, but in the outskirts of halos the cooling times can be significantly longer, ∼100 Myrs to 1 Gyr! For example, in Figure 8 of Faerman et al. (2020) the isentropic model shows that O VI gas, which peaks at radii > 100 kpc (Figure 6), has a cooling time of > 2 Gyrs.

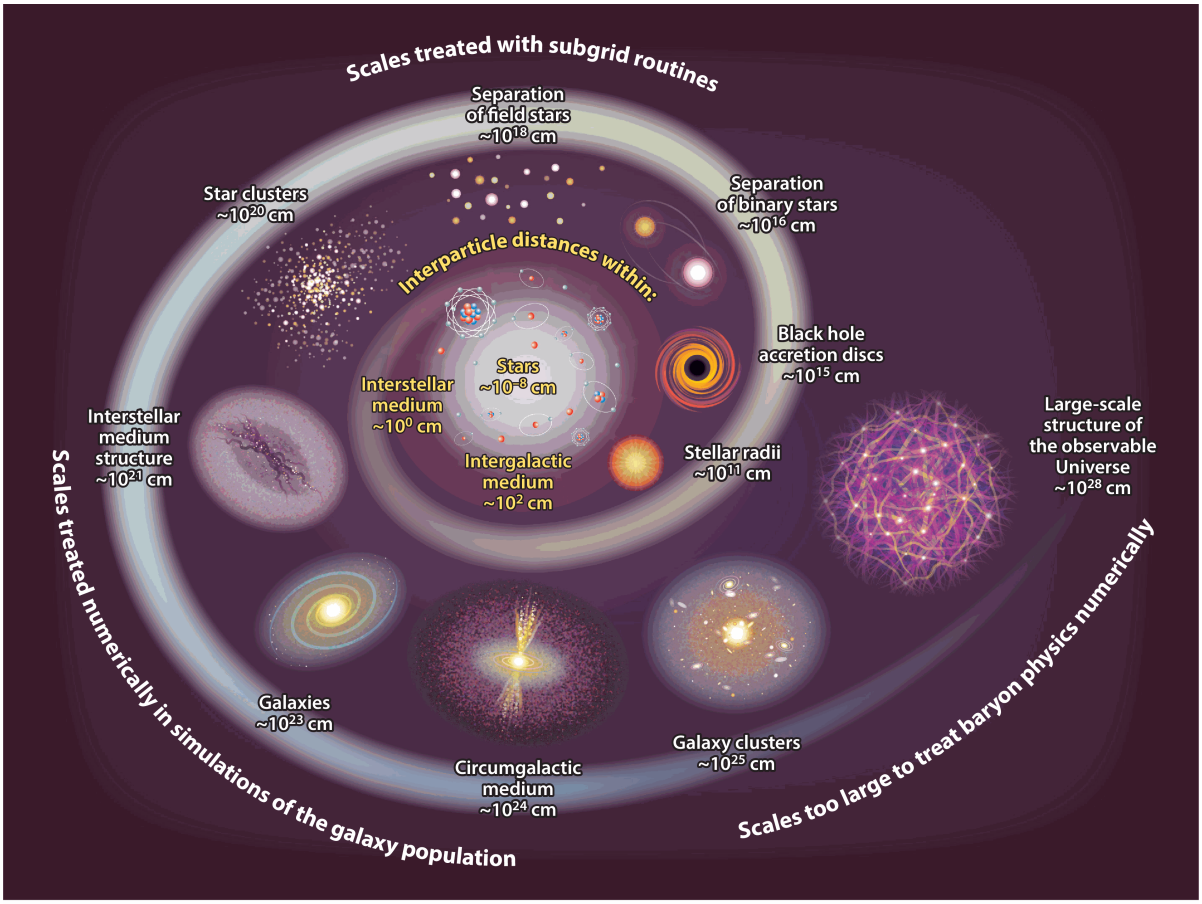

Crain RA, van de Voort F. 2023
Annu. Rev. Astron. Astrophys. 61:473–515

Figure 1.8: A schematic illustration of the breadth and range of physical processes influencing the formation and evolution of galaxies. This schematic from Crain & van de Voort (2023), demonstrates how cosmological, hydrodynamical simulations are able to follow cosmic structure formation up to 100 Mpc scales and switches to subgrid models for the smaller scales.

with the formation and evolution of stellar populations and the feedback associated with the accretion of gas onto super massive black holes. But as we have discovered throughout this thesis introduction, the efficiencies of feedback mechanisms are governed by microphysics which act on scales that are too small to parse out on the resolution level of big simulations. To combat this and achieve realistic results, simulations must rely on simplified subgrid models (Figure 1.8). These subgrid models tackle a wide array of physical processes (e.g. build up of the ISM, star formation, radiative processes in cosmic gas, element abundance evolution, supermassive black hole seeding and growth, etc) and are the building blocks of modern simulations. But, despite their importance, the parameters are poorly constrained and their implementation varies from simulation to simulation. To overcome these challenges, the main strategy has been to calibrate these parameters and determine the differences in the outcomes.

Tailoring subgrid prescriptions is able to reproduce many small scale galaxy properties and scaling relations relatively well (e.g., stellar masses, sizes of galaxies, Tully-Fisher relation, etc), but large-scale relations and properties (e.g., mass-metallicity relation, baryon fraction-halo mass relation, galaxy-absorber statistics, etc) are highly sensitive to tinkered with prescriptions. Because of these dependencies, for simulations to match observational results, they must be calibrated in specific ways. This leads to even more challenges when comparing observations between many simulations as they all have their own specific recipe for achieving the same end goal. Even though there are still challenges in the simulation community, their collective recipes provide a rich insight and foundation for which advancements in more sophisticated models and applications can build upon. By working together, both observational and theoretical astronomers can continue to further our understanding of the galaxy ecosystem and its evolution. To round out this section, I have included some of the key points from the summary in Crain & van de Voort (2023):

1. By regulating star formation with plausible quantities of energetic feedback associated with the formation of stars and the growth of black holes, the current generation of state-of-the art cosmological hydrodynamical simulations form a galaxy population with broadly realistic stellar masses and sizes.

2. Although the more realistic of these simulations were calibrated against present-day galaxy masses and sizes, the evolution of these quantities was not, and the observed evolutionary trends are also broadly reproduced.

3. Simulated galaxy populations exhibit the diversity of present day morphologies exemplified by the Hubble sequence, as a natural outcome of the diversity of galaxy assembly histories and the intrinsic properties of their host halos.

4. The simulations reproduce many key galaxy scaling relations, elucidating their origin. A key example is the stellar mas-halo relation, which has been shown to emerge primarily in response to gas expulsion in the low-mass regime and throttling of cooling from the CGM onto the ISM in more massive halos due to AGN feedback.

5. The simulations also illuminate the origin of scatter about scaling-relations, with key examples being the scatter in star-formation rate, and in metallicity, at fixed stellar

mass. Both can be explained in terms of the balance of gas flows into and out of galaxies, star formation, and black hole growth.

6. Once armed with a realistic model, examinations of partner simulations in which model components are adjusted or toggled has proven an effective approach to illuminating the sensitivity of galaxy properties and observables to physical processes.

4 My Recipe for the CGM

Theorists and the simulations they build aren't the only contributors to CGM recipes. Observational astronomers who study the CGM, like me, also get to have their say in the kitchen. But, our role is often very different than theorists. A lot of the time, our contributions to the recipe are limited by what ingredients we have available or what we can "harvest" (observe) from the garden/farm (CGM). But, we also have the special opportunity to write proposals and ask from time to go searching for the key ingredients that we want (i.e., write *HST* proposals and ask for observing time). This is the equivalent of searching different grocery stores for that elusive ingredient or spice so that you can finally test out that new recipe you have bookmarked or been crafting in your time off. For me, the elusive ingredient my collaborators and I were highly interested in was triply ionized carbon or C IV and spoiler alert... we found some!

4.1 Triply Ionized Carbon: My Favorite Ingredient

C IV is an "intermediate" ion that requires a potential energy of 47.89eV to ionize C III into C IV and is unique because in CGM conditions, it can form either through photo-ionization or collisional ionization. Additionally, C IV is observed in the CGM of galaxies across 13 Gyrs of cosmic time and as such, its a key ion that provides much insight into the chemical enrichment of these galaxy's halos.

Examples of its scientific power include its use to i) trace intergalactic medium enrichment from $z \approx 6$ to 2 (Becker et al., 2009; Simcoe et al., 2011), ii) measure the kinematic imprints of outflows from Lyman-Break Galaxies at the peak of cosmic formation (Turner et al., 2014), iii) trace the rise of the cosmic density of metals over the last six to eight Gyrs of the history of the universe (Cooksey et al., 2010; Hasan et al., 2020), and iv) has been an integral tracer for simulations and other high z studies (Bird et al., 2016; Burchett et al., 2016; Chen et al., 2001; Fox et al., 2007; Anand et al., 2025). When combined with higher (O VI) ionization species, C IV acts as a crucial metric to gauge the ionization structure and the processes (Werk et al., 2016) of the CGM at different stages of galaxy evolution, constraining the physical processes that both generate and distribute metals in and around galaxies (Berg et al., 2022a). However, despite C IV's strong ability to trace galactic reservoirs, it has been historically lacking from the spectral coverage of COS surveys (e.g. Tumlinson et al., 2011; Borthakur et al., 2015). My collaborators and I were fortunate enough to be awarded two proposals focused on observing C IV and my subsequent thesis work used this ion as our key ingredient to contribute to the main CGM recipe.

4.2 Key Motivating Questions

As we have talked about, results from the Hubble Space Telescope and the Comic Origins Spectrograph (*HST*/COS), have established that the CGM plays an essential role in a galaxy's evolution by hosting the gaseous reservoir that simultaneously feeds accreting material, replenishing fuel for future star formation, and keeps a record of metal enriched material ejected from the disk of the galaxy through winds and other feedback processes (Lehner & Howk, 2011; Peeples et al., 2014; Tumlinson et al., 2017; Faucher-Giguère & Oh, 2023). Observations have shown that this diffuse medium is multiphase with complex dynamics that are interrelated to the galaxy's potential to form stars (§1). However, there are still many questions regarding how feedback impacts the CGM and, more specifically, what this means for the ionization state (§2, 2.1.4). Thus, it is critical to quantify the connection between these halos and their host galaxies, since it can provide essential constraints on the specific events that transform galaxies. Without parsing out these intricate relationships and physical details, we cannot have a complete understanding of how galaxies evolve over time.

Some interesting key questions which remain unsolved in the CGM include:

1. Does a correlation exist between the pc-scale physics of black hole growth and the global, kpc-scale gas flows of the CGM in observations and how does this compare to commonly used simulations?

2. Does a dichotomy exist for C IV between star forming and passive galaxies, similar to the one observed in O VI?

3. What do combined observations of C IV and O VI reveal to us about the ionization state, temperature, and astrophysical processes responsible for this ionization mechanism in the CGM?

Throughout the upcoming chapters, I provide my observational contribution to the CGM recipe and begin to offer answers these questions[13].

> *A story a story; let it come, let it go.*
>
> – A Story A Story - Gail E. Haley

[13]Each of the following three chapters are already published or soon to be published work: Chapter 2 (Garza et al., 2024), Chapter 3 (Garza et al., 2025), Chapter 4 (Garza et al. ApJ submitted)

CHAPTER 2

CONNECTING GALAXY BLACK HOLE MASS WITH THE STATE OF THE CGM

It's the questions we can't answer that teach us the most. They teach us how to think. If you give a man an answer, all he gains is little fact. But give him a question and he will look for his own answers

– Kvothe, The Wise Man's Fear

1 Introduction

For decades, absorption-line experiments using bright background quasars (QSOs) have been recognized as an efficient way of studying diffuse gaseous atmospheres of the Milky Way and other galaxies (e.g. Bahcall & Spitzer, 1969; Bergeron, 1986; Werk et al., 2013). With the more recent addition of results from *HST*/COS, astronomers have established that this diffuse outer part of galaxies, called the circumgalactic medium (CGM), is a highly-ionized, massive, spatially extended reservoir of both fuel for future star formation and the byproducts of stellar evolution (Lehner & Howk, 2011; Peeples et al., 2014; Werk et al., 2014; Tumlinson et al., 2017). The properties of the CGM, particularly the highly ionized CGM traced by O VI, are linked to the star-forming properties of host galaxies (e.g. Tumlinson et al., 2011; Tchernyshyov et al., 2022). For this reason, the CGM can serve as an excellent testing ground for astrophysical models of galaxy-scale feedback. In this work, we focus on testing the cumulative effect of feedback from supermassive black holes (SMBHs) on the content of the cool CGM.

It is well-known that the properties of galactic SMBHs correlate with their parent galaxy properties. For example, Kormendy & Richstone (1995) found that black hole masses scale linearly with the absolute luminosity of the host bulge (or elliptical galaxy). This result inspired many investigations into other scaling relationships between these galaxy properties and their corresponding central black hole properties, which found an indirect link between galaxy formation and the growth of their SMBHs (Haehnelt et al., 1998; Magorrian et al., 1998; Saglia et al., 2016). In particular, both the relation between the mass of the central SMBH and the stellar dispersion of its host galaxy's bulge, M_{BH}-σ, and the bulge mass-M_{BH} correlation (Silk & Rees, 1998; Ferrarese & Merritt, 2000; Gebhardt et al., 2000; Häring & Rix, 2004; Reines & Volonteri, 2015), reflect the assertion that the mass of the SMBH is a fundamental property of a galaxy, reflective of its history (Kormendy & Ho, 2013; van den Bosch, 2016). To extend this further, we posit that there can be a significant (and observable) alteration of the CGM content of galaxies due to black hole activity over time due to the cumulative effect of the processes associated with black hole growth such as those envisioned in most kinetic-mode feedback scenarios (e.g., Best & Heckman, 2012).

Recently, analytical studies have shown that maintaining the large observed column densities of highly ionized gas in the CGM, traced by far ultraviolet (FUV) transitions like O VI, for longer than a Gyr requires a significant source of energy that cannot be supplied by galactic supernovae and stellar winds alone (Mathews & Prochaska, 2017, but see Faerman et al. (2020, 2022)). If these are the only energy sources, McQuinn & Werk (2018) asserts that much of a galaxy's energy budget must be expended in the CGM (rather than the ISM). SMBHs may provide a promising source of far-reaching intermittent feedback shocks that can keep the gas in the CGM warm and highly ionized ($T > 10^5$). More specifically, the energy released from building a SMBH not only exceeds the binding energy of the gas in the bulge (by orders of magnitude), but can easily exceed the binding energy of the entire gaseous halo (Oppenheimer, 2018). Therefore, even with a low efficiency of the SMBH rest mass energy being imparted to the gaseous halo over its history, the mass and the energetics of the CGM can be significantly affected.

In combination with established black hole scaling relations, these arguments imply that

the mass of a SMBH may be a key determinant for the content and kinematics of the CGM around L* galaxies. There are already established physical links (i.e. scaling relationships) for galaxies on black hole scales (sub-pc) and stellar-disk scales (kpc). If these relationships are combined with the expectation that the extended gaseous halos of galaxies fuel their star formation, it is possible that the evolution of a galaxy's central black hole likewise physically links to the properties of galactic gas on CGM scales (tens to hundreds of kpc). Our present survey, which we call COS-Holes, seeks to examine whether such a correlation exists between the pc-scale physics of black hole growth and the global, kpc-scale gas flows of the CGM that fuels star formation (Oppenheimer et al., 2020; Nelson et al., 2018a; Sanchez et al., 2019).

In the last five years, simulation work has already suggested that feedback from a galaxy's SMBH impacts the content and ionization state of its CGM, but they have differing views on the role the SMBH ultimately plays. Results from studies using the cosmological simulations TNG (Nelson et al., 2018b), EAGLE (Davies et al., 2019; Oppenheimer et al., 2020), and Romulus (Tremmel et al., 2017) suggest that the SMBH at the center of galaxies enriches the CGM by driving metals out of the disk and into the halo. However in EAGLE and TNG, galaxies that host more massive BHs can provide a significant amount of energy over time which transport baryons beyond the virial radius, ultimately reducing gas accretion, overall star formation, and the total density of the CGM. Using O vi, demonstrated to be a sensitive probe of SMBH feedback, Sanchez et al. (2019) reports a contrasting view to the role of the SMBH outlined above. Results from Romulus do not show evacuation of CGM gas into the IGM, but rather suggest that galaxies with more massive BHs are more likely to have a more-metal enriched (higher ion column density) CGM. Due to these opposing simulation predictions, it is imperative to empirically test the role SMBH feedback plays (if any) in setting the content of the CGM.

This work examines the observed relationship, if any, between black hole growth over long timescales (parameterized by a dynamically-measured SMBH mass) and the gas content and kinematics within the extended halos of galaxies. In addition, we compare these observations to predictions from cosmological simulations. Our novel sample of stellar- and halo-mass controlled nearby galaxies ($z < 0.005$; Figure 2.1) host a wide range of dynamically resolved SMBHs ($\log_{10}$ M$_{\rm BH} \sim$ 6.8-8.4) and FUV bright QSOs at impact parameters between 25 $<$ R$_{\rm proj}$ $<$ 130 kpc.

This chapter proceeds as follows: §2 describes the sample selection §2.1, FUV spectroscopy §2.1.1, and data reduction and analysis for the COS-Holes sample §2.3; §3 presents the BH mass estimates for archival data collected to increase the sample size; §4 presents general trends for the COS-Holes sample (§4.1), the radial profile for the COS-Holes+Literature sample (§4.2), multivariate analysis and statistics done on the sample (§4.2.1), and the minimum mass of carbon seen in the CGM of the sample (§4.3); §5 describes the three simulations used in this paper (§5.1) and presents the results of the simulated values compared to the results of the combined sample (§5.3); §6 presents a discussion of sSFR dependence in C iv ionization (§6.1) and whether BHs evacuate their CGMs or not (§6.2); lastly we present a summary of our conclusions in §7. In this work, we assume a flat-universe ΛCDM cosmology with $H_0 = 67.8$ km s^{-1} Mpc^{-1} and $\Omega_m = 0.308$ (Planck Collaboration et al., 2016).

2 Observation and Data Analysis

2.1 Sample Selection

The COS-Holes Survey consists of nine UV-bright QSOs, z $<$ 0.005, probing the halos of eight galaxies at impact parameters $R_{\rm proj} \sim$ 25-130 kpc as seen in Figure 2.1. To build the survey, we cross-matched the SDSS DR14 QSO catalog (Pâris et al., 2018) and the UVQS (Monroe et al., 2016) QSO catalogs with several published catalogs of galaxy BH masses (Kormendy & Ho, 2013; McConnell & Ma, 2013; Bentz & Katz, 2015; Läsker et al., 2016; van den Bosch, 2016; Terrazas et al., 2017) to search for FUV bright QSOs (GALEX $M_{\rm FUV} <$ 19) within 150 kpc projected distance from the galaxies in their rest frames. By design, the resulting sample contains galaxies that have dynamically determined SMBH masses (e.g. through stellar dynamics, ionized gas dynamics, CO molecular gas disk dynamics, maser disk dynamics etc) determined. We note that we did not select our galaxies based on assembly history or morphology. We acknowledge that recent results have shown that disruptions in the disk (either by merger or similar event) can be an important factor for how BHs grow and affect the CGM (Davies et al., 2022, 2024); however testing for these morphological differences in the galaxies and how that affects the properties of the CGM is beyond the scope of this work. The property cuts implemented for our sample, as described below, were strategically made to match similar cuts made for previous surveys searching for highly ionized gas (COS-Halos; Tumlinson et al., 2011; Werk et al., 2012) within the cool and intermediate temperature phase of the CGM (Tumlinson et al., 2017); what sets our sample apart, however, is our focus on galaxies that have accurately measured BH masses in order to determine how they impact the state of the CGM.

To start, we eliminate from the sample any galaxies in dense cluster environments (e.g. Virgo) which have already been shown to possess significantly less gas than galaxies in more isolated environments (Yoon et al., 2012; Burchett et al., 2018). We check the GALEX NUV magnitudes of our targets for large values of NUV-FUV colors, which would potentially indicate the presence of a strong Lyman Limit system ($N_{\rm HI} \geqslant 10^{17}$ cm^{-2}; LLS) along the line of sight that may have contaminated our transitions of interest. We note that this process does not introduce a bias to the sample selection since the LLS absorption would be at unrelated higher redshifts than our targets.

It is known that AGN feedback can be highly directional and not necessarily aligned with the spin axis of the galaxy (Bentz et al., 2023). However, we choose not to include QSOs that probe the halos of galaxies with black holes that are currently accreting as Seyferts or quasars themselves, as done in Berg et al. (2018). Instead, we are more interested in the long term effects the black hole has on the halo and and thus selected galaxies based on their stellar mass, redshift, and having a dynamically-measured black-hole mass available. None of the galaxies in our sample is classified as an AGN in the mid-infrared photometrically-selected sample of Asmus et al. (2020), using a method that has a 90% reliability in selecting AGN (Assef et al., 2018). We note however, that many of our galaxies do exhibit LINER-like emission in their central regions, possibly indicating a low-luminosity, accretion-powered active nucleus (e.g. Molina et al., 2018). LINER emission is quite common among nearby, L* spiral galaxies, and it can be related to AGN phenomena, although this relation is uncertain and poorly-quantified (Ho et al., 1997).

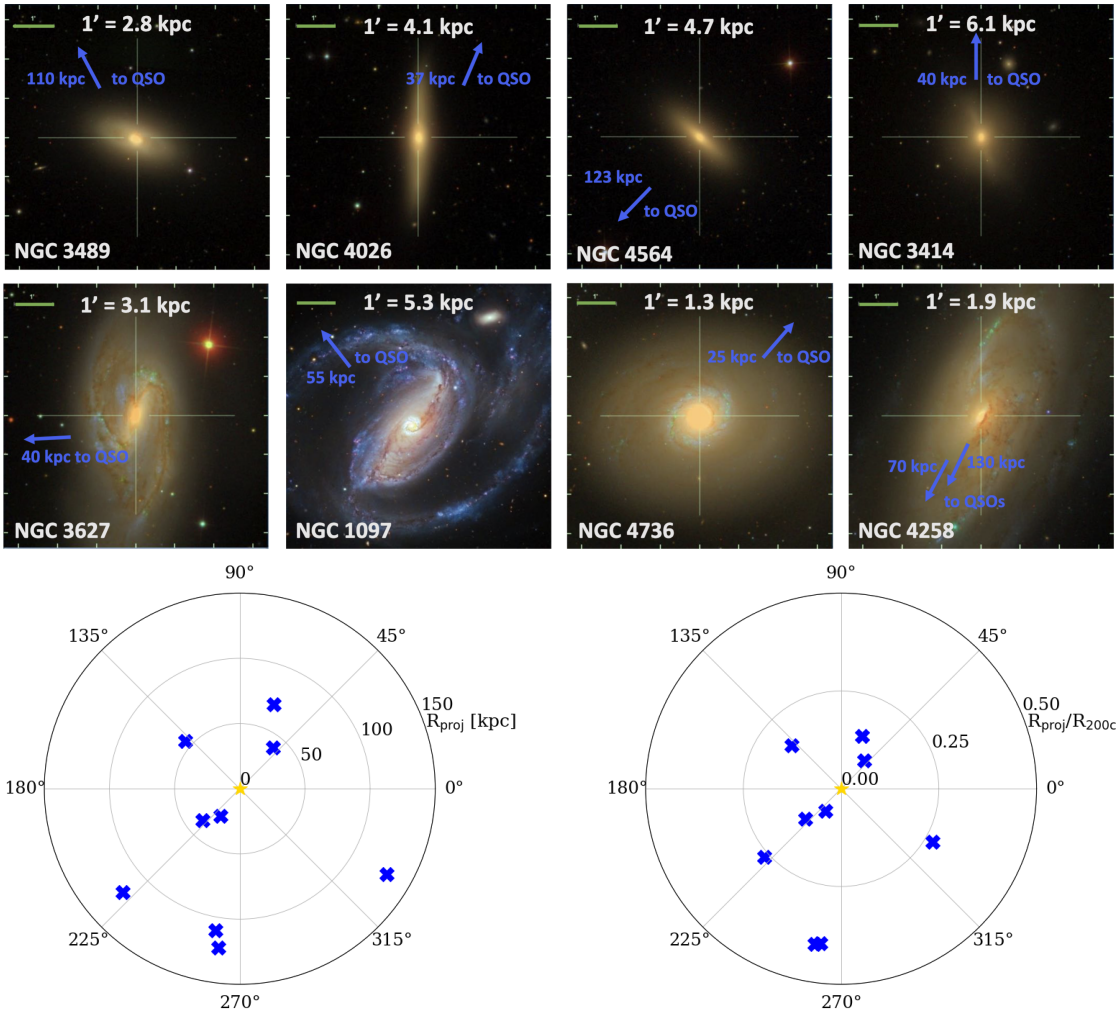

Figure 2.1: COS-Holes Target Galaxies & Distribution of QSO Position Angles. Top: SDSS images of each of the 8 target galaxies in the sample, with exception of NGC 1097, with the image from ESO. The physical scale (in kpc) in each galaxy's rest-frame is shown at the top of its 6'×6' stamp. The targeted QSOs lie outside of the shown FOV; blue arrows and text display the direction, and distance to each FUV-bright QSO. One galaxy, NGC 4258, has two UV-bright QSOs at <130 kpc. Bottom: Target figure showing the distribution of QSO position angles (blue x's) on the sky with respect to the target galaxies (shifted to the center, yellow star). On the left, the radial coordinate (R_{proj}) is in physical kpc at the galaxy redshift, and on the right, this coordinate is translated to the fraction of galaxy's virial radius, R_{proj}/R_{200c}, at which the sightline intercepts the halo. No knowledge of galaxy disk orientation or inclination with respect to the sightline is implied here.

Galaxy	RA (deg)	Dec (deg)	z	Morph	D (Mpc)	sSFR ($\log_{10}$ yr^{-1})	M_* ($\log_{10}M_\odot$)	M_{200c} ($\log_{10}M_\odot$)	M_{BH} ($\log_{10}M_\odot$)
(1)	(2)	(3)	(4)	(5)	(6)	(7)	(8)	(9)	(10)
NGC 1097	41.579	-30.275	0.0042	SB(s)b	14.50 a	-9.7	10.5	11.75	8.14±0.090
NGC 3414	162.818	27.975	0.0049	S0	25.20±2.74 b	-11.8	10.8	12.29	8.40 ± 0.07
NGC 3489	165.078	13.901	0.0022	SABa	11.98 c	-11.2	10.2	11.45	6.77±0.065
NGC 3627	170.063	12.991	0.0024	SAB(s)b	10.05±1.09 b	-10.3	10.8	12.41	6.92±0.048
NGC 4026	179.855	50.962	0.0033	S0	13.35 c	-12.2	10.4	11.66	8.26±0.120
NGC 4258	184.740	47.304	0.0015	SABbc	7.27±0.50 b	-10.9	10.9	12.51	7.58±0.030
NGC 4564	189.113	11.439	0.0038	S0	15.94 c	-12.4	10.4	11.63	7.94±0.140
NGC 4736	192.721	41.121	0.0010	Sab	5.00±0.79 b	-10.7	10.6	11.94	6.83±0.120

Table 2.1: Galaxy Sample Properties. Comments on columns: (1) galaxy name; (2-3) RA and Dec for the galaxy; (4) galaxy redshift; (5) Morphology; (6) assumed distance to galaxy where the letter beside the distance corresponds to one of the following references: (a) van den Bosch (2016), (b) Saglia et al. (2016), (c) Tonry et al. (2001) SBF corrected via Eq A1 in Blakeslee et al. (2010). ; (7) specific star formation rate: typical errors on SFRs derived from infrared photometry are 0.2 - 0.3 dex (Rieke et al., 2009; Terrazas et al., 2017) while stellar masses are accurate to about $\sim$ 50%. On average, for galaxies of these masses, sSFR errors will be on the order of a few - several tenths of a dex; (8) Stellar Mass; (9) Halo Mass; (10) SMBH Mass.

QSO	RA (deg)	Dec (deg)	z	R_{proj} (kpc)	R_{proj}/R_{200c}	Mag (FUV)	Mag (NUV)	N_{ORB}
(1)	(2)	(3)	(4)	(5)	(6)	(7)	(8)	(9)
UVQSJ024649.87-300741.5	41.707792	-30.128194	0.524	55.66	0.32	18.46	17.9	4
SDSSJ105115.75+280527.1	162.81564	28.090865	0.423	40.50	0.15	18.2	17.75	4
SDSSJ110139.76+142953.4	165.4157	14.498172	0.635	110.00	0.80	18.99	18.70	7
SDSSJ112304.91+125748.0	170.77049	12.963349	0.315	120.00	0.42	18.76	18.34	6
SDSSJ115901.72+510630.7	179.75718	51.108554	0.524	37.38	0.23	18.72	18.36	4
SDSSJ122046.61+464347.5	185.19421	46.729881	0.707	69.78	0.22	18.82	18.21	6
UVQSJ122208.10+461250.1	185.53375	46.213917	0.111	130.30	0.42	18.30	18.11	4
LBQS-1235+1123	189.43571	11.116143	0.949	123.10	0.77	18.99	17.93	7
SDSSJ124939.06+412243.5	192.41277	41.378773	0.368	25.52	0.13	18.62	18.55	6

Table 2.2: Background QSO Properties. Comments on columns: (1) QSO Identification; (2-3) RA and Dec for the QSO; (4) QSO redshift; (5) QSO impact parameter; (6) impact parameter normalized by virial radius; (7) FUV Magnitude; (8) NUV Magnitude; (9) Number of orbits.

In addition, there can be an azimuthal dependence of ion absorption in disk dominated galaxies. For example, it has been shown that there is a strong azimuthal dependence with Mg II (Bordoloi et al., 2011), but for O VI the correlation along the major and minor axes are less clear (Kacprzak et al., 2019). These dependencies have not been demonstrated for C IV and investigating them in the COS-Holes sample is beyond the scope of this work. Moreover, as seen in Figure 2.1, some of our galaxies are too face on to report accurate azimuthal angles. The remaining galaxies have azimuthal angles consistent with a random distribution, and thus any azimuthal angle dependence of CGM CIV will not play a significant role in driving the trends (or lack thereof) we observe.

Finally, the nearby galaxy NGC 4258 which has a highly accurate BH-mass measurement from megamaser kinematics (Miyoshi et al., 1995), is serendipitously intersected by two inner-CGM QSO sightlines at 70 and 130 kpc. We include both QSO targets in our final sample because it offers a rare opportunity to study subtle variations (e.g. column density, kinematics, etc.) within a single halo.

We selected a sample of galaxies with stellar masses spanning a narrow range around M* ($\approx 10^{10.5}$ $M_\odot$), since stellar mass has been found to correlate with ionized CGM content (e.g. Tchernyshyov et al. (2022)). We estimate the halo masses of our sample by following the same method as outlined in CGM^2 by Tchernyshyov et al. (2022). Using the stellar mass-halo relation, as defined in Tab J1 of Behroozi et al. (2019), in combination with the approach laid out in Hu & Kravtsov (2003), we convert the halo masses to match the convention where the average mass density within the halo radius is 200 times the critical density of the universe. We denote these halo masses and the corresponding virial radii as M_{200c} and R_{200c}. The final range of stellar and halo masses for the sample are $\log_{10}M_\star/M_\odot \sim$ 10.2-10.9 and $\log_{10}M_{halo}/M_\odot \sim$ 11.45-12.51 respectively. We note that a stellar mass of $\approx 10^{10.5}$ $M_\odot$, is representative of $L^\star$ galaxies, but also can also be a transitional stellar mass in terms of sSFR which is known to correlate with CGM properties in intermediate ionization states (Tchernyshyov et al., 2023). However, by keeping the range of stellar and halo masses relatively small we minimize the scatter due to these properties and enable a controlled examination of the role SMBHs and SFR play in shaping the properties of the CGM. The galaxy and QSO properties for the sample can be found in Tables 2.1 and 2.2 respectively.

2.1.1 Star Formation Rates

We obtain star formation rates (SFRs) for the COS-Holes sample from Terrazas et al. (2017) in §4. For the three galaxies in our survey not included in their sample (NGC 3489, NGC4026, and NGC 4564), we calculate their corresponding SFRs using the same methodology; we summarize the procedure here but a detailed description can be found in Bell (2003) and Terrazas et al. (2016). We calculate far-infrared (FIR) SFRs by using Eq. (A1) in Bell (2003) which uses 60 and 100 μm *IRAS* fluxes to estimate the FIR flux. We then estimate the total infrared (TIR) flux via TIR = 2 × FIR (Bell, 2003). Finally, the TIR-derived SFR is calculated using Eq. 12 in Kennicutt & Evans (2012):

$$\log_{10} \mathrm{SFR_{TIR}}(M_\odot \mathrm{yr}^{-1}) = \log_{10} L_{\mathrm{TIR}} - 43.41 \tag{2.1}$$

where L_{TIR} is the TIR luminosity calculated from the TIR flux estimates and distances to the galaxy (for consistency we use the same distances presented in (Terrazas et al., 2017);

for more detailed information, see Table 2.1). We note that for NGC 3489, only 65 and 90 μm fluxes from *AKARI* were available on NED[1] and we use those values to calculate its respective SFR. To present the calculated SFRs as $\log_{10}$sSFRs (which range between -12.4 and -9.7) in Table 2.1, we divide them by the stellar mass of the galaxy. Typical stellar mass uncertainties derived from SDSS photometry are ±50% (Blanton & Roweis, 2007; Kauffmann et al., 2003) (approximately 0.2 dex) and the SFR errors derived from infrared photemetry are approximately 0.2-0.3 dex (Rieke et al., 2009; Terrazas et al., 2017).

2.2 COS Spectroscopy

The quasar spectra for the COS-Holes survey were taken using the G160M grating on the Cosmic Origins Spectrograph (COS; Froning & Green, 2009; Green et al., 2012) on the Hubble Space Telescope as a part of a 55-orbit Cycle 29 HST Program (PID#16650). The primary spectral features of interest were absorption lines from the doublets C IV ($\lambda\lambda$1548, 1550) and Si IV ($\lambda\lambda$1393, 1402).

C IV is the highest ionization state transition available at these low redshifts ($z < 0.005$) where dynamical black hole masses are available, and is easily detectable in the UV. We note that C IV is an "intermediate" ion with a potential energy of 47.89 eV required to ionize C III into C IV. In collisional ionization equilibrium (CIE) C IV reaches a peak ion fraction at a temperature of 1.2×10^5 K ($10^{5.1}$) and falls rapidly at higher temperatures, with less than 10% at 1.6×10^5 K ($10^{5.2}$) (Gnat & Sternberg, 2007). In photoionization equilibrium (PIE), it peaks at a density of $n_H \approx 2\times10^{-5}$ cm^{-3} at $z = 0$ (Haardt & Madau, 2012; Khaire & Srianand, 2019). Thus, in CGM conditions, it can form either through photo-ionization or collisional ionization (Tumlinson et al., 2017). In EAGLE, Oppenheimer et al. (2020) found that C IV is a very good tracer of CGM gas between $T = 10^4 - 10^5$ K and $n_H = 10^{-5} - 10^{-3}$ cm^{-3}. While it is beyond the scope of this work to constrain the precise phase of C IV, we highlight that we are explicitly avoiding characterization of the hot CGM ($T \approx 10^6$ K).

The COS-Holes QSOs have FUV magnitudes of 18.2 - 19.0 and redshifts ranging from 0.3 − 0.9, and we observed each target QSO for between 4 and 7 orbits in G160M with a central wavelength of 1577 Å. Our exposure times were calculated to detect a 40 mÅ feature at 2σ, consistent with detected C IV around $\sim$ 0.1 - 1 L* galaxies in the literature (Borthakur et al., 2013; Bordoloi et al., 2014; Burchett et al., 2016). All spectra achieved a S/N of 10 - 12 per resel at the wavelengths of C IV.

We combine the CALCOS-generated x1D files using v3.1.1 of the COADD_X1D routine provided by the COS-GTO team (Danforth et al., 2016), which properly treats the error arrays of the input files using Poisson statistics. The code aligns the different exposures by determining a constant offset determined by cross-correlating strong ISM lines in a 10Å wide region of the spectrum. The COS line-spread function (LSF) is well described by a Gaussian convolved with a power law that extends to many tens of pixels beyond the line center (Green et al., 2012). These broad wings affect both the precision of our equivalent width measurements and complicate assessments of line saturation. We mediate these effects by fitting absorption lines with Voigt profiles that incorporate the COS LSF. Each COS resolution

[1]The NASA/IPAC Extragalactic Database (NED) is funded by the National Aeronautics and Space Administration and operated by the California Institute of Technology.

element at R ∼18,000 covers 16 km s^{-1} and is sampled by six raw pixels. We perform our analysis on the data binned by three native spectral pixels to a dispersion of $\Delta\lambda \approx 0.0367$ Å. The resulting science-grade spectra are characterized by a FWHM ≈ 16 km s^{-1}. We perform continuum fitting with the `linetools` package[2], an open-source code for analysis of 1D spectra.

2.3 Absorption Line Measurements

This section describes the methods used to measure and calculate key observational properties, presented in Table 2.3. §4 discusses the column densities versus key galaxy parameters (Figure 2.3).

2.3.1 Line identification with PyIGM

We manually assign line identifications and redshifts to all absorption features in the spectra using the `PyIGM IGMGuesses` GUI[3]. To make sure that we correctly attribute absorption to a COS-Holes galaxy's CGM rather than another absorber at a different redshift, we implement the following methodology. First, we identify absorption features at $z = 0$, the redshift of the Milky Way. We then identify any "proximate" absorption at the redshift of the QSO observed. Finally, we examine the spectra for Lyman series lines at redshifts $< z_{\rm QSO}$ to find serendipitous absorption systems. After identifying these features, we move to the redshift of the target galaxy to look for any absorption features within ∼300 km/s associated with C IV ($\lambda\lambda$1548, 1550), similar to the COS-Halos Survey (Werk et al., 2013). For this paper we specifically focus on C IV identifications and analysis even though other ions (e.g, Si IV $\lambda\lambda$1393, 1402) were observable; in future work we plan on analysing other ion absorption features present. We obtain preliminary line profile fits including the following parameters: central velocity v, column density N, and Doppler parameter, b; we then input these user specified parameters into a Voigt profile fitting program.

2.3.2 Voigt Profile Fitting

Based on the identifications from `PyIGM IGMGuesses` GUI, we measure C IV column densities, Doppler parameter, and the relative velocity of the absorption components using Voigt profile fitting with the package `veeper`[4], which uses `scipy.optimize.least_squares`[5] to perfrom a least squares minimization. In five of our QSO-galaxy line-of-sight pairs we detect C IV while the other four were non-detections and we report them as upper limits. In the spectral regions with no detected metal absorption, we calculate a 2σ upper limit on the column density as estimated by the apparent optical depth method (AODM) with the `linetools XSpectrum1D` package[6] over a 100 km s^{-1} velocity span centered on the galaxy redshift. By default, we use the stronger line at 1548Å to estimate 2σ equivalent width upper limits,

[2]https://doi.org/10.5281/zenodo.1036773
[3]https://doi.org/10.5281/zenodo.1045480
[4]https://zenodo.org/doi/10.5281/zenodo.10993983
[5]https://doi.org/10.1038/s41592-019-0686-2
[6]https://doi.org/10.5281/zenodo.1036773

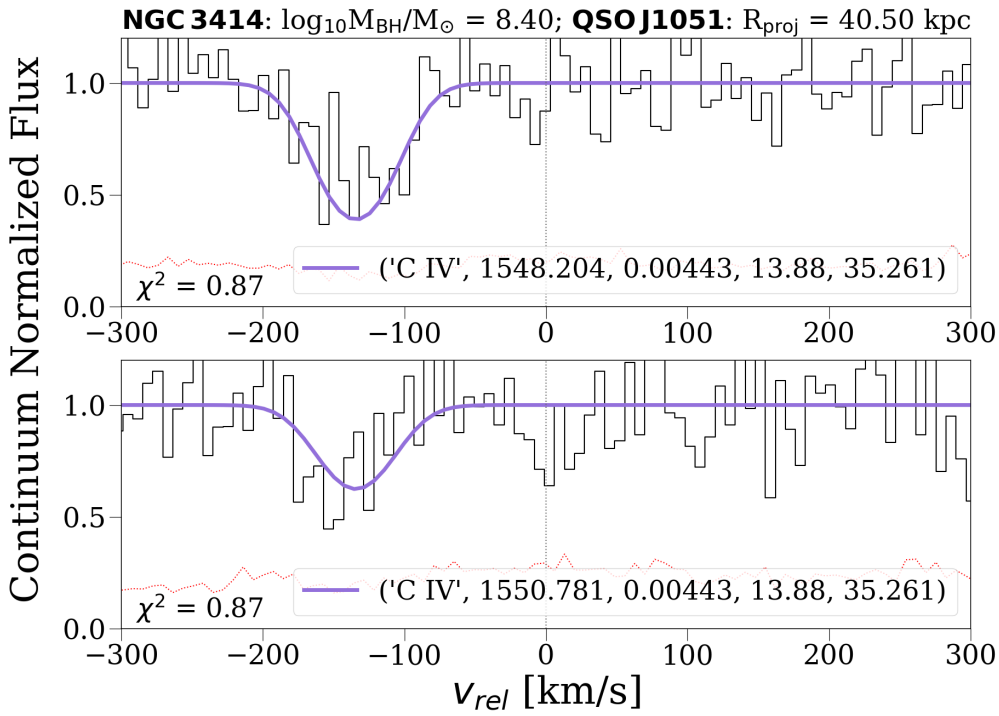

Figure 2.2: Representative C IV absorption feature of a QSO-galaxy pair (SDSSJ1051-NGC 3414) set in the rest frame of the galaxy. The colored line represents the Voigt profile fit due to the $\lambda\lambda$1548 1550 lines in the top and bottom panels respectively. The values in the labels correspond to the following: ionic species, wavelength, absorption feature redshift, column density ($\log_{10}N_{CIV}$) [cm^{-2}], and doppler parameter [km s^{-1}]. In the bottom left hand corner of the figure is the reduced chi squared for the fit made to each absorption feature. The spectra for the rest of the COS-Holes sample are presented in Appendix 8.

similar to the AOD method, using `linetools XSpectrum1D`, but in cases where there is blending or contamination, we use the 1550Å line. When multiple absorption components are found in a galaxy's search window, their column densities are summed, and then this total column density is associated with the galaxy. Figure 2.2 displays the line profile for the C IV ($\lambda\lambda$1548, 1550) absorption doublet for NGC 3414 as a representative Voigt profile for the entire COS-Holes sample. The spectra showing C IV (or upper limits) for the rest of the survey are presented in Appendix 8.

3 Archival Observations & BH Mass Estimations

We increase our sample size with CGM C IV measurements using published HST/COS data from Borthakur et al. (2013) (starbursts), Werk et al. (2013) (COS-Halos), Bordoloi et al. (2014) (COS-Dwarfs), and Lehner et al. (2020) (Project AMIGA). M31 has a measured SMBH mass of $\log_{10}M_{BH}/M_{\odot} = 8.15 \pm 0.24$ (Davis et al., 2017) and a stellar mass of $\log_{10}M_{\star}/M_{\odot} = 10.9 \pm 0.22$ (Williams et al., 2017), both of which are within range of the COS-Holes galaxy properties. Through the use of several QSO sightlines, it has a well studied CGM (Project AMIGA; Lehner et al. (2020)). To match the COS-Holes sample we only include sightlines from Project AMIGA if their corresponding impact parameter was $\leq$ 150 kpc and did not have any contamination from the Magellanic Stream; for a more detailed explanation of how this contamination was removed, see Lehner et al. (2020). If a sightline contained C IV and had multiple absorption features, we sum the measured N_{CIV} to present a total column density, similar to COS-Halos. We note that having a plethora of QSO sightlines provides the opportunity to compare single QSO-galaxy sightline derived CGM properties to a galaxy with multiple sightlines. However, with this reduced sample of Project AMIGA observations, we choose to take an average of the column densities to represent a singular mean N_{CIV} for the Project AMIGA observations. This allows us to have a consistent Literature sample and not bias any results towards features seen in M31.

Similarly to M31, we only include N_{CIV} measurements from galaxies if they had a stellar mass that fell within the range of our COS-Holes observations ($\log_{10}M_{\star}/M_{\odot} = 10^{10} - 10^{11}$); by making these cuts we add four galaxies from Borthakur et al. (2013), five from Bordoloi et al. (2014), and two from Werk et al. (2013) (COS-Halos) to the Literature sample. Since galaxies from these surveys do not have dynamically measured BH masses, we estimate the SMBH mass for each galaxy using the following approximation from Eq. 7 in Piotrowska et al. (2022); Saglia et al. (2016):

$$\log_{10}M_{BH} = 5.246 \times \log_{10}\sigma_c - 3.77 \tag{2.2}$$

where σ_c is the central stellar velocity dispersion of the galaxy, or the random line-of-sight motion of stars due to the galaxy's gravitational potential well.

We obtain central stellar velocity dispersion measurements from the SDSS DR7 value-added catalog[7] (Abdurro'uf et al., 2022) for our selected sample of galaxies from Borthakur et al. (2013) and Bordoloi et al. (2014). These SDSS σ_c values are the superposition of many individual stellar spectra that were Doppler shifted due to the star's motion within

[7] gal_info_dr7_v5_2

Galaxy	QSO ID	$z_{\rm abs}$	$\log_{10}$N$_{\rm CIV}$ (cm^{-2})	b (km s^{-1})	EW (mÅ)	$\lvert v_{\rm rel}\rvert$ (km s^{-1})
(1)	(2)	(3)	(4)	(5)	(6)	(7)
NGC 1097	UVQSJ0246	0.00426	14.14±0.05	55.60±7.58	323.84±33.38	2.01
NGC 1097	UVQSJ0246	0.00471	13.71±0.10	15.36±6.09	109.54±27.27	145.38
NGC 3414	SDSSJ1051	0.00443	13.88±0.05	35.26±6.06	235.30±26.86	148.32
NGC 3489	SDSSJ1101	0.00229	13.44±0.10	22.95±8.90	106.52±19.55	30.88
NGC 3627	SDSSJ1123	0.00287	13.89±0.07	85.00±18.33	230.70±41.64	152.24
NGC 4026	SDSSJ1159	0.0033	<13.24		<73.10	0
NGC 4258	SDSSJ1220	0.001494	<13.47		<60.32	0
NGC 4258	UVQSJ1222	0.001494	<13.39		<50.20	0
NGC 4564	LBQS-1235	0.0038	<13.40		<58.21	0
NGC 4736	SDSSJ1249	0.00054	13.75±0.05	32.39±6.30	186.38±17.07	148.55
NGC 4736	SDSSJ1249	0.00083	13.48±0.10	11.53±6.33	95.97±12.53	47.32
NGC 4736	SDSSJ1249	0.00111	13.86±0.05	37.78±5.91	217.64±19.25	43.94

Table 2.3: COS-Holes Measurements. Comments on columns: (1) galaxy name; (2) QSO identification that is shortened from full name; (3) redshift of the absorption coefficient; (4) C IV column density; (5) Doppler parameter; (6) equivalent width; (7) absolute value relative velocity of absorption component projected along the line of sight in the galaxy's frame.

each galaxy and their measurements were made by analyzing the integrated spectrum of the whole galaxy. We acknowledge that estimating measurements for σ_c can be complex due to several components that can dominate the integrated spectra, either from different stellar populations and/or kinematics in the bulge and the disk. However, these complexities were taken into account in the SDSS catalog where velocity dispersion estimates were only measured for spheroidal systems whose spectra satisfied certain specifications (e.g. galaxy type, $z < 0.4$, etc). In addition, it is recommended to only use SDSS velocity dispersion measurements > 70 km s^{-1} (due to the SDSS instrumental resolution) for spectra with a median per-pixel S/N > 10; for more information about how these velocity dispersions were measured and how their biases were corrected see Bernardi (2007).

All the galaxies from Borthakur et al. (2013) and Bordoloi et al. (2014) (nine total) have median per-pixel S/N > 10 and the average σ_c value for the galaxies with velocity dispersion measurements > 70 km s^{-1} is 111.59±17.18 km s^{-1}. Four galaxies from Bordoloi et al. (2014) have stellar velocity dispersion measurements < 70 km s^{-1}. We report these as upper limits and use 70 km s^{-1} in our $\log_{10}M_{BH}/M_{\odot}$ estimates which correspond to a value of $<$ 5.91. As this is close to the lower bound of the BH mass range for the COS-Holes survey, and the SDSS fiber spectra is not sensitive to BH estimates lower than this value, we do not believe that adding these BH mass estimations bias the new combined sample. For those galaxies drawn from the COS-Halos sample (Werk et al., 2013), where SDSS fiber spectra of the galaxies were not available, we use the python package `pPXF`[8] to analyze the Keck LRIS spectra (COS-Halos; Werk et al., 2012). This package calculates a central velocity dispersion from the optical LRIS spectrum; for more clarification on techniques see Koss et al. (2022). The uncertainties on the BH masses for the literature sample are roughly a factor of five larger than those from the COS-Holes sample with dynamically-measured BH-masses.

We use the package `KaplanMeierFitter` from the python package `LIFELINES`[9] which implements Greenwood's uncertainty estimate, to determine the average $\log_{10}M_{BH}/M_{\odot}$ for both the literature and the COS-Holes sample. Kaplan-Meier is a non-parametric technique of estimating the survival probability of a set of data and is useful since it assumes that censored observations (upper limits) have the same survival prospects as observations that continue to be followed. For the literature sample, with 95% confidence intervals, we find the average $\log_{10}M_{BH}/M_{\odot}$ to be 7.40(6.10, 7.71); this is comparable to the COS-Holes average $\log_{10}M_{BH}/M_{\odot}$ of 7.58(6.77, 8.255). This sample of 12 additional galaxies adds a wider range of galaxies black hole masses to the sample and statistical power to our analysis, especially in §4.2. The collective information for the additional Literature sample can be seen in Appendix 9 in Tables I.1 and I.2 respectively.

4 Observational Results

In this section we examine the effects of SMBH feedback on the state of the CGM in $\sim L^{\star}$ galaxies by examining the observational data. The section proceeds as follows: we investigate the relationship, if any, between N_{CIV} and M_{BH} for the COS-Holes sample §4.1; §4.2 describes analysis for the COS-Holes survey with the addition of a subset of published literature

[8] https://pypi.org/project/ppxf/
[9] https://doi.org/10.5281/zenodo.10456828

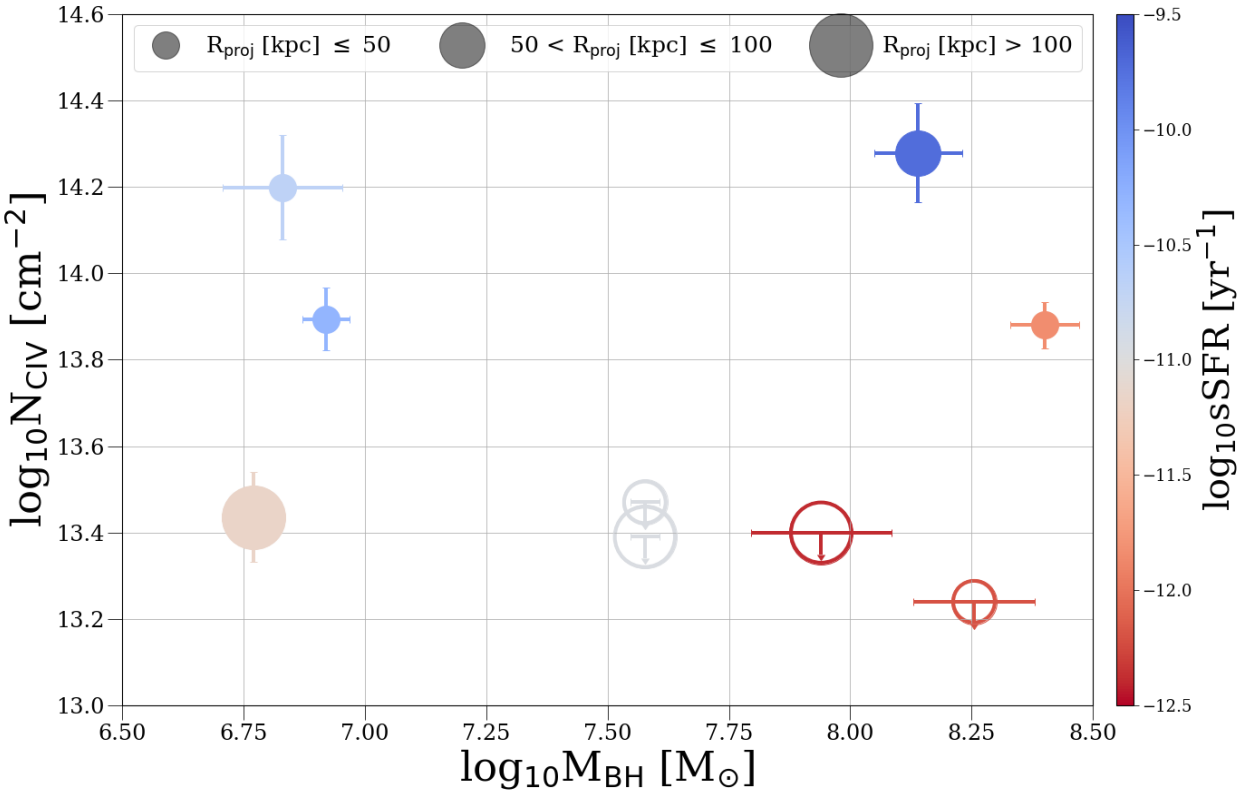

Figure 2.3: Measured C IV column densities versus $\log_{10}M_{BH}$. Each data point is colored with by the specific star formation rate (sSFR) and each marker size corresponds to the respective impact parameter. Unfilled circles represent 2σ upper limits. There is a wide spread in the C IV column densities as black hole mass increases; interestingly, there is a slight trend with sSFR and column density. Galaxies with low observed column density ($\log_{10}N_{CIV} \leq 13.5$) tend to be less star forming (sSFR $\lesssim$ -11.0) than galaxies with higher observed column density.

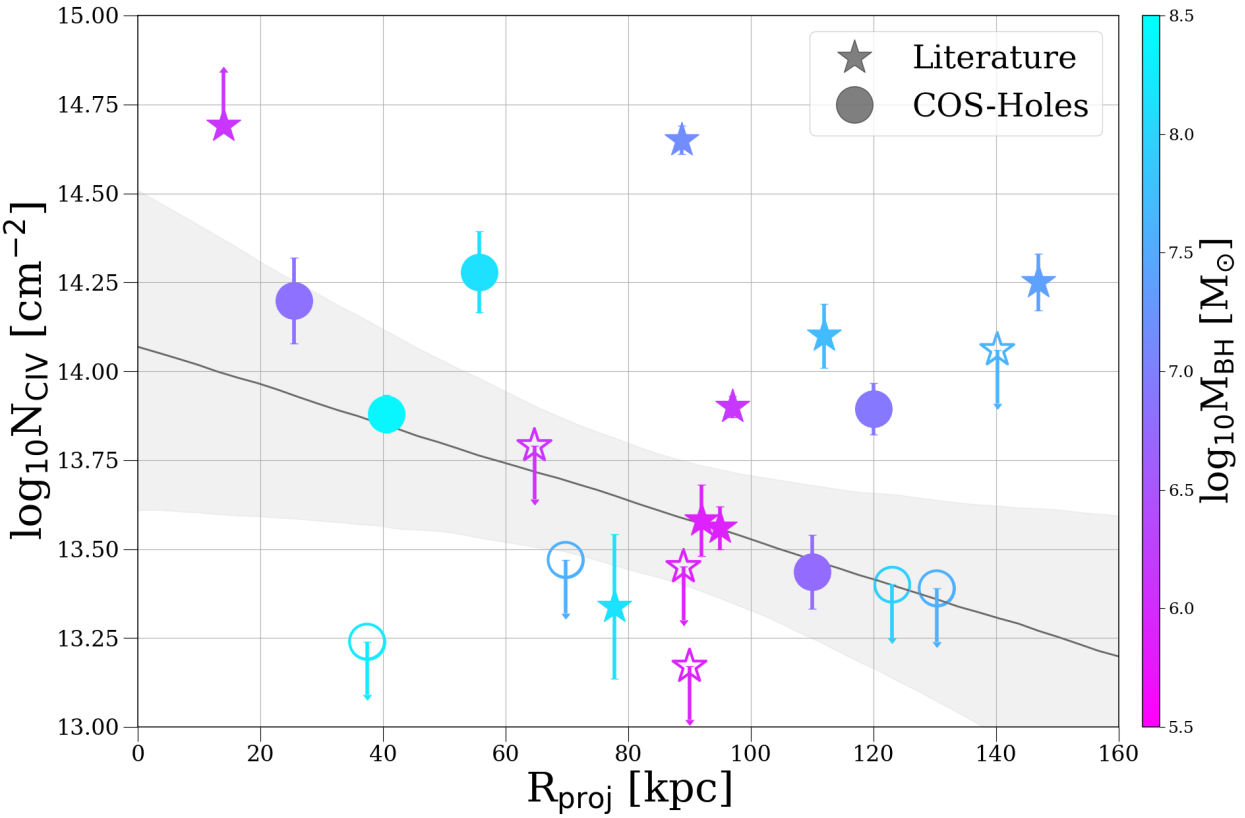

Figure 2.4: C IV column densities vs R_{proj}. Shown are C IV column densities assembled from previous QSO absorption line surveys probing the CGM of low-z, $\log_{10}M_{\star}/M_{\odot} = 10^{10} - 10^{11}$ galaxies, including Borthakur et al. (2013), Bordoloi et al. (2014), Werk et al. (2013), and Lehner et al. (2020) along side our COS-Holes detections. Each observation is colored by its corresponding SMBH mass, whether that be their dynamically measured BH mass or estimated using Equation 2.2. The dark grey line is a linear regression fit for the combined COS-Holes+Literature sample and is characterized by Equation 2.3 with the shaded grey region representing a 95% confidence interval. We find there is a wide scatter in the COS-Holes+Literature radial profiles as impact parameter increases. From this relation alone, we see very little observational evidence that feedback from a SMBH heavily impacts the ionization state of its CGM.

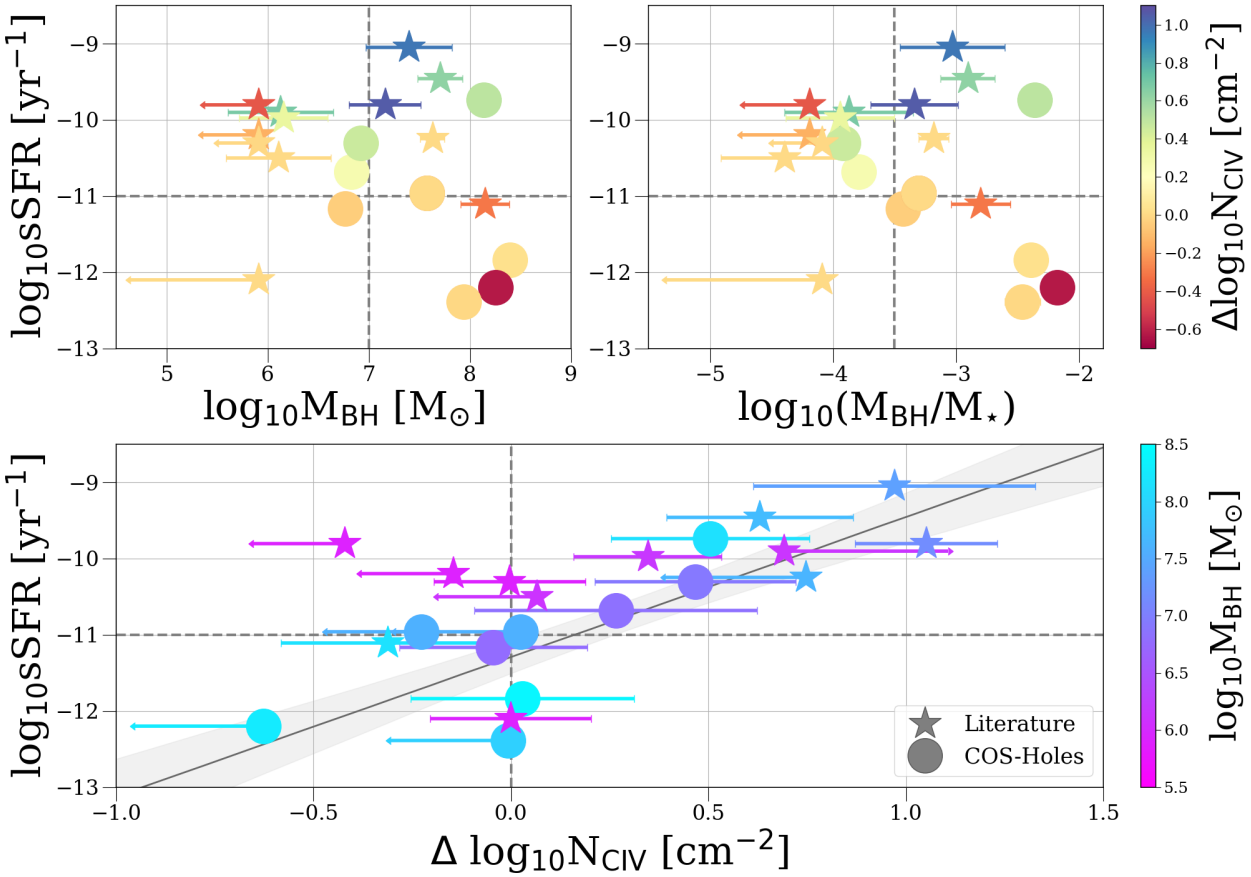

Figure 2.5: Investigating the role sSFR plays in driving the ionization content of the CGM across the combined sample's range of SMBH masses. Top panels: $\log_{10}$sSFR as a function of $\log_{10}M_{BH}$ (left panel) and $\log_{10}M_{BH}$ normalized by the stellar mass (right panel) colored by $\Delta\log_{10}N_{CIV}$ (C IV column density corrected for impact parameter). We present our upper limit observations that have higher column densities than those predicted by our model (Equation 2.8) as having a $\Delta\log_{10}N_{CIV}$ of zero (yellow coloring). Stars with arrows pointing to the left represent upper limits on the $\log_{10}M_{BH}$ estimations; for a more detailed description of how these BH masses were estimated, see §3. Bottom panel: $\log_{10}$sSFR as a function of $\Delta\log_{10}N_{CIV}$ colored by $\log_{10}M_{BH}$. The dark grey line is a linear regression, similar to the fit for Figure 2.4, and characterized by Equation 2.8 with 95% confidence intervals (the shaded grey region). This strong correlation between sFR and C IV suggests that sSFR is more closely tied to the ionization state of the CGM than the BH mass.

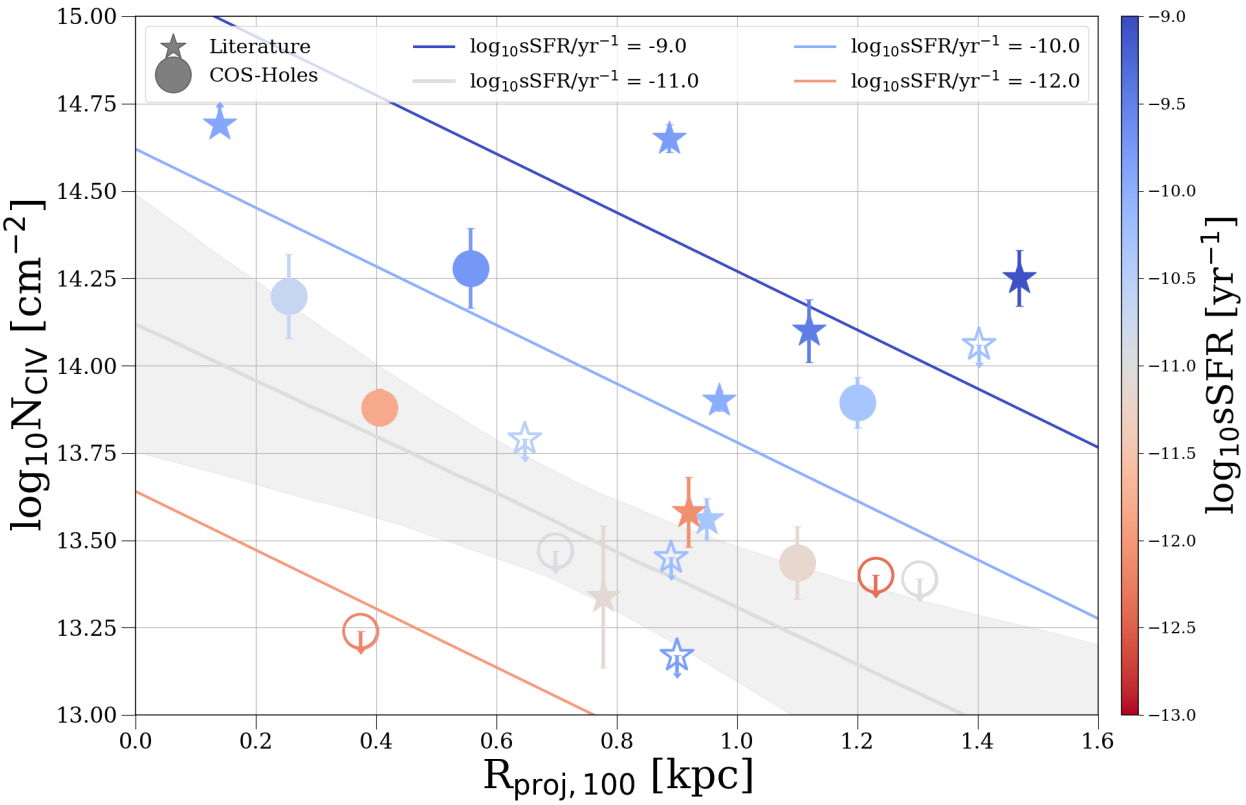

Figure 2.6: C IV column density as a function of $R_{proj,100}$ colored by log_{10}sSFR for the COS-Holes+Literature sample. The grey line is characterized by Equation 2.10 and has 95% confidence intervals depicted as the grey shaded regions. The other solid lines represent an evaluation of a single fit for column density as a function of $R_{proj,100}$ at different values of log_{10}sSFR. The value of log_{10}sSFR is denoted by their color and label. As log_{10} sSFR increases from -9.0 to -12.0, the regression intercept increases and closely follows the gradient of the observations. This is further evidence showing how dominant sSFR is within the combined sample.

observations; and §4.3 shows our estimate of the minimum mass of carbon in the CGM of our sample.

4.1 COS-Holes General Trends

In Figure 2.3, we show our measured N_{CIV} for each line of sight versus M_{BH}; each point is colored by its specific star formation rate (sSFR) and the size scales by impact parameter. We note that the two sightlines that intersect the halo of NGC 4258, colored in grey, are upper limits; even though the upper-limit observations are consistent with each other, studying the variations within this single halo is not possible with these two sightlines. For galaxies with a $\log_{10}M_{BH} < 7.0$ we find a 100% covering fraction and a 33% covering fraction for galaxies with a $\log_{10}M_{BH} > 7.0$. However, as black hole mass increases we show a large scatter of >1 dex in C IV column density for this range of M_{BH}. Due to this wide scatter and how small the sample size is, we suggest that there is no strong identifiable relationship between these two particular properties seen in the COS-Holes observations.

Interestingly, there is a different correlation with another galaxy property; across the M_{BH} range of our sample, galaxies that have low observed C IV column density ($\log_{10}N_{CIV} \lesssim 13.5$ cm^{-2}) are less star forming ($\log_{10}sSFR/M_\star < -11$) than galaxies with higher observed column density. Its difficult to determine if this trend is due to sample selection and if its causally or significantly correlated, since several factors could be influencing the C IV content of the CGM. Even so, it raises the question, how much is the SMBH feedback really impacting observed N_{CIV} in the CGM and do other galaxy parameters, like sSFR, play a larger role in setting the ionization state?

4.2 COS-Holes & Archival Data

To examine if a relationship dependent on BH mass is observable in the radial profile, we show $\log_{10}N_{CIV}$ versus impact parameter for COS-Holes and the 12 additional literature observations (§3) in Figure 2.4. Similar to Figure 2.3 the COS-Holes observations are represented by the circles and the literature observations are depicted as stars; all the observations are colored by their SMBH masses. $Log_{10}N_{CIV}$ weakly declines with the impact parameter within 150 kpc, a trend that has been discussed in a number of previous works (e.g. Bordoloi et al., 2014). Although there is significant scatter (> 1 dex) in the combined samples, we find that the average C IV column density of the literature sample detections (average $\log_{10}N_{CIV,Lit} = 13.98\pm0.08$ cm^{-2}) is comparable to the average C IV column density of the COS-Holes sample (average $\log_{10}N_{CIV,COS-Holes} = 13.94\pm0.09$ cm^{-2}). We find a 52% covering fraction for galaxies in the combined sample with C IV absorption above $\log_{10}N_{CIV} = 13.5$ cm^{-2}.

To characterize the radial profile for the combined samples and get a quantifiable constraint on the observed scatter mentioned above, we fit the relation between impact parameter and column density with a linear model (the dark grey line with a dark grey line where the shaded grey region represents the 95% confidence intervals). The mean column density at some R_{proj} is:

$$\log_{10} N_{C\,IV}/cm^{-2} = \alpha R_{proj}/kpc + \beta. \quad (2.3)$$

From examining the distribution of column density measurements in narrow R_{proj} ranges in Figure 2.4, it is clear that there is column density scatter beyond what can be explained by the observational uncertainties. We model this additional scatter about the $\log_{10}$ mean column density trend as a Gaussian distribution with mean zero and standard deviation σ. The prior probability distributions over these parameters are:

$$\alpha \sim \text{Normal}(0, 1^2) \tag{2.4}$$

$$\beta \sim \text{Uniform}(10, 16) \tag{2.5}$$

$$\sigma \sim \text{Gamma}(2, 4), \tag{2.6}$$

where the gamma distribution parameters are the shape and rate, respectively. The priors over α and β are broad but not infinite. The prior over σ is moderately informative: it has a mean of 1/2 and a standard deviation of $1/\sqrt{2} \approx 0.7$.

The dataset includes three kinds of measurements which require different likelihood functions: detections, upper limits, and lower limits. The likelihood for a detection is assumed to be a normal distribution with known mean and standard deviation. The result of convolution with the scatter term is also a normal distribution. The likelihood for an upper limit is an improper uniform distribution between negative infinity and the upper limit value. The convolution with the scatter term is the cumulative distribution function of a normal distribution with the mean column density trend and standard deviation σ. The likelihood and convolution with the scatter term for lower limits are similar to those of upper limits, but done in the opposite direction.

We implement this model using the `NumPyro`[10] probabilitistic programming library, which relies on `JAX`[11], and `ArviZ`[12]. To infer values of α, β, and σ, we run MCMC using the No-U-Turn Sampler (NUTS) and collect samples from the posterior probability distribution. The best-fit coefficients with 95% confidence intervals are α = -0.0057 (-0.016, 0.0042) and β = 14.08 (13.08, 14.93) respectively. Using this linear model we place constraints on the scatter in the combined COS-Holes+Literature sample and find that the slope of this relation is consistent with zero within error bars.

4.2.1 Is sSFR Directly Linked to the C IV Content of the CGM?

To investigate the possible trend suggested in Figure 2.3 between column density and other galaxy properties, we present the combined COS-Holes+Literature sample in three different ways as shown in Figure 2.5. In the top left panel we investigate sSFR as a function of black hole mass colored by $\Delta\log_{10}N_{CIV}$. These Δ $\log_{10}N_{CIV}$ values, which marginalize the large scatter in the radial profile (§4.2, were calculated by subtracting the observed column densities by values estimated from the best fit line depicted in Figure 2.4 (Equation 2.3) and is characterized by the following equation:

$$\Delta\log_{10}N_{CIV} = \log_{10}N_{CIV,obs} - \log_{10}N_{CIV,Eq3}. \tag{2.7}$$

We choose to color the data using these corrected column densities to normalize the observations with respect to impact parameter for the combined sample so we can focus on only

[10]https://github.com/pyro-ppl/numpyro
[11]https://jax.readthedocs.io/en/latest/
[12]https://doi.org/10.5281/zenodo.10436212

coeff (1)	mean (2)	σ (3)	95% CI (4)
Equation 2.9			
α (slope)	-0.87	0.49	(-1.85, 0.09)
γ ($\log_{10}$sSFR coeff)	0.57	0.21	(0.16, 0.98)
δ ($\log_{10}M_\star$ coeff)	-0.57	0.88	(-3.20, 1.25)
ϵ ($\log_{10}M_{BH}$ coeff)	0.26	0.33	(-0.43, 0.76)
β (intercept)	14.04	0.44	(13.14, 14.88)
Equation 2.10			
α (slope)	-0.84	0.45	(-1.73, 0.05)
γ ($\log_{10}$sSFR coeff)	0.49	0.17	(0.17, 0.84)
β (intercept)	14.13	0.38	(13.37, 14.89)

Table 2.4: Multivariate Linear Regression Coefficients. Comments on Columns: (1) Coefficient; (2) mean coefficient value; (3) standard deviation; (4) 95% confidence intervals.

four parameters: sSFR, M_{BH}, $M_\star$ and N_{CIV}. A similar relation is shown in the top right panel, where we present sSFR as a function of black hole mass normalized by stellar mass colored by Δ $\log_{10}N_{CIV}$. In both of the top panels there is a clear branching occurring at $\log_{10}M_{BH} > 7.0$ ($\log_{10}(M_{BH}/M_\star) \gtrsim$ -3.5); galaxies that have a $\log_{10}$sSFR greater than -11.0 appear to have an excess of C IV column density, while galaxies that have a $\log_{10}$sSFR less than -11.0 seem to have much lower C IV column densities.

However, when we show sSFR as a function of $\Delta\log_{10}N_{CIV}$ colored by black hole mass in the bottom panel, we see that this branching falls away to reveal a correlation between sSFR and column density. We fit a linear regression to this relation, using the same method and packages as described for Equation 2.3, and is characterized by the following equation:

$$\log_{10}\text{sSFR}/\text{yr}^{-1} = \alpha\Delta\log_{10}N_{CIV}/\text{cm}^{-2} + \beta. \tag{2.8}$$

The best-fit coefficients with 95% confidence intervals are α = 1.8 (1.1, 2.5) and β = -11.30 (-11.74, -10.88) respectively. Within this relation, we do not see any trends with respect to black hole mass, suggesting that the CGM properties are only loosely tied to black hole growth,if at all. In the CGM of our combined sample, the sSFR is more closely coupled with conditions in galactic atmospheres. Since CGM properties vary as a function of galaxy properties in various and complex ways, quantifying which of these is the primary driver of the ionization state is challenging. We present two methods of analysis in which we attempt to quantify the correlations seen within the combined sample, so we can further build our understanding of how CGM properties scale with galaxy properties.

4.2.2 Bayesian Analysis

To examine the effect of R_{proj}, sSFR, $M_\star$, and M_{BH} on the C IV column density at increasing impact parameter, we perform several multivariate linear regression analyses. Building upon the Bayseian linear regression model discussed in §4.2, we include the galaxy properties mentioned above. We center $\log_{10}\text{sSFR}/\text{yr}^{-1}$, $\log_{10}M_\star/M_\odot$, and $\log_{10}M_{BH}/M_\odot$ at -11.0 (typical

dividing point between star-forming and quenched galaxies), 10.5 (middle of the range for the combined sample), and 7.0 (middle of the range for our combined sample and point at which branching is seen in top panels of Figure 2.5) respectively. This operation makes the intercept β more interpretable but has essentially no effect on the linear relation slopes. We also divide R_{proj} by 100 ($R_{proj,100}$) so that all properties used in the regression would have a similar dynamic range. In addition, we acknowledge that there are some upper limit M_{BH} estimations for a few of our galaxies in the combined sample, however our multivariate linear regression treats these as detections; due to the error bars for these upper limits, this should not affect the best fit in a substantial way. The equation for our multivariate regression is described by the following:

$$\begin{aligned} \log_{10} N_{C\,IV}/cm^{-2} = \alpha R_{proj,100}/kpc \\ + \gamma \log_{10}(sSFR - (-11.0))/yr^{-1} \\ + \delta\ log_{10}(M_\star - 10.5)/M_\odot \\ + \epsilon \log_{10}(M_{BH} - 7.0)/M_\odot + \beta. \end{aligned} \tag{2.9}$$

Looking at the best fit mean coefficients and their standard deviations, given in Table 2.4, we can immediately rule out strong correlations with $\log_{10}M_\star$ and $\log_{10}M_{BH}$. Both of these parameters' mean coefficients have significance less than 1σ and are unlikely to be driving the regression or impacting the ionization. The most dominant galaxy parameter, which is greater than zero with a significance of nearly 3σ, is $\log_{10}$sSFR and is likely the main driving component in this relation. To test this assertion, we run a similar multivariate linear regression, but only including R_{proj} and sSFR, where the coefficients and statistics are shown in the bottom half of Table 2.4 and is characterized by the following equation:

$$\begin{aligned} \log_{10} N_{C\,IV}/cm^{-2} = \alpha R_{proj,100}/kpc \\ + \gamma \log_{10}(sSFR - (-11.0))/yr^{-1} + \beta. \end{aligned} \tag{2.10}$$

This relation is shown in Figure 2.6 as the grey line with its 95% confidence intervals depicted as the grey shaded regions. The coefficients and standard deviations for the new regression remain essentially the same with $\log_{10}M_\star$ and $\log_{10}M_{BH}$ removed, confirming that they are subdominant in setting the ionization content of the CGM of our combined sample. This is further demonstrated by the other multivariate linear regressions included in Figure 2.6 where $\log_{10}N_{CIV}$ is plotted as a function of $R_{proj,100}$ colored by $\log_{10}$sSFR; each line evaluates a single fit for column density as a function of $R_{proj,100}$ at different values of $\log_{10}$sSFR. As the value of sSFR increases, the regression intercept increases and changes the relation substantially, and follows the gradient of the observations, showing how dominant sSFR is within the combined sample. Based on the strong correlation seen in Figure 2.5, we suggest that sSFR of a galaxy is directly linked to the C IV content of the CGM.

4.2.3 Frequentist Analysis

We also investigate the relationship between $\log_{10}N_{CIV}$, $\log_{10}M_{BH}$, and $\log_{10}$sSFR using frequentist non-parameteric tests. We first use Kendall's rank correlation test (also known as a τ test) to check for a dependence between column density and black hole mass. Specifically,

we use the `cenken` function in the `NADA` R package (Lee, 2020), which can handle censoring (i.e., non-detections). The test p-value for a correlation between $\log_{10}N_{CIV}$ and $\log_{10}M_{BH}$ is greater than 0.05, indicating no evidence for a dependence. The test p-value for $\log_{10}N_{CIV}$ and $\log_{10}$sSFR is 0.017, which would correspond to about 2.3σ for a normal distribution: a somewhat significant correlation.

We repeat these tests on an impact-parameter-trend-corrected column density, $\Delta\log_{10}N_{CIV}$. The `cenken` function in `NADA` provides the Akritas-Theil-Sen estimator for the slope and the Turnbull estimator for the intercept of the linear relation between two variables. We use this functionality to determine the linear relation between $\log_{10}N_{CIV}$ and R_{proj}, use that linear relation to get a predicted $\log_{10}N_{CIV}$ for each observation, and subtract that from the observed value to get $\Delta\log_{10}N_{CIV}$. We then run Kendall's rank correlation tests from the previous paragraph replacing $\log_{10}N_{CIV}$ with $\Delta\log_{10}N_{CIV}$.

For $\Delta\log_{10}N_{CIV}$ and $\log_{10}M_{BH}$, we find a τ of 0.33 and a p-value of 0.85; for $\Delta\log_{10}N_{CIV}$ and $\log_{10}$sSFR we find a τ and p-value of 0.40 and 0.0094, respectively. The results for N_{CIV} and $\Delta\log_{10}N_{CIV}$ are comparable and consistent with results from §4.2.2, where we see no correlation between C IV column density and black hole mass, but there is a possible correlation with sSFR. This further supports our earlier conclusion that the SMBH does not have as significant effect on the state of the CGM as predicted, and that sSFR, with the stronger correlation, is more directly linked with the C IV content of the CGM.

4.3 Minimum Mass of Carbon in the CGM

Following the methods used in Bordoloi et al. (2014), we estimate the carbon mass in the CGM around our sample of $\sim L^\star$ galaxies. Bordoloi et al. (2014) obtained their upper limit on carbon mass (M_{carbon}) by applying a conservative ionization correction (assuming $f_{CIV} = 0.3$) to their values of C IV mass (M_{CIV}); these estimates were made by assuming ionization equilibrium and including collisional- and photo-ionization using the CLOUDY photoionization code (Ferland et al., 1998; Chatzikos et al., 2023). The minimum carbon mass can be written as:

$$M_{carbon} \gtrsim 1.12 \times 10^6\ M_\odot \left(\frac{N_{CIV,\,mean}}{10^{14}\ cm^{-2}}\right) \times \left(\frac{R_{proj}}{110\ kpc}\right)^2 \times \left(\frac{0.3}{f_{CIV}}\right) \times C_f. \tag{2.11}$$

This calculation assumes that these galaxies conform to global stellar metallicity relations and the gas-phase mass-metallicity relation.

Inserting typical values for the COS-Holes sample, $R_{proj} = 140$ kpc, covering fraction C_f[13] 44%, and mean column density of our detections $N_{CIV,mean} = 10^{13.94}$ cm^{-2}, we get a minimum mass of $M_{carbon}/M_\odot = 7.41 \times 10^5$. This is about a factor of 2.5 lower than the M_{carbon} value presented in Bordoloi et al. (2014) found for both star-forming and non star-forming dwarf galaxies using Voigt profile fitted N_{CIV} (1.9×10^6 $M_\odot$). Comparing this value to the total carbon mass in the ISM of $L^\star$ galaxies, we find that our minimum carbon mass is approximately a factor of three lower (e.g. Peeples et al., 2014).

We repeated this calculation for the whole COS-Holes+Literature sample ($R_{proj} = 150$ kpc, covering fraction $C_f = 52\%$, and mean column density of our detections $N_{CIV,mean} =$

[13] All C_f values are determined above $\log_{10}N_{CIV} = 13.5$ cm^{-2}

$10^{13.98}$ cm^{-2}) and just the star-forming galaxies ($\log_{10}$sSFR/yr$^{-1} \geq$ -11) in the COS-Holes+Literature sample (R_{proj} = 150 kpc, covering fraction C_f = 60%, and mean column density of our detections $N_{CIV,mean} = 10^{14.17}$ cm^{-2}) to find a minimum mass of carbon for both samples to be 1.11 $\times$ 10^6 $M_\odot$ and 1.98 $\times$ 10^6 $M_\odot$ respectively. These values are comparable to those reported in Bordoloi et al. (2014); the combined COS-Holes + Literature sample has a carbon mass 1.7 times lower than the value reported for both star-forming and non-star forming galaxies (1.9×10^6 $M_\odot$), while the the star-forming-galaxy-only combined sample has a carbon mass only a factor of 1.3 lower (2.6×10^6 $M_\odot$).

5 Simulation Results

In this section we compare the observational results of the combined COS-Holes+Literature sample to results from simulations. The section proceeds as follows: we describe the three simulations in §5.1.1,5.1.2, and 5.1.3 and discuss their various C IV column density predictions in §5.2; we compare the combined COS-Holes+Literature sample to simulated values from our three simulations in §5.3; and in §5.3.1 we mimic the COS-Holes survey across all three simulations used in §5.3.

5.1 Simulation Descriptions

Here, we briefly describe the three simulations to which we will compare our results. For more details on these well-known and widely used simulations, we refer the reader to the citations referenced throughout these sections.

5.1.1 Evolution and Assembly of GaLaxies and their Environments (EAGLE)

We compare our observations to a sample galaxies from the EAGLE main 'Reference' simulation volume (Ref-L100N1504), originally published in (Schaye et al., 2015; Crain et al., 2015). This (100 comoving Mpc)^3, 1504^3 dark matter and smooth particle hydrodynamic (SPH) particle run uses a heavily modified version of the N-body code GADGET (Springel, 2005). EAGLE applies the pressure-entropy SPH formulation from (Hopkins, 2013), extra parameters referred to as ANARCHY (Schaye et al., 2015), and assumes cosmology from the Planck Collaboration et al. (2013) ($\Omega_m = 0.307$, $\Omega_\Lambda = 0.693$, $H_0 = 67.77$ km s^{-1} Mpc^{-1}). The initial dark matter and SPH particle masses are $9.7\times10^6 M_\odot$ and $1.8\times10^6 M_\odot$ respectively.

EAGLE implements the following subgrid physics modules: radiative cooling (Wiersma et al., 2009a), star formation (Schaye & Dalla Vecchia, 2008), stellar evolution and metal enrichment (Wiersma et al., 2009b), stellar feedback (Dalla Vecchia & Schaye, 2012), BH formation accretion, feedback (Booth & Schaye, 2009; Rosas-Guevara et al., 2015). In regards to the black holes, EAGLE follows BHs from seed black hole particles with mass $10^5 h^{-1} M_\odot$ (where h=0.6777) placed at the center of every halo that exceeds a mass of $10^{10} h^{-1} M_\odot$. The BH particles grow via Bondi & Hoyle (1944) gas accretion as well as as mergers with other BHs using the prescription derived by Booth & Schaye (2009). Stellar and BH feedback operate via thermal prescriptions that heat surrounding gas to $10^{7.5}$ K and $10^{8.5}$ K, respectively. Further information on these processes and their calibrations are described in Crain

et al. (2015).

The BH energy feedback rate is calculated by tracking the accretion rate onto BHs using the efficiency

$$\dot{E}_{BH} = \frac{\epsilon_f \epsilon_r}{1-\epsilon_r} \dot{M}_{BH} c^2 \tag{2.12}$$

where $\epsilon_r = 0.1$ is the radiative efficiency of the accretion disk and $\epsilon_f = 0.15$ is the thermal feedback efficiency. The combined efficiency prefactors result in a total BH efficiency of 1.67% of the rest mass energy accreted onto the BH. The BH feedback operates via a single-mode thermal prescription that heats surround gas particles to $10^{8.5}$ K. Energy is stored until a gas particle or particles can be heated to this temperature to ensure that the feedback is numerically efficient.

5.1.2 Romulus25

We also compare our observations to galaxies from the cosmological volume ROMULUS25 (hereafter R25; Tremmel et al., 2017). The ROMULUS25 (25 Mpc)^3 volume was run with a ΛCDM cosmology from Planck Collaboration et al. (2016) with $\Omega_0 = 0.3086$, $\Lambda = 0.6914$, $h = 0.67$, $\sigma_8 = 0.77$. R25 is run using the smooth particle hydrodynamics code, Charm N-body GrAvity Solver (ChaNGa Menon et al., 2015). ChaNGa adopts the same models as GASOLINE (Wadsley et al., 2004, 2017), including the following physical prescriptions: cosmic UV background (Haardt & Madau, 2012), star formation (using a Kroupa, 2001 IMF), and blastwave supernova feedback (Ostriker & McKee, 1988; Stinson et al., 2012), which includes both SNIa and SNII (Thielemann et al., 1986; Woosley & Weaver, 1995). R25 has a Plummer softening length of 250 pc and a mass resolution of $3.4 \times 10^5 M_\odot$ and $2.1 \times 10^5 M_\odot$ for dark matter and gas, respectively.

R25 includes independent subgrid physics modules for the black hole formation, accretion, feedback, and dynamical friction as introduced in Tremmel et al. (2017). Unlike other simulations that use a threshold halo mass to initiate a BH seeding, BH seed particles with initial mass $10^6 M_\odot$ are required to form in dense, extremely low metallicity gas to better model SMBH populations across galaxy mass scales as described in as described in Tremmel et al. (2017) §5.1. The BH accretion utilizes a modified Bondi-Hoyle prescription that considers angular momentum support from nearby gas, resulting in a different physical growth model which uses fewer free parameters. Thermal feedback energy from the BH is imparted onto the 32 nearest gas particles every time step in the form

$$E_{BH} = \epsilon_r \epsilon_f \dot{M}_{BH} c^2 dt, \tag{2.13}$$

where the radiative and feedback efficiencies are $\epsilon_r = 0.1$ and $\epsilon_f = 0.02$, resulting in a total rest mass energy efficiency of 0.2%. The energy is released every timestep dt in contrast to the EAGLE prescription that stores energy until a surrounding gas particle can be heated to its threshold energy.

To calculate the ion column densities from the Romulus25 galaxy suite, we use the public analysis software, `Pynbody`[14] (Pontzen et al., 2013). Oxygen and metal enrichment from SN and winds is traced throughout the integration of the simulation. Then, ionization states

[14] https://pynbody.github.io/pynbody/index.html

are post-processed, assuming optically thin conditions, collicaiton ionization equilibrium, and a Haardt & Madau (2012) UV radiation field. Finally, we create models using the CLOUDY software package (Stinson et al., 2012; Ferland et al., 2013) for varying redshift, temperature, and density to calculate individual ion fractions for each gas particle in every simulated galaxy.

5.1.3 IllustrisTNG

The last cosmological simulation that we compare our galaxies to is the IllustrisTNG simulation, hereafter TNG. The TNG simulations were run with the moving mesh code AREPO (Springel, 2010), including a magnetic hydrodynamic (MHD) solver that is seeded with the cosmologically motivated initial conditions and then follows the magnetic field self-consistently (Pakmor & Springel, 2013). TNG utilizes values consistent with the Planck Collaboration et al. (2016) results ($\Omega_m = 0.3089$, $\Omega_\Lambda = 0.6911$, $h = 0.6774$).

The $(100\ \mathrm{Mpc})^3$ TNG simulation, also known as TNG100, is the middle of the three TNG volume series, providing a balance of volume and resolution, particularly for intermediate mass halos. The simulation implements several subgrid processes as part of the TNG model including primordial/metal-line radiative cooling on microphysical scales, star formation based on a two-phase subgrid ISM model, evolution of stellar populations and the expected chemical enrichment/mass loss, galactic-scale outflows from energy-driven, kinetic winds from stellar feedback, and the seeding, growth and feedback from BHs (Pillepich et al., 2018). Black holes seeds with mass $8 \times 10^5 h^{-1} M_\odot$ are initially seeded in halos of $5 \times 10^{10} h^{-1} M_\odot$.

The black hole prescriptions are introduced in Weinberger et al. (2017). Their dual-model AGN model, incorporates a 'thermal' mode injects thermal energy at high Eddington accretion rates and 'kinetic' mode injects kinetic energy at low Edditington accretion rates. The feedback efficiency for the thermal mode uses $\epsilon_r = 0.1$ $\epsilon_f = 0.2$ from Equation 5.1.1 for a total rest-mass accretion efficiency of $\sim 2\%$, which is distributed thermally over surrounding gas cells. The kinetic mode injects kinetic "pulses" at a total efficiency that can achieve $\sim 20\%$ of the accreted rest-mass energy (via the physical mechanism of Blandford & Znajek (1977)). Randomly oriented, jet-like pulsed feedback events apply energy directionally, imparting significant momentum stored across multiple timesteps to avoid dependence on the simulation timestep. This low accretion rate, kinetic mode generally dominates for late growing SMBHs above a threshold mass of $M_{\mathrm{BH}} \approx 10^{8.1}\, M_\odot$ (Davies et al., 2020; Terrazas et al., 2020).

5.2 Simulation Predictions

Using EAGLE, Oppenheimer et al. (2020) asserts that the efficiency with which a SMBH feedback energy is coupled to the CGM is critical for understanding the process of secular galaxy formation. This can be thought about in a three step pathway: (1) the formation of the halo, (2) the rapid growth of the BH, and (3) the lifting by AGN feedback of the baryonic halo reducing the supply of fuel for star formation. The last point is evidenced by a decrease in heavy metals in the CGM (such as C IV). These results were heavily based on the work by Davies et al. (2019) that published an inverse correlation between $\mathrm{M_{BH}}$ and f_{CGM} in EAGLE, suggesting a link between the BH and the removal of a significant portion of gas from the halo, essentially reducing CGM accretion and galactic star formation. Oppenheimer et al.

(2020) find that the galaxy BH mass is generally a good indicator of its past feedback history at masses above $\log_{10}M_{BH}/M_{\odot} \sim 7.0$. They used high-cadence snapshot outputs from the EAGLE simulation to determine that significant AGN episodes directly lift the CGM and significantly reduce (in some cases quenching) star formation on a < 100 Myr timescale. Ion tracers including C IV take longer ($0.5 - 2.5$ Gyr) to respond, but this sequence generally happens at $z > 1$ for L* galaxies meaning that this ion is an indicator of CGM gas content by $z = 0$.

TNG shows a dramatic decline in the covering factor of O VI from star-forming to quenched galaxies, as presented by Nelson et al. (2018b). Davies et al. (2020) explored both TNG and EAGLE to determine how CGM mass depends on BH mass, finding that the BH feedback energy released during the low-Eddington kinetic mode in TNG is most strongly anti-correlated with the gas content of halos in the mass range corresponding to our samples explored here. Hence, the BH mass itself is not directly deterministic for baryon lifting in TNG, but the energy released during the kinetic mode (Davies et al., 2020; Voit et al., 2023). This manifests itself in a strong anti-correlation between BH and CGM mass, but for BH masses that are above 10^8 $M_{\odot}$ where kinetic mode (and therefore baryon lifting) operate in TNG. Taking these results together, BH feedback drives the results of star-forming (less massive BHs) galaxies having higher O VI column density compared to quiescent (more massive BHs) galaxies (Nelson et al., 2018b). Hence, the driving force depleting ionized oxygen (and mostly likely C IV as well) is the ejection of mass from the CGM due to black hole feedback.

In contrast, Sanchez et al. (2019) uses R25 to examine the effects of SMBH feedback and star formation history (SFH) on the column densities of O VI in the CGM of galaxies. They determine that the host galaxy's SMBH transports metal-rich gas out of the galaxy disk where metals are formed and propagates it into the CGM. From these results they posit that galaxies with lower mass BHs (which have experienced less accretion and therefore less feedback) are likely to have a lower metallicity CGM and vice versa for galaxies with higher mass BHs leading them to have more metal-enriched material in their host CGM. Therefore, SMBH feedback impacts the total metal mass in the CGM (but not the total gas mass) and may play a critical role in galaxy quenching (Sanchez et al., 2021). In a follow up paper, Sanchez et al. (2024) measure the SMBH masses and CGM metal content from a sample of galaxies from R25. They find higher CGM metal fractions in galaxies with more massive black holes (compared to their host's stellar dispersion). In further contrast to EAGLE and TNG, Sanchez et al. (2024) find no correlation between M_{BH} and f_{CGM} indicating that in their galaxies, the SMBH's influence is more local, impacting the galaxy's disk and enriching the CGM without evacuating gas from the halo.

All of these simulations support the idea that SMBHs transport gas and metals into the CGM of the host galaxy. However, they differ on their predictions of how the mass of the SMBH regulates the amount of C IV present in the CGM. The COS-Holes survey provides the opportunity to constrain these feedback processes by comparing EAGLE, R25, and TNG predictions. §5.3 compares these theoretical SMBH feedback prescriptions with our observations.

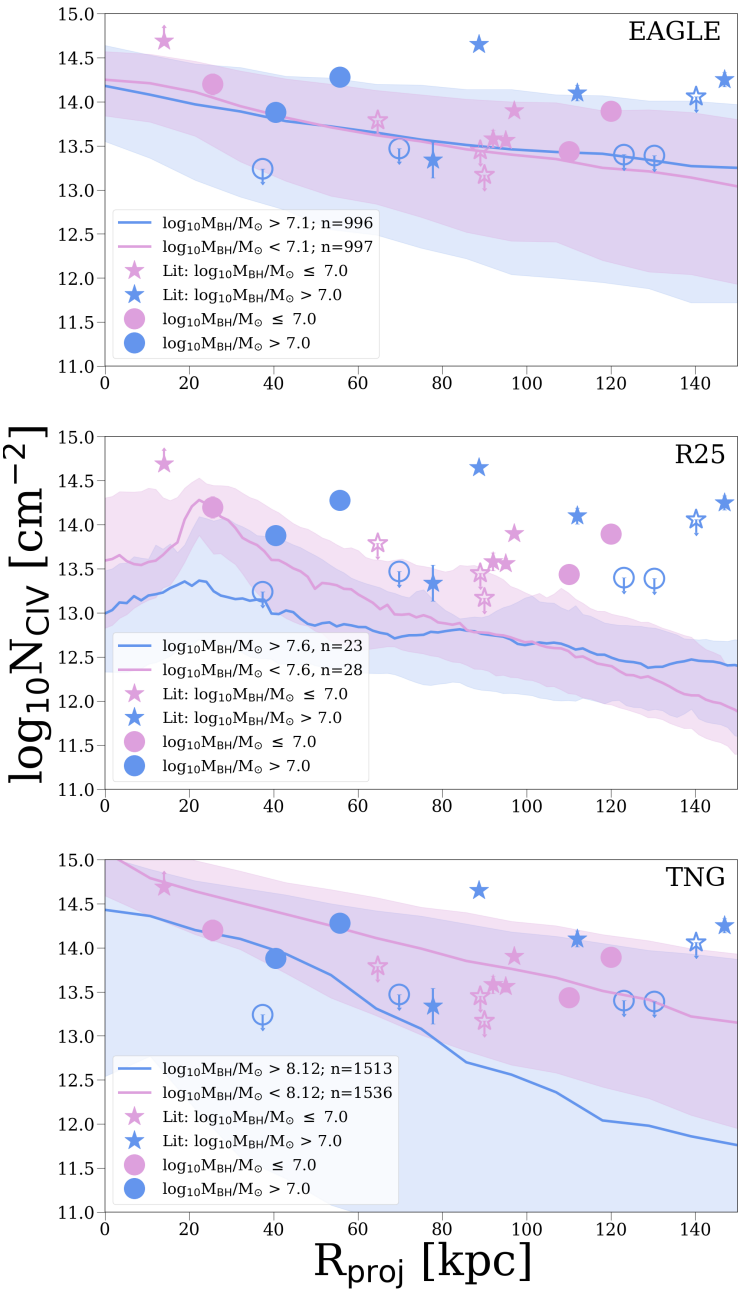

Figure 2.7: Column densities of the combined COS-Holes+Literature sample versus impact parameter compared to predictions from the EAGLE (top panel), R25 (middle panel) and TNG (bottom panel) simulations. Blue represents the "high" mass black hole sample ($\log_{10}M_{BH} > 7.0\ M_{\odot}$) while pink refers to the "low" mass black hole sample ($\log_{10}M_{BH} \leq 7.0\ M_{\odot}$). The corresponding blue and pink lines are the median C IV radial profile predictions from each simulation (also split based on black hole mass) each with 16-84% confidence spreads represented as the shaded region around each prediction. Like previous figures, unfilled markers represent an upper limit for that observation. Combined sample column densities agree reasonably with predictions from EAGLE and TNG and lie above the R25 predictions.

5.3 Comparison to Simulations

We begin our comparison to simulations by showing the entire observed sample (COS-Holes+Literature; $\log_{10}M_{BH}$ = 5.91 - 8.4 $M_{\odot}$) to the three simulations. In Figure 2.7, we split the observations into two bins divided by $\log_{10}M_{BH}$ = 7.0, a "low"-M_{BH} sample (10 observations, $\log_{10}M_{BH} \leq 7.0$) and a "high"-M_{BH} sample (11 observations, $\log_{10}M_{BH} > 7.0$). This split is strategically made to take advantage of the range of BH masses that make up the combined COS-Holes+Literature sample, but to also investigate the question, "do galaxies with similar stellar masses, but hosting differing SMBH masses show different CGM metal contents?"

We first make a broad-brush type comparison between data and simulations by choosing all galaxies with stellar masses between $\log_{10}M_{\star}/M_{\odot} = 10^{10} - 10^{11}$ in the three simulations, and dividing the samples into two M_{BH} bins in Fig. 2.7. This means that the split black hole mass is different amongst the simulations as they have different M_{BH} distributions as discussed in §5.1. In EAGLE there are 1993 central galaxies at $z = 0.00$ with a dividing $M_{BH}=10^{7.10}$ $M_{\odot}$. In R25 there are 52 central galaxies at $z = 0.05$ with a dividing $M_{BH}=10^{7.6}$ $M_{\odot}$. In TNG there are 3049 central galaxies at $z = 0.00$ with a dividing $M_{BH}=10^{8.12}$ $M_{\odot}$. The distribution of black hole masses for TNG is narrower and more massive than the distributions for EAGLE and R25; see §5.3.1 for more details. For EAGLE and TNG the C IV column density radial profiles were calculated using a projection along the z axis with a total depth of 2 Mpc, while for R25, they were averaged down to R_{200c}. We choose to plot the simulations predicted column densities versus the true projected impact parameter, R_{proj} [kpc], since it is a more direct measurement that does not rely on estimations from an indirectly observable property (like using R_{proj}/R_{200c} which uses dark matter mass).

The radial profiles shown in the top panel of Figure 2.7 show that the EAGLE simulation results are in reasonable agreement with the COS-Holes+Literature absorption observations. Interestingly that there is no discernible difference in the low and high BH mass samples (average $\log_{10}N_{CIV}$ = 13.6 cm^{-2} for both samples). We note that Oppenheimer et al. (2020) predicted an anti-correlation between C IV and M_{BH}, but we do not see such a correlation here. This likely is a result of the slightly larger stellar mass range probed by our COS-Holes galaxy sample compared to that of Oppenheimer et al. 2020 (10^{10-11} $M_{\odot}$ vs. $10^{10.2-10.7}$ $M_{\odot}$; Oppenheimer et al., 2020). Additionally, they found a measurable difference in the reduction of C IV column densities for only the highest *quartile* of BH masses, whereas here, we have divided the sample into two, leading us to have similar radial profiles for the split samples.

In the middle panel of Figure 2.7 where the observations are compared to N_{CIV} values from R25, we see that the mean predicted column density ($\log_{10}N_{CIV}$ = 12.8 cm^{-2}) is on average ∼1 dex below our combined sample; thus, there is little agreement between the combined sample and those predicted by R25. We see more of a difference between the low and high mass sample R25 predictions than EAGLE until ∼90 kpc where the two samples become more indiscernible. These results are comparable to averaged radial profiles presented in Fig 14 of Sanchez et al. (2024) ($\log_{10}N_{CIV}$ vs $\log_{10}(R_{proj}/R_{200c})$) at the same BH mass split but are under predicting the C IV column density observed.

For TNG, in the last panel of Figure 2.7, we see the largest differentiation between the low and high samples (average $\log_{10}N_{CIV}$ = 14.0 and 13.1 cm^{-2} respectively), which reasonably

overlaps with the C IV column densities for the combined sample. Interestingly, TNG has a much larger spread for their high-mass sample than any other simulation and sample. While we do see a population of low C IV values for high M_{BH}, there is also a population with high C IV for high M_{BH}. A fuller investigation determining why there is such a spread in C IV for high black hole masses is beyond the scope of this paper.

We note these general trends between each of the simulations, but we cannot directly compare them to the COS-Holes survey without reproducing the observed survey, which we now do in §5.3.1.

5.3.1 Mocking up the COS-Holes Survey

We create a mock up of the COS-Holes Survey of the nine sight lines by using the SMOHALOS (Simulation Mocker Of Hubble Absorption Line Observational Surveys) used first in Oppenheimer et al. (2016) across the three simulations. In our implementation here, SMOHALOS matches the impact parameter, stellar mass, and SFR of observed galaxies using a selection of central galaxies taken from $z = 0.00$ simulation outputs. We also attempt to match black hole mass, but only divide the sample into two using a black hole mass split, $M_{BH,split}$ that is defined differently for each simulation based on the distribution of simulated M_{BH} values. In SMOHALOS, the 1-σ range of BH masses in EAGLE spans $10^{6.65} - 10^{7.94} M_\odot$, in R25 spans $10^{7.27} - 10^{8.35} M_\odot$, and in TNG spans $10^{7.94} - 10^{8.43} M_\odot$. Briefly, we choose a sight line by selecting a random pixel in a C IV column density map at an impact parameter within 5 kpc of an observed sight line around a simulated galaxy that matches the observed galaxy. We use a projection along the z axis with a total depth of 2 Mpc. SMOHALOS selects a matching simulated galaxy by taking the observed galaxy values and adding a random error assuming a Gaussian dispersion, then finding the simulated galaxy that best fits the observed galaxy's dispersed values. We assume dispersions of 0.3 dex to $M_\star$ and 0.5 dex to SFR, therefore ensuring we are selecting galaxies that are similar to the COS-Holes sample but have a random scatter based on reasonable uncertainties in stellar masses and star formation rates.

We run SMOHALOS for 100 realizations, reporting the results in Table 2.5. We first report the median C IV column density from our observations noting the large range on the high M_{BH} sample due to upper limits (cf. Fig. 2.3) indicating the uncertainty in which the sample has more C IV. For the simulations, we are not limited by upper limits, therefore we present the equivalent of noiseless column densities for the median and $1-\sigma$ spread in their distribution.

The first result to note is how each simulation compares with the observed dataset. EAGLE has values that are consistent with both samples, R25 has values that are significantly lower than observations, and TNG agrees best with the high M_{BH} sample but appears to over-predict the low M_{BH} sample. In detail, TNG predicts the largest reduction in C IV with M_{BH} while EAGLE predicts the largest increase. This agrees with the trends in Fig. 2.7, but we note the SMOHALOS sample as well as the split M_{BH} are different. By selecting matched galaxies, we are sampling a distribution that has a much smaller difference than, for example TNG would predict for a typical galaxy in the bottom panel of that figure.

The second result to note is that the simulations all show 0.12 dex or less differences in their $\log_{10}N_{CIV}$ medians indicating that a COS-Holes is not large enough to distinguish

Dataset	M_{BH}(split)	Low M_{BH} N_{CIV} [cm^{-2}]	High M_{BH} N_{CIV} [cm^{-2}]
(1)	(2)	(3)	(4)
Observed	7.6	$13.44 - 13.47$	$< 13.40 - 13.88$
EAGLE	7.49	$13.59^{+0.63}_{-1.15}$	$13.71^{+0.53}_{-1.06}$
R25	8.10	$12.75^{+1.05}_{-0.77}$	$12.78^{+0.64}_{-0.63}$
TNG	8.23	$13.85^{+0.69}_{-1.49}$	$13.79^{+0.78}_{-2.61}$

Table 2.5: SMOHALOS Simulation C IV Comparison. Comments on columns: (1) Dataset- observed or simulation; (2) black hole mass used to divide sample; (3,4) median and 1-sigma split for N_{CIV} for low and high M_{BH} samples, respectively; for observations the best estimate for median given upper limits

the different behaviours across the simulations. Even if there exists different C IV absorption patterns relating to M_{BH}, our SMOHALOS exploration finds that COS-Holes is too insensitive due to its small sample size and heterogeneous sample of galaxies.

Finally, we estimate the number of sightlines needed to distinguish between different C IV distributions as a function of BH mass by replicating the results from R25. For a set sample size, we interpolate a C IV column density from a random impact parameter (between 0 and 150 kpc) and assign it to either the low or high BH mass sample to create a uniform sample. We fit these random replications to a linear regression model for increasing sample sizes iteratively to create a distribution. We determine that at least 60 sightlines for each high and low mass sample would be needed to distinguish between the samples with a 2σ confidence and over 100 sightlines in each sample to tell with a 3σ confidence.

6 Discussion

6.1 ΔN_{CIV} Dependence on sSFR

We find a $>2\sigma$ correlation between the impact-parameter-corrected column density (ΔN_{CIV}) and sSFR, as shown in Figure 2.5. In the top panels of Figure 2.5, we see a distinct split in ΔN_{CIV} between star-forming and non-starforming galaxies at $\log_{10}M_{BH} > 7.0$. This dividing point occurs at $\log_{10}$sSFR $\approx$ -11.0. This is consistent with star-forming ($\log_{10}$sSFR> -11.0) and passive ($\log_{10}$sSFR< -11.0) galaxies in the COS-Halos survey (Tumlinson et al., 2011). COS-Halos found that star-forming galaxies exhibited an OVI covering fraction >80%, and higher N_{OVI} than their passive galaxy counterparts ($f_C \approx 30\%$). Building off of these results, subsequent studies (Johnson et al., 2015b; Zahedy et al., 2019; Tchernyshyov et al., 2023) have established an evident dichotomy in the amount of O VI present in star-forming and passive galaxies. Controlling for stellar/halo mass, Tchernyshyov et al. (2023) demonstrated that this dichotomy persists at high statistical significance. For the first time, we tentatively confirm with $> 2\sigma$ significance that this correlation exists in the C IV-bearing gas phase as well, even when we control for other potential variables (see §4 for a discussion of our multivariate analysis).

There is little C IV coverage in other surveys of $L^\star$ galaxies, and our current sample size

is only 21 galaxies. The CIViL* survey (Berg et al., 2022b) will fill this gap in previous COS absorption-galaxy studies by adding NUV data covering C IV for many of the L* galaxies of COS-Halos and other surveys which also have O VI coverage. With the addition of data from this survey, we will be able to test whether C IV acts more like O VI than a tracer of the photo-ionized, 10^4K gas phase. Our current sample indicates that C IV is more O VI-like than "low-ion-like," where low-ionization state gas traced by singly and doubly ionized species shows no correlation with galaxy star-forming properties (Werk et al., 2013).

While we find a clear trend that exists between ΔN_{CIV} and sSFR (4.2.1), we note a possible second order connection between the sSFR and M_{BH} as they relate to N_{CIV} (Figure 2.5, top panels). As discussed above galaxies with higher sSFRs and M_{BH}s show higher C IV content in the CGM, while galaxies with similarly high black hole masses but low sSFR maintain lower C IV column densities. This split trend could indicate that the relationship between sSFR and black hole mass could result in varying N_{CIV} possibly connected to overmassive or undermassive black hole characteristics; however, other evolutionary factors such as galaxy formation time may also play a role (e.g. Sharma et al. (2020) connects overmassive black hole formation to earlier galaxy formation).

Results using EAGLE and TNG, have shown that there is an inter-relationship between intrinsic galaxy halo properties and the properties of the central galaxy such as sSFR (Davies et al., 2019, 2020). In these simulations, galaxies with overmassive BHs are more likely to be quenched, and vice vera (Davies et al., 2020, Fig 2), and these quenched systems almost always have an evacuated CGM; due to the BH's influence on the CGM of the central galaxy through suppressing cooling the total sSFR is reduced. Therefore, sSFR, BH mass (and its subsequent growth), and the CGM are highly interconnected. However, for our current sample (including the additional literature values), is too small to directly test these interdependent relationships seen in simulations. Exploring whether this sSFR vs N_{CIV} trend appears cosmological simulations could shed light on the underlying physics driving this apparent connection.

6.2 Do BHs evacuate their CGM?

Cosmological hydrodynamical simulation suites are now able to self-consistently recreate an array of galaxy observables (e.g., EAGLE, Schaye et al. (2015); Illustris-TNG (TNG), Pillepich et al. (2018); Romulus25, Tremmel et al. (2017)), including not only the galaxy mass function but specific SMBH-related observables including the AGN luminosity function (EAGLE, Rosas-Guevara et al., 2016) and the $M_{BH} - \sigma$ relation (IllustrisTNG, Sijacki et al. (2015); Romulus25, Tremmel et al. (2017)). From these simulations, numerical and analytical calculations predict that even a small percentage of the energy from SMBH assembly, when coupled to its surrounding halo, will unbind the CGM from the dark matter halo (Davies et al., 2019; Oppenheimer et al., 2020). This evacuation of the CGM has a preventative effect such that the reduction in CGM gas density leads to long cooling times for the gas in the inner halo (Davies et al., 2020); meanwhile, this lower global gas density (not short lived cavities or bubbles carved by AGN-mode feedback) causes galaxies to quench and stay quenched (Davies et al., 2021).

Both EAGLE (Oppenheimer et al., 2020) and TNG (Nelson et al., 2019) predict that the ionized gas in the CGM traced by C IV will be far lower-density (and thus lower measured

column density) in galaxies with over-massive black holes (relative to their stellar mass). In contrast, results from Sanchez et al. (2019) which used ROMULUS25 (Tremmel et al., 2017), suggest that galaxies with high mass BHs will have higher measured column densities (higher metallicity) in their CGM due to the BH ejecting material out into the diffuse parts of the halo. The COS-Holes observations directly tests these predictions to quantify the imprint of different implementations and efficiencies of BH feedback on the physical state of the CGM.

Comparing between the simulations (Figure 2.7), EAGLE and TNG agree better with the combined observed sample than R25. EAGLE appears to perform the best in matching the column densities of the Low $M_{\rm BH}$ sample as well as reproducing the $M_{\rm BH}$ values themselves. This may not be the case for every ion as Nelson et al. (2018b) finds TNG shows better agreement for O VI around the COS-Halos galaxies than found in EAGLE or EAGLE zoom simulations (Oppenheimer et al., 2016).

Interestingly, R25 seems to be under predicting the observed C IV column density. The AGN feedback in R25 has been shown to be more moderate in comparison to TNG and EAGLE (Tremmel et al., 2019; Chadayammuri et al., 2021; Jung et al., 2022), possibly due to R25's lack of metal cooling. Sanchez et al. (2024) shows that a result of this less powerful feedback is that the CGM of these galaxies are significantly less evacuated at these masses. However, it may be that the metal rich gas evacuated by the SMBH in these galaxies remains somewhat nearby to the galaxies, <50 kpc, as in the MW-mass galaxies explored by Sanchez et al. (2019), which may explain the predicted peak in $N_{\rm CIV}$ around 30-40 kpc and the subsequent decline at high impact parameter.

Despite the combined sample reasonably aligning with EAGLE and TNG, there is no striking evidence in the COS-Holes survey that more massive SMBHs have lower observed column densities, which would indicate this "cleared" CGM (Oppenheimer et al., 2020) or that more massive SMBHs have a more metal enriched CGM due to the BH ejecting material out into the halo (Sanchez et al., 2019). However, we note that from the SMOHALOS exploration (5.3.1), we do not yet have a sample large enough to determine if SMBHs are impacting the content or the ionization state of the CGM.

7 Summary & Conclusion

The COS-Holes survey, in combination with a detailed comparison to cosmological simulations, offers the first assessment of the role of BH growth in the regulation of the baryonic content of extended gaseous halos. Broadly, our observations, when combined with data from the literature, are in reasonable agreement with simulation predictions, but do not provide definitive evidence that SMBH feedback significantly impacts the state of the CGM, in either evacuation or through metal enrichment. While our results do not rule out that a galaxy's central SMBH plays an important role in setting the state of the CGM, we find that the sSFR is more correlated with properties of the CGM. Specifically, our key results are:

1. There is no identifiable relationship between the C IV content of the CGM and the mass of the assumed host galaxy's SMBH. We attribute this lack of a correlation to both the COS-Holes survey's small sample size and the large scatter of >1 dex in C IV column density as BH mass increases.

2. When we augment the COS-Holes sample of eight galaxies with 12 additional galaxies from the literature for which we can estimate SMBH masses from ground-based spectroscopy and which have C IV coverage along paired QSO sightlines, we again find no significant trend between CGM C IV column densities and SMBH mass with increasing impact parameter (Figure 2.4).

3. We find that galaxy sSFR is correlated with the ionized content of the CGM as traced by C IV; this is evidenced by a large spread in sSFR for $\log_{10}M_{BH} > 7.0$, where C IV strength shows clear dependence on sSFR but not M_{BH}. Our multivariate analysis tentatively confirms, with $>2\sigma$ significance, that a correlation between sSFR and CGM C IV content exists, similar to that of CGM O VI (Tchernyshyov et al., 2023). Combined with items 1 and 2, above, our results suggest that the mass of the SMBH is a subdominant factor in the processes that contribute to the content or ionization state of the z$\sim$0 CGM and that it is the galaxy sSFR that that is more tightly tied to the C IV-bearing gas phase of the CGM.

4. We compare C IV column densities to simulated column densities from the EAGLE, R25, and TNG simulations (Figure 2.7). Upon splitting the combined sample into two SMBH mass bins, we find there are only small differences in median column densities between different simulations.

   The combined COS-Holes + Literature sample measurements of N_{CIV} are in reasonable agreement with predictions from EAGLE and TNG, but are higher than predictions from R25.

5. We create a mock up of the nine lines of sight from the COS-Holes Survey in all three simulations: EAGLE, R25, and TNG. We conclude that COS-Holes does not contain enough QSO-galaxy pairs to distinguish the different behaviours across all three simulations. To do so, the sample size would need to be increased from 9 lines of sight to 120 lines of sight. See §5.3.1 and Table 2.5 for further details.

Since we targeted nearby, spatially extended galaxies with ancillary data (e.g., resolved ALMA and VLA maps of the molecular and neutral ISM, rotation curves, stellar population ages, and metallicity gradients), our QSO spectroscopy will enable a variety of studies well beyond the scope of the goals of this paper. For example, our observed absorption line kinematics will aid in differentiating between material recently launched from the central galaxy via feedback and gas accreting from the larger-scale environment (Bowen et al., 2016; Ho et al., 2017). Closer to the purview of the paper, this COS spectroscopy will also be crucial for differentiating between other AGN feedback prescriptions invoked in models and simulations that are in the public domain in addition to EAGLE and R25 described and used throughout this paper; these include TNG with dramatic SMBH feedback (Pillepich et al., 2018; Nelson et al., 2019) and the FIRE simulations suite (Anglés-Alcázar et al., 2017; Pandya et al., 2021). Given the significant investment in observational resources required to establish independent and well-constrained SMBH mass measurements and the rarity of UV-bright QSOs, it is unlikely that additional sightlines will become available until the next generation of ELTs and HWO are in active use. However, these future UV observatories will

be pivotal for increasing the sample size and allowing us to test the effect of SMBH feedback on the state of the CGM.

8 Appendix A: C IV Absorption Profiles

Figure 2.8 presents absorption line profiles for the COS-Holes sample. Some items of note are: (1) for NGC 4026 (QSO: SDSSJ1159) there is a prominent blend in λ1550 which we identified corresponds to H I λ1215 at z = 0.28; due to this contamination and no features in λ1548 we report an upper limit for the CIV column density; (2) for NGC 4258 (QSO: SDSSJ1220 and SDSSJ1222) and NGC 4564 (QSO: SDSSJ1235) we do not detect any CIV absorption, and report only upper limits on CIV column density.

9 Appenxix B: Literature Sample Galaxy and QSO Tables

We increase our COS-Holes sample size by adding values from Lehner et al. (2020) (Project AMIGA), Werk et al. (2013) (COS-Halos), Borthakur et al. (2013) (starbursts), and Bordoloi et al. (2014) (COS-Dwarfs). Project AMIGA (M31; $\log_{10}M_\star$ =9$\pm$2 $\times$ 10^{10} $M_\odot$, Williams et al. (2017); $\log_{10}M_{BH}$ = 8.15 $\pm$ 0.24, Davis et al. (2017); total SFR = 0.7 $M_\odot$ yr^{-1}, Lewis et al. (2015)) was specifically designed to span M31's project major and minor axis and intermediate orientations, thus it provides the unique opportunity to probe one high mass SMBH galaxy at increasing impact parameter. It is important to mention that there were data values that had possible contamination from the Magellanic Stream, however we only plot values they denote as uncontaminated; for more a more detailed explanation of how this contamination was removed see Lehner et al. (2020). Using this smaller sample of Project AMIGA observations, we take an average of the detections to report mean Project AMIGA column density. We use this single data point to represent the Project AMIGA observations.

We also include Borthakur et al. (2013) which found highly ionized gas traced by CIV in 80% of their starburst galaxies. They assert that it is extremely unlikely that these absorbers were photoionized from either the metagalactic background or the stellar radiation from the starburst; using CLOUDY models, they suggest that this observed CIV would arise from shock-ionization and be accelerated by the ram pressure of the wind and thus enriching the CGM. Similar high detections of CIV were seen in Bordoloi et al. (2014), where they detected the ion out to 100 kpc in their sample of sub-$L^\star$ galaxies. They find that strong CIV absorption observations were detected around star-forming galaxies and they are kinematically consistent with being bound to the dark matter halos of their hosts. In conclusion, they assert that the metallic content of the CGM around their galaxy sample is best explained by the addition of strong outflows in addition to tidal debris and ram pressure stripping. Taken together, both of these archival studies support the idea that energy-driven feedback is needed to explain the presence of highly ionized ions, such as CIV in the CGM. Thus, they are interesting samples to compare and expand upon the COS-Holes observations.

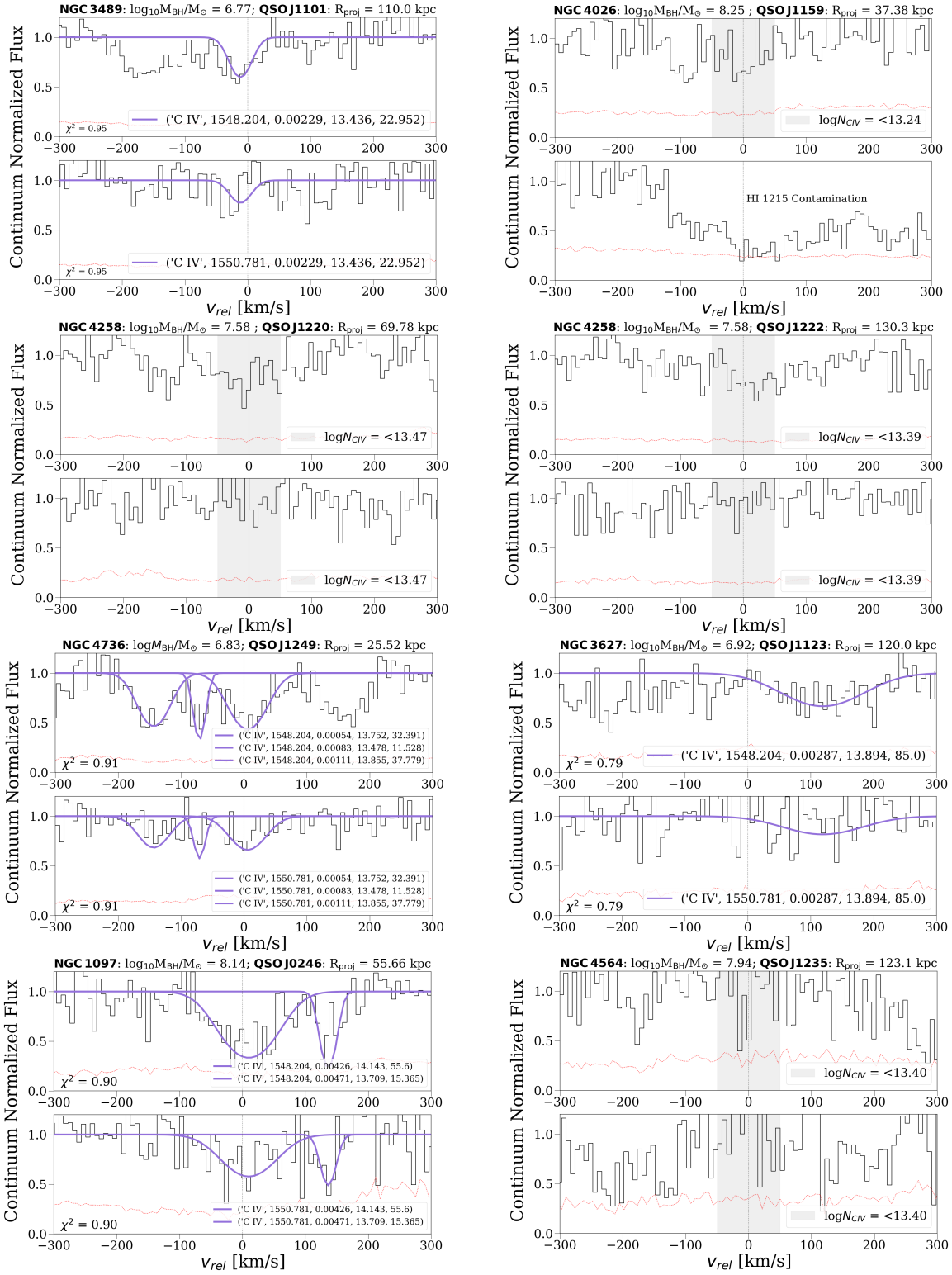

Figure 2.8: The remaining CIV absorption features for the COS-Holes survey. Same conventions are used as described in Figure 2.2.

Galaxy	RA (deg)	Dec (deg)	z	sSFR ($\log_{10}$yr^{-1})	M_* ($\log_{10}M_\odot$)	M_{BH} ($\log_{10}M_\odot$)	Ref
(1)	(2)	(3)	(4)	(5)	(6)	(7)	(8)
J102846.43+391842.9	157.194	39.312	0.1135	-9.8	10.5	7.16 ± 0.35	a
J132150.89+033034.1	200.462	3.509	0.0816	-10.3	10.8	7.63 ± 0.12	a
J140502.20+470525.9	211.259	47.091	0.1452	-9.0	10.4	7.4 ± 0.43	a
J154527.12+484642.2	236.363	48.778	0.0752	-10.5	10.5	6.11 ± 0.52	a
J0925+4535_227_334	141.379	45.533	0.014	-10.3	10.0	<5.91	b
J0959+0503_318_13	149.813	5.068	0.059	-9.9	10.0	6.13 ± 0.52	b
J1121+0325_73_198	170.362	3.445	0.023	-10.2	10.1	<5.91	b
J1211+3657_312_196	182.761	36.998	0.023	-9.8	10.1	<5.91	b
PG1202+281_165_95	181.183	27.878	0.051	-12.1	10.0	<5.91	b
J0910+1014_34_46	137.626	10.24	0.1427	-9.5	10.61	7.71 ± 0.22	c
J1619+3342_113_40	244.831	33.706	0.1414	-9.9	10.1	6.16 ± 0.44	c
M31	10.685	41.269	-0.00099	-11.1	10.9	8.15 ± 0.24	d

Table I.1: Literature Sample Galaxy Information. Comments on columns: (1) galaxy name; (2-3) RA and Dec; (4) redshift of the galaxy; (5) specific star formation; (6) stellar mass; (7) black hole mass; (8) reference sample where a, b, c, and d are Borthakur et al. (2013), Bordoloi et al. (2014), Werk et al. (2013), and Lehner et al. (2020) respectively.

QSO	RA (deg)	Dec (deg)	z	R_{proj} (kpc)	R_{proj}/R_{200c}	$\log_{10}N_{CIV}$ (cm^{-2})	Ref
(1)	(2)	(3)	(4)	(5)	(6)	(7)	(8)
J102847.00+391800.4	157.2	39.3	0.473	88.7	0.52	14.65 ± 0.04	a
J132144.97+033055.7	200.44	3.52	0.269	140.2	0.52	<14.06	a
J140505.77+470441.1	211.27	47.08	1.24	146.9	0.90	14.25 ± 0.08	a
J154530.23+484608.9	236.38	48.77	0.399	64.7	0.37	<13.79	a
J09525+4535	141.478	45.596	0.329	95.0	0.76	13.56 ± 0.06	b
J0959+0503	149.815	5.065	0.162	14.0	0.11	>14.69	b
PG1202+281	181.175	27.903	0.165	92.0	0.73	13.58 ± 0.10	b
J1121+0325	170.309	3.43	0.152	89.0	0.68	<13.45	b
J1211+3657	182.811	36.961	0.171	90.0	0.68	<13.17	b
J0910+1014	137.624	10.237	0.462	112.0	0.58	14.1 ± 0.09	c
J1619+3342	244.819	33.711	0.47	97.0	0.72	13.9 ± 0.03	c
HS0033+4300	9.096	43.278	0.12	30.5	0.133	14.1 ± 0.05	d
HS0058+4213	15.38	42.493	0.19	48.6	0.211	13.33 ± 0.18	d
RX_J0043.6+3725	10.927	37.422	0.08	50.5	0.22	13.85 ± 0.03	d
Zw535.012	9.087	45.665	0.048	59.7	0.26	12.99 ± 0.30	d
RX_J0050.8+3536	12.711	35.612	0.058	77.1	0.335	13.45 ± 0.07	d
IRAS_F00040+4325	1.652	43.708	0.163	93	0.404	13.23 ± 0.11	d
MRK352	14.972	31.827	0.015	131.7	0.573	13.5 ± 0.15	d
RX_J0043.6+3725	10.927	37.422	0.08	50.5	0.22	<12.92	d
RXS_J0118.8+3836	19.706	38.606	0.216	97.2	0.423	<12.9	d
RX_J0028.1+3103	7.045	31.063	0.5	139.1	0.605	<13.11	d
Project AMIGA Avg				77.79	0.33	13.34 ± 0.20	d

Table I.2: Literature Sample QSO Information. Comments on columns: (1) QSO ID; (2-3) RA and Dec; (4) redshift of the galaxy; (5) impact parameter; (6) impact parameter normalized by the virial radius; (7) CIV column density;(8) reference sample where a, b, c, and d are Borthakur et al. (2013), Bordoloi et al. (2014), Werk et al. (2013), and Lehner et al. (2020) respectively.

In addition, we also include Werk et al. (2013) which presented column density measurements of the CGM from QSO-galaxy pairs (low-z, L $\approx$ L*) drawn from the COS-Halos survey. One of their main results is finding that column densities derived for intermediate ionization state metal lines decrease with increasing impact parameter; they interpret this trend to mean there is a decline in the metal surface density profle of the CGM within its inner 160kpc. They also see that the gas kinematics derived from Voigt profile fits to their observations suggest that the CGM is mostly bound to its host galaxy's dark matter halo similar to results seen in Bordoloi et al. (2014). The collective information for Werk et al. (2013) and the rest of our additional literature sample can be seen in Table I.1 and I.2 respectively.

CHAPTER 3

THE DISCOVERY OF A C IV DICHOTOMY IN THE CGM OF L* GALAXIES

Look at you! Glowing like a solar fire. You're something special, Jim. You're gonna rattle the stars, you are!

– John Silver, Treasure Planet

1 Introduction

The diffuse gaseous atmosphere surrounding the star-filled inner region of a galaxy is known as its CGM. The CGM plays an essential role in a galaxy's evolution by hosting the gaseous reservoir that feeds the galaxy with gas, replenishing fuel for star formation, and keeping a record of metal-enriched material ejected from the disk through winds and other feedback processes (Lehner & Howk, 2011; Peeples et al., 2014; Werk et al., 2014; Tumlinson et al., 2017). The Hubble Space Telescope and the Cosmic Origins Spectrograph (*HST*/COS) have significantly advanced the study of the CGM over the past fifteen years, creating a compendium of gas around dwarf to L* galaxies (e.g., Werk et al., 2013; Bordoloi et al., 2014; Borthakur et al., 2015; Heckman et al., 2017; Berg et al., 2018; Lehner et al., 2018), with additional focus on specific demographics such as starbursts (Heckman et al., 2017) and active galactic nuclei (AGN) (Berg et al., 2018). However, many questions remain about how ongoing processes within galaxies impact the physical state of their CGM and vice-versa. Quantifying the connection between these halos and their host galaxies can provide essential constraints on the co-evolution of galaxies and the CGM.

Some progress has been made for the cool phase of the CGM (T $\sim 10^4$ K), where metal-enriched gas traced by Mg II has been used to compare the CGM content between star-forming and passive galaxies. The consensus is that the CGM of star-forming galaxies has higher Mg II equivalent widths and covering fractions than that of passive galaxies (Lan, 2020; Anand et al., 2021). Mg II is often associated with star-formation-driven winds (Rubin et al., 2014), showing a strong incidence rate along the minor axes of star-forming galaxies (Bordoloi et al., 2011). Other cool gas phase tracers such as H I, Si II, and C III show no statistically significant correlation with galaxy star-forming properties (Tumlinson et al., 2013; Werk et al., 2013).

For the warm phase, a seminal result from the COS-Halos survey found a dichotomy in the content of O VI in the CGM of star-forming and passive galaxies (Tumlinson et al., 2011). O VI, a likely tracer of highly ionized T $\sim 10^{5.5}$ K gas, is abundant in the halos of actively star-forming L* galaxies, while it is rarely found within 150 kpc of L* passive galaxies (Tumlinson et al., 2011; Johnson et al., 2015b; Zahedy et al., 2019). This dichotomy holds with greater than 3σ significance for stellar mass-controlled samples of low-redshift (z < 0.6) galaxies with $10^{10.1} < M_\star < 10^{10.9}$ (Tchernyshyov et al., 2023).

While high-ions and low-ions likely trace distinct gas phases of the CGM and show different correlations with galaxy star-forming properties, it is unclear where intermediate ionization state gas tracers such as Si IV and C IV fit for L* galaxies. For sub-L* galaxies ($\log M_\star/M_\odot \lesssim 10$), a tentative correlation was detected between C IV absorption strength and star formation mirroring the dichotomy seen in O VI for L* galaxies (Bordoloi et al., 2014). A similar case is probable for L $\approx$ L* galaxies, where these intermediate ions may trace warm photoionized material similar to low-ions and/or may be produced in part by collisional ionization, either in equilibrium or out of equilibrium, for example, by turbulent mixing layers (e.g. Kwak & Shelton, 2010). However, due to the wavelength coverage of available gratings on *HST*/COS, C IV and Si IV are rarely observed by CGM surveys prioritizing O VI, such as COS-Halos (Werk et al., 2013) and COS-GASS (Borthakur et al., 2015). For this reason, we initiated the C IV in L* galaxies (CIViL*) Survey to fill this notable gap in previous COS absorption galaxy

studies by providing NUV coverage of C IV for galaxy with existing O VI measurements in the CGM. For this work, we assume a flat-universe ΛCDM cosmology with $H_0 = 67.8$ km s^{-1} Mpc^{-1} and $\Omega_m = 0.308$ (Planck Collaboration et al., 2016).

2 Observation and Data Analysis

2.1 Sample Selection

The CIViL* Survey (PID#17076) more than doubles the number of literature sightlines that probe C IV in the inner CGM of L* galaxies. It consists of nine UV-bright QSOs, probing the halos of eleven low redshift ($z \lesssim 0.25$) galaxies. One of the main goals of this survey is to observe C IV in galaxies that have published O VI detections. To build the survey, we identified galaxies from COS-Halos (Werk et al., 2013) and COS-GASS (Borthakur et al., 2015) that would provide a valuable legacy dataset of C IV coverage within one virial radius. This sample of eleven galaxies is representative of the broad range in galaxy stellar mass ($\log_{10}M_\star/M_\odot \sim$ 10.1-11.4) and impact parameter ($R_{proj} \sim$ 20-224 kpc) of the L* galaxies observed in previous COS-CGM programs (e.g., Werk et al., 2013; Bordoloi et al., 2014; Borthakur et al., 2015; Heckman et al., 2017; Berg et al., 2018; Garza et al., 2024) in order to enable fair comparisons to other galaxies types in different stages of evolution.

In particular, the final sample was selected by maximizing the number of ∼L* galaxies that are simultaneously control matched in both $M_\star$ and R_{proj} within ±0.2 dex (see Berg et al., 2018, for more details) to previous COS-CGM programs that include a variety of special evolutionary phases of galaxies (i.e. starburst or AGN). Furthermore, the ratio of impact parameter to virial radius of the survey is well matched (within ±0.3 dex) to the distribution in the COS-Dwarfs (Bordoloi et al., 2014) survey which enables a similar comparison of radial profiles over the two decades of galaxy mass in a systemic fashion with C IV. At least 3 'normal' galaxies were control matched to the starburst or AGN galaxies, whilst at least 5 were matched to COS-Dwarf galaxies. Work utilizing this controlled match aspect of the sample to uncover the nature of highly ionized gas surrounding AGN hosts is forthcoming in Berg et al. (in prep.). The focus of this paper is the comparison between passive and star-forming ∼L* galaxies.

To create an average profile, normalized by the virial radius, we need the virial radii and virial masses. To estimate dark matter halo masses we use the same methodology as Tchernyshyov et al. (2022). We use the stellar mass-halo relation defined in Behroozi et al. (2019, see Tab J1 for fit parameters) in combination with the technique described in Hu & Kravtsov (2003). This technique converts the calculated halo masses, estimated using the galaxy stellar mass and redshift, such that the average mass density within the halo radius is 200 times the critical density of the universe. Using our newly converted virial halo masses (M_{200c}), we calculate virial radii (R_{200c}). These and other galaxy properties can be found in Table 3.1.

Galaxy	$z_{\rm gal}$	z_{qso}	sSFR ($\log_{10}$ yr^{-1})	M$_\star$ ($\log_{10}$ M$_\odot$)	R$_{\rm proj}$ (kpc)	R$_{\rm proj}$/R$_{\rm 200c}$	M$_{\rm 200c}$ ($\log_{10}$ M$_\odot$)	N$_{\rm CIV}$ ($\log_{10}$ cm^{-2})	ref
(1)	(2)	(3)	(4)	(5)	(6)	(7)	(8)	(9)	(10)
J1427+2629_45940	0.0330	0.364	-12.0	10.4	170	1.07	11.6	<13.14	ii
J1502+0649_41743	0.0460	0.288	-10.2	10.5	224	1.29	11.8	<13.55	ii
J1544+2740_28317	0.0320	0.163	<-12.1	10.1	196	1.49	11.4	<12.72	ii
J0226+0015_268_22	0.2274	0.615	<-11.8	10.8	80	0.32	12.3	<13.13	i
J0401-0540_67_24	0.2197	0.570	-10.1	10.1	83	0.60	11.5	>14.26	i
J0950+4831_177_27	0.2119	0.589	<-11.7	11.2	92	0.16	13.4	>14.22	i
J1016+4706_274_6	0.2520	0.822	-10.4	10.2	23	0.16	11.6	>14.48	i
J1016+4706_359_16	0.1661	0.822	-10.4	10.5	44	0.26	11.8	>14.66	i
J1342-0053_157_10	0.2270	0.326	-10.2	10.9	35	0.11	12.6	<13.71	i
J1342-0053_77_10	0.2013	0.326	<-11.0	10.5	32	0.19	11.8	<12.87	i
J1419+4207_132_30	0.1792	0.873	-9.5	10.6	88	0.46	12.0	>14.52	i

Table 3.1: CIViL* Galaxy Sample Properties and C IV Measurements. Comments on columns: (1) Galaxy name: for the COS-Halos galaxies it SDSS field identifier and galaxy identifier, where the first numberis the position angle in degrees from the QSO and the second number is the projected separation in arcseconds (impact parameter) from the QSO, for the COS-GASS the value is the COS-GASS ID; (2) galaxy redshift; (3) QSO redshift (4) specific star formation rate (sSFR): For more details on how the sSFRs were calculated for the galaxies in sample, refer to (Werk et al., 2012; Bordoloi et al., 2014; Borthakur et al., 2015; Garza et al., 2024). On average, for galaxies of these masses, sSFR errors will be on the order of a few - several tenths of a dex.; (5) stellar mass: stellar masses are accurate to about $\sim$ 50%; (6) impact parameter; (7)impact parameter normalized by virial radius ; (8) virial halo mass (9) C IV column density; (10) which survey the galaxy was matched to, either (i) COS-Halos (Werk et al., 2013) or (ii) COS-GASS (Borthakur et al., 2015).

2.2 COS Spectroscopy

The quasar spectra for the CIViL⋆ Survey were taken using either the G160M or the G185M grating on the Cosmic Origins Spectrograph (COS; Froning & Green, 2009; Green et al., 2012) on the Hubble Space Telescope as a part of a 52-orbit Cycle 29 HST Program (PID#17076). The primary spectral features of interest are absorption lines from the C IV doublet ($\lambda\lambda$1548, 1550) at the redshift of each host galaxy. The CIViL⋆ QSOs have FUV magnitudes of $\sim$ 17.0-18.4 and redshifts ranging from 0.032-0.252. Each target QSO was observed between 2-5 orbits in either G185M (targets matched to COS-Halos, Werk et al., 2013) or G160M (targets matched to COS-GASS, Borthakur et al., 2015), depending on the galaxy redshift. Our exposure times were calculated to detect a 50 mÅ feature at a confidence of 2σ. The S/N of the resultant spectra range from 5-12 per resel at the wavelengths of the C IV doublet.

We combine the CALCOS-generated x1D files using v3.1.1 of the COADD_X1D routine provided by the COS-GTO team (Danforth et al., 2016), which properly treats the error arrays of the input files using Poisson statistics. The IDL COADD_X1D routine was modified to injest new data from G185M grating. The code aligns the different exposures by determining a constant offset determined by cross-correlating strong ISM lines in a 10Å wide region of the spectrum. For data taken with the G160M grating, each COS resolution element at R $\sim$18,000 is sampled by six raw pixels at 12.23 mÅ per pixel. G185M spectra consist of three 35 Å stripes separated by two 64 Å gaps with an R $\sim$18,000 and typical spectral dispersion of 33 mÅ per pixel (0.2 Å per six-pixel resolution element). Both the G160M and G185M spectra are Nyquist sampled. For G160M we binned to nyquist sampling with 2 bins per resolution element. The spectra for G185M, which are slightly lower resolution, are well sampled and did not require binning. The resulting science-grade spectra are characterized by a FWHM $\approx$ 16 km s^{-1} and $\approx$ 38 km s^{-1} for G160M and G185M data, respectively. We perform continuum fitting with the `linetools` package[1] , an open-source code for analysis of 1D spectra.

2.3 Absorption Line Measurements

We determine absorption feature line identifications and redshifts in the CIViL⋆ spectra using using the `PyIGM IGMGuesses` GUI[2]. Since the redshifts of the galaxies in the CIViL⋆ survey are well known (see Table 3.1) CGM absorption features were identified by scanning the spectra for features within $\sim$300 km/s associated with the C IV doublet ($\lambda\lambda$1548, 1550). If blends or absorption other than C IV were present we followed the same identification methodology described in Garza et al. (2024).

Based on the manual identifications from the `PyIGM IGMGuesses` GUI, we measure the C IV column densities (N_{CIV}), Doppler parameter (b), and the relative velocity of the absorption components (v_{rel}) using Voigt profile fitting with the package `veeper`[3]. This package uses `scipy.optimize.least_squares`[4] to perform a least squares minimization to obtain

[1] https://github.com/linetools
[2] https://github.com/pyigm
[3] https://github.com/jnburchett/veeper
[4] https://github.com/scipy/scipy

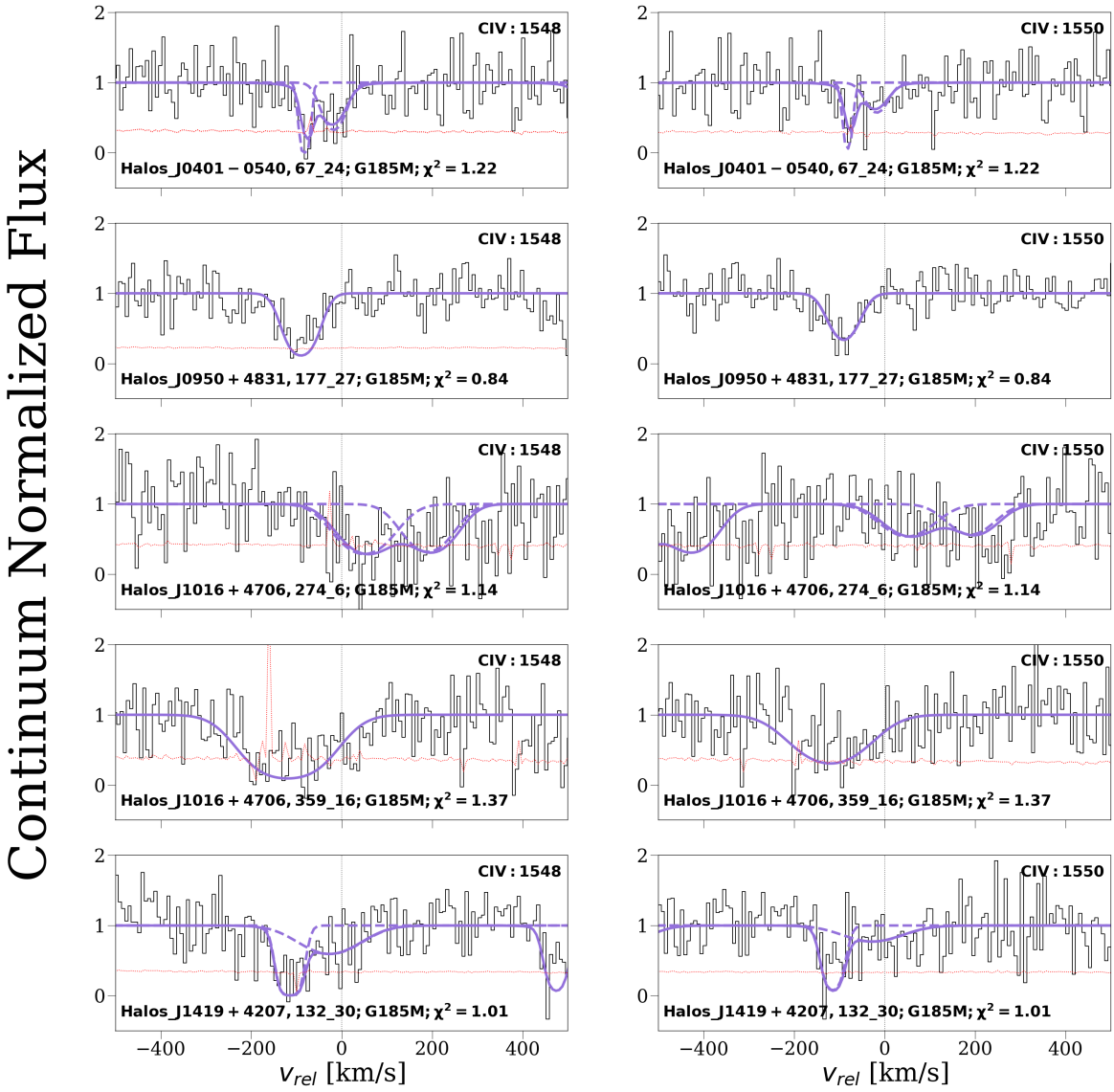

Figure 3.1: Regions of the HST/COS continuum spectrum showing the C IV $\lambda\lambda$ 1548 1550 line absorption features of the CIViL⋆ QSO-galaxy pairs set in the rest frame of each individual galaxy. For lines of sight that have multiple components, the individual fits are shown as the dashed purple line where the sum of the components is shown as the solid purple line. The red line in each spectrum represents the continuum flux error.

The bottom left corner has the QSO-Galaxy IDs and the reduced chi squared fit for the absorption features.

its measurements and incorporates the COS line spread function. Five of our QSO-Galaxy line-of-sight pairs show C IV detections (Figure 3.1); however, the absorption features are saturated so we report them as lower limits. When multiple absorption components are found in a galaxy's search window, their column densities are summed, and the resulting total column density is associated with the galaxy. The other five of the line-of-sight pairs

show no C IV absorption and we report them as upper limits. In these non-detection regions, we calculate a 2σ upper limit on the column density as estimated by the apparent optical depth method (AODM) with the `linetools XSpectrum1D` package[5] over a 100 km s^{-1} velocity span centered on the galaxy redshift. By default, we use the stronger line at 1548Å to estimate 2σ equivalent width upper limits, but in cases where there is blending or contamination, we use the 1550Å line. Our C IV column density measurements can be found in Table 3.1 and they are shown as a function of the impact parameter normalized by virial radius and stellar mass in panels 2 and 3 of Figure 3.2 respectively.

2.4 Archival Observations

Previous studies have shown that observable tracers of the CGM depend on galaxy mass, redshift, and environment (Bergeron, 1986; Bahcall et al., 1991; Chen et al., 2001; Stocke et al., 2006; Bordoloi et al., 2011; Werk et al., 2013; Johnson et al., 2015b; Burchett et al., 2016; Tejos et al., 2016; Bordoloi et al., 2018; Tchernyshyov et al., 2023), making them important variables to consider when studying the differences between the CGM of star-forming and passive galaxies. To address the effect of these galaxy properties, we increase our sample size with CGM C IV measurements using published HST/COS data from COS-Halos (Werk et al., 2013), COS-Dwarfs (Bordoloi et al., 2014), and COS-Holes (Garza et al., 2024). Eight out of eleven of our QSO-galaxy line-of-sight pairs are COS-Halos (Werk et al., 2013) galaxies, thus it is intuitive to include the two galaxies from the COS-Halos Survey that already have C IV observations. The COS-Holes Survey[6] (Garza et al., 2024) sits well within the stellar mass and impact parameter range of the CIViL* survey and adds nine observations to the sample. We also include observations from the COS-Dwarfs survey (Bordoloi et al., 2014) because, as mentioned in §2.1, the CIViL* survey is well matched with this survey's ratio of impact parameter to viral radius. By including observations from these three surveys we have a total combined C IV sample of 65 observations.

3 Results

In the top panel of Figure 3.2 we show the C IV detection fractions (C_f), with 2σ Wilson Binomial confidence intervals[7] for 8 equal sized radial bins. Our detection fractions show that as the normalized impact parameter increases, the detection fraction of C IV decreases; this declining profile, a trend described in several previous works (e.g. Bordoloi et al., 2014), is mirrored in the middle panel[8]. In the middle and bottom panel of Figure 3.2 we show the C IV column densities versus impact parameter normalized by virial radius or R_{proj}/R_{200c} (middle panel) and stellar mass, $\log_{10}M_\star/M_\odot$, (bottom panel) colored by specific star-formation rate ($\log_{10}$sSFR/yr^{-1}).

[5]https://github.com/linetools/linetools/tree/v0.3

[6]We note that results from Garza et al. (2024) suggest that C IV absorption does not show obvious variation as a function of SMBH mass.

[7]This method of calculating confidence intervals is better than normal approximations since it is asymmetric and can be used with small samples and skewed observations.

[8]In Appendix 6 we examine other binning methods and find these also result in a covering fraction that declines with the impact parameter.

Given the variation of CGM columns with galaxy mass and redshift found in previous studies (Tchernyshyov et al., 2023), for the rest of our analysis we restrict the sample to $\log_{10}M_\star/M_\odot \geq 9.5$, since below this limit the vast majority of galaxies are star forming. Additionally, stellar masses lower than this cutoff are mostly dwarf galaxies where it has been shown than their CGM contains ∼10% of metals in the cool phase (T ≈ 10^4 K) (Zheng et al., 2024). This is consistent with what we see in our lower mass sample, where most of the observations of C IV are upper limits. Introducing this cut leaves us with a sample of 46 observations of galaxies with redshifts between 0.0010 and 0.252, impact parameters of 14 to 224 kpc, and stellar masses between $10^{9.5}$ and $10^{11.2}$ $M_\odot$.

3.1 CIV-sSFR Dichotomy

We now examine the relation between C IV and sSFR to investigate whether a similar bimodality exists like the one using O VI (Kauffmann et al., 2003; Schiminovich et al., 2007; Tumlinson et al., 2011; Tchernyshyov et al., 2023). We plot $\log_{10}N_{CIV}/cm^{-2}$ versus $\log_{10}sSFR/yr^{-1}$ for the combined small sample in Figure 3.3. We separate the observations into two galaxy groups based on cuts made in previous works (Tumlinson et al., 2011; Tchernyshyov et al., 2023), divided into star-forming galaxies (sSFR $> 10^{-11}$ yr^{-1}, blue) and passive galaxies (sSFR $\leq 10^{-11}$ yr^{-1}, red). We paid special attention to galaxies within ± 0.2 dex of this cutoff, represented as the grey shaded area in Figure 3.3. Galaxies in this area are possibly transitioning between star-forming and passive and have subtleties that define their classification that a simple sSFR cut doesn't catch. For the galaxies that fall within this "grey" area, we referred to their optical spectra and morphology to determine their classification; for more details we refer the reader to Appendix 7.

We find detection fractions of 72^{+14}_{-18}% [21/29] for the star-forming sample and 23^{+27}_{-15}% [3/13] for the passive sample with 2σ Wilson Binomial confidence intervals above $\log_{10}N_{CIV}/cm^{-2}$ = 13.5[9]. Using `scipy.stats.anderson_ksamp`[10], we perform an Anderson-Darling test for k-samples[11] to compare the C IV column densities of the star-forming (33) and passive (13) sample. For this test we treat each observation as if it were a detection (i.e., not taking into account upper and lower limits); the Anderson-Darling test is useful when not taking into account known limits since the test is designed to examine the tails of distributions which makes it particularly sensitive to deviations in extreme values. We find that we can reject the null hypothesis that these two samples were drawn from the same distribution at a > 99.5% confidence level ($p = 0.0016$). We also explore statistical methods that take into account censored data (upper and lower limits) in Appendix 9; both of these alternative methods (interval-censored analysis: $p = 0.017$, two-sided k-sample test: $p = 0.034$) confirm our original finding that there is a bimodality between the C IV content in star-forming and passive galaxies with $>2\sigma$ confidence.

We also test the statistical significance of the correlation of N_{CIV} and sSFR by performing

[9] See Appendix 8 for an exploration of detection fractions using different detections thresholds

[10] https://github.com/scipy/scipy

[11] The k-sample Anderson-Darling test is a modification of the one-sample Anderson-Darling test. It tests the null hypothesis that k-samples are drawn from the same population without having to specify the distribution of that population.

a generalized Kendall's tau test using `scipy.stats.kendalltau`[12]. This test, which did not take into account upper or lower limits resulted in a $\tau = 0.29$ ($p = 0.004$) which leads us to reject the null hypothesis that there is no correlation between the C IV absorption and galaxy sSFR. Bordoloi et al. (2014) report a similar result for galaxies with $9 \leq \log_{10}M_\star/M_\odot \leq 10$ where they also rejected the null hypothesis that star-forming and passive galaxies draw from the same parent distribution of equivalent widths at a >99.5% confidence level. Similar KS and Kendall's tau tests using O VI column densities were performed by Tumlinson et al. (2011) where they used QSO-Galaxy pairs from the COS-Halos Survey (Werk et al., 2013). They also found that N_{OVI} and sSFR correlate at a $> 99\%$ confidence which led them to conclude that their results show a basic dichotomy between star-forming ("blue-cloud") and passive ("red-sequence") galaxies is present in the gaseous halos of their sample.

To compare between our result and the O VI-sSFR dichotomy, we recreate Fig. 3 from Tumlinson et al. (2011). We highlight galaxies in which C IV and O VI were both observed in dark, bold points. These observations overlay the lightly shaded O VI column densities from Tumlinson et al. (2011) and Werk et al. (2013) and C IV observations from the combined CIViL* and literature sample. Our results independently suggest a dichotomy between the halos of star-forming and passive galaxies as traced by C IV but overlaid with O VI, they statistically mirror the dichotomy discussed in Tumlinson et al. (2011).

3.2 Minimum Mass of Carbon in the CGM

We estimate the total mass of carbon in the CGM ~L* galaxies by following the method outlined in Bordoloi et al. (2014). By assuming a conservative ionization correction ($f_{CIV} = 0.3$, for more details please see §5 in Bordoloi et al., 2014) they obtained a lower limit on the carbon mass (M_{carbon}) which can be written as:

$$M_{\rm carbon} \gtrsim 1.12 \times 10^6\ {\rm M}_\odot \left(\frac{{\rm N_{CIV,\,mean}}}{10^{14}\ {\rm cm^{-2}}}\right) \times \left(\frac{\rm R_{proj}}{120\ {\rm kpc}}\right)^2 \times \left(\frac{0.3}{\rm f_{CIV}}\right). \quad (3.1)$$

Similarly to Bordoloi et al. (2014), we split our sample into three radial bins and then summed them to obtain the final lower limit on carbon mass. The mean column density within $R_{proj} < 40$ kpc is 2.10×10^{14} cm^{-2}, within 40 kpc $\leq R_{proj} < 80$ kpc is 1.44×10^{14} cm^{-2}, and within 80kpc $\leq R_{proj} < 120$ kpc is 1.65×10^{14} cm^{-2}.

We find a minimum carbon mass of $M_{carbon}/M_\odot \gtrsim 3.03 \times 10^6$. We note that the column densities derived using Voigt profile fits are saturated for some of the lines of sight in the sample and are thus probably underestimating the true column density; however, this is value is about a factor of 1.6 higher than the M_{carbon} value presented in Bordoloi et al. (2014) (1.9×10^6 M$_\odot$). Our minimum carbon mass is comparable to the total carbon mass in the ISM of L* galaxies, (e.g. Peeples et al., 2014; Bordoloi et al., 2014).

4 Discussion

Results from the COS-Dwarfs survey (Bordoloi et al., 2014) suggested a correlation between C IV absorption strength and sSFR of sub-L* galaxies within half the virial radius. The

[12]https://github.com/scipy/scipy

COS-Holes survey (Garza et al., 2024) tentatively confirmed with $\gtrsim 2\sigma$ significance that a correlation between sSFR and C IV-bearing CGM in L* galaxies is similar to that of O VI. The combined CIViL* observations with those from other COS-CGM surveys indicate that C IV is more O VI-like than "low-ion-like". This suggests that C IV is also tracing gas formed or maintained by star formation and/or feedback unlike other low-ionization state gas traced by singly and doubly ionized species (e.g. H I, Si II, C III, etc) which show no correlation with galaxy star-forming properties (Werk et al., 2013). In an upcoming paper, we will perform a detailed analysis of the kinematics and ionization state of C IV-bearing gas to provide more complete constraints on the physical conditions of the CGM of $\sim$L* galaxies.

CGM C IV also provides a potential avenue for exploring how galaxies sustain their star formation since the CGM is a large gaseous reservoir and a source for the galaxy's star-forming fuel (Tumlinson et al., 2017). To address this, we estimate the depletion time, $\tau_{\rm dep}$, as the CGM mass divided by the mean SFR, as the timescale over which star-formation could be maintained its current rate, given an available gas supply, and assuming no inflows of fresh fuel or recycling of the gas (Saintonge & Catinella, 2022). But how much fuel is actually available? To do this back of the envelope calculation, we use the minimum mass of carbon we estimate in §3.2 (for a conservative ionization correction) and translate it to a total hydrogen mass using a metallicity of $Z = 1/3$ (Prochaska et al., 2017) and the solar carbon abundance. This gives a lower limit of $\rm M_{CGM} \geq 2.83 \times 10^9\ M_\odot$ on the total gas mass in the CGM. Using the mean SFR in our sample, 1.5 $\rm M_\odot$/yr, the resulting lower limit on the depletion time is $\tau_{\rm dep} \geq 1.93$ Gyr.

Comparing our depletion time to depletion times presented in Fig. 6a of Péroux & Howk (2020), we find that our $\tau_{\rm dep}$ is fairly consistent with their molecular gas depletion timescale at z=0. Our depletion timescale is comparable or shorter than the dynamical timescale (taken to be 10% of the Hubble time) which suggests that the CGM and molecular gas available to galaxies, assuming no inflows of fresh fuel or recycling of the gas, slowly becomes insufficient to fuel star formation on its own (Péroux & Howk, 2020). Therefore, galaxies are most likely undergoing some resupply process either through the conversion of ionized gas from the CGM or IGM or through accretion from the IGM onto the disks of galaxies. Thus, gas in the CGM is only one piece of the large reservoir that galaxies use as fuel for future star formation.

5 Summary and Conclusion

In this work, we presented observations from the CIV in L* galaxies (CIViL*) Survey. The main results of this study are as follows.

1. The CIViL* Survey amplifies the diagnostic power of the current COS-CGM samples through the acquisition of 11 new C IV observations for L * galaxies.

2. We combine our observations from CIViL* with C IV observations (Werk et al., 2013; Bordoloi et al., 2014; Garza et al., 2024) for a final sample of 45 lines of sight. We separate the observations by their sSFR where we classify them as either star-forming (sSFR $> 10^{-11}$ yr^{-1}) or passive (sSFR $\leq 10^{-11}$ yr^{-1}).

3. We find a detection fraction of 72^{+14}_{-18}% [21/29] for the star-forming sample and 23^{+27}_{-15}% [3/13] for the passive sample. Using an Anderson-Darling test to compare C IV absorption in star-forming and passive galaxies, we find a dichotomy at a >99.5% confidence level.

4. Our discovery of a dichotomy in L* galaxies is similar to the one found using O VI bearing gas (Tumlinson et al., 2011; Tchernyshyov et al., 2023).

The results from this paper are the tip of the iceberg for what observations from the CIViL* Survey will reveal. This survey supplements the enormous investment of 483 orbits in previous COS-CGM surveys by placing one of the most consistent ion tracers of diffuse gas in the context of the baryon cycle over 10+ Gyrs of cosmic evolution. Not only does it close a gap in C IV coverage for low-z, L* galaxies it provides the opportunity to constrain how the baryon cycle differs among dwarf, star-forming, passive, and AGN-bearing galaxies. Future work carried out using the CIViL* survey data will examine the kinematics and ionization mechanisms of the C IV-traced gas phase of the CGM and the differences between the CGM of AGN hosts and star-forming galaxies.

6 Appendix A: Full Sample Detection Fractions

In addition to calculating covering fractions for equal radial bins, we created radial bins that had an equal amount of galaxies per bin. We list detection fractions from both of these scenarios in Table F.1. Again, our detection fractions reflect the declining radial profile seen in the middle panel of Figure 3.2.

7 Appendix B: Galaxies in the "Grey" Area

There are five galaxies in our sample that have sSFRs that fall within a "grey" area of ±0.2 dex around our cut off of $\log_{10}$sSFR/yr^{-1} = -11.0, or the area where galaxies are transition between star-forming and passive. To classify these galaxies as either star-forming or passive, we took extra steps in addition to looking at their sSFR. Our explanation our choice to denote a galaxy as either star-forming or passive is detailed below:

- SDSS J110404.25+314015.1 (COS-Dwarfs, 211_65, Bordoloi et al., 2014): We looked at the spectrum available through the Sloan Digital Sky Survey (SDSS) and observed strong emission lines indicative of a late type galaxy. We group this galaxy in the star-forming bin for our analysis.

- SDSS J082022.99+233447.4 (COS-Halos and COS-Dwarfs, 260_17, Werk et al., 2013; Bordoloi et al., 2014): We looked at the spectrum available through SDSS and observed both absorption and emission features. We investigated the galaxy's emission line ratios and compared them to an SDSS BPT diagram and saw what it lies within the star-forming region. In addition, this galaxy is a dusty, edge on disk galaxy with an $\log_{10}$sSFR/yr^{-1} = -10.9. Thus we place this galaxy in the star-forming group for our analysis.

bin width (1)	hit rate (2)	C_f (3)	2σ CI (4)
4 Equal Radial Bins (R_{proj}/R_{200c})			
0.0-0.5	16/23	0.70	(0.49, 0.84)
0.5-1.0	11/24	0.46	(0.28, 0.65)
1.0-1.5	1/11	0.09	(0.02, 0.38)
1.5-2.0	0/3	0.00	(0, 0)
8 Equal Radial Bins (R_{proj}/R_{200c})			
0.0-0.25	7/10	0.70	(0.40, 0.89)
0.25-0.5	9/13	0.69	(0.42, 0.87)
0.5-0.75	8/16	0.50	(0.28, 0.72)
0.75-1.0	3/8	0.38	(0.14, 0.69)
1.0-1.25	1/5	0.20	(0.04, 0.62)
1.25-1.5	0/7	0.00	(0, 0)
1.5-1.75	0/2	0.00	(0, 0)
1.75-1.0	0/1	0.00	(0, 0)
Equal Number of Galaxies Per Bin (R_{proj}/R_{200c})			
0.1-0.3	9/12	0.75	(0.47, 0.91)
0.3-0.5	7/13	0.54	(0.29, 0.77
0.6-0.7	6/12	0.50	(0.25, 0.75)
0.7-1.0	6/12	0.50	(0.25, 0.75)
1.0-2.0	0/12	0.00	(0, 0)

Table F.1: Full Sample Detection Fractions. Comments on columns: (1) width of the radial bins; (2) hit rate - the amount of detections above the threshold of $\log_{10}N_{CIV}/\mathrm{cm}^{-2}$ = 13.5 (3) detection fractions, (4) 2σ Wilson Binomial Confidence Intervals.

Galaxy Group (1)	hit rate (2)	C_f (3)	2σ CI (4)
Detection Threshold: $\log_{10}N_{CIV}/cm^{-2} = 13.5$			
SF	21/29	72%	(54, 85)
Non-SF	3/13	23%	(8, 50)
Detection Threshold: $\log_{10}N_{CIV}/cm^{-2} = 13.75$			
SF	18/33	54%	(38, 70)
Non-SF	2/13	15%	(4, 42)
Detection Threshold: $\log_{10}N_{CIV}/cm^{-2} = 14.0$			
SF	15/33	45%	(30, 62)
Non-SF	1/13	8%	(1, 33)

Table H.2: SF & Non-SF Detection Fractions. Comments on columns: (1) Galaxy Group - either star-forming (SF) or passive (Non-SF); (2) hit rate - the amount of detections above the indicated detection threshold (3) detection fractions, (4) 2σ Wilson Binomial Confidence Intervals.

- NGC 4258 (COS-Holes, Garza et al., 2024): We looked at the spectrum available on NED[13] and observed strong emission features indicative of a late type galaxy. We also investigated the morphology of NGC 4258 and found it to be a weakly barred spiral galaxy. Due to these findings we place this galaxy in the star-forming group for our analysis.

- NGC 3489 (COS-Holes, Garza et al., 2024): We looked at the spectrum available on NED and observed both emission and absorption features. Looking at the morphology we find that the galaxy is an intermediate spiral. Taking into consideration its sSFR ($\log_{10}$sSFR/yr^{-1} = -11.167) we group this in the passive galaxy group.

- SDSS J134252.23-005343.2 (COS-Halos, 77_10, Werk et al., 2013): We looked at the spectrum available in Werk et al. (2012) and determined that it is very clearly an early type galaxy from the spectrum with distinct absorption lines. We place this galaxy in the passive group for our analysis.

8 Appendix C: Star-Forming & Passive Detection Fractions

Here we compare the detection fractions calculated using different detection thresholds as shown in Table H.2. Upper limits exceeding the threshold are excluded from the analysis, counting as neither detections nor non-detections. The probability distribution for the detection fraction is characterized by a Beta distribution:

$$p(f|k,N) = Beta(\alpha = k + c, \beta = N - K + c) \tag{3.2}$$

[13]The NASA/IPAC Extragalactic Database (NED) is funded by the National Aeronautics and Space Administration and operated by the California Institute of Technology.

The likelihood of observing k detections in N trials given a detection probability f is given by the binomial distribution. The posterior probability distribution for f given an observed number of detections and assuming a Jeffreys' prior on f is a beta distribution with parameters $\alpha = k+1/2$ and $\beta = N-k+1/2$. This beta distribution arises from the normalization of a binomial probability mass function $P(k|N, f) \propto f^k(1-f)^{N-k}$ with respect to the parameter f rather than the count k. The statistical comparison of detection fractions is performed through Monte Carlo sampling from the respective beta distributions. For each pair of covering fractions, we examine ratio distributions $f_{\rm SF}/f_{\rm P}$. The results of these distributional comparisons across detection fraction thresholds are summarized as follows:

- **Detection Threshold of $\log_{10}N_{\rm CIV}/{\rm cm}^{-2} = 13.5$:** The analysis indicates that the star-forming detection fraction exceeds the passive detection fraction by a factor of 2–5, measured within the 68% credible interval. The probability of the passive detection fraction surpassing the star-forming detection fraction is $p = 1.2 \times 10^{-3}$, corresponding to a 3σ deviation under the assumption of normality.

- **Detection Threshold of $\log_{10}N_{\rm CIV}/{\rm cm}^{-2} = 13.75$:** The analysis indicates that the star-forming detection fraction exceeds the passive detection fraction by a factor of 2 to 7, measured within the 68% credible interval. The probability of the passive detection fraction surpassing the star-forming detection fraction is $p = 6.2 \times 10^{-3}$, corresponding to a 2.5σ deviation under the assumption of normality.

- **Detection Threshold of $\log_{10}N_{\rm CIV}/{\rm cm}^{-2} = 14.0$:** The analysis indicates that the star-forming detection fraction exceeds the passive detection fraction by a factor of 2 to 14, measured within the 68% credible interval. The probability of the passive detection fraction surpassing the star-forming detection fraction is $p = 4.8 \times 10^{-3}$, corresponding to a 2.6σ deviation under the assumption of normality.

9 Appendix D: Statistical Methods for Censored Data

For observations characterized by detection limits, where measurements are confined by lower and upper bounds, interval-censored statistical methods provide a practical, yet valid, analytical framework. For upper limits, we construct intervals from a common lower bound to the detection threshold, while for lower limits, we construct intervals from the saturation limit to a common upper bound. The implementation of interval-censored survival analysis thus accommodates both left-censored (upper limits) and right-censored (lower limits) data by transforming point constraints into comparable intervals. This approach maintains statistical validity in rank-based tests, as the specific values chosen for the common bounds do not affect the relative ordering of the observations, provided these bounds are consistently applied across all measurements and are outside the range of the measurements.

Interval-censored survival analysis was performed using the `interval` package in R to evaluate differences between the survival distributions of the passive and star-forming samples. The log-rank test with the `logrank1` score function was implemented to test the hypothesis that the survival distribution of the passive sample is stochastically less than that of the star-forming sample. This test yielded statistical significance at $p = 0.017$. A

subsequent two-sided k-sample test indicated that the survival distributions differ significantly ($p = 0.034$). These interval-censored survival analyses, which explicitly account for the censoring structure in the observations, provide statistical evidence for bimodality in the C IV content between star-forming and passive galaxies at $> 2\sigma$ significance.

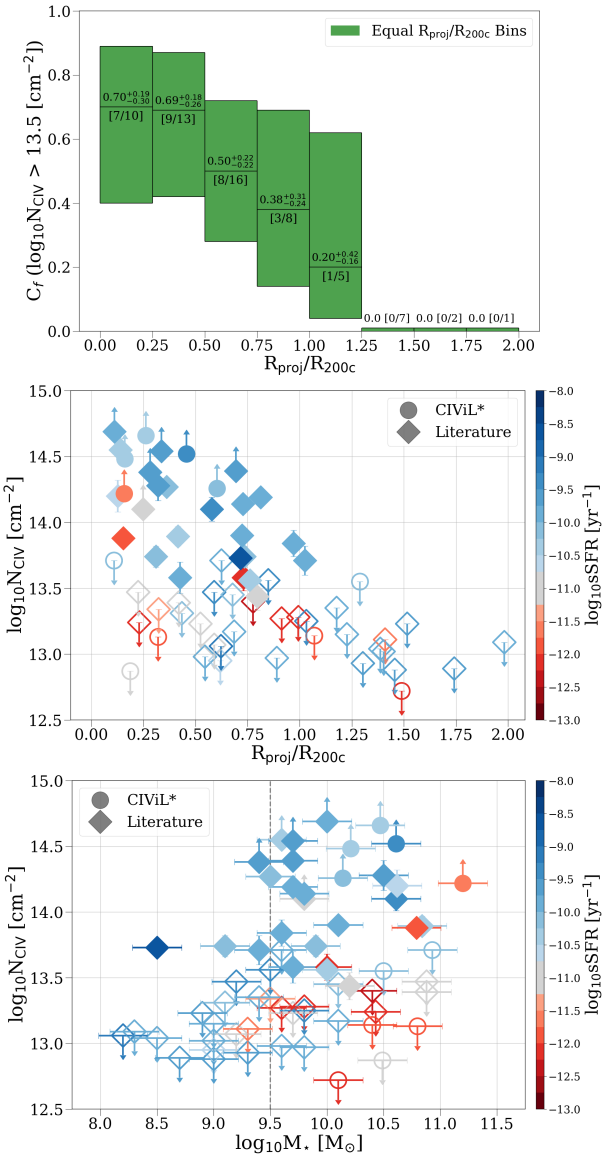

Figure 3.2: C IV detection fraction vs. normalized impact parameter & galaxy properties. **Top Panel:** The C IV detection fraction vs. normalized impact parameter. The shaded areas represent 2σ Wilson Binomial Confidence Intervals across equal width radial bins. Upper limits exceeding the threshold ($\log_{10}N_{CIV}/cm^{-2} = 13.5$) are excluded from the analysis. **Middle and Bottom Panels:** C IV column densities assembled from previous QSO absorption line surveys probing the CGM of low-z, galaxies (diamonds) with the new CIViL⋆ observations (circles) versus galaxy properties (middle: R_{proj}/R_{200c}; bottom: $\log_{10}M_\star/M_\odot$). Each observation is colored by its corresponding sSFR determined from a combination of emission-line spectroscopy and broadband photometry. Non-detections (upper limits) are represented with open symbols and arrows pointing down while saturated detections (lower limits) are represented as colored symbols with arrows pointing up. For the rest of the analysis we only use observations with a $\log_{10}M_\star/M_\odot \geq 9.5$.

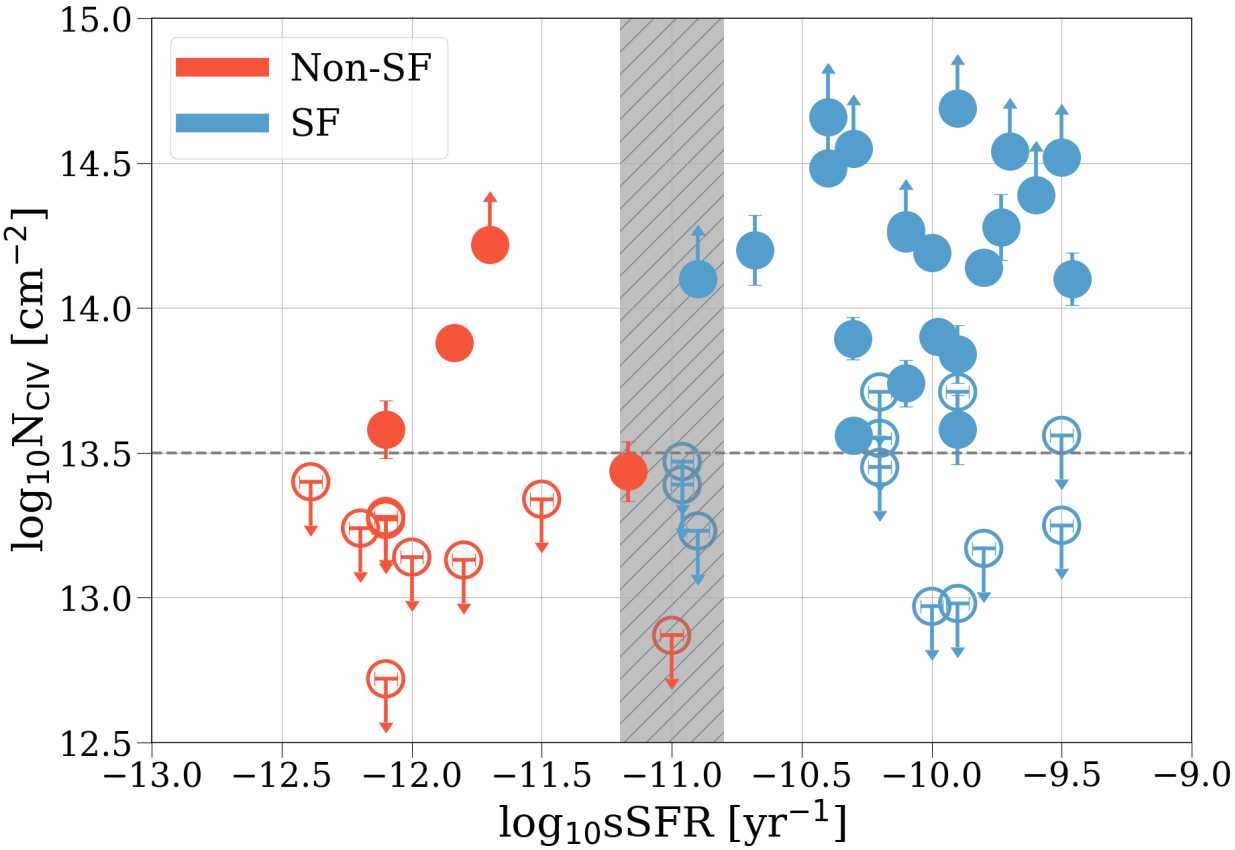

Figure 3.3: Measured C IV column densities versus sSFR for CIViL⋆ and the additional literature sample. The star forming galaxies (sSFR $> 10^{-11}$ yr^{-1}) are colored in blue while the passive galaxies (sSFR $\leq 10^{-11}$ yr^{-1}) are colored in red. For galaxies in the grey shaded area, we examine their spectra and morphology, in addition to sSFR for classification. Like the previous figure, non-detections (upper limits) are represented with open symbols and arrows pointing down while saturated detections (lower limits) are represented as colored symbols with arrows pointing up. The horizontal line signifies the detection limit of the sample. Above $\log_{10}N_{CIV}/cm^{-2} = 13.5$, the star forming and passive galaxy sample have detection fractions of $72^{+14}_{-18}\%$ [21/29] and $23^{+27}_{-15}\%$ [3/13], respectively. Upper limits exceeding the threshold are excluded from the analysis.

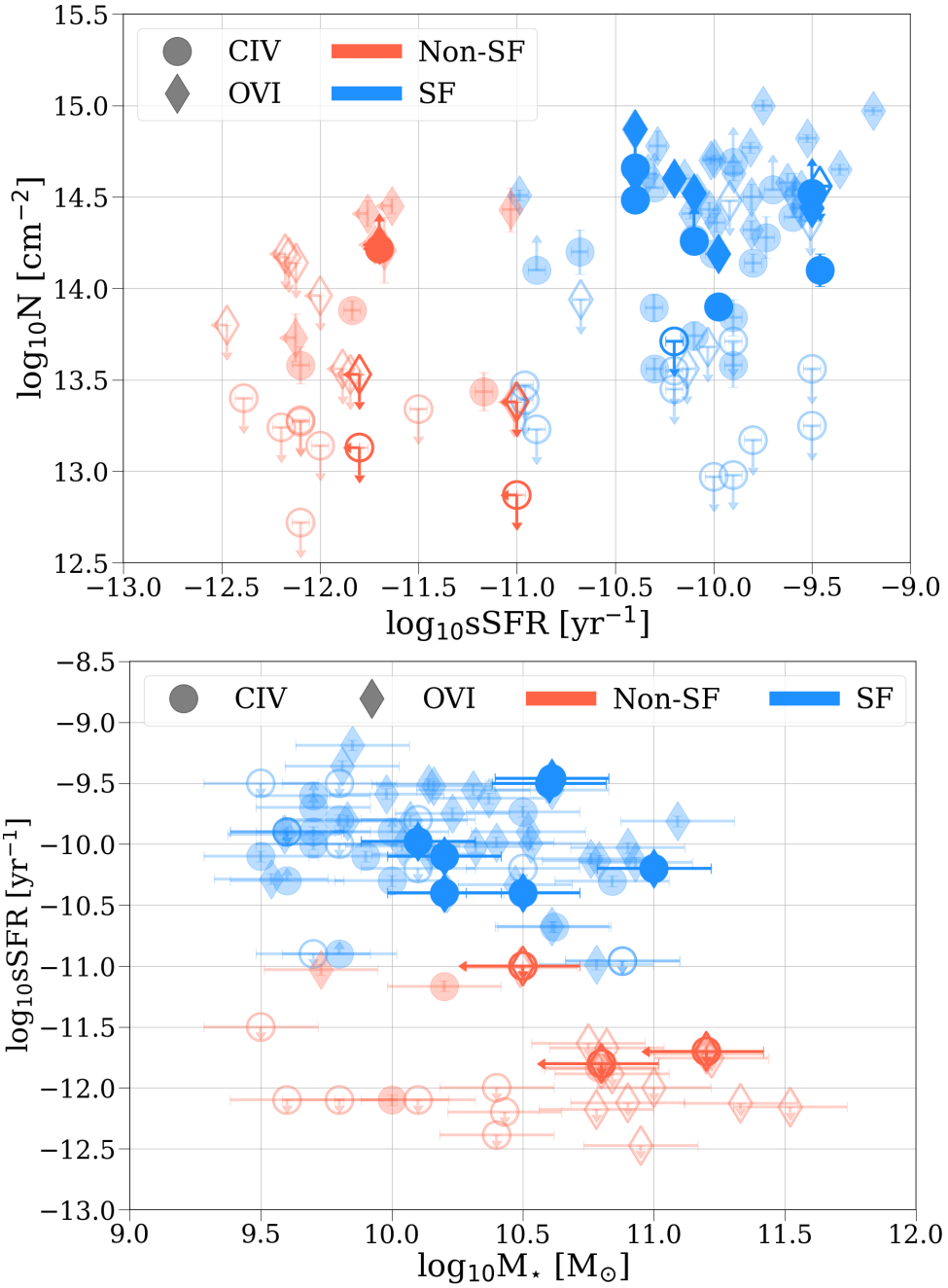

Figure 3.4: C IV and O VI correlations with galaxy properties. If the marker is dark/ bold, they are from galaxies where both ions were observed. These observations overlay lightly shaded O VI column densities from Tumlinson et al. (2011) and Werk et al. (2013) and C IV observations from the combined CIViL⋆ and literature sample. Similar coloring and limit convention as Figure 3.3. **Top:** $\log_{10}N_{CIV}/cm^{-2}$ and $\log_{10}N_{OVI}/cm^{-2}$ vs $\log_{10}sSFR/yr^{-1}$. **Bottom:** $\log_{10}N_{CIV}/cm^{-2}$ and $\log_{10}N_{OVI}/cm^{-2}$ vs $\log_{10}M_{\star}M_{\odot}$. The basic dichotomy observed between star-forming ("blue cloud") and passive ("red sequence") galaxies seen in O VI observations (Tumlinson et al., 2011; Johnson et al., 2015b; Zahedy et al., 2019; Tchernyshyov et al., 2023) is also seen in observations of C IV.

CHAPTER 4

ZONE OF AVOIDANCE: PINPOINTING PHYSICAL CONDITIONS OF GASEOUS HALOS

Lenny: "Skitch", how did we get here? Guy: I led you here... for I am Spartacus.
– That Thing You Do!

1 Introduction

The circumgalactic medium (CGM), or the diffuse gaseous atmosphere that surrounds galaxies, lies at the intersection of interactions between internal galactic processes and cosmic gas flows. Due to these interactions, the CGM plays host to a significant reservoir of ionized material (Tumlinson et al., 2017, and references within). Through of observations of this ionized gas and results from simulations of the diffuse gaseous medium, the CGM community has made strides in understanding the cyclical nature of this gas and has come to see it as a key regulator of galaxy processes. For example, it is believed that star formation in a galaxy is sustained through the combined efforts of gas accreting onto the galaxy and outflowing gas from internal galactic processes (e.g., Rubin et al., 2012; Ford et al., 2014; Muratov et al., 2015; Shattow et al., 2015; Christensen et al., 2016; Anglés-Alcázar et al., 2017; Rupke et al., 2019; Crain & van de Voort, 2023). However, the underlying small scale physical processes of these cycles are still mostly unresolved (e.g. origin of $T \sim 10^4$ gas, the survival and growth of this gas, and it's interactions with gas at other temperatures, etc.). These unresolved processes give rise to open questions in relation to the impact of these gas flows (e.g., how is the multiphase structure of gaseous halos produced and how does this medium affect the formation and evolution of galaxies. Faucher-Giguère & Oh, 2023). One way to begin tackling these open questions is to carefully characterize the ions that reside in the CGM and begin providing constraints on the physical properties of this ionized medium.

There are several ways to observe the CGM such as emission line mapping (Corlies & Schiminovich, 2016b; Piacitelli et al., 2022; Nielsen et al., 2024), Sunyaev-Zel'dovich cosmic microwave background anisotropies (Schaan et al., 2021; Bregman et al., 2022), and fast radio burst dispersion measurements (Ravi et al., 2023; Wu & McQuinn, 2023). However, a well documented method for observing the ions in this medium is through UV absorption-line spectroscopy using the Hubble Space Telescope and the Cosmic Origins Spectrograph (*HST/COS*). Surveys utilizing *COS* have established that the CGM is a multiphase medium comprised of many complex ionization states. Since it's installation, many surveys have dramatically furthered our understanding of this the temperatures and densities of the diffuse halos of nearby galaxies ($z \lesssim 0.5$) from intermediate mass galaxies ($\log_{10}M_\star/\mathrm{M}_\odot \approx 9.5$; e.g., Bordoloi et al., 2014, 2018) to Milky Way mass systems ($\log_{10}M_\star/\mathrm{M}_\odot \sim 10.8$; e.g., Werk et al., 2012; Stocke et al., 2006; Tumlinson et al., 2013; Werk et al., 2013, 2014; Peeples et al., 2014; Mathes et al., 2014; Borthakur et al., 2015; Johnson et al., 2015b; Werk et al., 2016; Borthakur et al., 2016; Heckman et al., 2017; Berg et al., 2018; Prochaska et al., 2019; Wilde et al., 2021; Tchernyshyov et al., 2022).

Different ions are used as tracers for different phases of this multiphase medium. For example, the cool phase of the CGM ($T \sim 10^4$ K) has been characterized by Mg II. This ion is more common around star-forming galaxies than passive galaxies (Lan, 2020; Anand et al., 2021) and is often used as a tracer of star-formation driven winds (Rubin et al., 2014), where it is observed to have a strong incident rate along the minor axes of star-forming galaxies (Bordoloi et al., 2011). However, other ions associated with the cool phase, such as H I, Si II, and C III show no statistically significant correlation with galaxy star-forming properties (Tumlinson et al., 2013; Werk et al., 2013). An ion that does show significant correlation with galaxy properties is O VI. Examples of this tracers power include: discovering a dichotomy

between the ionization content of star-forming (abundance of O VI) and passive (O VI is less common) L* galaxies (Kauffmann et al., 2003; Schiminovich et al., 2007; Tumlinson et al., 2011; Tchernyshyov et al., 2023) and placing a lower limit of 10^7 M$_\odot$ on the highly ionized metal mass in the CGM of L* galaxies (Tumlinson et al., 2011). Significant progress has been made using this tracer (e.g., Sembach et al., 2004; Tripp et al., 2008; Wakker & Savage, 2009; Tumlinson et al., 2011; Savage et al., 2014; Werk et al., 2016; Oppenheimer et al., 2016) and research suggests that O VI arises in warm/hot, more diffuse gas than the CGM of low ions. However, it is possible that this ion could reside in the intermediate/cool phase ($T \sim 10^{4-4.5}$, e.g.; Tripp et al., 2008), or sit at an interphase between these phases (e.g. ambient media or gas mixing).

One of the many influential studies that includes an abundance of O VI observations is the COS-Halos survey which provides a large sample of absorption-line spectroscopy observations for L $\approx$ L* galaxies at $z \sim 0.2$ (Tumlinson et al., 2013; Werk et al., 2013). This survey of 44 galaxies contains a wide range of star formation rates (SFRs) and morphologies (Werk et al., 2012), using background quasars at impact parameters $R_{\rm proj} \approx$ 10-160 kpc and successfully obtained an abundance of ion tracers such as H I, Mg II, C II, C III, Si III, Si IV, N V, and O VI. However, due to the wavelength coverage of available gratings on *HST/COS*, C IV was only observed in two lines of sight, despite arguably being one of the best tracers of galactic gas reservoirs across cosmic time (Chen et al., 2001; Fox et al., 2007; Becker et al., 2009; Cooksey et al., 2010; D'Odorico et al., 2010; Simcoe et al., 2011; Turner et al., 2014; Bird et al., 2016; Burchett et al., 2016; Hasan et al., 2020). With the introduction of the CIViL* survey (Garza et al., 2025), which specifically targeted C IV, in nine COS-Halos lines of sight, we now have the power to directly study intermediate and high ions in the same set of well-characterized L* galaxies. The combined power of the C IV and O VI observations, provide us with the unique opportunity to further constrain the ionization processes of both ions, relate them to galaxy properties, and improve our understanding about the gas flows that drive the evolution of these galaxies.

This paper proceeds as follows: Section 2 describes the FUV spectroscopy from *HST/COS* (§2.1) for both CIViL* (§2.1.1) and COS-Halos (§2.1.2); Section 3 presents the absorption feature analysis (§3.1), a quantitative comparison of ion kinematics (§3.2), and an empirical comparison of C IV, N V, and O VI ratios (§4.1); Section 4 investigates the physical properties of the multiphase CGM gas of our sample first to Cloudy models addressing a single-phase origin for the different ions (§4.2) and then compares the observations to a cooling flow model (§4.3); Section 5 discusses alternative scenarios and models to explore the observed columns; lastly we present a summary of our conclusions in Section 6. In this work we assume a flat-Universe ΛCDM cosmology with $H_0 = 67.8$ km s^{-1} Mpc^{-1} and $\Omega_m = 0.308$ (Planck Collaboration et al., 2016).

2 Observations and Measurements

2.1 COS Spectroscopy

The observations of the CGM gas used for our analysis were taken from the CIViL* survey, a targeted C IV absorption-line survey of L$\approx$ L* galaxies at $z \lesssim 0.25$ (Garza et al., 2025)

Galaxy	$z_{\rm gal}$	$z_{\rm qso}$	sSFR ($\log_{10}$ yr^{-1})	$M_\star$ ($\log_{10}$ M$_\odot$)	$R_{\rm proj}$ (kpc)	$R_{\rm proj}/R_{\rm 200c}$	$M_{\rm 200c}$ ($\log_{10}$ M$_\odot$)
(1)	(2)	(3)	(4)	(5)	(6)	(7)	(8)
J0226+0015_268_22	0.2274	0.615	<-11.8	10.8	80	0.32	12.3
J0401-0540_67_24	0.2197	0.570	-10.1	10.1	83	0.60	11.5
J0910+1014_34_46	0.1427	0.463	-9.5	10.6	112	0.58	12.0
J0950+4831_177_27	0.2119	0.589	<-11.7	11.2	92	0.16	13.4
J1016+4706_274_6	0.2520	0.822	-10.4	10.2	23	0.16	11.6
J1016+4706_359_16	0.1661	0.822	-10.4	10.5	44	0.26	11.8
J1342-0053_157_10	0.2270	0.326	-10.2	10.9	35	0.11	12.6
J1342-0053_77_10	0.2013	0.326	<-11.0	10.5	32	0.19	11.8
J1419+4207_132_30	0.1792	0.873	-9.5	10.6	88	0.46	11.9
J1619+3342_113_40	0.1414	0.471	-10.0	10.1	97	0.72	11.5

Table 4.1: Sample Galaxy Properties. Comments on columns: (1) Galaxy name: for the COS-Halos galaxies it SDSS field identifier and galaxy identifier, where the first number is the position angle in degrees from the QSO and the second number is the projected separation in arcseconds (impact parameter) from the QSO, for the COS-GASS the value is the COS-GASS ID; (2) galaxy redshift; (3) QSO redshift (4) specific star formation rate (sSFR): For more details on how the sSFRs were calculated for the galaxies in sample, refer to (Werk et al., 2012; Bordoloi et al., 2014; Borthakur et al., 2015; Garza et al., 2024). On average, for galaxies of these masses, sSFR errors will be on the order of a few - several tenths of a dex.; (5) stellar mass: stellar masses are accurate to about $\sim$ 50%; (6) impact parameter; (7) impact parameter normalized by virial radius ; (8) virial halo mass.

and the COS-Halos survey, an absorption-line study of L≈L* galaxies at $z \sim 0.2$ (Tumlinson et al., 2013; Werk et al., 2013)[1]. We briefly discuss each survey's spectra in the following sections but for more in depth information we refer the reader to Tumlinson et al. (2013) for COS-Halos and Garza et al. (2025) for CIViL*. For a compilation of parameters for the galaxy-QSO pairs that we use, see Table 4.1.

2.1.1 CIViL*

The quasar spectra for the CIViL* Survey was part of the accepted 52-orbit Cycle 29 HST Program (PID#17076, PI: Berg; Table 4.3). The CIViL* quasar sightlines were selected based on building a representative samples of L* galaxies ($10.1 \leq \log_{10}(M_\star/\mathrm{M}_\odot) \leq 11.4$) from COS-Halos and COS-GASS surveys that spanned a range of impact parameters ($20 \leq R_{\rm proj} \leq 224$ kpc). In order to maximize the ability to compare the CGM between galaxies of different masses (i.e. dwarf and L* galaxies) or in special evolutionary phases (e.g. AGN), the CIViL* sightlines were chosen such that each AGN and starburst galaxy from Berg et al. (2018) and Heckman et al. (2017) had an average of 3 control-matched L* galaxies, following the stellar mass and impact parameter matching criteria outlined in Berg et al. (2018). Furthermore, each dwarf galaxy from COS-Dwarfs (Bordoloi et al., 2014) have at least 5 control-matched L* galaxies that have an impact parameter normalized by the virial radius within $R_{\rm proj}/R_{\rm 200c} <$ 0.3 dex. Observations were taken using either the G160M (COS-GASS matched) or the G185M (COS-Halos matched) grating on the Cosmic Origins Spectrograph (COS; Froning & Green, 2009; Green et al., 2012) on the Hubble Space Telescope. The primary spectral features of interest are absorption lines from the C IV doublet ($\lambda\lambda$1548, 1550) at the redshift of each host galaxy; however the full wavelength coverage for each sightline spans $\lambda \approx$ 1340-1990 Å. Our exposure times were calculated to detect a 50 mÅ feature at a confidence of 2σ. The S/N of the resultant spectra range from 5-12 per resel at the wavelengths of the C IV doublet.

To combine the CALCOS-generated x1D files, we use v3.1.1 of the COADD_X1D routine provided by the COS-GTO team (Danforth et al., 2016); this method properly treats the error arrays of the input files using Poisson statistics. The IDL COADD_X1D routine was modified to injest new data from G185M grating. The code aligns the different exposures by determining a constant offset determined by cross-correlating strong ISM lines in a 10Å wide region of the spectrum. For data taken with the G160M grating at lifetime position (LP) 6, each COS resolution element at R ∼13,000 is sampled by six raw pixels at ∼16 mÅ per pixel. This spectral resolution of data obtained at LP6 is ∼30% lower than values obtained for the COS-Halos data which was observed at LP2. G185M spectra (LP1) consist of three 35 Å stripes separated by two 64 Å gaps with an R ∼18,000 and typical spectral dispersion of 33 mÅ per pixel (0.2 Å per six-pixel resolution element).

Both the G160M and G185M spectra are Nyquist sampled. For G160M we binned to Nyquist sampling with 2 bins per resolution element. The spectra for G185M, which are slightly lower resolution, are well sampled and did not require binning. The resulting science-grade spectra are characterized by a FWHM $\approx$ 16 km s^{-1} and $\approx$ 38 km s^{-1} for G160M and

[1]For information regarding the sample selection of the COS-Halos survey, we refer the reader to §2.1 of Tumlinson et al. (2013).

G185M data, respectively. We perform continuum fitting with the `linetools` package[2], an open-source code for analysis of 1D spectra.

2.1.2 COS-Halos

The quasar spectra for the COS-Halos survey were taken using the G130M and G160M grating on the Cosmic Origins Spectrograph (COS; Froning & Green, 2009; Green et al., 2012) on the Hubble Space Telescope as a part of the Large Cycle 17 HST Program (PID#11598). The data reduction and analysis was initially performed and outlined in Tumlinson et al. (2013); Werk et al. (2013). We outline their process as follows: They used the FUV channel detectors in TAGFLASH model and tuned the central wavelengths (CENWAVEs) to avoid placing the 14 Å gap between FUV detector segments at the position of OVI for the targeted galaxies. This is based on the reshift of the system and was done to ensure that O VI would be covered at the short wavelength end of the G130M setting.

The COS data was uniformly processed by CALCOS (v2.12) with standard parameters and reference files. Tumlinson et al. (2013) performed thier own co-additions to merge the exposures obtained with different CENWAVEs and the two gratings. This procedure operaties on the gross cross vectors stored in the CALCOS x1D output files, and tracks the count rates in each raw pixe; each COS resolution element at R $\sim$ 18,000 covers $\simeq$ 16 km s^{-1} and is sampled by six raw pixels. Exposures taken at the same grating and CENWAVE were added first. This coadd was then summed with exposures in the same grating at different CENWAVEs, followed by a sum of the two grating spectra to produce a single 1D trace from 1150-1800 Å. The resulting 1D, flat-corrected summed spectra were then binned by 3 raw pixels to give final science-grade spectra with $\sim$2 bins and S/N $\sim$ 10-12 per COS resolution element (FWHM $\approx$ 18 km s^{-1}).

Ion	$\log_{10}N$ (cm^{-2})	$\sigma(N)$ (cm^{-2})	$\log_{10}N_{\rm AODM}$ (cm^{-2})	$\sigma(N_{\rm ADOM})$ (cm^{-2})
(1)	(2)	(3)	(4)	(5)
J0226+0015_268_22				
C IV	<13.13		<13.13	
N V	<13.24		<13.24	
O VI	<13.53		<13.53	
J0401-0540_67_24				
Si III	12.91	0.06	12.91	0.06
C III	13.72	0.43	>14.00	
C III	13.97	0.15	>14.00	
C IV	>14.06		>14.26	
C IV	>13.82		>14.26	
N V	<13.40		<13.40	
O VI	14.25	0.10	14.52	0.02
O VI	14.25	0.08	14.52	0.02

[2]https://github.com/linetools

Table continued from previous page

Ion	$\log_{10}N$ (cm^{-2})	$\sigma(N)$ (cm^{-2})	$\log_{10}N_{ADOM}$ (cm^{-2})	$\sigma(N_{ADOM})$ (cm^{-2})
(1)	(2)	(3)	(4)	(5)
J0910+1014_34_46				
Si III	13.42	0.15	>13.28	
Si III	12.39	0.31	>13.28	
C IV	14.16	0.05	14.10	0.09
C IV	13.29	0.17	14.10	0.09
N V	<12.98		<12.98	
O VI	14.66	0.09	>14.56	
J0950+4831_177_27				
Si III	13.78	0.05	>13.73	
Si III	12.50	0.14	>13.73	
C III	17.59	0.14	>14.43	
C III	13.26	0.28	>14.43	
C III	13.26	0.15	>14.43	
C IV	>14.22		>14.22	
N V	<13.66		<13.66	
O VI	14.26	0.04	14.24	0.05 0
J1016+4706_274_6				
Si III	15.83	0.35	>13.87	
Si III	13.31	0.15	>13.87	
Si III	13.36	0.10	>13.87	
Si III	12.74	0.11	>13.87	
C III	14.62	0.15	>14.58	
C III	15.70	5.70	>14.58	
C III	14.05	0.26	>14.58	
C IV	>14.23		>14.48	
C IV	>14.13		>14.48	
N V	<13.62		<13.62	
O VI	14.36	0.05	14.87	0.02
O VI	14.78	0.03	14.87	0.02
J1016+4706_359_16				
Si III	13.32	0.06	>13.74	
Si III	13.21	0.05	>13.74	
Si III	13.52	0.75	>13.74	
C IV	>14.66		>14.66	
N V	13.89	0.06	14.17	0.05
N V	13.68	0.09	14.17	0.05
O VI	14.68	0.03	14.63	0.03
J1342-0053_157_10				
C IV	<13.71		<13.71	
N V	<13.67		<13.67	

Table continued from previous page

Ion	$\log_{10}N$ (cm^{-2})	$\sigma(N)$ (cm^{-2})	$\log_{10}N_{ADOM}$ (cm^{-2})	$\sigma(N_{ADOM})$ (cm^{-2})
(1)	(2)	(3)	(4)	(5)
O VI	14.60		14.60	0.02
J1342-0053_77_10				
C IV	<12.87		<12.87	
N V	<12.8		<12.8	
O VI	<14.56		<14.56	
J1419+4207_132_30				
Si III	12.21	0.21	>13.29	
Si III	13.29	0.04	>13.29	
C III	14.23	0.1	>14.11	
C III	13.23	0.29	>14.11	
C IV	>14.38		>14.52	
C IV	>13.95		>14.52	
N V	<13.50		<13.50	
O VI	13.79	0.22	14.44	0.07
O VI	14.34	0.08	14.44	0.07
J1619+3342_113_40				
Si IV	13.14	0.06	13.19	0.08
C IV	13.02	0.15	13.90	0.03
C IV	13.80	0.03	13.90	0.03
N V	<13.21		<13.21	
O VI	14.21	0.03	14.19	0.04

Extended Table 4.1: Compiled Metal-line Profile Fit Column Densities. Comments on columns: (1) metal ion name; (2) log column density of the fitted component and (3) associated error; (4) the AODM column density and (5) associated error for reference.

Ion	b_D (km s^{-1})	$\sigma(b_D)$ (km s^{-1})	Δv_{sys} (km s^{-1})	$\sigma(\Delta v_{sys})$ (km s^{-1})
(1)	(2)	(3)	(4)	(5)
J0226+0015_268_22				
C IV				
N V				
O VI				
J0401-0540_67_24				
Si III	42.00	7.7.0	-57.3	5.20
C III	12.70	8.10	-65.20	5.80
C III	25.10	7.50	-13.90	6.30

Table continued from previous page

Ion	b_D (km s^{-1})	$\sigma(b_D)$ (km s^{-1})	Δv_{sys} (km s^{-1})	$\sigma(\Delta v_{sys})$ (km s^{-1})
(1)	(2)	(3)	(4)	(5)
C IV	8.50	5.81	-82.06	3.77
C IV	25.98	12.73	-17.85	8.54
N V				
O VI	33.30	7.70	-59.30	6.80
O VI	27.90	6.00	6.00	5.50
J0910+1014_34_46				
Si III	23.30	6.70	-109.50	3.80
Si III	17.40	22.80	-47.20	14.40
C IV	20.70	2.60	-97.20	1.80
C IV	23.70	13.90	-28.70	8.00
N V				
O VI	100.00	22.30	-105.30	17.20
J0950+4831_177_27				
Si III	47.60	3.20	-93.80	2.20
Si III	32.00	14.90	-295.50	9.60
C III	20.80	1.50	-90.20	2.80
C III	9.70	8.80	-195.90	3.80
C III	17.20	9.60	16.00	5.20
C IV	33.37	4.54	-89.97	3.32
N V				
O VI	52.90	5.70	-44.40	3.90
J1016+4706_274_6				
Si III	10.60	3.10	30.80	6.50
Si III	31.90	17.20	101.20	6.80
Si III	22.90	6.80	170.50	5.20
Si III	18.00	7.20	248.00	4.60
C III	11.40	35.80	31.40	109.90
C III	39.70	82.60	127.70	127.80
C III	28.40	8.40	250.20	12.60
C IV	60.00	30.75	50.04	30.58
C IV	51.80	40.92	190.46	27.50
N V				
O VI	24.30	3.80	38.40	2.30
O VI	174.70	10.60	168.40	9.50
J1016+4706_359_16				
Si III	38.70	7.20	-129.20	5.90
Si III	34.00	-0.0	-4.40	3.70
Si III	12.50	7.90	-68.30	2.50
C IV	85.00	9.92	-119.07	6.75
N V	27.80	5.50	-67.90	3.60

Table continued from previous page

Ion	b_D (km s^{-1})	$\sigma(b_D)$ (km s^{-1})	$\Delta v_{\rm sys}$ (km s^{-1})	$\sigma(\Delta v_{\rm sys})$ (km s^{-1})
(1)	(2)	(3)	(4)	(5)
N V	37.20	11.80	-162.30	7.20
O VI	72.00	5.10	-77.60	3.70
J1342-0053_157_10				
C IV				
N V				
O VI	122.20	7.10	55.20	5.20
J1342-0053_77_10				
C IV				
N V				
O VI				
J1419+4207_132_30				
Si III	9.90	11.90	8.20	5.90
Si III	35.40	3.60	-106.70	2.40
C III	56.80	11.30	-81.80	7.70
C III	61.00	-0.0	49.70	46.20
C IV	20.85	9.24	-114.35	4.71
C IV	75.00	52.14	-25.64	47.75
N V				
O VI	22.70	19.60	-6.90	12.00
O VI	27.70	7.80	-100.00	4.90
J1619+3342_113_40				
Si IV	16.80	4.00	1.40	2.60
C IV	9.10	4.90	-78.50	2.60
C IV	21.70	2.00	-16.80	1.40
N V				
O VI	51.80	5.50	-9.60	3.70

Extended Table 4.2: Compiled Metal-line Profile Fit Kinematics. Comments on columns: (1) metal ion name; (2) component Doppler width and (3) associated error. We note that two of the component Doppler parameter errors of especially weak absorption lines are given as -0.0, a red flag that the fits should not be trusted in those particular instances; (4) component velocity and (5) associated error.

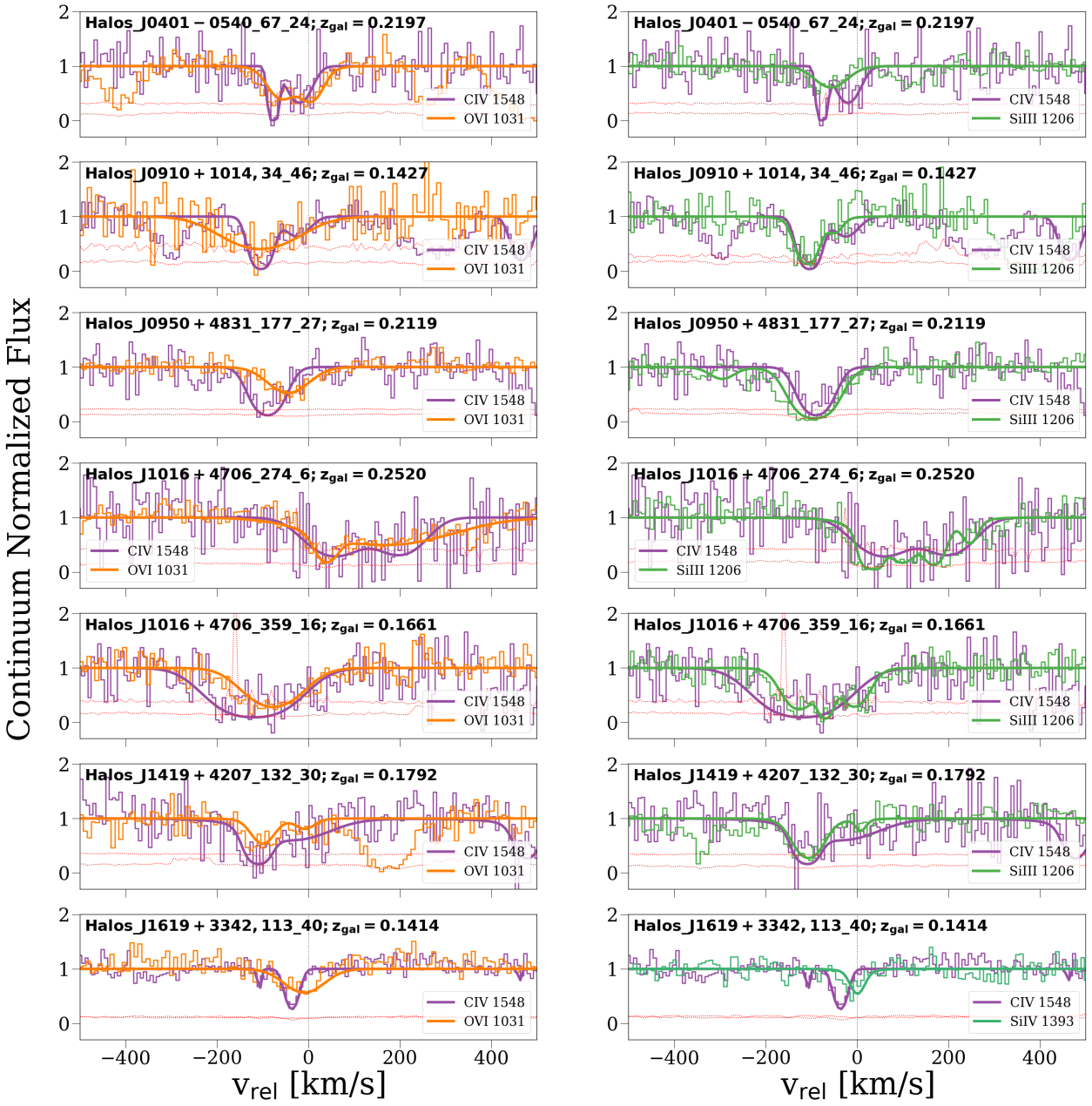

Figure 4.1: Left Panel: HST/COS continuum spectrum showing the C IV λ 1548 line (CIViL*) and O VI λ 1031 (COS-Halos) absorption features of the QSO-galaxy pairs and the set in the rest frame of each individual galaxy. **Right Panel**: HST/COS continuum spectrum showing the C IV λ 1548 line (CIViL*) and Si III λ 1206 (COS-Halos) absorption features of the QSO-galaxy pairs and the set in the rest frame of each individual galaxy. QSO-galaxy pair J1619+3342, 113_40 did not have any Si III detection so we compare C IV to Si IV instead. The red line in each spectrum represents the continuum flux error. Despite overall correspondence between the velocity ranges the absorption features are detected, we see differences between the component structure of C IV; in some lines of sight there are impressive alignments in the component structure while others have some misalignment.

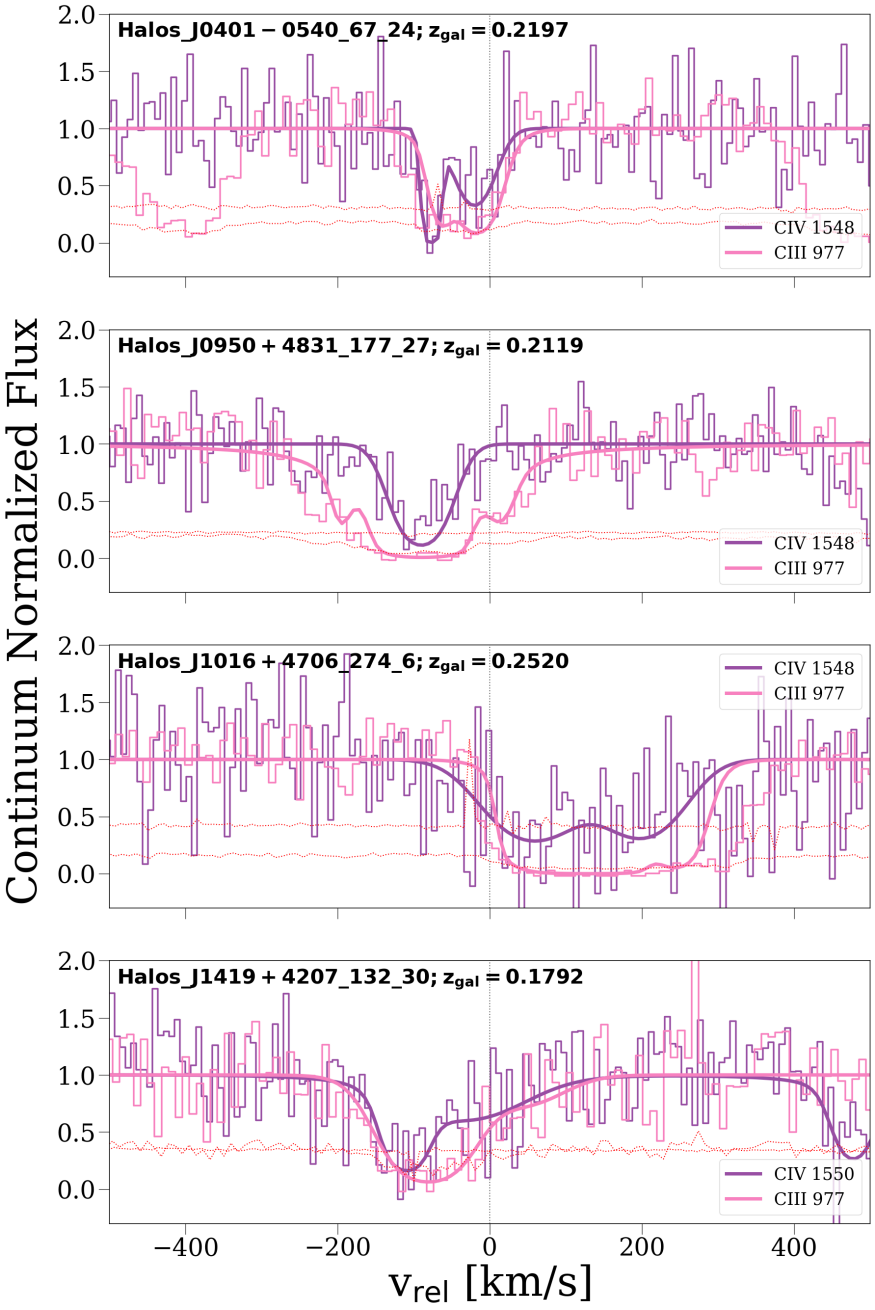

Figure 4.2: HST/COS continuum spectrum showing the C IV λ 1548 line (CIViL*) and C III λ 977 (COS-Halos) absorption features of the QSO-galaxy pairs and the set in the rest frame of each individual galaxy. The red line in each spectrum represents the continuum flux error. We note that the absorption features for C III are particularly saturated and result in high column density measurements. Specifically for J0950+4831_177_27 this results in a $\log_{10}N_{CIII}$ value of 17.59 (as published in Werk et al., 2013). We include this value in Extended Table 4.1 but exclude it from Figure 4.5 as it is the consequence of the Voigt profile having difficulty taking into account the incredibly high saturation. Similar to Figure 4.1 we see good correspondence over the velocity ranges of absorption, however, just like Werk et al. (2016), we see that some lines of sight have strong-ion absorption, but no low-ion absorption.

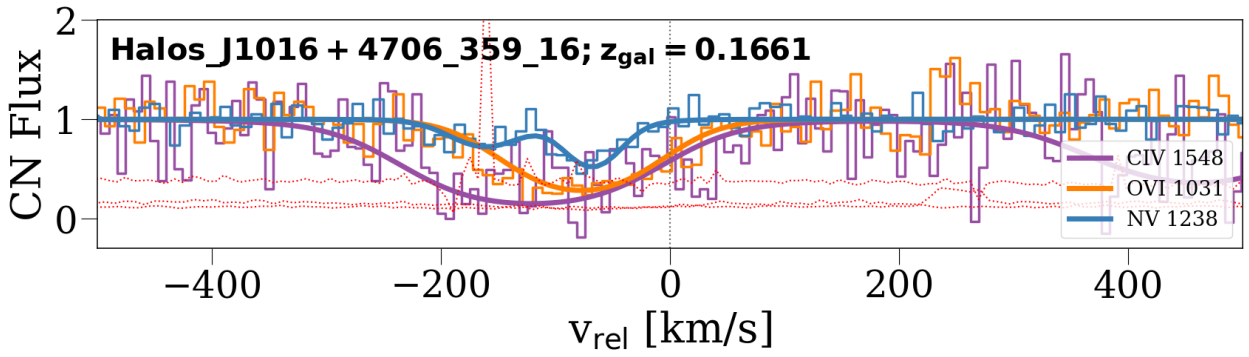

Figure 4.3: HST/COS continuum normalized (CN) spectrum showing the C IV λ 1548 line (CIViL*), O VI λ 1031 (COS-Halos), and N V λ 1238 absorption features of QSO-galaxy pair J1016+4706_359_16 et in the rest frame of the galaxy. The red line in each spectrum represents the continuum flux error. For our sample, this is the only line of sight that has a detection feature for these three ions.

3 Gas Kinematics

In this section, we present the kinematics for the observed C IV absorption from the CIViL* survey and compare these kinematics to those from other ions. We obtained the C IV column densities and kinematics by Voigt profile fitting (for a more detailed description of this process see Garza et al., 2025). We also discuss whether these observed absorptions are consistent with being bound to the dark matter halo of the host galaxy and compare them to a simple model of radiatively cooling gas §4.3.

3.1 Profile Fitting

Garza et al. (2025) summarizes the CIViL* Voigt profile fitting procedure for C IV. We briefly repeat the relevant details. The procedure used to preform fits and derive the column density N, Doppler b_D parameter, and the velocity offset Δv_{sys} for each component utilizes the Voigt profile fitting package `veeper`[3]. This package uses `scipy.optimize.least_squares`[4] to perform a least squares minimization to obtain its measurements and incorporates the COS line spread function. We adopt a < 15 km s^{-1} wavelength calibration error for the COS wavelength solution and note that the spectral dispersion for the G185M grating is on average 80.3 mÅ or 0.482 Å resel^{-1}, where one "resel" (or resolution element) is defined as 6 pixels (James et al., 2022). Similar to Werk et al. (2012), we highlight that there is $\pm$25 km s^{-1} systematic error directly from the target galaxy redshift.

Similarly for the COS-Halos data, the Voigt profile fitting and qualitative assessment of the spectra is described in Tumlinson et al. (2011), Werk et al. (2013), and Tumlinson et al. (2013), however we repeat the necessary details. The COS-Halos team created a procedure to complete the fits and derive N, b_D and Δv_{sys} for each component utilizes the iterative

[3]https://github.com/jnburchett/veeper
[4]https://github.com/scipy/scipy

Sightline	Si III	Si IV	C III	C IV	N V	O VI
J0226+0015_268_22	0	0	0	0	0	0
J0401-0540_67_24	1	0	2	2	0	2
J0910+1014_34_46	2	0	0	2	0	1
J0950+4831_177_27	2	1	3	1	0	1
J1016+4706_274_6	4	0	3	2	0	2
J1016+4706_359_16	3	0	0	1	2	1
J1342-0053_157_10	2	3	1	0	0	1
J1342-0053_77_10	0	0	0	0	0	0
J1419+4207_132_30	2	0	2	2	0	2
J1619+3342_113_40	0	1	0	2	0	1

Figure 4.4: Visual representation of number of the components for each ion per sightline. The number of components are colored as follows: non-detections are in grey, a singular component is colored red, two components are shown in orange, three components are colored light green, and four components is colored in dark green. We find that for 70% of the sample C IV has the same number of components as O VI. For 40% of the sample C IV has the same number of components as Si III and C III.

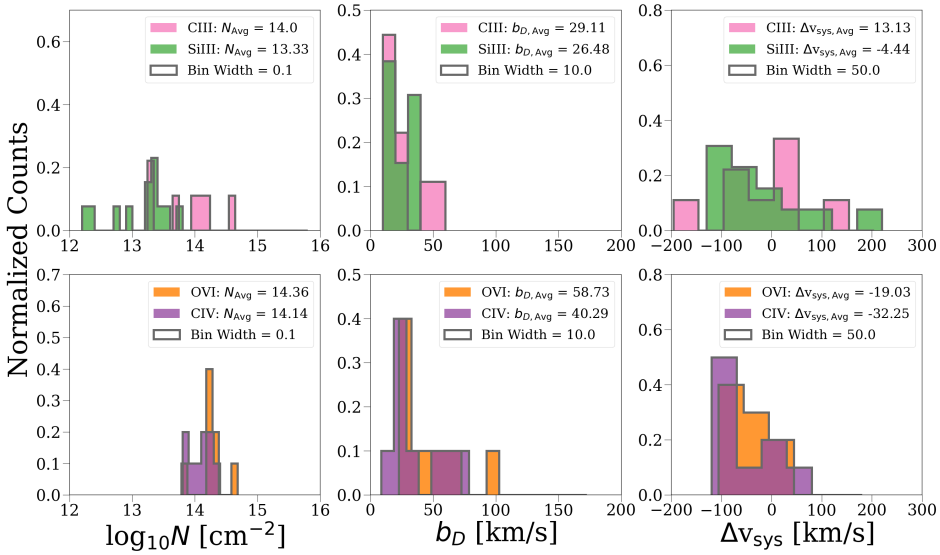

Figure 4.5: Histograms of CIViL* column density (N), Doppler parameter (b_D), and Δv_{sys} (the difference between the galaxy systemic redshift and the component velocity centroid) for Si III (green) and C III (pink) in the upper panels and C IV (purple) and O VI (orange) in the lower panels. We note that for the column densities (left panels), 72% of the observations are saturated and are thus lower limits. We also note that the *highly* saturated C III component observation (noted in Figure 4.2 and listed in Extended Table 4.1) is not included in the upper left panel.

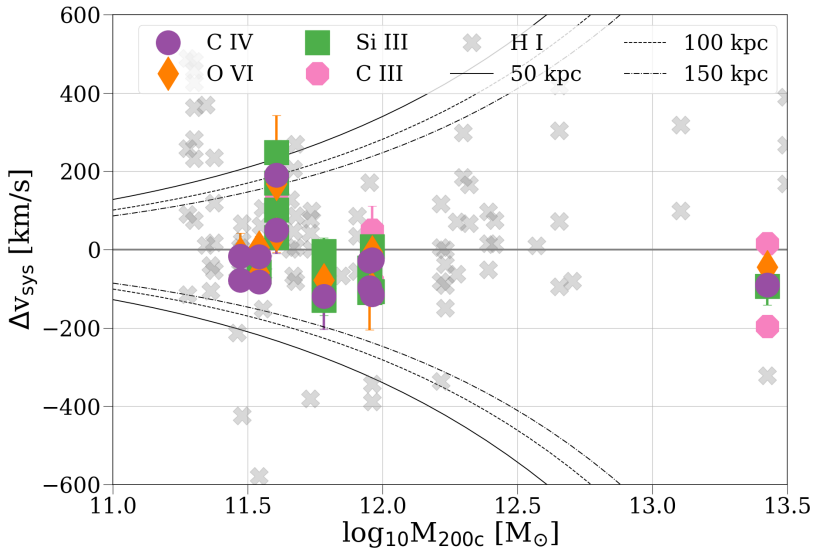

Figure 4.6: The difference between the galaxy systemic redshift (the assumed "rest" frame) and the velocity centroids as a function of virial halo mass (M_{200c}) for C IV (circles), O VI (diamonds), Si III (squares), C III (hexagons), and H I (x's) for each Voigt profile fitted component. The various curved lines show the mass-dependent escape velocities at R_{proj} = 50, 100, and 150 kpc. We find that most of the component ion velocities do not exceed the escape velocities of the galaxies. Therefore, we conclude that most of the ions, but especially C IV and O VI are bound to the dark matter halos of their host galaxies.

fitting program that uses the MPFIT software[5]. They adopt a $\pm$10 km s^{-1} as the systemic uncertainty associated with the first-order and higher terms of the COS wavelength solution[6]. When they examine the velocity centroids relative to the galaxy systemic redshift (where the typical systemic uncertainty is $\sim$25 km s^{-1}, Werk et al., 2012), the root-square-sum gives a total error in the component velocity centroids of $\pm$30 km s^{-1}. We summarize the results of the Voigt profile fitting from Garza et al. (2025) and Werk et al. (2013) for C IV versus key low and intermediate ions in Extended Table 4.1 and 4.2.

3.2 Quantitative Comparison of C IV Kinematics to other Ions

In Figure 4.1, 4.2, and 4.3 we compare C IV spectra and fits to O VI (left panel of Figure 4.1), Si III (right panel of Figure 4.1, one of the most commonly detected metal species in the COS-Halos data set), C III (Figure 4.2, a lower ionized version of C IV), and show the only line of sight in our sample that has C IV, O VI, and N V detection (Figure 4.3). We note that these Figures are presenting already published Voigt profiles and are *not* refitting the data; we tabulate previously published fitting parameters for COS-Halos lines of sight along side those of CIViL* for each component in Extended Table 4.1 and 4.2. We find that in 70% of the QSO-Galaxy pairs in our sample, C IV has the same number of components as O VI; for the other two ions, Si III and C III, which are lower ionization ions, we find that C IV has the same number of components 40% of the time. We show a visual representation of these component comparisons in Figure 4.4. The number of components are colored as follows: non-detections are in grey, a singular component is colored red, two components are shown in orange, three components are colored green, and four components is colored in yellow. We find that for 70% of the sample C IV has the same number of components as O VI. For 40% of the sample C IV has the same number of components as Si III and C III.

In Figures 4.1, 4.2, and 4.3 we confirm the result from Werk et al. (2013, 2016) that there is generally good correspondence between velocity ranges over which absorption is detected among the systems that exhibit strong O VI, and expand upon this statement to now include C IV absorption. A key finding of the kinematic comparisons in Werk et al. (2016), is the relationship between low and high ionization states of gas along the same COS-Halos sightlines is not straightforward since these relationships can vary substantially on a sightline-to-sightline basis. Adding C IV to the mix, doesn't change this previous finding as we also see a variety in the kinematic alignment of the ions observed in our sample. Some sightlines have impressive alignments in component structure, some have misalignment (e.g. saturation, different number of components, etc), and some sightlines have strong high-ion absorption but no low-ion absorption present.

Figure 4.5 empirically summarizes the results from the Voigt profiles presented in Figures 4.1 and 4.2 As we are plotting the properties of each component structure for each ion, the sample sizes for each ion are as follows: 9 total components for C III, 13 total components for Si III, 10 total components for C IV, and 10 total components for O VI. The column densities (N - left panel), Doppler parameters (b_D - middle panel) and the difference between the

[5]https://github.com/segasai/astrolibpy/tree/master/mpfit

[6]This systematic uncertainty also trickles down to the relative component velocity centroids and fitted b_D values. For more information on these uncertainties and other sample error budgets, see Table 3 in Tumlinson et al. (2013)

galaxy systemic redshift and the velocity centroids of each component (Δv_{sys} - right panel) are represented as histograms for the low ions (Si III and C III) in the upper panels and the intermediate ions (C IV, and O VI) in the lower panels. The histograms are normalized so that the sum of the counts is one; this is analogous to a probability mass function for a discrete variable where the sum of probabilities for all the values equals one. This way we can compare our distributions of ion components even though they have different sized populations.

One main takeaway from comparing the distributions in this manner, is that the C IV and O VI distributions look very similar across all three panels. Using `scipy.stats.anderson_ksamp`[7], we perform an Anderson-Darling test for k-samples[8] to compare the column densities, Doppler parameters and change in velocities of C IV and O VI. For this test we treat each component as if it were a detection (i.e., not taking into account lower limits or saturation); the Anderson-Darling test is useful when not taking into account known limits since the test is designed to examine the tails of distributions which makes it particularly sensitive to deviations in extreme values. First looking at the column densities, we find that we can reject the null hypothesis that these two samples were drawn from the same distribution at a 75-95% confidence level, but cannot reject the null hypothesis at $\geq$ 97.5% confidence levels (p = 0.046). For both the Doppler parameter and Δv_{sys} comparisons, we find that we cannot reject the null hypothesis that they are from the same parent distribution at all confidence levels (75-99.9%) with p-values of 0.25 for both comparisons. So for high levels of statistical significance, it is likely that the components comprising the C IV and O VI samples are drawn from the same parent distribution. This result, coupled with the established star-forming and passive dichotomy for C IV (Garza et al., 2024) and O VI (Tumlinson et al., 2011; Tchernyshyov et al., 2023) and kinematic alignment, suggest that there may be a physical connection between these two ions.

Figure 4.6 shows the velocity centroids for each Voigt profile fitted component for all the ions shown in Figure 4.1 and 4.2 as a function of the virial halo mass. In the background is H I data from Tumlinson et al. (2013). In the COS-Halos survey (Tumlinson et al., 2013; Werk et al., 2013), H I absorption is almost always associated with O VI absorbers; by studying their kinematics, Tumlinson et al. (2013) suggested that the gas where they reside is typically cooler at $< 10^5$ K. We include H I in the background of this figure to provide the context of this cooler gas.

We compare these velocities with the escape velocities of the halos in which they reside. We follow the same methodology as Garza et al. (2024, 2025) to estimate our dark matter halo masses. For a more in depth description of this method please refer to the aforementioned publications, however we present a brief explanation here: we use the stellar-halo mass relation defined in (Behroozi et al., 2019, for fit parameters, refer to Table J1) together with the technique described in Hu & Kravtsov (2003) to estimate halo masses (M_{200c}) that are calibrated such that the average mass density within the halo radius is 200 times the critical density of the Universe.

To calculate the escape velocities as a function of halo mass, we assume a spherically

[7]https://github.com/scipy/scipy

[8]The k-sample Anderson-Darling test is a modification of the one-sample Anderson-Darling test. It tests the null hypothesis that k-samples are drawn from the same population without having to specify the distribution of that population.

symmetric Navarro-Frenk-White profile (Navarro et al., 1997, with concentration parameter, $c = 15$) at three different radii ($R_{\rm proj} = 50$, 100, and 150 kpc; dashed lines in Figure 4.6). We see that most of the ions except H I do not exceed the escape velocities and conclude that most of the ions, but especially C IV and O VI are bound to the dark matter halos of their host galaxies. This differs from high-z galaxies ($z > 6$), where low ions, such as Mg II, have been found to not be bound to the dark matter halos of the host galaxies (Bordoloi et al., 2024).

4 Physical Conditions

The combination of the CIViL* survey with previous work provides us with a range of ions: C IV, N V, and O VI. The ionization energies for the formation of these ions are 47.9, 77.5, and 113.9 eV respectively, and in collisional ionization (CI), they trace gas at similar temperatures of $1-3\times10^5$ K, probing the warm/hot CGM. However, species at intermediate ionization potentials, such as C IV and O VI, sometimes show a preference for PI and CI or have contributions from both (Tumlinson et al., 2017). It is also important to note that, historically, the kinematics of intermediate ions are often found to be more similar to low-ions than to high-ions (e.g., Burchett et al., 2015). These previous notions are now in slight contestation with the recent results from the CIViL* survey (Garza et al., 2025) and the kinematics results of this publication. Motivated by these results, in this section we compare the column densities of these ions to two different ionization models to estimate the physical properties, i.e. gas temperature and density, in the multiphase CGM. The column densities used in this section are listed in Extended Table 4.1 for individual component values for each QSO-Galaxy pair and their ratios are shown in Figure 4.7.

4.1 C IV, O VI, N V Ratios vs Galaxy Properties

As shown in §3, C IV and O VI are kinematically coincident. This additional connection in combination with the dichotomous relationship both these ions have with star forming and passive galaxies (Tumlinson et al., 2011; Garza et al., 2025) suggest that they might be forming under the same gas conditions. To explore these connections, we use the relationship between the C IV/O VI and N V/O VI ratio as a diagnostic tool (Fox et al., 2004; Indebetouw & Shull, 2004).

To directly compare the absorption profile characteristics of C IV to O VI and other metal ions (e.g. Si III and C III), we use the method derived in Werk et al. (2016). This method was used to match O VI components with those of low- and intermediate-ionization state species using their best fitting velocity centroids from their Voigt profile analysis. A main part of this method is that two distinct components of the element for which other ions are being compared to (i.e. C IV for this study) cannot have the same matching low or intermediate-ion component. The component with the best matching velocity centroid wins; the other component(s) is typically left unmatched. The benefit of this simple matching technique is it quickly quantifies a general relationship between ions of different ionization. A disadvantage of this method is it is possible that absorbers could be matched with an absorber that happens to lie at a similar velocity but is not physically associated.

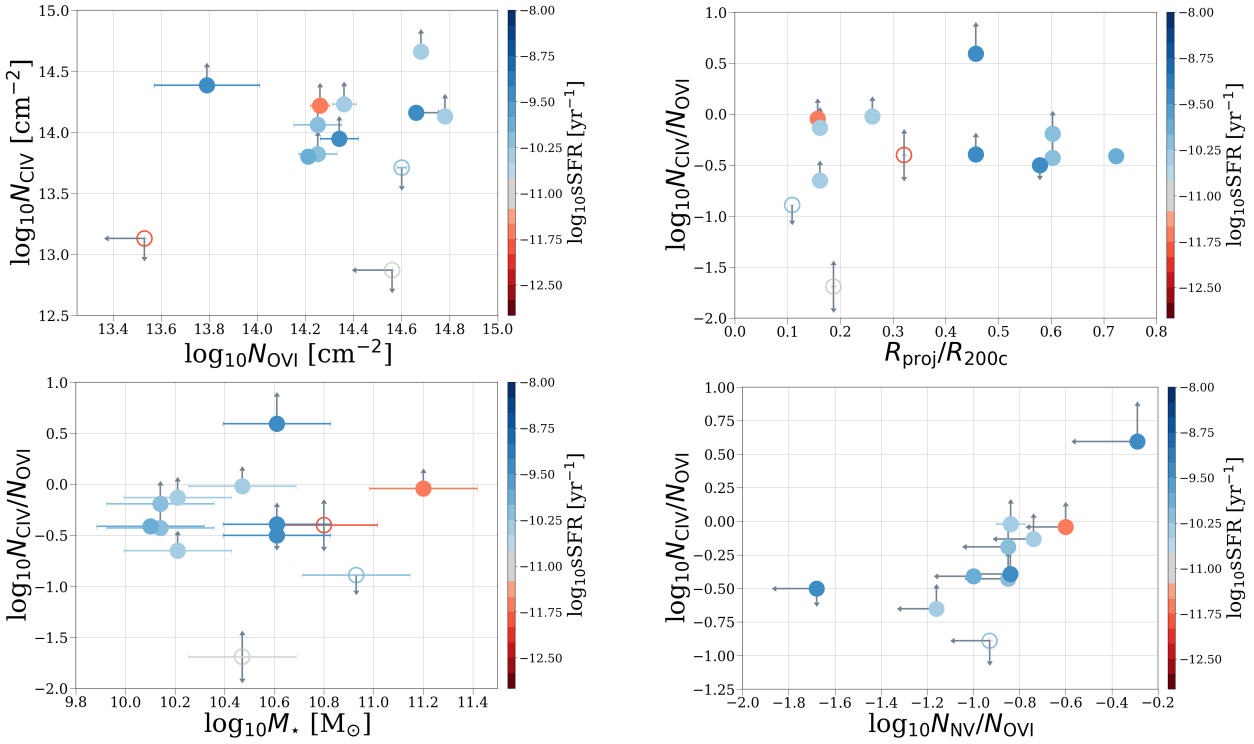

Figure 4.7: Column density C IV, O VI, and N V ratios colored by the specific star formation rate. **Top Left Panel**: C IV column density vs O VI column density. **Top Right Panel**: The ratio of C IV column density and O VI column density as a function of impact parameter normalized by the viral radius ($R_{\rm proj}/R_{\rm 200c}$). **Bottom Left Panel**: $N_{\rm CIV/OVI}$ as a function of stellar mass. **Bottom Right Panel**: $N_{\rm CIV/OVI}$ vs the ratio of N V column density and O VI column density ($N_{\rm NV/OVI}$). These empirical plots showcase the ratios we use to understand the gas properties through Cloudy modeling in §4.2. We note that the open circles denote that the top column density or column density ratio value is unconstrained via an upper limit value.

Figure 4.7 shows these matched component ratios for the QSO-galaxy pairs listed in Table 4.1 and how they compare to galaxy properties. In the upper left panel, ($N_{\rm C\ IV}$ vs. $N_{\rm O\ VI}$) we see that C IV and O VI have similar column densities values, with an average 13.9 and 14.5 cm^{-2} of respectively. This translates into $N_{\rm C\ IV}/N_{\rm O\ VI}$ ratio values that are fairly consistent across the range of both normalized impact parameter ($R_{\rm proj}/R_{\rm 200c}$ = 0-0.8, upper right panel) and stellar mass ($\log_{10}M_\star$ = 9.8-11.4, lower left panel) with an average value of $\sim$ -0.4. The lower right panel shows the relationship between $N_{\rm C\ IV}/N_{\rm O\ VI}$ and $N_{\rm N\ V}/N_{\rm O\ VI}$. The common denominator ($N_{\rm O\ VI}$) for both ratios, the similar column density values for both C IV and O VI, and the saturation of C IV combined with many non-detections of N V make it challenging to evaluate any statistical significance. These empirical plots showcase the column density values and resulting ratios we use throughout the rest of this section to investigate the physical properties of the gas.

4.2 Gas properties from column density ratios

The measured ratios of column densities of different ions can be used to constrain the underlying properties of the gas these ions trace. For example, in collisional ionization, C IV, N V, and O VI are all very sensitive to the gas temperature. Similarly, in the photoionized regime, the ion fractions are functions of the gas density. We now use Cloudy models to examine what the measured column densities of these ions and their ratios reveal about the underlying gas properties. Our main result is that for most of the objects in our sample, the three ions cannot form in the same gas phase, requiring multiphase CGM. However, it is important to note that the observed ratios we report are based on individual component structures. Due to the medium resolution of *HST/COS* we can only resolve spectroscopic structures >10 km s^{-1}. Therefore we may not be capturing any component structures less than this kinematic window. In this section we examine simple models, with constant density and temperature gas. In Section 5 we address possible caveats to our result and mention briefly some more detailed and sophisticated models, which are beyond the scope of this study and will be addressed in future work.

4.2.1 General case

For constant density and temperature gas, the column of ion i of element X can be written as $N_{X,i} = n_H A_X Z f_i L$, where n_H is the hydrogen density, A_X is the elemental abundance, Z is the metallicity relative to solar, f_i is the ion fraction, and L is the pathlength along the line of sight. Assuming the column densities of two ions of different elements form in the same phase (with some density, temperature, and metallicity), their ratio is then given by $N_{X,i}/N_{Y,j} = A_X f_i / A_Y f_j$. We use the solar elemental abundances from Asplund et al. (2009), and calculate the ion fractions for a wide range of densities and temperatures using Cloudy 17 (Ferland et al., 2017), assuming the fiducial, $z = 0.2$ metagalactic radiation field (MGRF) from Khaire & Srianand (2019)[9] and optically thin gas. The resulting theoretical

[9]In this work, we ignore the contribution of the galaxy to the total ionizing flux. Faerman & Werk (2023) estimate that for the COS-Halos galaxies SFR and redshift, the galactic radiation field is sub-dominant at $r/R_{\rm vir} \geq 0.1$ (see their section 6.2.2), and all the objects in our sample are at larger projected distances.

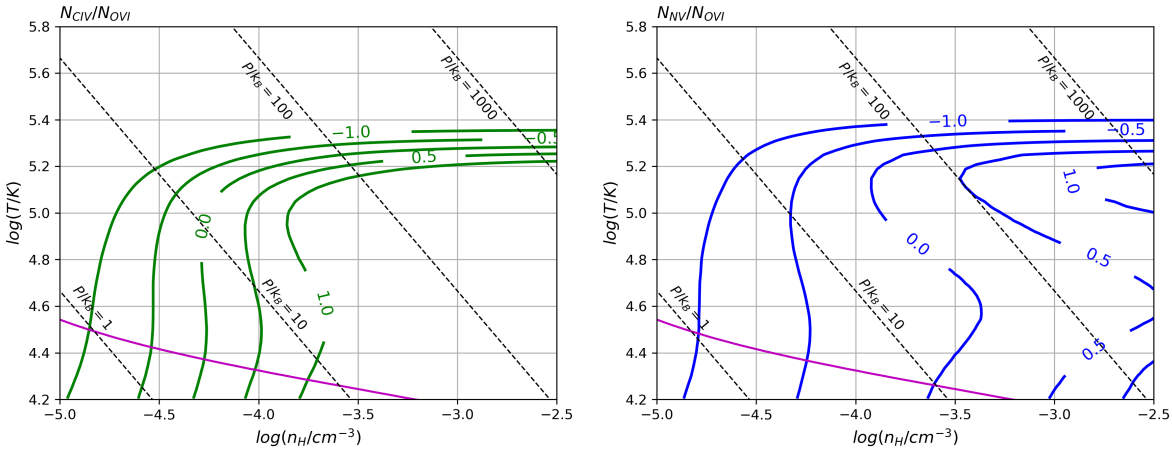

Figure 4.8: Column density ratios in the gas temperature-density parameter space, for $N_{\rm C\ IV}/N_{\rm O\ VI}$ (left) and $N_{\rm N\ V}/N_{\rm O\ VI}$ (right). The thick solid contours indicate fixed $\log_{10}(N_1/N_2)$ of the given quantity along each line of sight for the range of ratios observed in the lower right panel of Figure 4.7 ($\sim$ -1.0 - 1.0), whereas the dashed contours indicate isobars of the pressure indicated. The magenta solid contour shows the gas cooling/heating equilibrium temperature as a function of density. In Figure 4.9 we plot our observations using the temperature and density constraints in these two Figure panels.

column density ratios are shown in Figure 4.8 in the density-temperature ($n-T$) parameter space by the thick solid contours for C IV/O VI (left panel) and N V/O VI (right).

The C IV/O VI ratio changes rapidly with temperature in the collisional ionization equilibrium (CIE) regime (at high densities), and more gradually as a function of density in the PI regime (at low temperatures). O VI probes gas at a higher ionization than C IV, and the C IV/O VI ratio increases toward lower temperatures and higher gas densities. The N V/O VI ratio (right panel) behaves similarly. In this work we adopt the KS19 MGRF, and verify that using the Haardt & Madau (2012) field has a negligible effect on our results.

In addition to the column density ratios, the thin dashed black contours in the figure show constant pressure curves, ranging from $P/k_B \sim 1000$ K cm^{-3}, expected in the central regions of galactic halos, to $\sim 1-10$ K cm^{-3}, at their outskirts. Finally, the magenta thick curve shows the gas cooling/heating equilibrium temperature, T_{eq}, as a function of the gas density. T_{eq} is also a function of the gas metallicity, and is calculated here for $Z = 0.3$ solar.

4.2.2 Can single-phase CGM reproduce the observed column ratios?

Using the ratios shown in Figure 4.8 we now test the simplest scenario in which the three ions originate in the same gas phase. We do this by comparing the ratios given by the measured column densities for each of the objects in our sample to the model ratios.

First, in the left panel of Figure 4.9, we plot the model predictions (curves), which show the ratios as functions of temperature for a few constant densities (i.e. vertical slices from Figure 4.8). The solid curve shows the ratios for CIE (at high densities), whereas the dashed, dashed-dotted and dotted curves are for densities of $n_{\rm H} = 10^{-4}$, 3×10^{-5}, and 10^{-5} cm^{-3}, respectively, and include the effects of photoionization. Comparing these curves to the

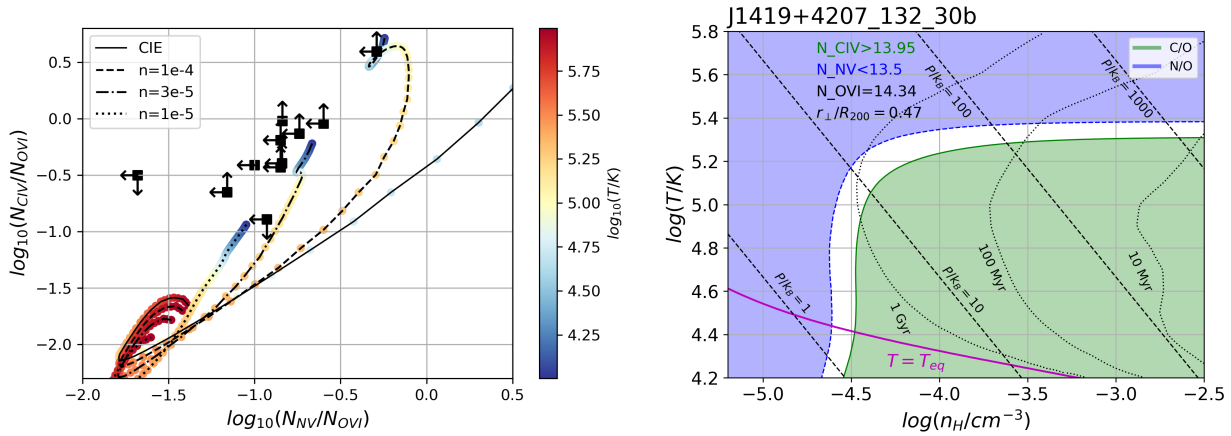

Figure 4.9: Left: Column density ratios, $N_{\rm C\ IV}/N_{\rm O\ VI}$ vs $N_{\rm N\ V}/N_{\rm O\ VI}$ - comparison of observations (markers) and ionization models (curves). The curves are shown for CIE (solid) and a few gas densities (dashed, dot-dashed, and dotted). The color along the curve shows the gas temperature, from 10^6 K (red) to 10^4 K (blue). **Right:** Gas density and temperature constraints for a specific object, with limits on both N V and C IV. The gap between the regions allowed by each ratio suggests that the three ions cannot form in the same phase. Black dashed curves show the gas pressure, and dotted - cooling time (for $Z = 0.3$).

observed ratios (markers) shows that for most objects, the measured column density ratios are inconsistent with single-phase equilibrium models. To address this in more detail, we examine individual objects and show how the measured ratios constrain the gas properties in $n-T$ space. We address the most common case in the right panel of Figure 4.9, and show examples for other scenarios in Figure 4.14 in the Appendix.

For about half the objects in our sample (7/13), $N_{\rm C\ IV}$ is saturated and $N_{\rm O\ VI}$ is measured, resulting in a lower limit on the C IV/O VI ratio. This provides an upper limit on the gas temperature and a lower limit on the density (shown by the green-shaded region in the right panel of Figure 4.9). For $N_{\rm N\ V}$ the observations provide mostly upper limits. This gives upper limits on the N V/O VI ratio and corresponds to a lower limit on the gas temperature or an upper limit on the density (blue-shaded region in the right panel of Figure 4.9). If the C IV or N V column density is measured, the result is a narrow band in $n-T$ space allowed by the column density ratio with O VI (see left panel of Figure 4.14). For most of the objects in our sample (9/13), the regions allowed by each ratio do not overlap and instead create a "zone of avoidance". This is also visible in the left panel of Figure 4.9, where most of the measured N V/O VI (C IV/O VI) column density ratios are lower (higher) than allowed by the models (curves). We discuss some additional scenarios for these cases in Section 5.

The remaining (four) objects in our sample are divided into two cases. For two lines of sight, there are upper limits on both the C IV and N V columns, resulting in allowed regions in $n-T$ space that do overlap, allowing single-phase gas for all three ions (see right panel in Figure 4.14). Finally, for two objects the combination of limits on column densities does not provide useful constraints on the ratios, and we do not show them here.

We note that an upper limit on $N_{\rm C\ IV}$ or $N_{\rm N\ V}$ and the resulting ratios with O VI often allow gas in two regimes - cool gas at low densities, dominated by photoionization, or warm/hot

gas dominated by collisional ionization. For example, in the right panel of Figure 4.9, we can see that the N V/O VI ratio (shaded blue) allows gas in two regions, at temperatures below $\approx 2 \times 10^5$ K and densities below $\approx 10^{-4}$ cm^{-3}, or temperatures and densities above these thresholds. In the first scenario, the gas thermal pressure is low, $\lesssim 10$ K cm^{-3}, which can be indicative of gas at the outskirts of the CGM (see discussion in McQuinn & Werk, 2018), and its cooling time can be long, at least $t_{\rm cool} \gtrsim 1$ Gyr (black dotted curves), and much longer when the gas temperature is closer to T_{eq} (magenta curve). In the second scenario, the warm/hot gas has higher thermal pressures, with $P/k_B \gtrsim 100$ K cm^{-3}, more consistent with inner parts of the CGM. Since the gas density in this regime is not constrained, the cooling time can be a few Gyr or lower, scaling as n^{-1}. A lower limit for $N_{\rm C\ IV}$, on the other hand, allows gas below a given temperature and above some density (shaded green).

To summarize, we demonstrated that for most objects in our sample, the measured column density ratios of C IV, N V, and O VI are inconsistent with forming in a single gas phase. Motivated by this, we now examine a more detailed physical model allowing for gas at different temperatures.

4.3 Comparison to Cooling-Flow Model

In Figure 4.10 we explore a simple cooling flow model to investigate the origins of our C IV, N V, and O VI observations. To do this we employ the model introduced by Heckman et al. (2002) and follow the formulation presented in Bordoloi et al. (2017). We briefly describe the model in §4.3.1. We then compare the cooling flow model to our observations in §4.3.2.

4.3.1 Cooling-Flow Model Description

As described in §3.2, we find that C IV absorption-line profiles are very similar to that of O VI; this similarity between the profiles coupled with the observed dichotomy between passive and star-forming galaxies that both C IV and O VI exhibit (Garza et al., 2025) suggests some physical connection between the two ions. To investigate this hypothesis, we begin by seeing if collisional ionization processes could be the dominant producer of C IV in the inner CGM of our sample of galaxies.

It has been suggested that if an ion is collisionally ionized in radiatively cooling flows, then its total column density is proportional to the Doppler parameter, b_D, of the corresponding absorption line (e.g., Heckman et al., 2002; Lehner et al., 2011; Bordoloi et al., 2017). Following Heckman et al. (2002) and Bordoloi et al. (2017), the column density of a cooling region in a cooling flow is

$$N_{\rm cool} = n\ v_{\rm cool}\ t_{\rm cool}. \tag{4.1}$$

where $v_{\rm cool}$ is the cooling velocity, $t_{\rm cool}$ is the cooling time, and n is the hydrogen number density.

In this situation, gas cools radiatively at a temperature T and a metallicity Z,

$$t_{\rm cool} = \frac{3k_{\rm B}T}{n\Lambda(T,Z)} \tag{4.2}$$

such that the product of $nt_{\rm cool}$ will only depend on T and Z, where $k_{\rm B}$ is the Boltzmann constant and $\Lambda(T, Z)$ [erg cm^3 s^{-1}] is the cooling function. Bordoloi et al. (2017) makes the approximation that the electron density (n_e) is the same as the ion density ($n_e = n$); thus, if we combine Equations 4.1 and 4.2 we see that

$$N_{\rm cool} = \frac{3k_BT}{\Lambda(T,Z)} v_{\rm cool} \ [{\rm cm}^{-2}], \tag{4.3}$$

which shows that $N_{\rm cool}$ is independent of density for radiatively cooling gas. Equation 4.3 can also be rewritten for any specific metal ion X, and taking the ionic fraction at temperature T_X as $f_X(T)$, we can write

$$N_{X,i} = \frac{3k_BT_X}{\Lambda(T_X,Z)} v_{\rm cool} \left(\frac{X}{H}\right)_\odot Z f_X \ [{\rm cm}^{-2}]. \tag{4.4}$$

We note that a prediction of this model is that $N_{X,i}$ is proportional to $v_{\rm cool}$ and T is the only independent (but constrainable) parameter. Observationally, the temperature is not directly measured or estimated, but a limit can be inferred from the Doppler parameters, b_D-values, derived from Voigt profile fitting the absorption features.

To compare the model to observations, the cooling flow velocities need to relate to an observed physical property. It has been suggested that b_D is a function of both the thermal and non-thermal motions of the gas (e.g., Heckman et al., 2002; Lehner et al., 2011; Zheng et al., 2017; Bordoloi et al., 2017). If there is no flow, the absorption lines have a width soley due to thermal broadening ($b_{\rm th}$). However, in the case of radiatively cooling gas, the observed line width is due to a combination of thermal broadening and broadening due to cooling flow ($b_{\rm nth}$) so that $b_D^2 = b_{\rm th}^2 + b_{\rm nth}^2 = 2b_BT/m + b_{\rm nth}^2$ [km s^{-1}], where m is the atomic mass of the element. Based on these assumptions, Heckman et al. (2002) proposed that $v_{\rm cool}$ could be identified as the non-thermal broadening such that the equation can now be written as

$$b_D^2 = 2k_BT/m + v_{\rm cool}^2. \tag{4.5}$$

or put simply, $b_D \sim v_{\rm cool}$, and we can now compare a physical property to the model predictions[10]. In §4.3.2 we compare our observed linewidths and column densities to column density predictions calculated using Equation. 4.4.

4.3.2 Comparison to Observations

In Figure 4.10 we investigate how the model column density predictions from §4.3.1 compare to observed column densities for C IV, O VI, and N V from Extended Table 4.1. These column densities are plotted against v_{cool} predictions from the model and observed line widths b_D. We follow the convention of Bordoloi et al. (2017) and adjust the line width so that it contains 99.7% (3σ) of the total absorption for any absorption line profile from its Voigt profile fit:

$$b_{D,99.7} = 3b_D/\sqrt{2}. \tag{4.6}$$

[10]For a further clarification of the assumption that $b_D \sim v_{\rm cool}$, we refer the reader to §3.1 and §4 of Bordoloi et al. (2017) where they walk through a detailed analysis of the equations for this scenario.

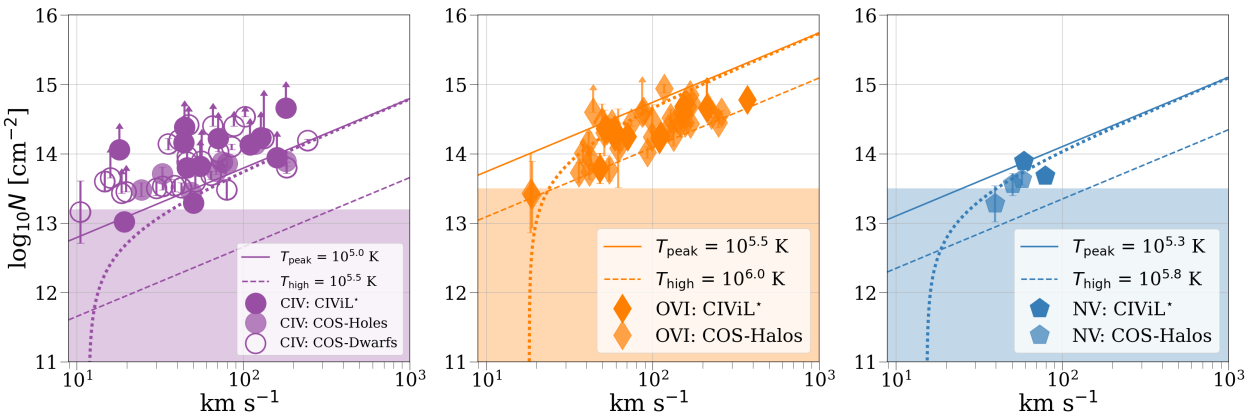

Figure 4.10: Observed C IV (left panel; purple circles), O VI (middle panel; orange diamonds), and N V (right panel) component column densities vs line widths ($b_{D,99.7}$). The x-axis corresponds to the observed line widths for the data and v_{cool} for the model predictions ($b_D \sim b_{D,99.7} \sim v_{cool}$) in km s^{-1}. We note that we only plot observations with $b_{D,99.7}$ values $\geq$ 10 km s^{-1}. The various lines show the predicted cooling-flow column densities at different temperatures assuming 0.3Z$_\odot$; the solid lines and dashed lines were calculated without thermal broadening taken into account while the dotted line takes into account thermal broadening for just the peak temperature of each ion. The horizontal line in each panel represents the average upper limit value for the ion presented in the panel with the shaded region acting as a visual representation of the possible values these upper limits could be across the range of velocities. The horizontal lines for each ion are as follows: 13.2 for C IV (Bordoloi et al., 2014; Garza et al., 2024) and 13.5 for O VI and N V (Werk et al., 2013, 2016). The cooling-flow models match the O VI and N V observations fairly well as the data lies between the cooling flow model for $T = 10^{5.5-6.0}$ K and $T = 10^{5.3-5.8}$ K for O VI and N V respectively. However, the C IV observations do not follow the cooling flow model and lie above the model predictions.

We also include C IV column density observations and line width measurements from COS-Dwarfs (Bordoloi et al., 2014, sub-L* galaxies), COS-Holes (Garza et al., 2024, L$\approx$L*) and O VI and N V observations from COS-Halos (Tumlinson et al., 2011; Werk et al., 2013, L $\approx$ L*).

The lines show the predicted cooling-flow column densities at different temperatures; the solid lines and dashed lines were calculated without thermal broadening taken into account while the dotted line takes into account thermal broadening for just the peak temperature of each ion. The ion fractions and cooling functions were calculated assuming CIE in 0.3Z$_\odot$ and are tabulated in Table 4.2. We also note that we utilize the solar abundances from Asplund et al. (2009). Both O VI and N V are consistent with the prediction of the cooling flow model within a range of typical temperatures ($T_{\rm OVI} = 10^{5.5-6.0}$ K and $T_{\rm NV} = 10^{5.3-5.8}$ K). However, the C IV columns are higher than predicted by the model. To quantify how much higher C IV is than the cooling-flow model predictions, we subtract the model column density predictions from the observations using the following equation at peak temperature:

$$\Delta \log_{10} N = \log_{10} N_{\rm obs} - \log_{10} N_{\rm model,Eq4.4}. \quad (4.7)$$

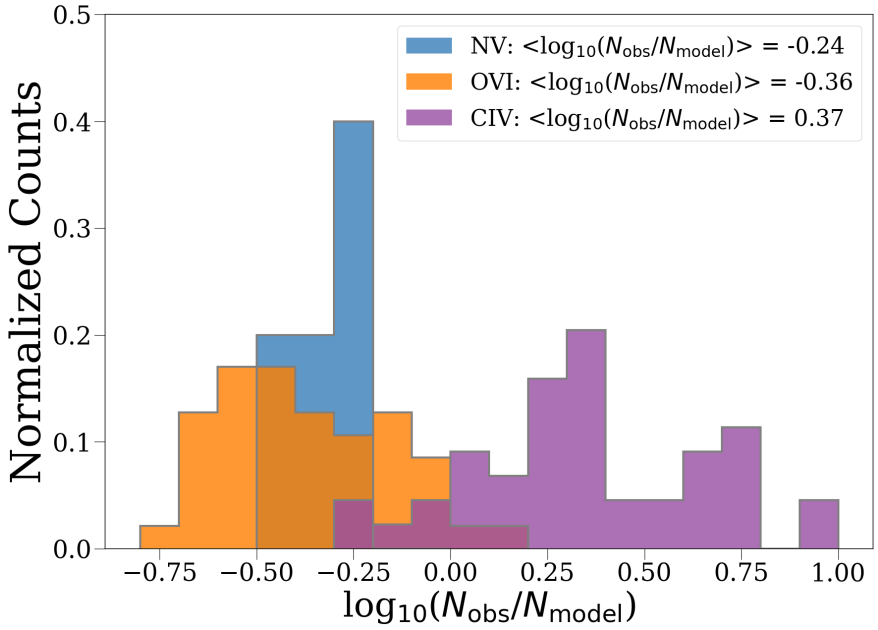

Figure 4.11: Normalized distributions of the ratio between the observed C IV, O VI, and N V column densities from the peak temperature cooling flow model (not taking into account thermal broadening, Eq 4.4). The normalized distributions are set so that the sum of the counts equals one; the counts per bin (bin with is equal to 0.1) are divided by the number of observations for each ion. We find that on average, C IV is ∼2.5 ($\log_{10}$ 0.4) times higher than the model predictions.

The probability density distributions of the calculated $\Delta\log_{10}N$ values for C IV, O VI, and N V are shown in Figure 4.11.

The $\Delta\log_{10}N$ values for C IV are positive meaning that on average, the observations of C IV were ∼2.5 times higher than the model. Since C IV has a lower ionization energy, one possible scenario for why C IV observations lie above the cooling-flow model predictions is that it has contributions both from the warm/hot phase and from a cool photoionized phase. The warm/hot phase is believed to be where O VI forms and is well described by the cooling flow model. We examine this scenario in more detail in Section 5.1.

5 Discussion

Our study is one of the first times an examination of C IV, O VI, and N V has ever been conducted in the CGM for every line-of-sight in a sample of low-z L* galaxies. We aim to frame this exploration of physical processes in the context of the seminal work presented in Werk et al. (2016) for O VI and N V and utilize the considerable efforts by previous studies which depict the CGM as a highly ionized diffuse medium that plays host to complex mechanisms (Sembach et al., 2003; Fox et al., 2004, 2006, 2009; Tumlinson et al., 2005; Tripp et al., 2008; Lehner et al., 2009, 2011; Wakker & Savage, 2009; Narayanan et al., 2010, 2011, 2012; Savage et al., 2011, 2014; Muzahid et al., 2012; Wakker et al., 2012; Hussain et al., 2015; Zahedy et al., 2019; Rudie et al., 2019; Dutta et al., 2020, 2021; Zahedy et al., 2021;

$\log_{10}T_X$ (K) (1)	f_X (2)	$\log_{10}\Lambda(T_X, Z)$ (erg cm^3 s^{-1}) (3)
	C IV	
5.0	0.27	-21.786
5.5	0.0035	-22.046
	O VI	
5.5	0.23	-22.046
6.0	0.0046	-22.592
	N V	
5.3	0.24	-21.891
5.7	0.0031	-22.487

Table 4.2: Cooling Flow Model Parameters for Each Ion. Comments on columns: (1) Temperature of cooling metal ion; (2) ionic fraction of X at temperature T_X; (3) cooling function

Qu et al., 2022; Sameer et al., 2024, and references within). Through the comparisons to radiative cooling flow-models and Cloudy modeling, we find that even though C IV and O IV are kinematically coincident and they both exhibit a dichotomy in star-forming and passive galaxies (Tumlinson et al., 2011; Garza et al., 2025)[11], they, together with the N V, cannot be physically explained by just single phase gas. We now explore some scenarios and models that may produce multiphase conditions which result in ionized gas containing C IV, O VI, and N V[12]. The comparisons in this discussion are qualitative as a more detailed analysis is beyond the scope of this work.

5.1 Cool C IV and N V Depletion

One option is that the C IV column has a contribution from two different phases, for example warm/hot and cool gas. This scenario has two-fold motivation: first, theoretical - the ionization energy needed to form C IV (47.9 eV), enabling formation in either warm/hot or cool, low density gas (see also models by Faerman & Werk, 2023), and second, empirical - as shown in Figure 4.10, the measured $N_{\rm C\ IV}$ is higher than expected from the cooling gas model, for example. The implication of this scenario is that the C IV column originating in the same phase as the OVI is a fraction of the measured value, and these lower C IV columns and C IV/O VI ratios allow for higher ionization gas, either at higher temperatures or lower densities. Figure 4.12 (left) shows the constraints from C IV columns lower by a factor of 2.5 than the measured values.

[11]The interpretation of an O VI dichotomy has been a topic of discussion since it was discovered in 2011. The addition of C IV observations from the CIViL* provides the opportunity to investigate why we see this dichotomy between the ionization state of star-forming and passive galaxies. As we are pinpointing the physical conditions of the halos, fully addressing this dichotomy is a little beyond the scope of the paper.

[12]We note that we are explicitly investigating intermediate/high ions. For more in depth discussions on lower ionization states, we refer the reader to studies such as COS-Halos (Werk et al., 2013), COS-GASS (Borthakur et al., 2015), and the COS CGM Compendium (Lehner et al., 2018, 2019)

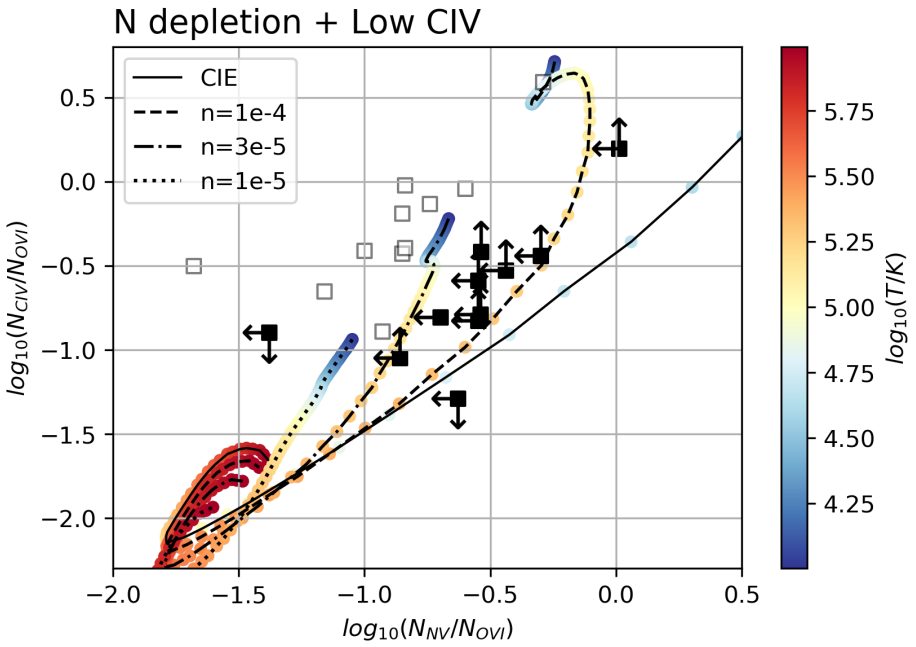

Figure 4.12: Column density ratios for lowered C IV and N V depletion (filled squares). Grey markers show the original measured ratios (see Figure 4.9) for comparison.

Another option is that the nitrogen is depleted, also affecting the column density ratio through the elemental abundance. This assumption that nitrogen gas in the CGM is under-abundant comes from the fact that many of the COS-Halos sightlines, including the ones used in this work, do not detect N V. This is particullary relevent when making use of nitrogen to oxygen ratios. We do not address the specific scenario which causes nitrogen depletion (which can be interesting for future work and was discussed briefly in §2.2 of Werk et al., 2016) and implement this as higher N V fractions that form in the warm/hot phase, and are lowered by some factor due to lower than solar N/O ratio[13], resulting in the same measured N V/O VI ratios as without depletion. We show these in the right panel of Figure 4.12 for N V columns that are depleted by a factor of 2 and lower $N_{\rm C\ IV}$. In this combined scenario, many of the adjusted ratios are consistent with the models. The grey faded markers show the original, measured ratios, for comparison.

These two scenarios extend the allowed range of gas temperatures and densities. In CIE the ion fractions are very sensitive to the gas temperature, and a factor of 2 in column density or abundance leads to a small change, $\Delta T \approx 0.1$ dex. The change in the allowed gas density is more significant, up to $\Delta n \approx 0.5$ dex. Specifically, these scenarios allow overlap between the different ratios, i.e. consistency of the observed C IV, N V, and O VI, with single-phase

[13]As discussed in Werk et al. (2016), the N/O ratio can be sub-solar in metal poor environments that include ionized gas from H II regions (Henry, 1993), neutral gas damped Lyα systems (DLAs, e.g., Reimers et al., 1992; Prochaska et al., 2002; Battisti et al., 2012; Zafar et al., 2014), sub-DLAs (e.g., Battisti et al., 2012; Tripp et al., 2005), and Lyman limit systems (e.g., Jenkins et al., 2005). On the other hand, N V has been detected alongside other high ionization absorbers that provide a check on the nitrogen abundance. In these cases, there was no evidence for nitrogen under-abundance (Savage et al., 2002; Tripp et al., 2006, 2011).

gas. This allows gas at temperatures $\lesssim 1.5 \times 10^5$ K and densities $\lesssim 3 - 5 \times 10^{-5}$ cm^{-3}. At these conditions, gas has thermal pressures of $\lesssim 10$ K cm^{-3}, suggesting the outer regions of the CGM. Furthermore, this also decreases the gap between the allowed regions at higher densities and pressures. A lower C IV fraction associated with the O VI or stronger N V depletion can further close the gap.

5.2 Other Possible Ionization Processes

The CGM is a intricate medium whose description has primarily been driven by observations. However, there exist a multitude of complex models that that may be able to more accurately describe what the observations reveal other than strictly photoionization and collisional ionization models (e.g., Gnat & Sternberg, 2007). These include, but are not limited to, non-dynamical radiative cooling models (Edgar & Chevalier, 1986; Gnat & Sternberg, 2007), non-equilibrium ionization models (Gnat & Sternberg, 2007; Oppenheimer & Schaye, 2013b; Kumar & Chen, 2025), non-equilibrium ionization via flash photoionization from fossil AGN (Oppenheimer & Schaye, 2013c), equilibrium and non-equilibrium turbulent mixing layers (Begelman & Fabian, 1990; Slavin et al., 1993; Kwak & Shelton, 2010; Kwak et al., 2011; Fielding et al., 2020; Tan & Oh, 2021; Tan et al., 2021a), conductive interfaces between cool clouds and a hot medium (Borkowski et al., 1990; Gnat et al., 2010), supersonic shock ionization modeling (Dopita & Sutherland, 1996; Heckman et al., 2002; Allen et al., 2008; Gnat & Sternberg, 2009; Grimes et al., 2009), radial density distributions (Faerman & Werk, 2023), and galactic winds (Chevalier & Clegg, 1985; Schneider et al., 2018; Fielding & Bryan, 2022). Several of these models have been used to physically describe the highly ionized components of Galactic high velocity clouds (HVCs, Shapiro & Field, 1976; Sembach et al., 2003; Fox et al., 2004; Wakker et al., 2012; Savage et al., 2014).

By combining the results presented in COS-Halos Werk et al. (2013, 2016) with results from the CIViL* survey we show that the CGM of nearby L* galaxies can not be defined by gas originating from a singular phase; we assert that any model that aims to successfully describe the CGM needs to be able to accurately predict the kinematic correspondence seen at all levels of ionization but also take into account that these ions do not all live in the same phase. Turbulent mixing layer (TML) models are a promising pathway that can potentially accomplish both of these critical tasks as they describe the interface of cold and hot gas interacting (Begelman & Fabian, 1990; Binette et al., 2009; Kwak & Shelton, 2010; Kwak et al., 2011, 2015; Gronke & Oh, 2018; Ji et al., 2019; Fielding et al., 2020; Tan & Oh, 2021; Tan et al., 2021a; Chen et al., 2023). These models implement Kevin-Helholtz instability, which drives the turbulent mixing and populate the now mixing gas with intermediate temperatures (10^{4-6} K). As we have described and shown throughout the previous sections of this paper, this is where the intermediate ions like C IV, O IV, and N V reside.

For example, Chen et al. (2023) developed an analytic, 1.5-dimensional model for TMLs that explicitly includes the impact of turbulence driven by the shear flow, a process that likely dominates over the physical conduction and viscosity in most regimes. Using the ion abundances table from Trident (Hummels et al., 2017), which are tabulated using Cloudy (Ferland et al., 1998), under the assumption of ionization equilibrium assuming a background radiation field from Haardt & Madau (2012), Chen et al. (2023) uses the temperature and

density profiles obtained from their 1.5D model to calculate the ion fraction at any position in the mixing layer assuming $z = 0$ and solar metallicity.

However, they do note that the predicted column densities (presented in Figure 20) are more demonstrative than definitive, especially for CGM assumptions. With this in mind, we compare our observations to the values presented in their paper and use their publicly available notebook[14] to predict column densities for a third solar metallicity. The predicted column densities for C IV, N V, and O VI (assuming $z = 0$ and solar metallicity) are $\log_{10}N$ = 12.17, 11.40, and 11.92 respectively. Assuming third solar metallicity values from Asplund et al. (2009), we find the predictions for the ions to be $\log_{10}N$ = 7.56, 6.65, and 15.28 respectively for C IV, N V, and O VI. Most of the model predictions are lower than our sample of measurement values for all three of the ions, ranging from between $\sim$ 1-3 dex lower for the solar metallicity predictions and $\sim$ 6-7.5 dex lower for the third solar metallicity predictions. However, looking at their ratios we find $\log_{10}(N_{\rm C\ IV}/N_{\rm O\ VI})$ = 0.25 and $\log_{10}(N_{\rm N\ V}/N_{\rm O\ VI})$ = -0.52 for solar metallically. We find that these predicted ratios are similar to our observed ratios, as seen in the left panel of Figure 4.9; a natural explanation for the column densities being too-low, but the correct ratio is predicted is that a typical sightline intersects several TMLs. This similarity between observed and predicted ratios reiterates that all three ions are inconsistent with single-phase equilibrium models.

Another way to use TMLs is to focus on how their small scale physical processes lead to different distributions in gas density and temperature. One could then see test how these processes manifest in the ionic columns observed in absorption from CGM gas. Faerman et al. (2025) investigated two potential scenarios in the CGM that could lead to a distribution in both density and temperature: (i) a lognormal density distribution, which could arise in isothermal and adiabatic turbulence or as a superposition of many physical processes influencing the CGM and (ii) fluctuations driven by the the cooling and mixing of gas where intermediate-temperature gas resides can reside in turbulent mixing layers around cool gas clouds or in gas that is cooling radiatively from the hot/virial phase. Using the Cloudy 17.00 code (Ferland et al., 2017), they obtain ion fractions as a function of gas temperature and density for photoionized gas in the presence of a MGRF, assuming the parameters in Khaire & Srianand (2019), at a reshift of $z = 0.2$. To directly compare to observations, Faerman et al. (2025) uses their ion fraction estimations to calculate a total model column density; they compare the best fits to of their column density calculations to the column densities reported in the COS-Halos survey (Werk et al., 2013) in Fig. 4-6 of their paper.

Only one sightline is both in the sample used by Faerman et al. (2025) and the sample presented in this work, J1016+4706_274_6. For this galaxy, 274_6, the column density observations ($\log_{10}$(N/cm^{-2})) are C IV $>$ 14.5, N V $<$ 13.6, and O VI = 14.87. The turbulent model predicts C IV columns of 14-14.5 for $\sigma \sim 0.6$. This is consistent with about half of the observed column (lower limit) in cool phase. For the mixing layers model, the C IV column is $\approx$ 14, N V $\approx$ 13, and the O VI is $\approx$ 13.5. These are lower than observed, but may be consistent with a higher fraction in the warm/hot phase. For the cooling gas scenario, the model suggests C IV $\approx$ 14, N V $<$ 14, and O VI $\approx$ 15. This is consistent with N V and O VI coming from cooling gas, while some of the C IV originates in completely cool gas (as

[14]https://github.com/ziruichen11/1.5D_mixing/tree/main; The specifics can be found in the column_density_calculation folder

suggested earlier by the cooling flow model and our models discussed in §4).

Comparing to our observations to Chen et al. (2023) and Faerman et al. (2025) is just the beginning of what can be done with this new sample set. More comparisons are needed to get a complete picture of where these new observations lie in relation to the current modeling sample. We encourage researchers with an interest in complex modeling and simulations of the CGM to use our kinematic parameters (see Extended Table 4.2) to compare with their results and further constrain their models.

6 Summary and Conclusions

By combining legacy COS-Halos observations (Werk et al., 2012, 2013) with new C IV observations from CIViL* (Garza et al., 2025), this study provides a unique opportunity to examine intermediate and high ions in the same set of nearby ($z \lesssim 0.25$) L* galaxies. For one of the first times ever in a systematic fashion, we were able to compare the kinematics of C IV to both low and high ionization states and use these ions to provide constraints on the physical conditions within the CGM of our sample. We explored predictions from both single-phase CI+PI Cloudy models and a cooling-flow model in relation to our observations. The main results of this study are as follows:

1. We find that there is generally good correspondence between the velocity ranges over which there is strong C IV absorption and absorption from other low and high ionization states (O VI and Si III, Figure 4.1; C III, Figure 4.2; N V and O VI, Figure 4.3), however there is a variance in alignment between sightlines. Some exhibit impressive alignments in component structure, some have misalignment, and some slightlines have strong high-ion absorption, but no low-ion absorption present. We conclude that the relationship between low and high ionization states of gas along COS-Halos sightlines is not straightfoward.

2. Figure 4.5 empirically represents the information of the combined voigt profile fits for all the ions presented in Figures 4.1, 4.2, and 4.3. Using an Anderson-Darling test for k-samples, we find that for high levels of statistical significance ($> 95\%$) we can not reject the null hypothesis that the measurements for C IV and O VI (for both column density, Doppler parameter, and change in systemic velocity) are drawn from the same parent distributions. Therefore it is likely that the components comprising the C IV and O VI samples are drawn from the same parent distribution; these results suggest that C VI and O VI are *potentially* kinematically coincident and have a physical connection. We also find that all the ions we examined are bound to the dark matter halos of their host galaxies (Figure 4.6).

3. In Figures 4.8 and 4.9 we explore if a single-phase CGM can reproduce the observed column density ratios and individual column densities for our sample of C IV, N V, and O VI. Comparing models to the observed/measured values/ratios (Fig 4.9), we find that the observation ratios are inconsistent with single-phase equilibrium models. We further explore this by looking at the observations and model predictions for individual objects (Right Panel of Figure 4.9). For the majority of our sample, the regions allowed

by the column densities (and thus ratios) do not overlap creating a "zone of avoidance", solidifying our earlier result that all three ions are most likely *not* coexisting in the same phase. There are only two objects in our sample that have conditions in which a single phase for all three ions is possible; these objects have a detection for O VI and have upper limit values for both C VI and N V.

4. To investigate the origins of C IV, N V, and O VI, we explored the cooling flow model under collisional ionization (Heckman et al., 2002; Bordoloi et al., 2017). We find that both O VI and N V are consistent with the predictions of the model within a typical range of temperatures (Figure 4.10), but the column densities for C IV are ∼2.5 times higher than the predictions from the model (Figure 4.11). Since C IV has a lower ionization energy than N V and O VI, it is possible that C VI has contributions from both the warm/hot phase and from the cool photoionized phase and this could be why the C IV observations were higher than the model predictions.

5. One scenario for why our observations cannot be described by a single-phase photoionization equilibrium or CIE model is that C IV itself has contributions from two different phases. If true, then the C IV column originating in the same phase as O VI is a fraction of the measured value. Thus, lower C IV columns and resulting C IV/O VI ratios allow for higher ionization gas, either at higher temperatures or lower densities; by lowering the C IV column densities by a factor of 2.5 (Figure 4.11) the observations become more consistent with CIE model predictions. Another option is that N V is depleted, which can also affect the column density ratios through elemental abundance. We show ratios with N V depleted by a factor of 2 and the lower C IV column densities in Figure 4.12. In this combined scenario, many of the markers are consistent with the models; this consistency translates to the new range of temperatures and densities allowed, which result in all three ions being allowed to form in a single gas phase.

6. Through our observational analysis of C IV and O VI and comparisons to various model predictions, we find that these ions can be reproduced with a single phase model (e.g. the green shaded region in the right panel of Figure 4.9). However with the combination of N V, it is very challenging to reproduce a single phase that describes all three ions. Any successful model of the CGM which incorporates multiphase conditions must result in ionized gas containing C IV, N V, and O VI that is kinematically coexist, but "avoids" existing at the same temperature and density.

7. We qualitatively compare our results to the TML model developed in Chen et al. (2023), and find that their column density predictions at solar are ∼1-3 dex lower than our range of measurements for C IV, N V, and O VI. However, their column density ratios (i.e., $\log_{10}(N_{\mathrm{C\ IV}}/N_{\mathrm{O\ VI}})$ and $\log_{10}(N_{\mathrm{N\ V}}/N_{\mathrm{O\ VI}})$) are reasonable and fall within our range of expected values based on observations (left panel of Figure 4.9). At third solar metallicity, their predicted column densities are ∼6-7.5 dex lower than our range of observations, and do not have ratios within our expected range.

8. We also compare our measured column densities to predictions from Faerman et al. (2025), who uses a few different models to address density and temperature distribu-

tions, where only one of the galaxies, 274_6, is also in our sample. The turbulent model is consistent with about half of the observed column for C IV in the cool phase. For the mixing layer model, the column densities for C IV, N V, and O VI are lower than observed, but may be consisted with a higher fraction in the warm/hot phase. And lastly for the cooling gas scenario, the model is consistent with N V and O VI coming from the cooling gas, while some of the C IV originates in completely cool gas (as suggested by the results from comparisons to the cooling flow model discussed in S4.3.2).

In conclusion, our results are consistent with a multiphase CGM where C IV and O VI are similar only to a certain extent. As we suggest in our discussion, there is evidence of higher levels of complexity than we explored with our models. Further work implementing C IV into more sophisticated models and simulations is crucial to forming a more complete picture of the CGM.

7 Appendix A: CIViL* Sample & Non-Detection Spectra

To build the CIViL* survey, 13 sightlines, around 11 FUV-bright QSOs, were selected from the COS-Halos and COS-GASS curveys to obtain a census of C IV in the circumgalactic medium of a control-matched sample of L* galaxies. Table 4.3 lists the properties of our targets where we list the J2000 right ascension (R.A.) and declination (Dec), the program identification (PID) of the HST program the sightline was matched from, the COS grating used for the observation of our targets, the central wavelength used for observation, the number of orbits, and the signal-to-noise ratio (S/N) per COS resolution element of the COS spectra bear the C IV transition. We also present the rest of the spectra from the CIViL* survey in Figure 4.13. These non absorption feature (upper limits) observations were first presented in Garza et al. (2025). We do not use sightlines matched to COS-GASS galaxies (J1427+2632 (45940), J1502+0649 (41743), and J1544+2740 (28317)) for the analysis in this paper and just use the upper limit values for the three COS-Halos matched sightlines (J0226+0015_268_22, J1342-0053_157_10, and J1342-0053_177_10), whose values are included in Extended Table 4.1. There were two other sightlines in the initial CIViL* proposal (Berg et al., 2022b) that are not included in Figure 4.13 or for our analysis. Sightline J0958+3204 (33737) had two Hubble Observation Problem Reports (HOPRs) filed for it due to repeat failed observations, however no usable spectra was able to be obtained. For sightline J0910+1014 we were unable to obtain science-grade spectra and thus, did not include it in the sample. However this sightline fortuitously already had COS-Halos C IV measurements for galaxy 34_46; we use the previously published spectra and voigt profile fits for our analysis.

Target (1)	R.A. (2)	Dec (3)	PID (4)	Grating (5)	Central Wavelength (6)	Orbits (7)	S/N (8)
J0226+0015_268_22	36.5603	0.2583	11598	G185M	1904	3	5.17
J0401-0540_67_24	60.4541	-5.6824	11598	G185M	1885	3	8.33
J0910+1014_34_46	137.624	10.2371	11598	G185M	1882	4	-
J0950+4831_177_27	147.5031	48.5248	11598	G185M	1972	4	9.34
J1016+4706_274_6	154.0942	47.112	11598	G185M	1900	4	5.46
J1016+4706_359_16	154.0942	47.112	11598	G185M	1904	3	7.21
J1342-0053_157_10	205.715	-0.8959	11598	G185M	1955	3	6.43
J1342-0053_77_10	205.715	-0.8959	11598	G185M	1955	3	8.45
J1419+4207_132_30	214.7925	42.1297	11598	G185M	1922	4	5.65
J0958+3204_33737	149.714	32.073	12603	G160M	1523	3	-
J1427+2629_45940	216.954	26.484	12603	G160M	1589	5	12.5
J1502+0649_41743	225.517	6.823	12603	G160M	1533	2	8.6
J1544+2740_28317	236.034	27.673	12603	G160M	1623	5	14.89

Table 4.3: Sample Summary. Comments on columns: (1) The 13 sightlines from our HST program have the PID 17076; (2) & (3) are the target coordinates in degrees; (4) The PID the sightline was referenced/matched from; (5) the COS Grating; (6) central wavelength for observations; (7) orbits used; (8) The signal-to-noise estimation per resolution element around $\sim$ 1548 Å. For both J0910+1014_34_46 (unable to obtain science grade spectra) and J0958+3204_33737 (failed observations) we are unable to report a S/N.

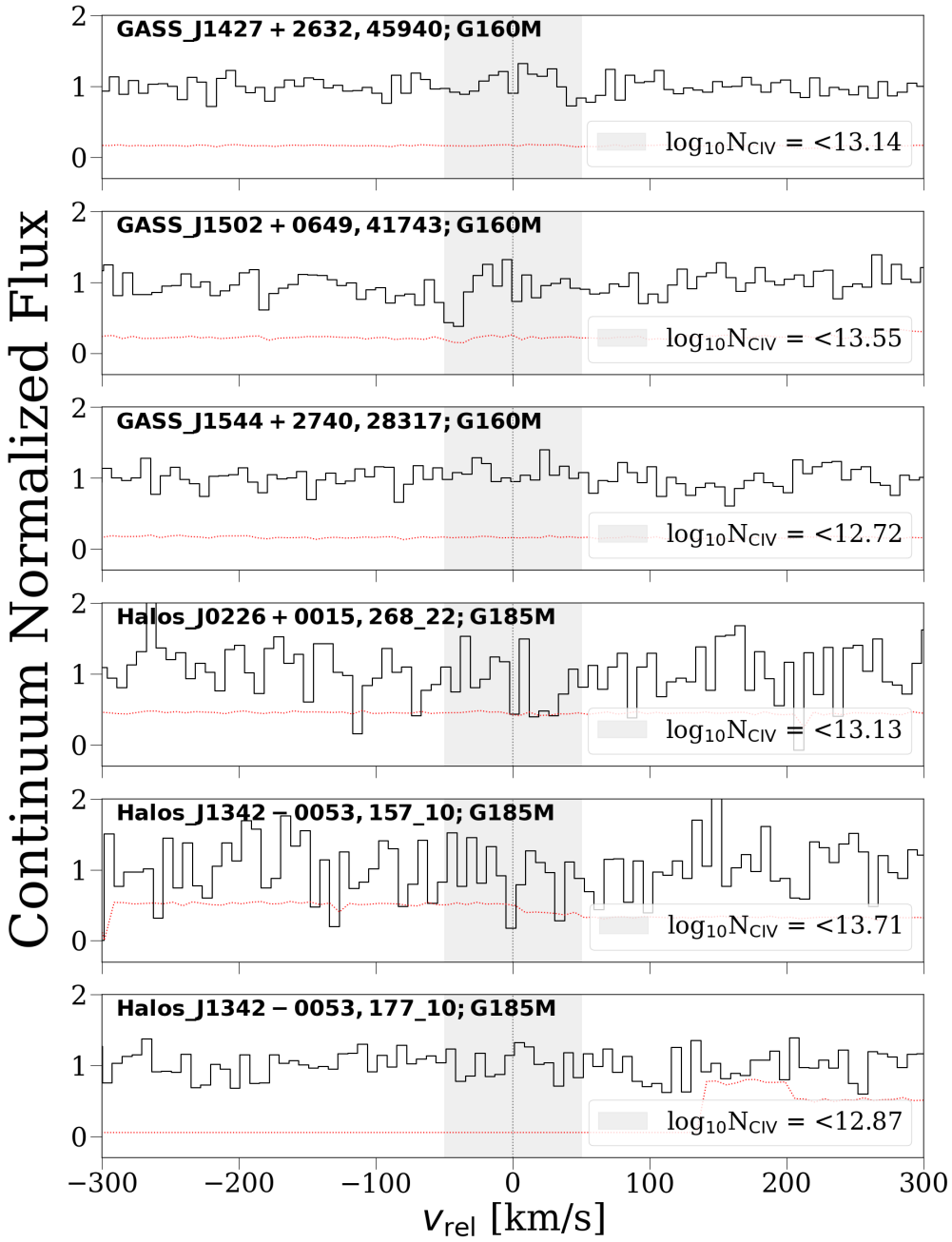

Figure 4.13: Spectra from the CIViL* survey with no prominent absorption features. We denote our upper limit column density estimations in the legend for each sightline. We do not use COS-GASS matched sightlines J1427+2632 (45940), J1502+0649 (41743), and J1544+2740 (28317) for this paper's analysis.

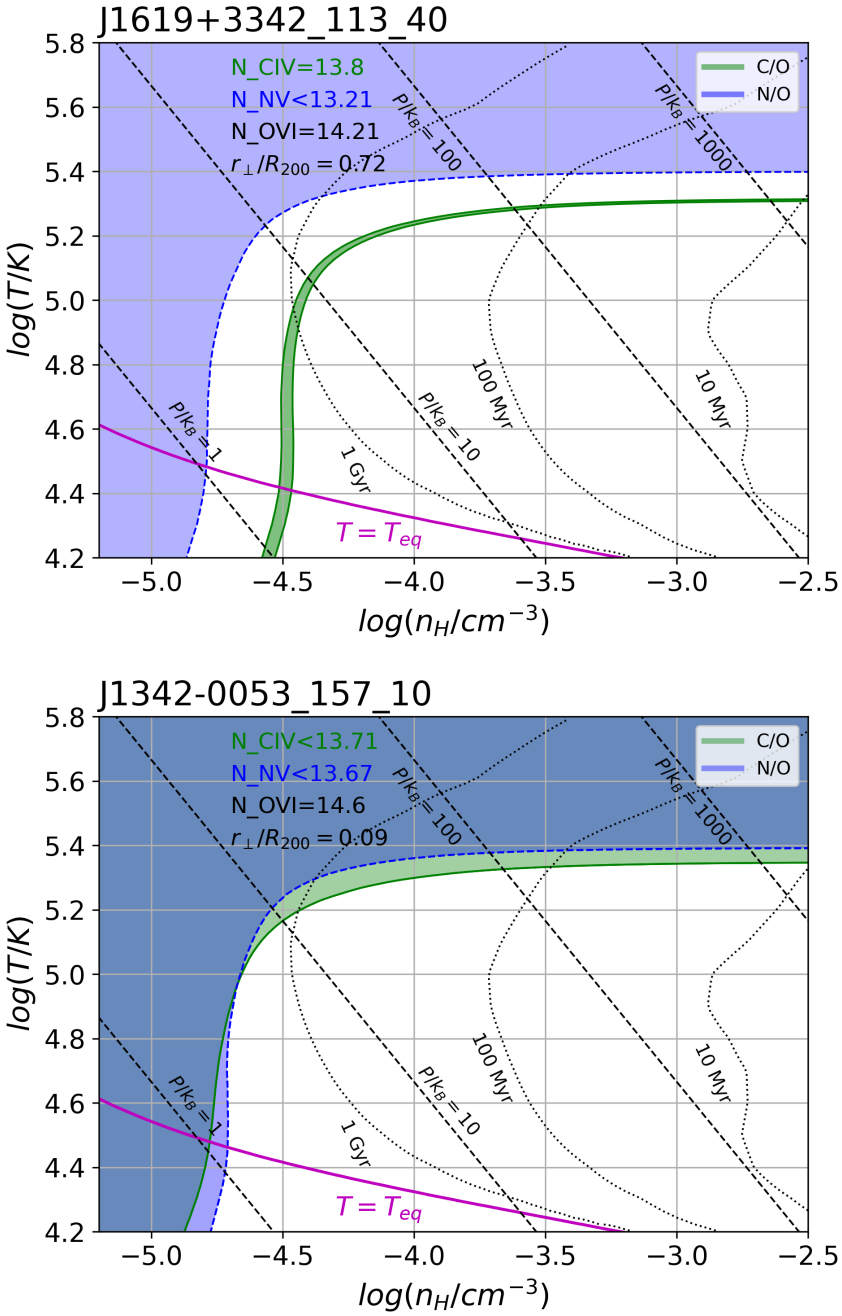

Figure 4.14: Constraints on gas density and temperature from column density ratios for individual objects. The two example cases are (**i, Left Panel**) C IV/O VI constraint and (**iii, Right Panel**) consistent with single phase gas. The first case require multiphase gas (C IV and N V cannot come from the same phase). Black dashed curves show gas pressure.

8 Appendix B: Gas Density and Temperature Constraints for Individual Objects

As we discussed in S4.2.2, we examined individual objects and looked a how the measured ratios constrain the gas properties in the density-temperature space. The two objects in Figure 4.14, show differing C IV measurements. The upper left panel shows a C IV detection and the lower panel shows a C IV upper limit measurement. These images supplement the descriptions already presented in §4.2.2.

CHAPTER 5

CONCLUSIONS

Who's the wild man now?!

– D-Bob, Rudy, 1993

1 Summary: Finding the Common Thread

The primary goal of this dissertation has been to connect the internal galaxy processes of star formation (Chapters 2 and 3) and the external processes of cosmic gas flows to the physical conditions of the CGM (Chapter 4). Throughout my work, I have demonstrated the power of using triply ionized carbon (C IV) to trace the diffuse gas of galactic atmospheres where these internal and external process interact. This intermediate ion is unique because in CGM conditions, it can form either through photo-ionization (PI) or collisional ionization (CI) and traces $T \simeq 10^{4-5.5}$ gas. This dissertation relied heavily on new C IV observations from the COS-Holes (Garza et al., 2024) and CIViL* (Garza et al., 2025) surveys, as C IV has been, up until now, seriously lacking from galaxy-selected COS surveys of L* galaxies. Other key C IV observations used include data from the COS-Halos survey (Tumlinson et al., 2013; Werk et al., 2013), the COS-Dwarfs survey (Bordoloi et al., 2014), and starburst observations from Borthakur et al. (2013).

The chapters of my work individually highlight what C IV reveals about the ionization state of CGM gas. My observations are used to quantify the radial profile of triply ionized carbon in the context of feedback mechanisms, compare to theoretical predictions from well known cosmological hydrodynamical simulations and analytical models, and used in combination with O VI and N V to constrain the current understanding of the physical properties in diffuse galactic atmospheres. Together, these chapters deepen our knowledge of the role C IV plays in the evolution of galaxies.

Chapter 2 reveals that with a larger sample size of C IV observations, it may be possible to distinguish between simulation predictions for the evacuation or enrichment of the CGM by supermassive black hole (SMBH) feedback. C IV was found to have a tentative strong positive correlation with specific star formation rate (sSFR) and no identifiable relationship with SMBH mass. Chapter 3 built upon this tentative correlation explored in Chapter 2 and discovered a C IV dichotomy between star-forming (an abundance of C IV) and passive (C IV was not as commonly observed) L* galaxies. This discovery is even more exciting since it supplements the already established dichotomy of O VI in star-forming and passive galaxies (Tumlinson et al., 2011; Tchernyshyov et al., 2023). These results suggest that C IV is more "O VI" like than low-ion like and hints at a possible physical connection between the two ions.

Chapter 4 explores C IV and O VI in further detail by studying their kinematics and column density ratios to see potential implications for the physical conditions of the CGM. Both C IV and O VI are kinematically coincident and bound to their host galaxy. We find that in addition to their similar dichotomy in star-forming and passive galaxies and strong correspondence in velocities, these ions can be explained by a single gas phase, although not well constrained. However, using Cloudy modeling, the ratios of C IV to O VI and N V to O VI, revealed that, all three of these ions can very rarely be described using a single phase (i.e., arise in gas in the same temperature and density). Using a radiative cooling-flow model, O VI was found to be consistent with the predictions for a range of temperatures under collisional ionization conditions, but C IV observations were on average 2.5 times higher than the model predictions. This suggests that C IV most likely has contributions from photoionization (PI) and collisional ionization (CI) with PI being the stronger contribution. Thus, for any model

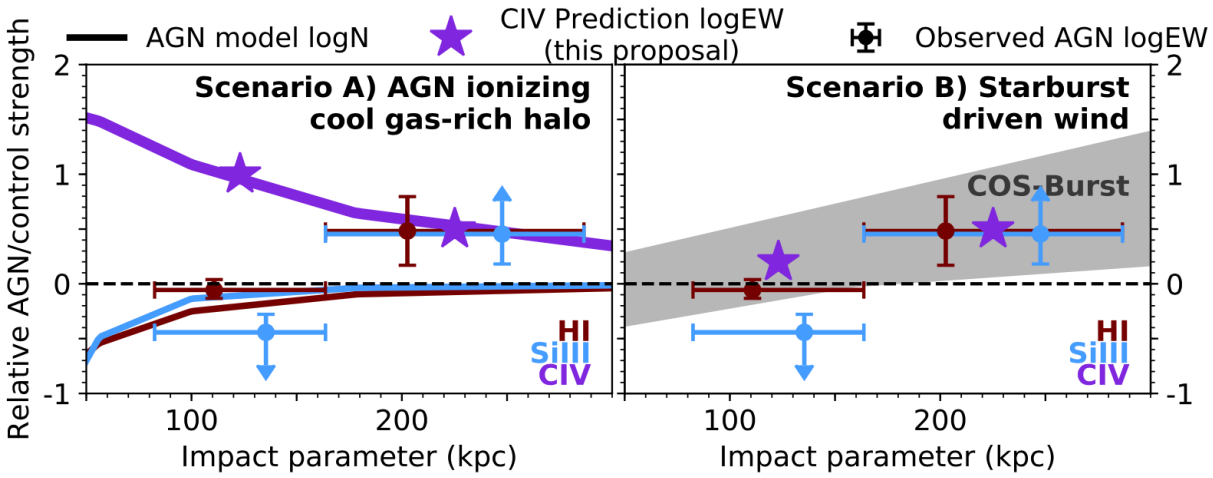

Figure 5.1: Uncovering the nature of highly ionized gas surrounding AGN and starburst galaxies. The relative strength of three key ions (H I, Si III, and C IV; dark red, light blue, and purple respectively) in the CGM surrounding AGN, normalized by the strength found in a comparable non-AGN halo. The surrounding lines denote this relative ratio predicted by the presence of AGN photoionization models (in units of column density, $\log/\mathrm{cm}^{-2}$), while the circular datapoints show the relative rest-frame equivalent width ratios (logEW) observed for H I and Si III in the COS-AGN survey. The purple stars denote, the predicted strengths of C IV in two toy models. **Scenario 1 (left panel):** the AGN resides in halos rich in cool gas, but the AGN's radiation has ionized the gas accordingly. **Scenario 2 (right panel):** a previous starburst driven wind is propagating through the halo, resulting in an enhancement of all ions (as observed by COS-Burst, gray shaded region). Figure from Berg et al. (2022b).

to accurately reproduce the conditions based on observations, it needs to meet both of these criteria: (i) have a kinematic correspondence for intermediate (C IV) and high ions (O VI) *but also reflect* (ii) but "avoids" existing at the same temperature and density (i.e., exhibit multiphase gas).

Together my body of work confirms that the galactic atmospheres of L* galaxies are dynamic and are multiphase. This work also solidifies C IV as an excellent tracer that can be used to constrain model predictions and work in tandem with other ion tracers to reveal key physical properties and conditions of the CGM.

2 Together We Shall Cast Ourselves into the Future!

It has been a wonderful ride dear reader. We have talked through the story of our current understanding of the CGM, seen many a garden and cooking metaphor, debated the power of SMBH feedback, made C IV discoveries, and investigated the temperatures and densities of galactic atmospheres. As we near the end of this dissertation, it is only fair that we conclude by looking to the bright future CGM studies. There is so many things yet to research and I barely scratched the surface with my work. However, as the bulk of my work was analyzing

new observations, there is a wealth of work that can be done and its implications are plentiful. In these next few sections, I discuss only a handful of pathways one can take based off my findings. So dear reader, let's together "CAST OURSELVES INTO THE FUTURE![1]".

2.1 We Need More Observations!

One of the main conclusions of Chapter 2 is that the COS-Holes sample was not large enough to distinguish between the results of the three simulations we compared the observations to (to determine whether the CGM is evacuated or enriched by SMBH feedback). In Chapter 3 we see that there is a disparity between the amount of detections of C IV between star-forming and passive galaxies, resulting in the discovery of a dichotomy similar to that found for O VI. However, there is a significantly less amount of passive galaxies in the sample to begin with; there are 46 star-forming galaxies compares to 13 passive galaxies. A path forward to further rounding out our knowledge of difference between star-forming and passive galaxies is to increase our numbers of C IV and O VI observations around passive L* galaxies; by boosting the number of observations of passive galaxies we could further tease out the observed dichotomy and compare constraints on passive galaxies to the ones on made for star-forming ones (as touched upon in earlier Chapters of this dissertation). In essence, my thesis work has set the stage for using C IV as a tracer to distinguish between evolutionary theories, but is in need of a stellar cast (i.e., more observations) to take the results the rest of the way.

2.1.1 Galaxies with Dynamically Measured SMBH Masses

I particularly want to discuss the potential that more observations of galaxies with dynamically measured SMBH masses provides. As we discussed in Chapter 2, the relation between mass of the central SMBH and the stellar dispersion of its host galaxy's bulge, $M_{BH} - \sigma$, and the bulge mass-M_{BH} correlation (Silk & Rees, 1998; Ferrarese & Merritt, 2000; Gebhardt et al., 2000; Häring & Rix, 2004; Reines & Volonteri, 2015), reflect that the mass of a SMBH is a fundamental property of a galaxy and reflective of its history (Kormendy & Ho, 2013; van den Bosch, 2016). And as demonstrated, the CGM *can*, even with a small sample size, shows altered content due to the cummulative activity of the SMBH (Figure 3, Chapter 2). For galaxies with a $\log_{10}M_{BH} < 7.0$ (Garza et al., 2024) found a 100% detection fraction and a 33% detection fraction for galaxies with $\log_{10}M_{BH} > 7.0$. With an increased sample size, we could see if this trend continues or is refuted.

The challenge in increasing the sample size, lies in the difficulty of determining the mass of a SMBH. Precise measurements of SMBH masses are very hard to measure due to the difficulty of directly probing the motion of objects in the vicinity of SMBHs, as this is where the gravitational potential of SMBHs exert a dominant influence. In fact, we have only been able to effectively resolve individual stars or gas clouds around the center of our Milky Way galaxy, Sagittarius A* (Schödel et al., 2002; Ghez et al., 2005; Gillessen et al., 2009; GRAVITY Collaboration et al., 2018). The only path forward to dynamically measuring SMBH masses is to measure the collective motion of stars or gas within a given regions as

[1]Note that this part must be read in the voice of Emma Thompson as Professor Trelawney

a whole; this is done using highly spatially resolved observations (e.g., observations from *HST*) and large adaptive optics assisted ground based telescopes. Thus, only on order of hundreds of SMBHs in nearby galaxies have been measured using dynamical techniques.

Despite these challenges, the number of nearby galaxies with dynamically measured SMBH masses is rising by the month (e.g., Pilawa et al., 2025; Kabasares et al., 2024) which provides a fortuitous opportunity. The results from Garza et al. (2024), would be the perfect evidence to use for a mini HST proposal to increase the number of C IV observations for galaxies with these precise SMBH mass measurements. One would simply need to comb through the recent literature to tabulate all the new galaxies with dynamically measured SMBH mass measurements and screen them for any nearby QSOs to use to observe the CGM. Once a healthy sample has been established, one could either propose to use archival observations (if available) or observe new targets. If there are not enough QSO targets avalaliable around this potential new set of galaxies, all is not lost. [ADD SOMETHING ABOUT THE POTENTIAL POWER OF LSST TO DISCOVER NEW QSOS, Need to talk with David, JF, and Jake for estimates of how many new QSOs LSST might find in the first year(s).]

2.1.2 Why is there so little N V?

One of the glaringly obvious things missing from Chapter 4 is N V observations. This is not a mistake, there is just barely any observations of N V in L* galaxies, and we are still not fully sure why that is. Werk et al. (2016) investigated whether this non-detection of N V in the majority of COS-Halos sightlines was due to an under abundance of nitrogen with respect to oxygen. They note that the N/O ratio is sometimes subsolar in metal poor environments (e.g., Reimers et al., 1992; Prochaska et al., 2002; Battisti et al., 2012; Zafar et al., 2014; Tripp et al., 2005; Jenkins et al., 2005), but on the flip side has been found to be rather abundant and observed with other highly ionized absorbers (Savage et al., 2002; Tripp et al., 2006, 2011). To further investigate this tension, Werk et al. (2016) looked at various nitrogen ion ratios under photoionization conditions. They found that lower ionization state nitrogen ions are consistent under photoionization, but it is difficult to explain the N V/O VI ratio with a simple PI model. Bordoloi et al. (2017) builds upon these results and shows that N V observations are fairly consistent with their radiatively cooling-flow model (see Chapter 4 for more explanation of the model and comparison to observations).

Although not much progress has been made in observing N V, there has been a lot of progress in understanding why there may not be a lot of N V to observe to begin with (e.g., Buie et al., 2018, 2020a,b, 2022). Using a series of chemodynamical simulations of an isotropic turbulent media using the MAIHEM package, Buie et al. (2018) explored how various ions may change under turbulent conditions. The results from these turbulent media runs reproduced many features of the CGM as dictated by observations, such as a clumping (Pieri et al., 2014) of low ionization state ions at the inner halo of a galaxy (Liang & Chen, 2014) and high ions more abundant in the outer CGM (Werk et al., 2016; Johnson et al., 2015b; Oppenheimer et al., 2016, 2018). However, unlike observations, in these turbulent isotropic simulations, N V was seen to have column densities of similar magnitude to those of O VI. This discrepancy could be a consequence of the shocks present with higher turbulent runs, which causes thermal runaway. Additionally, N V is ionized faster than O VI, which lead Buie et al. (2018) to conclude that N V present in the CGM of star-forming galaxies is

able to quickly ionize to N VI leaving little trace of N V. Building upon these results, Buie et al. (2020a) and (Buie et al., 2020b) modify MAIHEM to simulate a stratified medium in a NFW gravitational potential to allow for more effective cooling at higher velocity dispersions. This modified simulation, with an average one-dimensional velocity dispersion of $\approx$40 km s^{-1}, produced a CGM that matches many of the observed ionic column densities and ratios. The biggest difference from these runs compared to Buie et al. (2018) is that the column density ratio of N V to O VI is suppressed (i.e. lower columns of N V) from its equilibrium value due to a combinations of radiative cooling and cooling from turbulent mixing. The results from these studies really emphasize that turbulent mixing models are the path forward to getting a more complete understanding of the kinematic structure of the multiphase medium around star forming galaxies.

Even though simulations predict that there is little N V to observe in the CGM of star-forming galaxies, there is a chance there is enough N V available for observations. Chapter 4 showed the constraining potential of N V and just a few more observations along the same line of sights could provide the data needed to ease some of the current tension. By obtaining just a few more orbits of these lines of sight by the Hubble Space Telescope, we could have a new set of weak N V detections or better constraints on the current upper limits. As of right now, the data threshold on N V is $\sim 10^{13.5}$ cm^{-2} (Werk et al., 2016); if that detection threshold was lower even by 0.5 dex, we might be able to shed more light on the multiphase nature of the CGM. These musings would be the perfect mini HST proposal as we already have evidence of the power of N V in Chapter 4.

2.2 Disentangling AGN and Star-Formation Driven Feedback

We talked a lot about star-formation driven wind playing a large role in regulating the evolution of galaxies in the Introduction, but barely talked about AGN and their feedback processes. Similar to stellar outflows/winds, AGNs and their negative feedback play a critical role in regulating the growth of stellar mass in galaxies by heating and expelling gas from the galaxy (Schawinski et al., 2007; Schaye et al., 2015; Terrazas et al., 2016; Ellison et al., 2021). Additionally, the AGN accretion phase is thought to be triggered by a preceding starburst event, which funnels gas into the centers of the host galaxies (Wild et al., 2007; Yesuf et al., 2014). This shows how AGN and star-formation driven feedback are interconnected and can be hard to disentangle.

Recent surveys of the CGM surrounding starburst (COS-Burst, Heckman et al., 2017) and AGN host galaxies (COS-AGN, Berg et al., 2018) have revealed surprising results concerning the gaseous halos of these active galaxies. Both surveys have found an excess of cool gas (as traced by H I and Si III) at large impact parameters (the excess in AGN are shown as the blue and red points in Figure 5.1). For AGN, these measured enhancements are at odds with expectations from AGN photo-ionization models (blue and red curves in Figure 5.1). On the other hand, the observed equivalent widths are more consistent with AGN photoionization models at smaller impact parameters. From the currently obseved ions, it remains unclear if AGN: (i) reside in cool, gas rich halos (Vito et al., 2014), but the halos are subjected to the AGN's photoionizing spectrum at small impact parameters (left panel of Figure 5.1, Oppenheimer et al., 2016) or (ii) have retained gas from the previous starburst events (grey region in the right panel of Figure 5.1).

Previous studies of C IV in L* galaxies only enable comparisons with AGN beyond 150 kpc, yet C IV is expected to be a sensitive diagnostic of AGN photoionization *within* $\approx$ 150 kpc (purple line and symbols in left panel of Figure 5.1) and thus is required at small impact parameters to distinguish between the two scenarios. Specifically, C IV should decrease in strength with increasing impact parameter in the presence of an AGN, whilst an increasing C IV profile indicates a star-burst driven wind propagating through the halo, as observed in Heckman et al. (2017). The carefully constructed CIViL* sample of non-AGN, non-starbursting L* galaxies provides the opportunity to entable a precise, consistent comparison between starbursts and AGN using an identical control sample of L* galaxies. Berg et al. (in prep) plans to use the measurements from the CIViL* survey to pin down the nature of gaseous halos during events associated with the cession of star-formation in galaxies.

Teddy: It's time for your next adventure. Larry: I have no idea what I'm gonna do tomorrow. Teddy: How exciting...

– Night at the Museum 3

BIBLIOGRAPHY

Abdurro'uf, Accetta, K., Aerts, C., et al. 2022, ApJS, 259, 35, doi: 10.3847/1538-4365/ac4414

Ackermann, M., Ajello, M., Allafort, A., et al. 2013, Science, 339, 807, doi: 10.1126/science.1231160

Adelberger, K. L., Steidel, C. C., Shapley, A. E., & Pettini, M. 2003, ApJ, 584, 45, doi: 10.1086/345660

Allen, M. G., Groves, B. A., Dopita, M. A., Sutherland, R. S., & Kewley, L. J. 2008, ApJS, 178, 20, doi: 10.1086/589652

Anand, A., Nelson, D., & Kauffmann, G. 2021, MNRAS, 504, 65, doi: 10.1093/mnras/stab871

Anand, A., Aguilar, J., Ahlen, S., et al. 2025, arXiv e-prints, arXiv:2504.20299, doi: 10.48550/arXiv.2504.20299

Anderson, M. E., Bregman, J. N., & Dai, X. 2013, ApJ, 762, 106, doi: 10.1088/0004-637X/762/2/106

Anderson, M. E., Churazov, E., & Bregman, J. N. 2016, MNRAS, 455, 227, doi: 10.1093/mnras/stv2314

Andrews, B. H., & Thompson, T. A. 2011, ApJ, 727, 97, doi: 10.1088/0004-637X/727/2/97

Anglés-Alcázar, D., Faucher-Giguère, C.-A., Quataert, E., et al. 2017, MNRAS, 472, L109, doi: 10.1093/mnrasl/slx161

Armillotta, L., Fraternali, F., & Marinacci, F. 2016, MNRAS, 462, 4157, doi: 10.1093/mnras/stw1930

Armillotta, L., Fraternali, F., Werk, J. K., Prochaska, J. X., & Marinacci, F. 2017, MNRAS, 470, 114, doi: 10.1093/mnras/stx1239

Asmus, D., Greenwell, C. L., Gandhi, P., et al. 2020, MNRAS, 494, 1784, doi: 10.1093/mnras/staa766

Asplund, M., Grevesse, N., Sauval, A. J., & Scott, P. 2009, ARA&A, 47, 481, doi: 10.1146/annurev.astro.46.060407.145222

Assef, R. J., Stern, D., Noirot, G., et al. 2018, ApJS, 234, 23, doi: 10.3847/1538-4365/aaa00a

Axford, W. I., Leer, E., & Skadron, G. 1977, in International Cosmic Ray Conference, Vol. 11, International Cosmic Ray Conference, 132

Bahcall, J. N., Jannuzi, B. T., Schneider, D. P., et al. 1991, ApJ, 377, L5, doi: 10.1086/186103

Bahcall, J. N., & Spitzer, Lyman, J. 1969, ApJ, 156, L63, doi: 10.1086/180350

Barcos-Muñoz, L., Leroy, A. K., Evans, A. S., et al. 2017, ApJ, 843, 117, doi: 10.3847/1538-4357/aa789a

Barcos-Muñoz, L., Aalto, S., Thompson, T. A., et al. 2018, ApJ, 853, L28, doi: 10.3847/2041-8213/aaa28d

Barkana, R., & Loeb, A. 2001, Phys. Rep., 349, 125, doi: 10.1016/S0370-1573(01)00019-9

Battisti, A. J., Meiring, J. D., Tripp, T. M., et al. 2012, ApJ, 744, 93, doi: 10.1088/0004-637X/744/2/93

Becker, G. D., Rauch, M., & Sargent, W. L. W. 2009, ApJ, 698, 1010, doi: 10.1088/0004-637X/698/2/1010

Begelman, M. C., & Fabian, A. C. 1990, MNRAS, 244, 26P

Behroozi, P., Wechsler, R. H., Hearin, A. P., & Conroy, C. 2019, MNRAS, 488, 3143, doi: 10.1093/mnras/stz1182

Bell, A. R. 1978a, MNRAS, 182, 147, doi: 10.1093/mnras/182.2.147

—. 1978b, MNRAS, 182, 443, doi: 10.1093/mnras/182.3.443

Bell, E. F. 2003, ApJ, 586, 794, doi: 10.1086/367829

Benjamin, R. A. 1994, PhD thesis, University of Texas, Austin

Benson, A. J., Bower, R. G., Frenk, C. S., et al. 2003, ApJ, 599, 38, doi: 10.1086/379160

Bentz, M. C., & Katz, S. 2015, PASP, 127, 67, doi: 10.1086/679601

Bentz, M. C., Onken, C. A., Street, R., & Valluri, M. 2023, ApJ, 944, 29, doi: 10.3847/1538-4357/acab62

Berg, T., Bordoloi, R., Ellison, S. L., Oppenheimer, B. D., & Werk, J. K. 2022a, The C IV in L* galaxies (CIViL*) survey - Pinpointing the physical conditions and evolutionary stages of gaseous halos, HST Proposal. Cycle 30, ID. #17076

—. 2022b, The C IV in L* galaxies (CIViL*) survey - Pinpointing the physical conditions and evolutionary stages of gaseous halos, HST Proposal. Cycle 30, ID. #17076

Berg, T. A. M., Ellison, S. L., Tumlinson, J., et al. 2018, MNRAS, 478, 3890, doi: 10.1093/mnras/sty962

Bergeron, J. 1986, A&A, 155, L8

Bergeron, J., & Boissé, P. 1991, A&A, 243, 344

Bergeron, J., & Stasińska, G. 1986, A&A, 169, 1

Bernardi, M. 2007, AJ, 133, 1954, doi: 10.1086/512611

Berruyer, N., & Frisch, H. 1983, A&A, 126, 269

Bertone, S., De Lucia, G., & Thomas, P. A. 2007, MNRAS, 379, 1143, doi: 10.1111/j.1365-2966.2007.11997.x

Best, P. N., & Heckman, T. M. 2012, MNRAS, 421, 1569, doi: 10.1111/j.1365-2966.2012.20414.x

Binette, L., Drissen, L., Ubeda, L., et al. 2009, A&A, 500, 817, doi: 10.1051/0004-6361/200811132

Binney, J. 1977, ApJ, 215, 483, doi: 10.1086/155378

Bird, S., Rubin, K. H. R., Suresh, J., & Hernquist, L. 2016, MNRAS, 462, 307, doi: 10.1093/mnras/stw1582

Birnboim, Y., & Dekel, A. 2003, MNRAS, 345, 349, doi: 10.1046/j.1365-8711.2003.06955.x

Blakeslee, J. P., Cantiello, M., Mei, S., et al. 2010, ApJ, 724, 657, doi: 10.1088/0004-637X/724/1/657

Blandford, R. D., & Ostriker, J. P. 1978, ApJ, 221, L29, doi: 10.1086/182658

Blandford, R. D., & Znajek, R. L. 1977, MNRAS, 179, 433, doi: 10.1093/mnras/179.3.433

Blanton, M. R., & Roweis, S. 2007, AJ, 133, 734, doi: 10.1086/510127

Blondin, J. M., Wright, E. B., Borkowski, K. J., & Reynolds, S. P. 1998, ApJ, 500, 342, doi: 10.1086/305708

Bolatto, A. D., Warren, S. R., Leroy, A. K., et al. 2013, Nature, 499, 450, doi: 10.1038/nature12351

Bondi, H., & Hoyle, F. 1944, MNRAS, 104, 273, doi: 10.1093/mnras/104.5.273

Booth, C. M., Agertz, O., Kravtsov, A. V., & Gnedin, N. Y. 2013, ApJ, 777, L16, doi: 10.1088/2041-8205/777/1/L16

Booth, C. M., & Schaye, J. 2009, MNRAS, 398, 53, doi: 10.1111/j.1365-2966.2009.15043.x

Bordoloi, R., Prochaska, J. X., Tumlinson, J., et al. 2018, ApJ, 864, 132, doi: 10.3847/1538-4357/aad8ac

Bordoloi, R., Wagner, A. Y., Heckman, T. M., & Norman, C. A. 2017, ApJ, 848, 122, doi: 10.3847/1538-4357/aa8e9c

Bordoloi, R., Lilly, S. J., Knobel, C., et al. 2011, ApJ, 743, 10, doi: 10.1088/0004-637X/743/1/10

Bordoloi, R., Tumlinson, J., Werk, J. K., et al. 2014, ApJ, 796, 136, doi: 10.1088/0004-637X/796/2/136

Bordoloi, R., Simcoe, R. A., Matthee, J., et al. 2024, ApJ, 963, 28, doi: 10.3847/1538-4357/ad1b63

Borkowski, K. J., Balbus, S. A., & Fristrom, C. C. 1990, ApJ, 355, 501, doi: 10.1086/168784

Borthakur, S., Heckman, T., Strickland, D., Wild, V., & Schiminovich, D. 2013, ApJ, 768, 18, doi: 10.1088/0004-637X/768/1/18

Borthakur, S., Heckman, T., Tumlinson, J., et al. 2015, ApJ, 813, 46, doi: 10.1088/0004-637X/813/1/46

—. 2016, ApJ, 833, 259, doi: 10.3847/1538-4357/833/2/259

Bowen, D. V., & Chelouche, D. 2011, ApJ, 727, 47, doi: 10.1088/0004-637X/727/1/47

Bowen, D. V., Chelouche, D., Jenkins, E. B., et al. 2016, ApJ, 826, 50, doi: 10.3847/0004-637X/826/1/50

Bravo-Guerrero, J., & Stevens, I. R. 2017, MNRAS, 467, 3788, doi: 10.1093/mnras/stx327

Bregman, J. N., Hodges-Kluck, E., Qu, Z., et al. 2022, ApJ, 928, 14, doi: 10.3847/1538-4357/ac51de

Breitschwerdt, D., Dogiel, V. A., & Völk, H. J. 2002, A&A, 385, 216, doi: 10.1051/0004-6361:20020152

Breitschwerdt, D., McKenzie, J. F., & Voelk, H. J. 1991, A&A, 245, 79

—. 1993, A&A, 269, 54

Brüggen, M., & Scannapieco, E. 2016, ApJ, 822, 31, doi: 10.3847/0004-637X/822/1/31

Buie, E., Scannapieco, E., & Mark Voit, G. 2022, ApJ, 927, 30, doi: 10.3847/1538-4357/ac4bc2

Buie, II, E., Fumagalli, M., & Scannapieco, E. 2020a, ApJ, 890, 33, doi: 10.3847/1538-4357/ab65bc

Buie, II, E., Gray, W. J., & Scannapieco, E. 2018, ApJ, 864, 114, doi: 10.3847/1538-4357/aad8bd

Buie, II, E., Gray, W. J., Scannapieco, E., & Safarzadeh, M. 2020b, ApJ, 896, 136, doi: 10.3847/1538-4357/ab9535

Burchett, J. N., Tripp, T. M., Wang, Q. D., et al. 2018, MNRAS, 475, 2067, doi: 10.1093/mnras/stx3170

Burchett, J. N., Tripp, T. M., Prochaska, J. X., et al. 2015, ApJ, 815, 91, doi: 10.1088/0004-637X/815/2/91

Burchett, J. N., Tripp, T. M., Bordoloi, R., et al. 2016, ApJ, 832, 124, doi: 10.3847/0004-637X/832/2/124

Cantalupo, S., Arrigoni-Battaia, F., Prochaska, J. X., Hennawi, J. F., & Madau, P. 2014, Nature, 506, 63, doi: 10.1038/nature12898

Cecil, G., Bland-Hawthorn, J., & Veilleux, S. 2002, ApJ, 576, 745, doi: 10.1086/341861

Chadayammuri, U., Tremmel, M., Nagai, D., Babul, A., & Quinn, T. 2021, MNRAS, 504, 3922, doi: 10.1093/mnras/stab1010

Chatzikos, M., Bianchi, S., Camilloni, F., et al. 2023, Rev. Mexicana Astron. Astrofis., 59, 327, doi: 10.22201/ia.01851101p.2023.59.02.12

Chen, H.-W., Lanzetta, K. M., & Webb, J. K. 2001, ApJ, 556, 158, doi: 10.1086/321537

Chen, Y.-M., Tremonti, C. A., Heckman, T. M., et al. 2010, AJ, 140, 445, doi: 10.1088/0004-6256/140/2/445

Chen, Z., Fielding, D. B., & Bryan, G. L. 2023, ApJ, 950, 91, doi: 10.3847/1538-4357/acc73f

Chevalier, R. A., & Clegg, A. W. 1985, Nature, 317, 44, doi: 10.1038/317044a0

Chevalier, R. A., & Gardner, J. 1974, ApJ, 192, 457, doi: 10.1086/153077

Chisholm, J., Tremonti, C. A., Leitherer, C., & Chen, Y. 2017, MNRAS, 469, 4831, doi: 10.1093/mnras/stx1164

Choi, E., Ostriker, J. P., Naab, T., Oser, L., & Moster, B. P. 2015, MNRAS, 449, 4105, doi: 10.1093/mnras/stv575

Christensen, C. R., Davé, R., Governato, F., et al. 2016, ApJ, 824, 57, doi: 10.3847/0004-637X/824/1/57

Cioffi, D. F., McKee, C. F., & Bertschinger, E. 1988, ApJ, 334, 252, doi: 10.1086/166834

Coker, C. T., Thompson, T. A., & Martini, P. 2013, ApJ, 778, 79, doi: 10.1088/0004-637X/778/1/79

Cooksey, K. L., Thom, C., Prochaska, J. X., & Chen, H.-W. 2010, ApJ, 708, 868, doi: 10.1088/0004-637X/708/1/868

Cooper, J. L., Bicknell, G. V., Sutherland, R. S., & Bland-Hawthorn, J. 2009, ApJ, 703, 330, doi: 10.1088/0004-637X/703/1/330

Cooper, T. J., Simcoe, R. A., Cooksey, K. L., O'Meara, J. M., & Torrey, P. 2015, ApJ, 812, 58, doi: 10.1088/0004-637X/812/1/58

Corlies, L., & Schiminovich, D. 2016a, ApJ, 827, 148, doi: 10.3847/0004-637X/827/2/148

—. 2016b, ApJ, 827, 148, doi: 10.3847/0004-637X/827/2/148

Crain, R. A., & van de Voort, F. 2023, ARA&A, 61, 473, doi: 10.1146/annurev-astro-041923-043618

Crain, R. A., Schaye, J., Bower, R. G., et al. 2015, MNRAS, 450, 1937, doi: 10.1093/mnras/stv725

Crocker, R. M., Krumholz, M. R., Thompson, T. A., Baumgardt, H., & Mackey, D. 2018, MNRAS, 481, 4895, doi: 10.1093/mnras/sty2659

Dale, J. E., Ercolano, B., & Bonnell, I. A. 2012, MNRAS, 424, 377, doi: 10.1111/j.1365-2966.2012.21205.x

Dalla Vecchia, C., & Schaye, J. 2012, MNRAS, 426, 140, doi: 10.1111/j.1365-2966.2012.21704.x

Danforth, C. W., Keeney, B. A., Tilton, E. M., et al. 2016, ApJ, 817, 111, doi: 10.3847/0004-637X/817/2/111

Das, H. K., Choudhury, P. P., & Sharma, P. 2021, MNRAS, 502, 4935, doi: 10.1093/mnras/stab382

Davé, R., Rafieferantsoa, M. H., Thompson, R. J., & Hopkins, P. F. 2017, MNRAS, 467, 115, doi: 10.1093/mnras/stx108

Davies, J. J., Crain, R. A., McCarthy, I. G., et al. 2019, MNRAS, 485, 3783, doi: 10.1093/mnras/stz635

Davies, J. J., Crain, R. A., Oppenheimer, B. D., & Schaye, J. 2020, MNRAS, 491, 4462, doi: 10.1093/mnras/stz3201

Davies, J. J., Crain, R. A., & Pontzen, A. 2021, MNRAS, 501, 236, doi: 10.1093/mnras/staa3643

Davies, J. J., Pontzen, A., & Crain, R. A. 2022, MNRAS, 515, 1430, doi: 10.1093/mnras/stac1742

—. 2024, MNRAS, 527, 4705, doi: 10.1093/mnras/stad3456

Davis, B. L., Graham, A. W., & Seigar, M. S. 2017, MNRAS, 471, 2187, doi: 10.1093/mnras/stx1794

Dekel, A., & Birnboim, Y. 2006, MNRAS, 368, 2, doi: 10.1111/j.1365-2966.2006.10145.x

Dekel, A., & Silk, J. 1986, ApJ, 303, 39, doi: 10.1086/164050

Dekel, A., & Woo, J. 2003, MNRAS, 344, 1131, doi: 10.1046/j.1365-8711.2003.06923.x

Diesing, R., & Caprioli, D. 2018, Phys. Rev. Lett., 121, 091101, doi: 10.1103/PhysRevLett.121.091101

D'Odorico, V., Calura, F., Cristiani, S., & Viel, M. 2010, MNRAS, 401, 2715, doi: 10.1111/j.1365-2966.2009.15856.x

Donahue, M., & Voit, G. M. 2022, Phys. Rep., 973, 1, doi: 10.1016/j.physrep.2022.04.005

Dopita, M. A., & Sutherland, R. S. 1996, ApJS, 102, 161, doi: 10.1086/192255

Draine, B. T. 2011, Physics of the Interstellar and Intergalactic Medium

Du, X., Shapley, A. E., Martin, C. L., & Coil, A. L. 2016, ApJ, 829, 64, doi: 10.3847/0004-637X/829/2/64

Dursi, L. J., & Pfrommer, C. 2008, ApJ, 677, 993, doi: 10.1086/529371

Dutta, R., Fumagalli, M., Fossati, M., et al. 2020, MNRAS, 499, 5022, doi: 10.1093/mnras/staa3147

—. 2021, MNRAS, 508, 4573, doi: 10.1093/mnras/stab2752

Edgar, R. J., & Chevalier, R. A. 1986, ApJ, 310, L27, doi: 10.1086/184775

Efstathiou, G. 1992, MNRAS, 256, 43P, doi: 10.1093/mnras/256.1.43P

Ellison, S. L., Wong, T., Sánchez, S. F., et al. 2021, MNRAS, 505, L46, doi: 10.1093/mnrasl/slab047

Elmegreen, B. G., & Scalo, J. 2004, ARA&A, 42, 211, doi: 10.1146/annurev.astro.41.011802.094859

Emerick, A., Bryan, G. L., & Mac Low, M.-M. 2018, ApJ, 865, L22, doi: 10.3847/2041-8213/aae315

Everett, J. E., Zweibel, E. G., Benjamin, R. A., et al. 2008, ApJ, 674, 258, doi: 10.1086/524766

Fabian, A. C., Nulsen, P. E. J., & Canizares, C. R. 1984, Nature, 310, 733, doi: 10.1038/310733a0

Faerman, Y., Pandya, V., Somerville, R. S., & Sternberg, A. 2022, ApJ, 928, 37, doi: 10.3847/1538-4357/ac4ca6

Faerman, Y., Piacitelli, D. R., McQuinn, M., & Werk, J. K. 2025, ApJ, 983, 176, doi: 10.3847/1538-4357/ada773

Faerman, Y., Sternberg, A., & McKee, C. F. 2020, ApJ, 893, 82, doi: 10.3847/1538-4357/ab7ffc

Faerman, Y., & Werk, J. K. 2023, ApJ, 956, 92, doi: 10.3847/1538-4357/acf217

Faucher-Giguère, C.-A., Hopkins, P. F., Kereš, D., et al. 2015, MNRAS, 449, 987, doi: 10.1093/mnras/stv336

Faucher-Giguère, C.-A., Kereš, D., & Ma, C.-P. 2011a, MNRAS, 417, 2982, doi: 10.1111/j.1365-2966.2011.19457.x

—. 2011b, MNRAS, 417, 2982, doi: 10.1111/j.1365-2966.2011.19457.x

Faucher-Giguère, C.-A., & Oh, S. P. 2023, ARA&A, 61, 131, doi: 10.1146/annurev-astro-052920-125203

Faucher-Giguère, C.-A., & Quataert, E. 2012, MNRAS, 425, 605, doi: 10.1111/j.1365-2966.2012.21512.x

Ferland, G. J., Korista, K. T., Verner, D. A., et al. 1998, PASP, 110, 761, doi: 10.1086/316190

Ferland, G. J., Porter, R. L., van Hoof, P. A. M., et al. 2013, Rev. Mexicana Astron. Astrofis., 49, 137. https://arxiv.org/abs/1302.4485

Ferland, G. J., Chatzikos, M., Guzmán, F., et al. 2017, Rev. Mexicana Astron. Astrofis., 53, 385, doi: 10.48550/arXiv.1705.10877

Fermi, E. 1949, Physical Review, 75, 1169, doi: 10.1103/PhysRev.75.1169

Ferrarese, L., & Merritt, D. 2000, ApJ, 539, L9, doi: 10.1086/312838

Field, G. B. 1965, ApJ, 142, 531, doi: 10.1086/148317

Fielding, D., Quataert, E., Martizzi, D., & Faucher-Giguère, C.-A. 2017a, MNRAS, 470, L39, doi: 10.1093/mnrasl/slx072

Fielding, D., Quataert, E., McCourt, M., & Thompson, T. A. 2017b, MNRAS, 466, 3810, doi: 10.1093/mnras/stw3326

Fielding, D. B., & Bryan, G. L. 2022, ApJ, 924, 82, doi: 10.3847/1538-4357/ac2f41

Fielding, D. B., Ostriker, E. C., Bryan, G. L., & Jermyn, A. S. 2020, ApJ, 894, L24, doi: 10.3847/2041-8213/ab8d2c

Ford, A. B., Davé, R., Oppenheimer, B. D., et al. 2014, MNRAS, 444, 1260, doi: 10.1093/mnras/stu1418

Fox, A., & Davé, R., eds. 2017, Astrophysics and Space Science Library, Vol. 430, Gas Accretion onto Galaxies, doi: 10.1007/978-3-319-52512-9

Fox, A. J., Ledoux, C., Petitjean, P., & Srianand, R. 2007, A&A, 473, 791, doi: 10.1051/0004-6361:20077640

Fox, A. J., Prochaska, J. X., Ledoux, C., et al. 2009, A&A, 503, 731, doi: 10.1051/0004-6361/200911717

Fox, A. J., Savage, B. D., & Wakker, B. P. 2006, ApJS, 165, 229, doi: 10.1086/504800

Fox, A. J., Savage, B. D., Wakker, B. P., et al. 2004, ApJ, 602, 738, doi: 10.1086/381024

Fox, A. J., Wakker, B. P., Savage, B. D., et al. 2005, ApJ, 630, 332, doi: 10.1086/431915

Fraternali, F., Marasco, A., Armillotta, L., & Marinacci, F. 2015, MNRAS, 447, L70, doi: 10.1093/mnrasl/slu182

Froning, C. S., & Green, J. C. 2009, Ap&SS, 320, 181, doi: 10.1007/s10509-008-9758-y

Fujita, A., & Mac Low, M.-M. 2018, MNRAS, 477, 531, doi: 10.1093/mnras/sty715

Fumagalli, M., Hennawi, J. F., Prochaska, J. X., et al. 2014, ApJ, 780, 74, doi: 10.1088/0004-637X/780/1/74

Fumagalli, M., O'Meara, J. M., & Prochaska, J. X. 2011a, Science, 334, 1245, doi: 10.1126/science.1213581

Fumagalli, M., Prochaska, J. X., Kasen, D., et al. 2011b, MNRAS, 418, 1796, doi: 10.1111/j.1365-2966.2011.19599.x

Gabor, J. M., & Davé, R. 2012, MNRAS, 427, 1816, doi: 10.1111/j.1365-2966.2012.21640.x

Gabor, J. M., Davé, R., Finlator, K., & Oppenheimer, B. D. 2010, MNRAS, 407, 749, doi: 10.1111/j.1365-2966.2010.16961.x

Gallazzi, A., Brinchmann, J., Charlot, S., & White, S. D. M. 2008, MNRAS, 383, 1439, doi: 10.1111/j.1365-2966.2007.12632.x

Garza, S. L., Werk, J. K., Berg, T. A. M., et al. 2025, ApJ, 978, L12, doi: 10.3847/2041-8213/ad9c69

Garza, S. L., Werk, J. K., Oppenheimer, B. D., et al. 2024, ApJ, 970, 115, doi: 10.3847/1538-4357/ad4ecc

Gauthier, J.-R., Chen, H.-W., & Tinker, J. L. 2010, ApJ, 716, 1263, doi: 10.1088/0004-637X/716/2/1263

Gebhardt, K., Bender, R., Bower, G., et al. 2000, ApJ, 539, L13, doi: 10.1086/312840

Ghez, A. M., Salim, S., Hornstein, S. D., et al. 2005, ApJ, 620, 744, doi: 10.1086/427175

Gillessen, S., Eisenhauer, F., Trippe, S., et al. 2009, ApJ, 692, 1075, doi: 10.1088/0004-637X/692/2/1075

Gilman, R. C. 1972, ApJ, 178, 423, doi: 10.1086/151800

Glidden, A., Cooper, T. J., Cooksey, K. L., Simcoe, R. A., & O'Meara, J. M. 2016, ApJ, 833, 270, doi: 10.3847/1538-4357/833/2/270

Gnat, O., & Sternberg, A. 2007, ApJS, 168, 213, doi: 10.1086/509786

—. 2009, ApJ, 693, 1514, doi: 10.1088/0004-637X/693/2/1514

Gnat, O., Sternberg, A., & McKee, C. F. 2010, ApJ, 718, 1315, doi: 10.1088/0004-637X/718/2/1315

GRAVITY Collaboration, Abuter, R., Amorim, A., et al. 2018, A&A, 615, L15, doi: 10.1051/0004-6361/201833718

Green, J. C., Froning, C. S., Osterman, S., et al. 2012, ApJ, 744, 60, doi: 10.1088/0004-637X/744/1/6010.1086/141956

Grenier, I. A., Black, J. H., & Strong, A. W. 2015, ARA&A, 53, 199, doi: 10.1146/annurev-astro-082214-122457

Grimes, J. P., Heckman, T., Aloisi, A., et al. 2009, ApJS, 181, 272, doi: 10.1088/0067-0049/181/1/272

Gronke, M., & Oh, S. P. 2018, MNRAS, 480, L111, doi: 10.1093/mnrasl/sly131

—. 2020a, MNRAS, 492, 1970, doi: 10.1093/mnras/stz3332

—. 2020b, MNRAS, 494, L27, doi: 10.1093/mnrasl/slaa033

Gronke, M., Oh, S. P., Ji, S., & Norman, C. 2022, MNRAS, 511, 859, doi: 10.1093/mnras/stab3351

Haardt, F., & Madau, P. 2012, ApJ, 746, 125, doi: 10.1088/0004-637X/746/2/125

Haehnelt, M. G., Natarajan, P., & Rees, M. J. 1998, MNRAS, 300, 817, doi: 10.1046/j.1365-8711.1998.01951.x

Hafen, Z., Faucher-Giguère, C.-A., Anglés-Alcázar, D., et al. 2017, MNRAS, 469, 2292, doi: 10.1093/mnras/stx952

Haid, S., Walch, S., Seifried, D., et al. 2018, MNRAS, 478, 4799, doi: 10.1093/mnras/sty1315

Haislmaier, K. J., Tripp, T. M., Katz, N., et al. 2021, MNRAS, 502, 4993, doi: 10.1093/mnras/staa3544

Häring, N., & Rix, H.-W. 2004, ApJ, 604, L89, doi: 10.1086/383567

Hasan, F., Churchill, C. W., Stemock, B., et al. 2020, ApJ, 904, 44, doi: 10.3847/1538-4357/abbe0b

Hayes, M., Melinder, J., Östlin, G., et al. 2016, ApJ, 828, 49, doi: 10.3847/0004-637X/828/1/49

Heckman, T., Borthakur, S., Wild, V., Schiminovich, D., & Bordoloi, R. 2017, ApJ, 846, 151, doi: 10.3847/1538-4357/aa80dc

Heckman, T. M., Alexandroff, R. M., Borthakur, S., Overzier, R., & Leitherer, C. 2015, ApJ, 809, 147, doi: 10.1088/0004-637X/809/2/147

Heckman, T. M., Armus, L., & Miley, G. K. 1990, ApJS, 74, 833, doi: 10.1086/191522

Heckman, T. M., Lehnert, M. D., & Armus, L. 1993, in Astrophysics and Space Science Library, Vol. 188, The Environment and Evolution of Galaxies, ed. J. M. Shull & H. A. Thronson, 455, doi: 10.1007/978-94-011-1882-8_25

Heckman, T. M., Lehnert, M. D., Strickland, D. K., & Armus, L. 2000, ApJS, 129, 493, doi: 10.1086/313421

Heckman, T. M., Norman, C. A., Strickland, D. K., & Sembach, K. R. 2002, ApJ, 577, 691, doi: 10.1086/342232

Heckman, T. M., & Thompson, T. A. 2017, in Handbook of Supernovae, ed. A. W. Alsabti & P. Murdin, 2431, doi: 10.1007/978-3-319-21846-5_23

Helder, E. A., Vink, J., Bykov, A. M., et al. 2012, Space Sci. Rev., 173, 369, doi: 10.1007/s11214-012-9919-8

Henley, D. B., Kwak, K., & Shelton, R. L. 2012, ApJ, 753, 58, doi: 10.1088/0004-637X/753/1/58

Hennawi, J. F., Prochaska, J. X., Cantalupo, S., & Arrigoni-Battaia, F. 2015, Science, 348, 779, doi: 10.1126/science.aaa5397

Henry, A., Scarlata, C., Martin, C. L., & Erb, D. 2015, ApJ, 809, 19, doi: 10.1088/0004-637X/809/1/19

Henry, R. B. C. 1993, MNRAS, 261, 306, doi: 10.1093/mnras/261.2.306

Ho, L. C., Filippenko, A. V., & Sargent, W. L. W. 1997, ApJ, 487, 568, doi: 10.1086/304638

Ho, S. H., Martin, C. L., Kacprzak, G. G., & Churchill, C. W. 2017, ApJ, 835, 267, doi: 10.3847/1538-4357/835/2/267

Hodges-Kluck, E., Cafmeyer, J., & Bregman, J. N. 2016, ApJ, 833, 58, doi: 10.3847/1538-4357/833/1/58

Hopkins, P. F. 2013, MNRAS, 428, 2840, doi: 10.1093/mnras/sts210

Hu, W., & Kravtsov, A. V. 2003, ApJ, 584, 702, doi: 10.1086/345846

Hummels, C. B., Smith, B. D., & Silvia, D. W. 2017, ApJ, 847, 59, doi: 10.3847/1538-4357/aa7e2d

Humphrey, P. J., Buote, D. A., Canizares, C. R., Fabian, A. C., & Miller, J. M. 2011, ApJ, 729, 53, doi: 10.1088/0004-637X/729/1/53

Hussain, T., Muzahid, S., Narayanan, A., et al. 2015, MNRAS, 446, 2444, doi: 10.1093/mnras/stu2285

Hutton, S., Ferreras, I., Wu, K., et al. 2014, MNRAS, 440, 150, doi: 10.1093/mnras/stu185

Iffrig, O., & Hennebelle, P. 2015, A&A, 576, A95, doi: 10.1051/0004-6361/201424556

Indebetouw, R., & Shull, J. M. 2004, ApJ, 605, 205, doi: 10.1086/382186

Ipavich, F. M. 1975, ApJ, 196, 107, doi: 10.1086/153397

Ishiki, S., & Okamoto, T. 2017, MNRAS, 466, L123, doi: 10.1093/mnrasl/slw253

Ishiki, S., Okamoto, T., & Inoue, A. K. 2018, MNRAS, 474, 1935, doi: 10.1093/mnras/stx2833

Jacob, S., Pakmor, R., Simpson, C. M., Springel, V., & Pfrommer, C. 2018, MNRAS, 475, 570, doi: 10.1093/mnras/stx3221

James, B. L., Berg, D. A., King, T., et al. 2022, ApJS, 262, 37, doi: 10.3847/1538-4365/ac8008

Jenkins, E. B., Bowen, D. V., Tripp, T. M., & Sembach, K. R. 2005, ApJ, 623, 767, doi: 10.1086/428878

Jennings, F., Beckmann, R. S., Sijacki, D., & Dubois, Y. 2023, MNRAS, 518, 5215, doi: 10.1093/mnras/stac3426

Ji, S., Oh, S. P., & Masterson, P. 2019, MNRAS, 487, 737, doi: 10.1093/mnras/stz1248

Ji, S., Oh, S. P., & McCourt, M. 2018, MNRAS, 476, 852, doi: 10.1093/mnras/sty293

Jiang, Y.-F., & Oh, S. P. 2018, ApJ, 854, 5, doi: 10.3847/1538-4357/aaa6ce

Johnson, J. A. 2019, Science, 363, 474, doi: 10.1126/science.aau9540

Johnson, S. D., Chen, H.-W., & Mulchaey, J. S. 2015a, MNRAS, 452, 2553, doi: 10.1093/mnras/stv1481

—. 2015b, MNRAS, 449, 3263, doi: 10.1093/mnras/stv553

Jones, T., Stark, D. P., & Ellis, R. S. 2018, ApJ, 863, 191, doi: 10.3847/1538-4357/aad37f

Jones, T. W., Gaalaas, J. B., Ryu, D., & Frank, A. 1997, ApJ, 482, 230, doi: 10.1086/304145

Jung, S. L., Rennehan, D., Saeedzadeh, V., et al. 2022, MNRAS, 515, 22, doi: 10.1093/mnras/stac1622

Kabasares, K. M., Cohn, J. H., Barth, A. J., et al. 2024, ApJ, 966, 132, doi: 10.3847/1538-4357/ad2f36

Kacprzak, G. G., Vander Vliet, J. R., Nielsen, N. M., et al. 2019, ApJ, 870, 137, doi: 10.3847/1538-4357/aaf1a6

Kauffmann, G., Heckman, T. M., White, S. D. M., et al. 2003, MNRAS, 341, 33, doi: 10.1046/j.1365-8711.2003.06291.x

Kennicutt, R. C., & Evans, N. J. 2012, ARA&A, 50, 531, doi: 10.1146/annurev-astro-081811-125610

Kereš, D., & Hernquist, L. 2009, ApJ, 700, L1, doi: 10.1088/0004-637X/700/1/L1

Kereš, D., Katz, N., Fardal, M., Davé, R., & Weinberg, D. H. 2009, MNRAS, 395, 160, doi: 10.1111/j.1365-2966.2009.14541.x

Kereš, D., Katz, N., Weinberg, D. H., & Davé, R. 2005, MNRAS, 363, 2, doi: 10.1111/j.1365-2966.2005.09451.x

Khaire, V., & Srianand, R. 2019, MNRAS, 484, 4174, doi: 10.1093/mnras/stz174

Kim, C.-G., & Ostriker, E. C. 2015, ApJ, 802, 99, doi: 10.1088/0004-637X/802/2/99

Klassen, M., Pudritz, R. E., Kuiper, R., Peters, T., & Banerjee, R. 2016, ApJ, 823, 28, doi: 10.3847/0004-637X/823/1/28

Klein, R. I., McKee, C. F., & Colella, P. 1994, ApJ, 420, 213, doi: 10.1086/173554

Kormendy, J., & Ho, L. C. 2013, ARA&A, 51, 511, doi: 10.1146/annurev-astro-082708-101811

Kormendy, J., & Richstone, D. 1995, ARA&A, 33, 581, doi: 10.1146/annurev.aa.33.090195.003053

Kornei, K. A., Shapley, A. E., Martin, C. L., et al. 2012, ApJ, 758, 135, doi: 10.1088/0004-637X/758/2/135

Koss, M. J., Trakhtenbrot, B., Ricci, C., et al. 2022, ApJS, 261, 6, doi: 10.3847/1538-4365/ac650b

Kroupa, P. 2001, MNRAS, 322, 231, doi: 10.1046/j.1365-8711.2001.04022.x

Krumholz, M. R., & Matzner, C. D. 2009, ApJ, 703, 1352, doi: 10.1088/0004-637X/703/2/1352

Krymskii, G. F. 1977, Akademiia Nauk SSSR Doklady, 234, 1306

Kuiper, R., Klahr, H., Beuther, H., & Henning, T. 2011, ApJ, 732, 20, doi: 10.1088/0004-637X/732/1/20

—. 2012, A&A, 537, A122, doi: 10.1051/0004-6361/201117808

Kuiper, R., Turner, N. J., & Yorke, H. W. 2016, ApJ, 832, 40, doi: 10.3847/0004-637X/832/1/40

Kumar, S., & Chen, H.-W. 2025, arXiv e-prints, arXiv:2501.13170, doi: 10.48550/arXiv.2501.13170

Kwak, K., Henley, D. B., & Shelton, R. L. 2011, ApJ, 739, 30, doi: 10.1088/0004-637X/739/1/30

Kwak, K., & Shelton, R. L. 2010, ApJ, 719, 523, doi: 10.1088/0004-637X/719/1/523

Kwak, K., Shelton, R. L., & Henley, D. B. 2015, ApJ, 812, 111, doi: 10.1088/0004-637X/812/2/111

Lamers, H. J. G. L. M., & Levesque, E. M. 2017, Understanding Stellar Evolution, doi: 10.1088/978-0-7503-1278-3

Lan, T.-W. 2020, ApJ, 897, 97, doi: 10.3847/1538-4357/ab989a

Läsker, R., Greene, J. E., Seth, A., et al. 2016, ApJ, 825, 3, doi: 10.3847/0004-637X/825/1/3

Lau, M. W., Prochaska, J. X., & Hennawi, J. F. 2016, ApJS, 226, 25, doi: 10.3847/0067-0049/226/2/25

Lee, L. 2020, NADA: Nondetects and Data Analysis for Environmental Data. https://CRAN.R-project.org/package=NADA

Lehner, N., & Howk, J. C. 2011, Science, 334, 955, doi: 10.1126/science.1209069

Lehner, N., Howk, J. C., & Wakker, B. P. 2015, ApJ, 804, 79, doi: 10.1088/0004-637X/804/2/79

Lehner, N., O'Meara, J. M., Fox, A. J., et al. 2014, ApJ, 788, 119, doi: 10.1088/0004-637X/788/2/119

Lehner, N., Prochaska, J. X., Kobulnicky, H. A., et al. 2009, ApJ, 694, 734, doi: 10.1088/0004-637X/694/2/734

Lehner, N., Wotta, C. B., Howk, J. C., et al. 2018, ApJ, 866, 33, doi: 10.3847/1538-4357/aadd03

—. 2019, ApJ, 887, 5, doi: 10.3847/1538-4357/ab41fd

Lehner, N., Zech, W. F., Howk, J. C., & Savage, B. D. 2011, ApJ, 727, 46, doi: 10.1088/0004-637X/727/1/46

Lehner, N., Howk, J. C., Tripp, T. M., et al. 2013, ApJ, 770, 138, doi: 10.1088/0004-637X/770/2/138

Lehner, N., Berek, S. C., Howk, J. C., et al. 2020, ApJ, 900, 9, doi: 10.3847/1538-4357/aba49c

Lehnert, M. D., Le Tiran, L., Nesvadba, N. P. H., et al. 2013, A&A, 555, A72, doi: 10.1051/0004-6361/201220555

Leroy, A. K., Walter, F., Martini, P., et al. 2015, ApJ, 814, 83, doi: 10.1088/0004-637X/814/2/83

Lewis, A. R., Dolphin, A. E., Dalcanton, J. J., et al. 2015, ApJ, 805, 183, doi: 10.1088/0004-637X/805/2/183

Li, Z., Hopkins, P. F., Squire, J., & Hummels, C. 2020, MNRAS, 492, 1841, doi: 10.1093/mnras/stz3567

Liang, C. J., & Chen, H.-W. 2014, MNRAS, 445, 2061, doi: 10.1093/mnras/stu1901

Liang, C. J., & Remming, I. 2020, MNRAS, 491, 5056, doi: 10.1093/mnras/stz3403

Lockhart, K. E., Kewley, L. J., Lu, J. R., et al. 2015, ApJ, 810, 149, doi: 10.1088/0004-637X/810/2/149

Magorrian, J., Tremaine, S., Richstone, D., et al. 1998, AJ, 115, 2285, doi: 10.1086/300353

Mandelker, N., van den Bosch, F. C., Springel, V., & van de Voort, F. 2019, ApJ, 881, L20, doi: 10.3847/2041-8213/ab30cb

Marinacci, F., Binney, J., Fraternali, F., et al. 2010, MNRAS, 404, 1464, doi: 10.1111/j.1365-2966.2010.16352.x

Martin, C. L. 2005, ApJ, 621, 227, doi: 10.1086/427277

Martin, C. L., Shapley, A. E., Coil, A. L., et al. 2012, ApJ, 760, 127, doi: 10.1088/0004-637X/760/2/127

—. 2013, ApJ, 770, 41, doi: 10.1088/0004-637X/770/1/41

Martin, D. C., Matuszewski, M., Morrissey, P., et al. 2015, Nature, 524, 192, doi: 10.1038/nature14616

Martizzi, D., Faucher-Giguère, C.-A., & Quataert, E. 2015, MNRAS, 450, 504, doi: 10.1093/mnras/stv562

Mastrodemos, N., Morris, M., & Castor, J. 1996, ApJ, 468, 851, doi: 10.1086/177741

Matejek, M. S., & Simcoe, R. A. 2012, ApJ, 761, 112, doi: 10.1088/0004-637X/761/2/112

Mathes, N. L., Churchill, C. W., Kacprzak, G. G., et al. 2014, ApJ, 792, 128, doi: 10.1088/0004-637X/792/2/128

Mathews, W. G., & Prochaska, J. X. 2017, ApJ, 846, L24, doi: 10.3847/2041-8213/aa8861

Matzner, C. D. 2002, ApJ, 566, 302, doi: 10.1086/338030

McConnell, N. J., & Ma, C.-P. 2013, ApJ, 764, 184, doi: 10.1088/0004-637X/764/2/184

McCormick, A., Veilleux, S., Meléndez, M., et al. 2018, MNRAS, 477, 699, doi: 10.1093/mnras/sty634

McCourt, M., Oh, S. P., O'Leary, R., & Madigan, A.-M. 2018, MNRAS, 473, 5407, doi: 10.1093/mnras/stx2687

McCourt, M., O'Leary, R. M., Madigan, A.-M., & Quataert, E. 2015, MNRAS, 449, 2, doi: 10.1093/mnras/stv355

McCourt, M., Sharma, P., Quataert, E., & Parrish, I. J. 2012, MNRAS, 419, 3319, doi: 10.1111/j.1365-2966.2011.19972.x

McDowell, J. C., Clements, D. L., Lamb, S. A., et al. 2003, ApJ, 591, 154, doi: 10.1086/375289

McKee, C. F. 1989, ApJ, 345, 782, doi: 10.1086/167950

McKee, C. F., & Ostriker, J. P. 1977, ApJ, 218, 148, doi: 10.1086/155667

McKee, C. F., van Buren, D., & Lazareff, B. 1984, ApJ, 278, L115, doi: 10.1086/184237

McQuinn, M., & Werk, J. K. 2018, ApJ, 852, 33, doi: 10.3847/1538-4357/aa9d3f

Meier, D. S., Walter, F., Bolatto, A. D., et al. 2015, ApJ, 801, 63, doi: 10.1088/0004-637X/801/1/63

Meléndez, M., Veilleux, S., Martin, C., et al. 2015, ApJ, 804, 46, doi: 10.1088/0004-637X/804/1/46

Mellema, G., Kurk, J. D., & Röttgering, H. J. A. 2002, A&A, 395, L13, doi: 10.1051/0004-6361:20021408

Menon, H., Wesolowski, L., Zheng, G., et al. 2015, Computational Astrophysics and Cosmology, 2, 1, doi: 10.1186/s40668-015-0007-9

Miyoshi, M., Moran, J., Herrnstein, J., et al. 1995, Nature, 373, 127, doi: 10.1038/373127a0

Mo, H. J., Yang, X., van den Bosch, F. C., & Jing, Y. P. 2004, MNRAS, 349, 205, doi: 10.1111/j.1365-2966.2004.07485.x

Molina, M., Eracleous, M., Barth, A. J., et al. 2018, ApJ, 864, 90, doi: 10.3847/1538-4357/aad5ed

Monroe, T. R., Prochaska, J. X., Tejos, N., et al. 2016, AJ, 152, 25, doi: 10.3847/0004-6256/152/1/25

Morlino, G., & Caprioli, D. 2012, A&A, 538, A81, doi: 10.1051/0004-6361/201117855

Muratov, A. L., Kereš, D., Faucher-Giguère, C.-A., et al. 2015, MNRAS, 454, 2691, doi: 10.1093/mnras/stv2126

—. 2017, MNRAS, 468, 4170, doi: 10.1093/mnras/stx667

Muzahid, S., Srianand, R., Bergeron, J., & Petitjean, P. 2012, MNRAS, 421, 446, doi: 10.1111/j.1365-2966.2011.20324.x

Naab, T., & Ostriker, J. P. 2017, ARA&A, 55, 59, doi: 10.1146/annurev-astro-081913-040019

Narayanan, A., Savage, B. D., & Wakker, B. P. 2012, ApJ, 752, 65, doi: 10.1088/0004-637X/752/1/65

Narayanan, A., Wakker, B. P., Savage, B. D., et al. 2010, ApJ, 721, 960, doi: 10.1088/0004-637X/721/2/960

Narayanan, A., Savage, B. D., Wakker, B. P., et al. 2011, ApJ, 730, 15, doi: 10.1088/0004-637X/730/1/15

Navarro, J. F., Frenk, C. S., & White, S. D. M. 1997, ApJ, 490, 493, doi: 10.1086/304888

Nelson, D., Genel, S., Vogelsberger, M., et al. 2015, MNRAS, 448, 59, doi: 10.1093/mnras/stv017

Nelson, D., Pillepich, A., Springel, V., et al. 2018a, MNRAS, 475, 624, doi: 10.1093/mnras/stx3040

Nelson, D., Kauffmann, G., Pillepich, A., et al. 2018b, MNRAS, 477, 450, doi: 10.1093/mnras/sty656

Nelson, D., Pillepich, A., Springel, V., et al. 2019, MNRAS, 490, 3234, doi: 10.1093/mnras/stz2306

Nielsen, N. M., Churchill, C. W., Kacprzak, G. G., Murphy, M. T., & Evans, J. L. 2015, ApJ, 812, 83, doi: 10.1088/0004-637X/812/1/83

Nielsen, N. M., Fisher, D. B., Kacprzak, G. G., et al. 2024, Nature Astronomy, 8, 1602, doi: 10.1038/s41550-024-02365-x

Noh, Y., & McQuinn, M. 2014, MNRAS, 444, 503, doi: 10.1093/mnras/stu1412

Oppenheimer, B. D. 2018, MNRAS, 480, 2963, doi: 10.1093/mnras/sty1918

Oppenheimer, B. D., Davé, R., Kereš, D., et al. 2010, MNRAS, 406, 2325, doi: 10.1111/j.1365-2966.2010.16872.x

Oppenheimer, B. D., & Schaye, J. 2013a, MNRAS, 434, 1063, doi: 10.1093/mnras/stt1150

—. 2013b, MNRAS, 434, 1043, doi: 10.1093/mnras/stt1043

—. 2013c, MNRAS, 434, 1063, doi: 10.1093/mnras/stt1150

Oppenheimer, B. D., Schaye, J., Crain, R. A., Werk, J. K., & Richings, A. J. 2018, MNRAS, 481, 835, doi: 10.1093/mnras/sty2281

Oppenheimer, B. D., Crain, R. A., Schaye, J., et al. 2016, MNRAS, 460, 2157, doi: 10.1093/mnras/stw1066

Oppenheimer, B. D., Davies, J. J., Crain, R. A., et al. 2020, MNRAS, 491, 2939, doi: 10.1093/mnras/stz3124

Ostriker, J. P., & McKee, C. F. 1988, Reviews of Modern Physics, 60, 1, doi: 10.1103/RevModPhys.60.1

Pakmor, R., & Springel, V. 2013, MNRAS, 432, 176, doi: 10.1093/mnras/stt428

Pandya, V., Fielding, D. B., Anglés-Alcázar, D., et al. 2021, MNRAS, 508, 2979, doi: 10.1093/mnras/stab2714

Pâris, I., Petitjean, P., Aubourg, É., et al. 2018, A&A, 613, A51, doi: 10.1051/0004-6361/201732445

Peeples, M. S., Werk, J. K., Tumlinson, J., et al. 2014, ApJ, 786, 54, doi: 10.1088/0004-637X/786/1/54

Péroux, C., & Howk, J. C. 2020, ARA&A, 58, 363, doi: 10.1146/annurev-astro-021820-120014

Piacitelli, D. R., Solhaug, E., Faerman, Y., & McQuinn, M. 2022, MNRAS, 516, 3049, doi: 10.1093/mnras/stac2390

Pieri, M. M., Mortonson, M. J., Frank, S., et al. 2014, MNRAS, 441, 1718, doi: 10.1093/mnras/stu577

Pilawa, J., Liepold, E. R., Ma, C.-P., Walsh, J. L., & Greene, J. E. 2025, arXiv e-prints, arXiv:2504.01071, doi: 10.48550/arXiv.2504.01071

Pillepich, A., Springel, V., Nelson, D., et al. 2018, MNRAS, 473, 4077, doi: 10.1093/mnras/stx2656

Piotrowska, J. M., Bluck, A. F. L., Maiolino, R., & Peng, Y. 2022, MNRAS, 512, 1052, doi: 10.1093/mnras/stab3673

Pittard, J. M., Dyson, J. E., Falle, S. A. E. G., & Hartquist, T. W. 2005, MNRAS, 361, 1077, doi: 10.1111/j.1365-2966.2005.09268.x

Planck Collaboration, Ade, P. A. R., Aghanim, N., et al. 2013, A&A, 557, A52, doi: 10.1051/0004-6361/201220941

—. 2016, A&A, 594, A13, doi: 10.1051/0004-6361/201525830

Pontzen, A., Roškar, R., Stinson, G. S., et al. 2013, pynbody: Astrophysics Simulation Analysis for Python

Prescott, M. K. M., Martin, C. L., & Dey, A. 2015, ApJ, 799, 62, doi: 10.1088/0004-637X/799/1/62

Prochaska, J. X., Henry, R. B. C., O'Meara, J. M., et al. 2002, PASP, 114, 933, doi: 10.1086/342354

Prochaska, J. X., Weiner, B., Chen, H. W., Mulchaey, J., & Cooksey, K. 2011, ApJ, 740, 91, doi: 10.1088/0004-637X/740/2/91

Prochaska, J. X., Bloom, J. S., Chen, H.-W., et al. 2004, ApJ, 611, 200, doi: 10.1086/421988

Prochaska, J. X., Werk, J. K., Worseck, G., et al. 2017, ApJ, 837, 169, doi: 10.3847/1538-4357/aa6007

Prochaska, J. X., Burchett, J. N., Tripp, T. M., et al. 2019, ApJS, 243, 24, doi: 10.3847/1538-4365/ab2b9a

Ptuskin, V. S., Voelk, H. J., Zirakashvili, V. N., & Breitschwerdt, D. 1997, A&A, 321, 434

Puchwein, E., & Springel, V. 2013, MNRAS, 428, 2966, doi: 10.1093/mnras/sts243

Putman, M. E., Peek, J. E. G., & Joung, M. R. 2012, ARA&A, 50, 491, doi: 10.1146/annurev-astro-081811-125612

Putman, M. E., Saul, D. R., & Mets, E. 2011, MNRAS, 418, 1575, doi: 10.1111/j.1365-2966.2011.19524.x

Qu, Z., Lindley, R., & Bregman, J. N. 2022, ApJ, 924, 86, doi: 10.3847/1538-4357/ac35cd

Ravi, V., Catha, M., Chen, G., et al. 2023, arXiv e-prints, arXiv:2301.01000, doi: 10.48550/arXiv.2301.01000

Rees, M. J., & Ostriker, J. P. 1977, MNRAS, 179, 541, doi: 10.1093/mnras/179.4.541

Reimers, D., Vogel, S., Hagen, H. J., et al. 1992, Nature, 360, 561, doi: 10.1038/360561a0

Reines, A. E., & Volonteri, M. 2015, ApJ, 813, 82, doi: 10.1088/0004-637X/813/2/82

Ribaudo, J., Lehner, N., Howk, J. C., et al. 2011, ApJ, 743, 207, doi: 10.1088/0004-637X/743/2/207

Richter, P., Savage, B. D., Tripp, T. M., & Sembach, K. R. 2004, ApJS, 153, 165, doi: 10.1086/421297

Rieke, G. H., Alonso-Herrero, A., Weiner, B. J., et al. 2009, ApJ, 692, 556, doi: 10.1088/0004-637X/692/1/556

Rosas-Guevara, Y., Bower, R. G., Schaye, J., et al. 2016, MNRAS, 462, 190, doi: 10.1093/mnras/stw1679

Rosas-Guevara, Y. M., Bower, R. G., Schaye, J., et al. 2015, MNRAS, 454, 1038, doi: 10.1093/mnras/stv2056

Rosen, A. L., Krumholz, M. R., McKee, C. F., & Klein, R. I. 2016, MNRAS, 463, 2553, doi: 10.1093/mnras/stw2153

Roussel, H., Wilson, C. D., Vigroux, L., et al. 2010, A&A, 518, L66, doi: 10.1051/0004-6361/201014567

Rubin, K. H. R., Prochaska, J. X., Koo, D. C., & Phillips, A. C. 2012, ApJ, 747, L26, doi: 10.1088/2041-8205/747/2/L26

Rubin, K. H. R., Prochaska, J. X., Koo, D. C., et al. 2014, ApJ, 794, 156, doi: 10.1088/0004-637X/794/2/156

Rudie, G. C., Steidel, C. C., Pettini, M., et al. 2019, ApJ, 885, 61, doi: 10.3847/1538-4357/ab4255

Rupke, D. S., Veilleux, S., & Sanders, D. B. 2002, ApJ, 570, 588, doi: 10.1086/339789

—. 2005a, ApJS, 160, 87, doi: 10.1086/432886

—. 2005b, ApJS, 160, 115, doi: 10.1086/432889

—. 2005c, ApJ, 632, 751, doi: 10.1086/444451

Rupke, D. S. N. 2018, Galaxies, 6, 138, doi: 10.3390/galaxies6040138

Rupke, D. S. N., & Veilleux, S. 2015, ApJ, 801, 126, doi: 10.1088/0004-637X/801/2/126

Rupke, D. S. N., Coil, A., Geach, J. E., et al. 2019, Nature, 574, 643, doi: 10.1038/s41586-019-1686-1

Saglia, R. P., Opitsch, M., Erwin, P., et al. 2016, ApJ, 818, 47, doi: 10.3847/0004-637X/818/1/47

Saintonge, A., & Catinella, B. 2022, ARA&A, 60, 319, doi: 10.1146/annurev-astro-021022-043545

Sakamoto, K., Okumura, S. K., Ishizuki, S., & Scoville, N. Z. 1999, ApJ, 525, 691, doi: 10.1086/307910

Sakamoto, K., Aalto, S., Wilner, D. J., et al. 2009, ApJ, 700, L104, doi: 10.1088/0004-637X/700/2/L104

Salak, D., Nakai, N., Miyamoto, Y., Yamauchi, A., & Tsuru, T. G. 2013, PASJ, 65, 66, doi: 10.1093/pasj/65.3.66

Salak, D., Tomiyasu, Y., Nakai, N., et al. 2018, ApJ, 856, 97, doi: 10.3847/1538-4357/aab2ac

Salem, M., & Bryan, G. L. 2014, MNRAS, 437, 3312, doi: 10.1093/mnras/stt2121

Sales, L. V., Marinacci, F., Springel, V., & Petkova, M. 2014, MNRAS, 439, 2990, doi: 10.1093/mnras/stu155

Sameer, Lehner, N., Howk, J. C., et al. 2024, ApJ, 975, 264, doi: 10.3847/1538-4357/ad7af2

Sanchez, N. N., Tremmel, M., Werk, J. K., et al. 2021, ApJ, 911, 116, doi: 10.3847/1538-4357/abeb15

Sanchez, N. N., Werk, J. K., Tremmel, M., et al. 2019, ApJ, 882, 8, doi: 10.3847/1538-4357/ab3045

Sanchez, N. N., Werk, J. K., Christensen, C., et al. 2024, ApJ, 967, 100, doi: 10.3847/1538-4357/ad39eb

Savage, B. D., Kim, T. S., Wakker, B. P., et al. 2014, ApJS, 212, 8, doi: 10.1088/0067-0049/212/1/8

Savage, B. D., Lehner, N., & Narayanan, A. 2011, ApJ, 743, 180, doi: 10.1088/0004-637X/743/2/180

Savage, B. D., Sembach, K. R., Tripp, T. M., & Richter, P. 2002, ApJ, 564, 631, doi: 10.1086/324288

Scannapieco, E., & Brüggen, M. 2015, ApJ, 805, 158, doi: 10.1088/0004-637X/805/2/158

Schaan, E., Ferraro, S., Amodeo, S., et al. 2021, Phys. Rev. D, 103, 063513, doi: 10.1103/PhysRevD.103.063513

Schawinski, K., Thomas, D., Sarzi, M., et al. 2007, MNRAS, 382, 1415, doi: 10.1111/j.1365-2966.2007.12487.x

Schawinski, K., Urry, C. M., Simmons, B. D., et al. 2014, MNRAS, 440, 889, doi: 10.1093/mnras/stu327

Schaye, J., & Dalla Vecchia, C. 2008, MNRAS, 383, 1210, doi: 10.1111/j.1365-2966.2007.12639.x

Schaye, J., Dalla Vecchia, C., Booth, C. M., et al. 2010, MNRAS, 402, 1536, doi: 10.1111/j.1365-2966.2009.16029.x

Schaye, J., Crain, R. A., Bower, R. G., et al. 2015, MNRAS, 446, 521, doi: 10.1093/mnras/stu2058

Schiminovich, D., Wyder, T. K., Martin, D. C., et al. 2007, ApJS, 173, 315, doi: 10.1086/524659

Schlickeiser, R. 1989a, ApJ, 336, 243, doi: 10.1086/167009

—. 1989b, ApJ, 336, 264, doi: 10.1086/167010

Schneider, E. E., & Robertson, B. E. 2017, ApJ, 834, 144, doi: 10.3847/1538-4357/834/2/144

Schneider, E. E., Robertson, B. E., & Thompson, T. A. 2018, ApJ, 862, 56, doi: 10.3847/1538-4357/aacce1

Schödel, R., Ott, T., Genzel, R., et al. 2002, Nature, 419, 694, doi: 10.1038/nature01121

Sedov, L. I. 1959, Similarity and Dimensional Methods in Mechanics

Sembach, K. R., Tripp, T. M., Savage, B. D., & Richter, P. 2004, ApJS, 155, 351, doi: 10.1086/425037

Sembach, K. R., Wakker, B. P., Savage, B. D., et al. 2003, ApJS, 146, 165, doi: 10.1086/346231

Shapiro, P. R., & Field, G. B. 1976, ApJ, 205, 762, doi: 10.1086/154332

Sharma, P., McCourt, M., Parrish, I. J., & Quataert, E. 2012a, MNRAS, 427, 1219, doi: 10.1111/j.1365-2966.2012.22050.x

Sharma, P., McCourt, M., Quataert, E., & Parrish, I. J. 2012b, MNRAS, 420, 3174, doi: 10.1111/j.1365-2966.2011.20246.x

Sharma, R. S., Brooks, A. M., Somerville, R. S., et al. 2020, ApJ, 897, 103, doi: 10.3847/1538-4357/ab960e

Shattow, G. M., Croton, D. J., & Bibiano, A. 2015, MNRAS, 450, 2306, doi: 10.1093/mnras/stv653

Shopbell, P. L., & Bland-Hawthorn, J. 1998, ApJ, 493, 129, doi: 10.1086/305108

Sijacki, D., Vogelsberger, M., Genel, S., et al. 2015, MNRAS, 452, 575, doi: 10.1093/mnras/stv1340

Silk, J. 1977, ApJ, 211, 638, doi: 10.1086/154972

Silk, J., & Rees, M. J. 1998, A&A, 331, L1, doi: 10.48550/arXiv.astro-ph/9801013

Simcoe, R. A., Cooksey, K. L., Matejek, M., et al. 2011, ApJ, 743, 21, doi: 10.1088/0004-637X/743/1/21

Slavin, J. D., Shull, J. M., & Begelman, M. C. 1993, ApJ, 407, 83, doi: 10.1086/172494

Sobacchi, E., & Sormani, M. C. 2019, MNRAS, 486, 205, doi: 10.1093/mnras/stz792

Socrates, A., Davis, S. W., & Ramirez-Ruiz, E. 2008, ApJ, 687, 202, doi: 10.1086/590046

Somerville, R. S., & Davé, R. 2015, ARA&A, 53, 51, doi: 10.1146/annurev-astro-082812-140951

Somerville, R. S., & Primack, J. R. 1999, MNRAS, 310, 1087, doi: 10.1046/j.1365-8711.1999.03032.x

Sparre, M., Pfrommer, C., & Vogelsberger, M. 2019, MNRAS, 482, 5401, doi: 10.1093/mnras/sty3063

Springel, V. 2005, MNRAS, 364, 1105, doi: 10.1111/j.1365-2966.2005.09655.x

—. 2010, MNRAS, 401, 791, doi: 10.1111/j.1365-2966.2009.15715.x

Springel, V., & Hernquist, L. 2003a, MNRAS, 339, 312, doi: 10.1046/j.1365-8711.2003.06207.x

—. 2003b, MNRAS, 339, 289, doi: 10.1046/j.1365-8711.2003.06206.x

Steidel, C. C., Erb, D. K., Shapley, A. E., et al. 2010, ApJ, 717, 289, doi: 10.1088/0004-637X/717/1/289

Stern, J., Fielding, D., Faucher-Giguère, C.-A., & Quataert, E. 2019, MNRAS, 488, 2549, doi: 10.1093/mnras/stz1859

—. 2020, MNRAS, 492, 6042, doi: 10.1093/mnras/staa198

Stern, J., Hennawi, J. F., Prochaska, J. X., & Werk, J. K. 2016, ApJ, 830, 87, doi: 10.3847/0004-637X/830/2/87

Stewart, K. R., Kaufmann, T., Bullock, J. S., et al. 2011, ApJ, 738, 39, doi: 10.1088/0004-637X/738/1/39

Stinson, G. S., Brook, C., Prochaska, J. X., et al. 2012, MNRAS, 425, 1270, doi: 10.1111/j.1365-2966.2012.21522.x

Stocke, J. T., Keeney, B. A., Danforth, C. W., et al. 2013, ApJ, 763, 148, doi: 10.1088/0004-637X/763/2/148

Stocke, J. T., Penton, S. V., Danforth, C. W., et al. 2006, ApJ, 641, 217, doi: 10.1086/500386

Strickland, D. K., & Heckman, T. M. 2007, ApJ, 658, 258, doi: 10.1086/511174

—. 2009, ApJ, 697, 2030, doi: 10.1088/0004-637X/697/2/2030

Strickland, D. K., & Stevens, I. R. 2000, MNRAS, 314, 511, doi: 10.1046/j.1365-8711.2000.03391.x

Strong, A. W., Moskalenko, I. V., & Ptuskin, V. S. 2007, Annual Review of Nuclear and Particle Science, 57, 285, doi: 10.1146/annurev.nucl.57.090506.123011

Su, M., Slatyer, T. R., & Finkbeiner, D. P. 2010, ApJ, 724, 1044, doi: 10.1088/0004-637X/724/2/1044

Suresh, J., Rubin, K. H. R., Kannan, R., et al. 2017, MNRAS, 465, 2966, doi: 10.1093/mnras/stw2499

Tan, B., & Oh, S. P. 2021, MNRAS, 508, L37, doi: 10.1093/mnrasl/slab100

Tan, B., Oh, S. P., & Gronke, M. 2021a, MNRAS, 502, 3179, doi: 10.1093/mnras/stab053

—. 2021b, MNRAS, 502, 3179, doi: 10.1093/mnras/stab053

Tang, Y., Giavalisco, M., Guo, Y., & Kurk, J. 2014, ApJ, 793, 92, doi: 10.1088/0004-637X/793/2/92

Taylor, G. 1950, Proceedings of the Royal Society of London Series A, 201, 159, doi: 10.1098/rspa.1950.0049

Tchernyshyov, K., Werk, J. K., Wilde, M. C., et al. 2022, arXiv e-prints, arXiv:2211.06436, doi: 10.48550/arXiv.2211.06436

—. 2023, ApJ, 949, 41, doi: 10.3847/1538-4357/acc86a

Tejos, N., Prochaska, J. X., Crighton, N. H. M., et al. 2016, MNRAS, 455, 2662, doi: 10.1093/mnras/stv2376

Terrazas, B. A., Bell, E. F., Henriques, B. M. B., et al. 2016, ApJ, 830, L12, doi: 10.3847/2041-8205/830/1/L12

Terrazas, B. A., Bell, E. F., Woo, J., & Henriques, B. M. B. 2017, ApJ, 844, 170, doi: 10.3847/1538-4357/aa7d07

Terrazas, B. A., Bell, E. F., Pillepich, A., et al. 2020, MNRAS, 493, 1888, doi: 10.1093/mnras/staa374

Thielemann, F. K., Nomoto, K., & Yokoi, K. 1986, A&A, 158, 17

Thom, C., Tumlinson, J., Werk, J. K., et al. 2012, ApJ, 758, L41, doi: 10.1088/2041-8205/758/2/L41

Thompson, T. A., & Krumholz, M. R. 2016, MNRAS, 455, 334, doi: 10.1093/mnras/stv2331

Thompson, T. A., Quataert, E., Zhang, D., & Weinberg, D. H. 2016, MNRAS, 455, 1830, doi: 10.1093/mnras/stv2428

Thornton, K., Gaudlitz, M., Janka, H. T., & Steinmetz, M. 1998, ApJ, 500, 95, doi: 10.1086/305704

Tinsley, B. M. 1980, Fund. Cosmic Phys., 5, 287, doi: 10.48550/arXiv.2203.02041

Tonry, J. L., Dressler, A., Blakeslee, J. P., et al. 2001, ApJ, 546, 681, doi: 10.1086/318301

Tremmel, M., Karcher, M., Governato, F., et al. 2017, MNRAS, 470, 1121, doi: 10.1093/mnras/stx1160

Tremmel, M., Quinn, T. R., Ricarte, A., et al. 2019, MNRAS, 483, 3336, doi: 10.1093/mnras/sty3336

Tripp, T. M., Aracil, B., Bowen, D. V., & Jenkins, E. B. 2006, ApJ, 643, L77, doi: 10.1086/505264

Tripp, T. M., Jenkins, E. B., Bowen, D. V., et al. 2005, ApJ, 619, 714, doi: 10.1086/426729

Tripp, T. M., Sembach, K. R., Bowen, D. V., et al. 2008, ApJS, 177, 39, doi: 10.1086/587486

Tripp, T. M., Meiring, J. D., Prochaska, J. X., et al. 2011, Science, 334, 952, doi: 10.1126/science.1209850

Tumlinson, J., Peeples, M. S., & Werk, J. K. 2017, ARA&A, 55, 389, doi: 10.1146/annurev-astro-091916-055240

Tumlinson, J., Shull, J. M., Giroux, M. L., & Stocke, J. T. 2005, ApJ, 620, 95, doi: 10.1086/426961

Tumlinson, J., Thom, C., Werk, J. K., et al. 2011, Science, 334, 948, doi: 10.1126/science.1209840

—. 2013, ApJ, 777, 59, doi: 10.1088/0004-637X/777/1/59

Tunnard, R., Greve, T. R., Garcia-Burillo, S., et al. 2015, ApJ, 800, 25, doi: 10.1088/0004-637X/800/1/25

Turner, M. L., Schaye, J., Steidel, C. C., Rudie, G. C., & Strom, A. L. 2014, MNRAS, 445, 794, doi: 10.1093/mnras/stu1801

—. 2015, MNRAS, 450, 2067, doi: 10.1093/mnras/stv750

Uhlig, M., Pfrommer, C., Sharma, M., et al. 2012, MNRAS, 423, 2374, doi: 10.1111/j.1365-2966.2012.21045.x

van de Voort, F., Schaye, J., Altay, G., & Theuns, T. 2012, MNRAS, 421, 2809, doi: 10.1111/j.1365-2966.2012.20487.x

van de Voort, F., Schaye, J., Booth, C. M., Haas, M. R., & Dalla Vecchia, C. 2011, MNRAS, 414, 2458, doi: 10.1111/j.1365-2966.2011.18565.x

van den Bosch, R. C. E. 2016, ApJ, 831, 134, doi: 10.3847/0004-637X/831/2/134

van Dokkum, P. G., Nelson, E. J., Franx, M., et al. 2015, ApJ, 813, 23, doi: 10.1088/0004-637X/813/1/23

Veilleux, S., Cecil, G., & Bland-Hawthorn, J. 2005, ARA&A, 43, 769, doi: 10.1146/annurev.astro.43.072103.150610

Veilleux, S., Maiolino, R., Bolatto, A. D., & Aalto, S. 2020, A&A Rev., 28, 2, doi: 10.1007/s00159-019-0121-9

Veilleux, S., Rupke, D. S. N., & Swaters, R. 2009, ApJ, 700, L149, doi: 10.1088/0004-637X/700/2/L149

Vito, F., Maiolino, R., Santini, P., et al. 2014, MNRAS, 441, 1059, doi: 10.1093/mnras/stu637

Vogelsberger, M., Genel, S., Springel, V., et al. 2014, MNRAS, 444, 1518, doi: 10.1093/mnras/stu1536

Voit, G. M., Bryan, G. L., O'Shea, B. W., & Donahue, M. 2015, ApJ, 808, L30, doi: 10.1088/2041-8205/808/1/L30

Voit, G. M., Meece, G., Li, Y., et al. 2017, ApJ, 845, 80, doi: 10.3847/1538-4357/aa7d04

Voit, G. M., Oppenheimer, B. D., Bell, E. F., Terrazas, B., & Donahue, M. 2023, arXiv e-prints, arXiv:2309.14818, doi: 10.48550/arXiv.2309.14818

Wadsley, J. W., Keller, B. W., & Quinn, T. R. 2017, MNRAS, 471, 2357, doi: 10.1093/mnras/stx1643

Wadsley, J. W., Stadel, J., & Quinn, T. 2004, New A, 9, 137, doi: 10.1016/j.newast.2003.08.004

Wakker, B. P., & Savage, B. D. 2009, ApJS, 182, 378, doi: 10.1088/0067-0049/182/1/378

Wakker, B. P., Savage, B. D., Fox, A. J., Benjamin, R. A., & Shapiro, P. R. 2012, ApJ, 749, 157, doi: 10.1088/0004-637X/749/2/157

Walch, S., & Naab, T. 2015, MNRAS, 451, 2757, doi: 10.1093/mnras/stv1155

Walter, F., Bolatto, A. D., Leroy, A. K., et al. 2017, ApJ, 835, 265, doi: 10.3847/1538-4357/835/2/265

Webber, W. R. 1998, ApJ, 506, 329, doi: 10.1086/306222

Weinberger, R., Springel, V., Hernquist, L., et al. 2017, MNRAS, 465, 3291, doi: 10.1093/mnras/stw2944

Weiner, B. J., Coil, A. L., Prochaska, J. X., et al. 2009, ApJ, 692, 187, doi: 10.1088/0004-637X/692/1/187

Werk, J. K., Prochaska, J. X., Thom, C., et al. 2012, ApJS, 198, 3, doi: 10.1088/0067-0049/198/1/3

—. 2013, ApJS, 204, 17, doi: 10.1088/0067-0049/204/2/17

Werk, J. K., Prochaska, J. X., Tumlinson, J., et al. 2014, ApJ, 792, 8, doi: 10.1088/0004-637X/792/1/8

Werk, J. K., Prochaska, J. X., Cantalupo, S., et al. 2016, ApJ, 833, 54, doi: 10.3847/1538-4357/833/1/54

Westmoquette, M. 2013, Nature, 499, 416, doi: 10.1038/499416a

White, S. D. M., & Frenk, C. S. 1991, ApJ, 379, 52, doi: 10.1086/170483

White, S. D. M., & Rees, M. J. 1978, MNRAS, 183, 341, doi: 10.1093/mnras/183.3.341

Whitworth, A. 1979, MNRAS, 186, 59, doi: 10.1093/mnras/186.1.59

Wiersma, R. P. C., Schaye, J., & Smith, B. D. 2009a, MNRAS, 393, 99, doi: 10.1111/j.1365-2966.2008.14191.x

Wiersma, R. P. C., Schaye, J., Theuns, T., Dalla Vecchia, C., & Tornatore, L. 2009b, MNRAS, 399, 574, doi: 10.1111/j.1365-2966.2009.15331.x

Wild, V., Kauffmann, G., Heckman, T., et al. 2007, MNRAS, 381, 543, doi: 10.1111/j.1365-2966.2007.12256.x

Wilde, M. C., Werk, J. K., Burchett, J. N., et al. 2021, ApJ, 912, 9, doi: 10.3847/1538-4357/abea14

Williams, B. F., Dolphin, A. E., Dalcanton, J. J., et al. 2017, ApJ, 846, 145, doi: 10.3847/1538-4357/aa862a

Wilson, C. D., Rangwala, N., Glenn, J., et al. 2014, ApJ, 789, L36, doi: 10.1088/2041-8205/789/2/L36

Woosley, S. E., & Weaver, T. A. 1995, ApJS, 101, 181, doi: 10.1086/192237

Wu, X., & McQuinn, M. 2023, ApJ, 945, 87, doi: 10.3847/1538-4357/acbc7d

Yang, Y., & Ji, S. 2023, MNRAS, 520, 2148, doi: 10.1093/mnras/stad264

Yesuf, H. M., Faber, S. M., Trump, J. R., et al. 2014, ApJ, 792, 84, doi: 10.1088/0004-637X/792/2/84

Yoon, J. H., Putman, M. E., Thom, C., Chen, H.-W., & Bryan, G. L. 2012, ApJ, 754, 84, doi: 10.1088/0004-637X/754/2/84

York, D. G., Khare, P., Vanden Berk, D., et al. 2006, MNRAS, 367, 945, doi: 10.1111/j.1365-2966.2005.10018.x

Zafar, T., Centurión, M., Molaro, P., et al. 2014, Mem. Soc. Astron. Italiana, 85, 363, doi: 10.48550/arXiv.1401.8221

Zahedy, F. S., Chen, H.-W., Johnson, S. D., et al. 2019, MNRAS, 484, 2257, doi: 10.1093/mnras/sty3482

Zahedy, F. S., Chen, H.-W., Cooper, T. M., et al. 2021, MNRAS, 506, 877, doi: 10.1093/mnras/stab1661

Zhang, D. 2018, Galaxies, 6, 114, doi: 10.3390/galaxies6040114

Zhang, D., & Chevalier, R. A. 2019, MNRAS, 482, 1602, doi: 10.1093/mnras/sty2769

Zhang, D., & Davis, S. W. 2017, ApJ, 839, 54, doi: 10.3847/1538-4357/aa6935

Zhang, D., Davis, S. W., Jiang, Y.-F., & Stone, J. M. 2018, ApJ, 854, 110, doi: 10.3847/1538-4357/aaa8e4

Zhang, D., Thompson, T. A., Murray, N., & Quataert, E. 2014, ApJ, 784, 93, doi: 10.1088/0004-637X/784/2/93

Zhang, D., Thompson, T. A., Quataert, E., & Murray, N. 2017, MNRAS, 468, 4801, doi: 10.1093/mnras/stx822

Zheng, Y., Peek, J. E. G., Werk, J. K., & Putman, M. E. 2017, ApJ, 834, 179, doi: 10.3847/1538-4357/834/2/179

Zheng, Y., Faerman, Y., Oppenheimer, B. D., et al. 2024, ApJ, 960, 55, doi: 10.3847/1538-4357/acfe6b

Zhu, G., & Ménard, B. 2013, ApJ, 770, 130, doi: 10.1088/0004-637X/770/2/130

Zhu, G., Ménard, B., Bizyaev, D., et al. 2014, MNRAS, 439, 3139, doi: 10.1093/mnras/stu186

Zirakashvili, V. N., Breitschwerdt, D., Ptuskin, V. S., & Voelk, H. J. 1996, A&A, 311, 113

Zschaechner, L. K., Ott, J., Walter, F., et al. 2016, ApJ, 833, 41, doi: 10.3847/1538-4357/833/1/41

Zweibel, E. G. 2013, Physics of Plasmas, 20, 055501, doi: 10.1063/1.4807033

—. 2017, Physics of Plasmas, 24, 055402, doi: 10.1063/1.4984017